Germanium Nanocrystal Solar Cells

A DISSERTATION
SUBMITTED TO THE FACULTY OF THE GRADUATE SCHOOL
OF THE UNIVERSITY OF MINNESOTA
BY

Zachary Charles Holman

IN PARTIAL FULFILLMENT OF THE REQUIREMENTS
FOR THE DEGREE OF
DOCTOR OF PHILOSOPHY

Uwe R. Kortshagen, Advisor

SEPTEMBER 2010

Acknowledgements

I thank my advisor, wife, parents, lab mates, and funding sources for their invaluable contributions to this dissertation.

Abstract

Greenhouse gas concentrations in the atmosphere are approaching historically unprecedented levels from burning fossil fuels to meet the ever-increasing world energy demand. A rapid transition to clean energy sources is necessary to avoid the potentially catastrophic consequences of global warming. The sun provides more than enough energy to power the world, and solar cells that convert sunlight to electricity are commercially available. However, the high cost and low efficiency of current solar cells prevent their widespread implementation, and grid parity is not anticipated to be reached for at least 15 years without breakthrough technologies.

Semiconductor nanocrystals (NCs) show promise for cheap multi-junction photovoltaic devices. To compete with photovoltaic materials that are currently commercially available, NCs need to be inexpensively cast into dense thin films with bulk-like electrical mobilities and absorption spectra that can be tuned by altering the NC size. The Group II-VI and IV-VI NC communities have had some success in achieving this goal by drying and then chemically treating colloidal particles, but the more abundant and less toxic Group IV NCs have proven more challenging. This thesis reports thin films of plasma-synthesized Ge NCs deposited using three different techniques, and preliminary solar cells based on these films.

Germanium tetrachloride is dissociated in the presence of hydrogen in a nonthermal plasma to nucleate Ge NCs. Transmission electron microscopy and X-ray diffraction indicate that the particles are nearly monodisperse (standard deviations of 10-

15% the mean particle diameter) and the mean diameter can be tuned from 4-15 nm by changing the residence time of the Ge NCs in the plasma.

In the first deposition scheme, a Ge NC colloid is formed by reacting nanocrystalline powder with 1-dodecene and dispersing the functionalized NCs in a solvent. Films are then formed on substrates by drop-casting the colloid and allowing it to dry. As-deposited films are electrically insulating due to the long hydrocarbon molecules separating neighboring particles; however, mass spectrometry shows that annealing treatments successfully decompose these molecules. After annealing at 250 °C, Ge NC films exhibit conductivities as large as 10^{-6} S/cm.

In the second film deposition scheme, a Ge NC colloid is formed by dispersing Ge NCs in select solvents without further surface modification. While these "bare" NCs quickly agglomerate and flocculate in nearly all non-polar solvents, they remain stable in benzonitrile and 1,2-dichlorobenzene, among others. Thin-film field-effect transistors have been fabricated by spinning Ge NC colloids onto substrates and the films have been subjected to various annealing procedures. The devices show *n*-type, *p*-type, or ambipolar behavior depending on the annealing conditions, with Ge NC films annealed at 300 °C exhibiting electron saturation mobilities greater than 10^{-2} cm^2/Vs and on-to-off ratios of 10^4.

The final film deposition scheme involves the impaction of Ge NCs onto substrates downstream of the synthesis plasma via acceleration of the NCs through an orifice. This technique produces highly uniform films with densities greater than 50% of the density of bulk Ge. By varying the size of the Ge NCs, we have measured films with

band gaps ranging from the bulk value of 0.7 eV to over 1.1 eV for films of 4 nm Ge NCs.

Having deposited dense thin films with tunable band gaps and respectable mobilities, we have begun fabricating bilayer solar cells consisting of heterojunctions between Ge NC films and P3HT, Si NCs, or Si wafers. Preliminary devices exhibit open-circuit voltages and short-circuit currents as large as 0.3 V and 4 mA/cm^2, respectively.

Table of Contents

Acknowledgements i
Abstract ii
Table of Contents v
List of Tables ix
List of Figures x

CHAPTER 1 INTRODUCTION

1.1 Solar power outlook 1
1.2 Nanocrystal solar cells 5
1.3 The case for germanium 9
1.4 Status of germanium nanocrystal research 11
1.5 Scope of this dissertation 13
1.6 References 17

CHAPTER 2 SYNTHESIS AND CHARACTERIZATION OF GERMANIUM NANOCRYSTALS

2.1 Outline 20
2.2 Introduction 21
2.3 Experimental 24
2.4 Results and discussion 26
2.5 Conclusions 38
2.6 Future work 38
2.7 References 41

CHAPTER 3 SOLUTION-PROCESSED GERMANIUM NANOCRYSTAL THIN FILMS

3.1 Outline 45
3.2 Introduction 46

3.3 Experimental 48
3.4 Results and discussion 53
3.5 Conclusions 69
3.6 Future work 71
3.7 References 72

CHAPTER 4 BARE GERMANIUM NANOCRYSTALS IN SOLUTION

4.1 Outline 75
4.2 Introduction 76
4.3 Experimental 79
4.4 Results and discussion 80
4.5 Conclusions 91
4.6 Future work 92
4.7 References 93

CHAPTER 5 GERMANIUM AND SILICON NANOCRYSTAL THIN-FILM FIELD-EFFECT TRANSISTORS

5.1 Outline 96
5.2 Introduction 97
5.3 Experimental 98
5.4 Results and discussion 101
5.5 Conclusions 116
5.6 Future work 117
5.7 References 119

CHAPTER 6 IMPACTION OF GERMANIUM NANOCRYSTALS

6.1 Outline 122
6.2 Introduction 123
6.3 Background 126

6.4 Experimental 129
6.5 Model description 133
6.6 Results and discussion 138
6.7 Conclusions 154
6.8 Future work 156
6.9 References 158

CHAPTER 7 QUANTUM CONFINEMENT IN GERMANIUM NANOCRYSTAL THIN FILMS

7.1 Outline 161
7.2 Introduction 162
7.3 Experimental 163
7.4 Results and discussion 165
7.5 Conclusions 171
7.6 Future work 171
7.7 References 175

CHAPTER 8 GERMANIUM NANOCRYSTAL SOLAR CELLS

8.1 Outline 177
8.2 Introduction 178
8.3 Experimental 181
8.4 Results and discussion 184
8.5 Conclusions 189
8.6 Future work 190
8.7 References 191

BIBLIOGRAPHY 192

APPENDIX

A.1 Copyright permissions 203
A.2 Processing recipes 204

List of Tables

5.1 Germanium surface Fermi level vs. ambient 118

List of Figures

1-1 Absorption spectra of CdSe NCs 6

1-2 Conductance of a hydrazine-treated PbSe NC film 8

1-3 Open-circuit voltage of a PbSe NC Schottky solar cell vs. NC size 9

1-4 Shift in the conduction band edge of Ge and Si NCs vs. NC size 11

2-1 Schematic and photograph of Ge NC plasma synthesis apparatus 25

2-2 TEM images of Ge NCs of various sizes 27

2-3 Ge NC diameter and standard deviation vs. residence time 28

2-4 Ge NC diameter vs. total gas flow rate 30

2-5 (a) Photographs of plasmas of varying dimensions. (b) Ge NC diameter vs. plasma electrode separation 31

2-6 Ge NC diameter vs. plasma power 32

2-7 (a) XRD data and (b),(c) TEM images of Ge NCs synthesized at low and high power 34

2-8 Raman spectra of Ge NCs synthesized with various powers 35

2-9 Power required to make crystalline NCs vs. H_2/Ar ratio 36

3-1 Schematic of devices for two-probe conductivity measurements 51

3-2 AES spectra of Ge NCs synthesized with various H_2/Ar ratios 55

3-3 FTIR spectra of Ge NCs synthesized with various H_2/Ar ratios 56

3-4 FTIR spectra of neat 1-dodecene, Ge NC powder, and hydrogermylated Ge NCs 58

3-5 SEM and TEM images of Ge NCs thin films cast from mesitylene 60

3-6 I-V characteristics of as-deposited and annealed Ge NC films 61

3-7 Mass spectra showing desorption products when Ge NCs are annealed 64

3-8 Sample weight loss and FTIR signal decrease vs. annealing temperature 65

3-9 XRD spectra of as-deposited and annealed Ge NC films 68

3-10 SEM images of as-deposited and annealed Ge NC films 69

4-1 Solvents used to solubilize bare Ge NCs 81

4-2 (a) Photograph and (b) measured concentration of Ge NCs remaining in solution after filtering 82
4-3 Ge NC post-filtration concentration vs. solvent dielectric constant 85
4-4 Ge NC post-filtration concentration vs. solvent Hansen Solubility Parameters.....86
4-5 SEM images of thin and thick Ge NC films cast from benzonitrile 87
4-6 Molar absorptivity of colloidal Ge NCs of various sizes in benzonitrile ..88
4-7 Energy band diagram of bulk Ge.....89
4-8 Photograph of three sizes of colloidal Ge NCs in benzonitrile.....90
4-9 Energy of two Ge absorption features vs. NC size 91
5-1 (a) Schematic, (b) photograph, and (c),(d) SEM images of Ge and Si NC FETs.....102
5-2 Transfer and output characteristics for Ge NC FETs annealed at 300 and 600 °C and an unannealed Si NC FET 104
5-3 Field-effect mobility of Ge NC films vs. annealing temperature 106
5-4 FTIR spectra of neat DCB, Ge and Si NC powders, and Ge and Si NCs cast from DCB 108
5-5 Atomic concentration of H and Cl in Ge NC films vs. annealing temperature 110
5-6 FTIR spectra of neat DCB and as-deposited and annealed Ge NC films 111
5-7 Partial pressure of H_2 and HCl desorbing from Ge NCs vs. temperature 112
5-8 Transfer characteristics of annealed Ge NC FETs vs. air exposure time 114
5-9 Ge NC size vs. annealing temperature.....115
6-1 Cartoon of a supersonic impactor 128
6-2 Schematics of the (a) impaction apparatus and (b) orifice holder 130
6-3 Profiles of the gas (a) Mach number, (b) temperature, (c) density, and (d) velocity in the supersonic jet.....136

6-4 Photograph of impacted Ge NC films....139
6-5 SEM images and photograph of patterned Ge NC films 140
6-6 SEM images of fluffy and dense Ge NC films 141
6-7 Relative density of Ge NC films vs. pressure ratio across the orifice 144
6-8 Modeled Ge NC impaction velocity vs. pressure ratio across the orifice 144
6-9 Modeled Ge NC velocity vs. position relative to orifice, changing the pressure ratio 146
6-10 Relative density of Ge NC films vs. position relative to orifice 148
6-11 Modeled Ge NC velocity vs. position relative to orifice 148
6-12 Modeled Ge NC velocity vs. position relative to orifice, changing the upstream pressure....150
6-13 Modeled Ge NC velocity vs. position relative to orifice, changing the gas temperature 151
6-14 Relative density of Ge NC films vs. pressure ratio across the orifice, comparing He and Ar gases 152
6-15 XRD spectra of impacted films of Ge NCs of various sizes....154
6-16 Photograph of patterned, impacted, luminescent Si NC film 157
7-1 (a),(b) TEM images of Ge NCs, (c) SEM image of an impacted Ge NC film, and (d) photograph of three impacted films 164
7-2 (a) Absorption coefficient and (b) square-root of the absorption coefficient of impacted Ge NC films 167
7-3 Approximate optical bandgap of films vs. NC size 169
7-4 Field-effect mobility of imopacted Ge NC films vs. annealing temperature 172
7-5 (a) Raman spectra of Ge NCs synthesized with various powers and (b) conductivity of Ge NC films vs. plasma power 173
7-6 Conductivity of Ge NC films vs. H_2/Ar ratio measured (a) in N_2 ambient and (b) in air 173
7-7 Conductivity of Ge NC films vs. film density 174

8-1 Examples of solar cell architectures using NC films from the literature 179
8-2 Schematic of solar cells fabricated on ITO-coated glass 182
8-3 SEM image of a Ge NC film on a Si solar cell substrate.....183
8-4 Schematic of solar cells fabricated on Si wafers 183
8-5 (a) Energy diagram and (b) I-V characteristics of a Ge NC/P3HT bilayer solar cell 185
8-6 (a) Energy diagram and (b) I-V characteristics of a Si NC/P3HT bilayer solar cell 186
8-7 (a) Energy diagram, (b) SEM image, (c) I-V characteristic, (d) IPCE curve, and (e) light sensitivity data of a Si NC/Ge NC bilayer solar cell.....187
8-8 I-V characteristics for Ge NC/Si wafer bilayer solar cells with (a) Al and (b) ITO top contacts 189
8-9 I-V characteristics showing roll-over in (a) Ge NC/Si wafer and (b) CdTe solar cells. 189

1

Introduction

1.1 Solar power outlook

According to the 2004 World Energy Assessment, the 2001 world primary energy usage was 4×10^{20} J, or an average power consumption of 13 TW.[1] In an adaptation of the 1992 Intergovernmental Panel on Climate Change assessment, Hoffert *et al.* reported that approximately 25 TW of primary power will be required by 2035, at which point a minimum of 10 TW of carbon-free energy will be needed to stabilize the atmospheric CO_2 concentrations at the historically unprecedented level of 550 ppm.[2] Clean, renewable energy sources currently provide less than 1 TW of energy. Technically feasible global hydropower resources are estimated at 1.5 TW, of which 0.6 TW has already been tapped; wind resources are estimated at 2–4 TW; harvestable terrestrial geothermal resources are estimated to be a few TW; and 15% of the world's total land mass would need to be dedicated to growing biomass for energy generation in order to

produce 10 TW of carbon-neutral power.[3] By contrast, 120,000 TW of solar energy strikes the earth's surface. Assuming 10% solar-energy-to-electricity conversion efficiency (solar modules with better efficiencies are currently available), the sunlight incident on half of Arizona could provide all of the United States' primary energy. While all renewable sources will likely be present in our future energy mix, it is clear that solar must play a large role. The issue is not one of energy availability, but economics.

Solar energy is converted to electricity via photovoltaic or solar cells which currently have limited market share due to their high cost-to-power-output ratio. Crystalline Si wafer-based solar cells—which consist of a *p*-*n* junction sandwiched between a metal electrode and glass coated with a conductive transparent electrode—dominate the market and produce electricity at a cost of 25-50 ¢/kWh, compared to 1-4 ¢/kWh for coal power (2002 US data).[3] Silicon photovoltaics have followed a learning curve for the past 40 years in which a doubling of the cumulative module* production has resulted in a 20% decrease in module cost.[4] If this trend were maintained, the 10 times cost reduction necessary for solar power to compete with fossil fuel sources would not be reached until after 2025, assuming continued growth in the photovoltaics market.[5] At that point, less than 1 TW of solar power would be installed. Furthermore, Surek predicted in his recent review of the photovoltaics industry that the learning curve can only be sustained for a few more years.[4] These grim statistics have spurred calls for the development of breakthrough photovoltaic technologies.

* A module is a collection of photovoltaic cells wired together and encapsulated in some sort of protective packaging. Customers buy modules—not individual cells—which can then be installed on rooftops, etc.

There are two approaches to the problem: cut costs or increase module energy output. Both approaches will need to play a role in achieving affordable solar power since module outputs cannot be increased by more than a few times and total costs would not be sufficiently reduced even if 10% efficient modules were free. For a typical 3 kW residential Si photovoltaic installation, modules account for ~65% of the total cost while the inverter (~12%), mounting structures (~10%), and installation (~10%)—collectively referred to as the "balance of systems"—account for the rest.[6] Of the module cost, roughly 60% comes from the Si wafers (including the labor, capital, etc. to produce the wafers), depending on the widely varying polysilicon feedstock price.[7] The balance arises from other materials costs (metal, glass, transparent conductor, module framing materials), labor, depreciation, etc. These solar cells typically use wafers on the order of 200 μm thick since kerf and yield losses increase with thinner, more brittle wafers. However, comparable light absorption can be achieved with a semiconductor layer 100 times thinner. As a result, module prices can be significantly reduced by moving away from wafers to thin films, which is the present push in industry. In 1997, Little and Nowlan calculated that thin-film modules should be roughly one-third the price of Si wafer-based modules of equivalent power output,[8] although this cost savings has not yet been entirely realized since thin-film manufactures have not yet achieved the same economies of scale as Si photovoltaic manufacturers. It should be noted that more than just semiconductor material costs can be saved with thin-film modules, since new manufacturing opportunities arise such as replacing heavy, rigid glass substrates with cheap, flexible metal foil or plastic. Balance-of-systems costs like mounting hardware

and installation fees will be reduced with module costs, since thin flexible solar cells can be integrated directly into building materials such as roofing tiles. Thus, it is conceivable that a thin-film photovoltaic installation of comparable efficiency to a Si installation could produce electricity at one-third or one-quarter the *total* cost. However, a major challenge in thin-film solar cells is obtaining efficiencies comparable to Si photovoltaics.

The second approach to reducing the cost per kilowatt-hour is to increase the module energy output, which depends on the sunlight-to-electricity power conversion efficiency, the lifetime of the modules (since the price is discounted over the lifetime to obtain the cost per kilowatt-hour), and the intensity of the solar irradiation incident on the module (photovoltaic systems in California generate more power than those in Iceland). The main factor of interest to materials scientists and device engineers is efficiency, the importance of which cannot be underestimated. It is tempting to think that modules that are half the efficiency but half the cost are just as good as their full-efficiency, full-cost counterparts, but this is false. Balance-of-systems costs such as installation and mounting hardware scale with the area installed, and will be appreciably larger for less efficient modules. Thus, an x-fold increase in module efficiency will result in a greater-than-x reduction in the cost per kilowatt-hour.

The theoretical conversion efficiency limit for a single *p-n* junction solar cell is 31%, but this limit can be increased to 55% by adding three additional junctions in series.[9,10] The idea behind these tandem or multi-junction solar cells is that the large-bandgap top junction will selectively absorb incident blue and UV light and convert it to electricity while allowing less energetic photons to pass through to subsequent junctions.

The next, smaller-bandgap junction will selectively absorb green light, the following junction yellow light, etc. With this design, all incident wavelengths are absorbed while minimizing thermalization losses that occur when a material absorbs light that is much more energetic than its bandgap. While the best single junction cell fabricated had an efficiency of 25%, triple-junction cells have been fabricated with efficiencies as large as 32%.[11] Regrettably, they are expensive. The bandgap of a bulk material is fixed, requiring a different material for each junction. Each material brings its own set of difficulties, including high costs for the GaInP and GaAs junctions commonly used. In short, there is a lack of materials from which to choose, and this is a challenge faced in thin-film devices as well as in wafer-based devices.

1.2 Nanocrystal solar cells

Semiconductor nanocrystals (NCs) or quantum dots are uniquely suited to simultaneously lower costs and increase efficiencies of photovoltaic devices. They can be deposited as thin films—most often, but not necessarily, from colloidal solutions—on inexpensive, flexible substrates. In addition, quantum confinement allows the optical properties of a material to be decoupled from its electrical, chemical, and mechanical properties. When crystals are smaller than the Bohr exciton radius—the length scale of the Coulomb attraction between an excited electron-hole pair—their optical properties become size dependent. This includes the absorption spectra, which researchers have tuned across the entire visible spectrum for some quantum dots (Fig. 1-1).[12] It is therefore conceivable that a multi-junction solar cell could be constructed using a single

material, where the crystallite size in each junction is chosen to selectively absorb the desired portion of the incident sunlight spectrum.

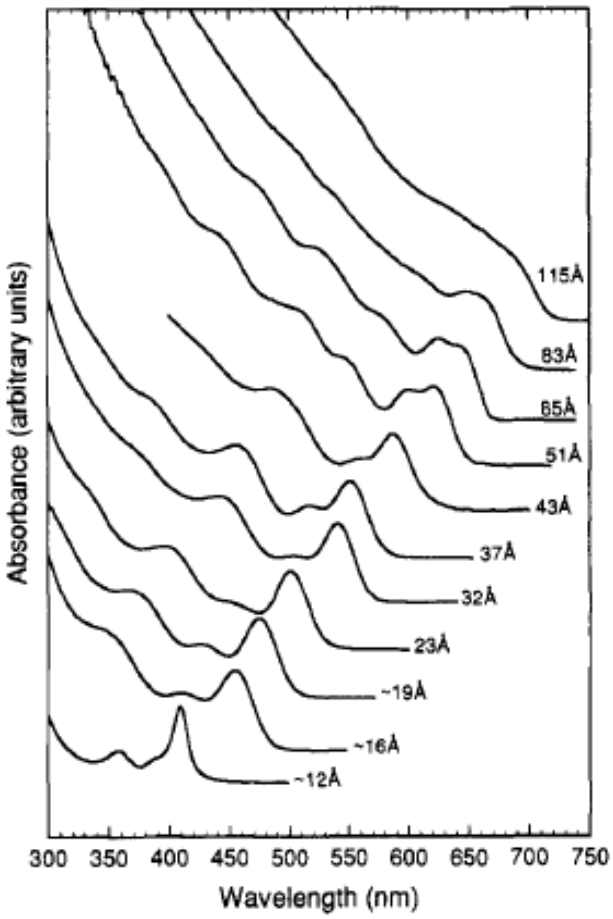

Figure 1-1. Absorption spectra of CdSe quantum dots showing the shift of the excitonic absorption features over the visible spectrum with changing NC size. Adapted from [12].

The first solar cells to employ quantum dots were hybrid devices utilizing polymer in conjunction with NCs. In 2002, Huynh et al. made 1.7% efficient devices by spin-coating a blend of colloidal CdSe nanorods and poly-3(hexylthiophene).[13] Absorption in the devices was dominated by the NCs for wavelengths greater than 650 nm and the authors were able to change the external quantum efficiency at these wavelengths by altering the nanorod diameter. This indicates that the rods were quantum

confined and the range of wavelengths over which the devices successfully generated electricity could be tuned via the crystallite size.

The same research group fabricated the first reported all-NC photovoltaic devices in 2005 using a blend of CdSe and CdTe nanorods spun from a colloidal solution.[14] After sintering the films at 400˚ C in air, power conversion efficiencies as large as 2.9% were obtained under simulated sunlight. The authors went to great lengths to argue that the driving force in these devices was not the formation of a Schottky barrier at one of the electrodes or even a p-n junction within the semiconductor film, but rather directed diffusion within each of the two semiconducting phases. Remarkably, the respectable efficiencies were obtained despite the fact that films of CdSe or CdTe nanorods individually were highly resistive. Carrier transport is often a problem in films of NCs because of large interparticle spaces, surface trap states, and large energies required to add a carrier to a nanocrystal.

There have been recent improvements in transport in certain quantum dot systems, such as the more than ten orders of magnitude increase in conductivity observed by Talapin and Murray in PbSe NC films upon hydrazine chemical treatment (reproduced in Fig. 1-2).[15] These developments led to three recent publications of NC-only solar cells in which a Schottky barrier is formed at the junction of the metal electrode and a film of spherical quantum dots.[16-18] The devices were made by dip- or spin-coating substrates in PbS or PbSe NCs to form thin films which were then subjected to chemical treatments to improve transport in two of the three cases. A metal electrode evaporated on top formed a Schottky barrier with the film, and the authors clearly demonstrated that

a built-in potential resulting from the barrier was present in the films and drove the devices under illumination. Large short-circuit currents of over 20 mA/cm^2 were measured although the open-circuit voltages were low because of the narrow bandgaps of PbSe and PbS. However, all three groups saw excitonic features in the quantum efficiency spectra indicating quantum confinement of the NC films, and Luther et al. showed that the open-circuit voltage of their devices could be controllably increased by decreasing the NC size (Fig. 1-3). This demonstrates the potential power of quantum dot photovoltaics: tunable spectral sensitivity and thus device performance. Finally, efficiencies of 2.1% were measured under solar simulation and over 4% IR power conversion efficiencies were achieved despite only modest conductivities (5×10^{-5} S/cm) and mobilities (10^{-3} cm^2/Vs) in the NC films.

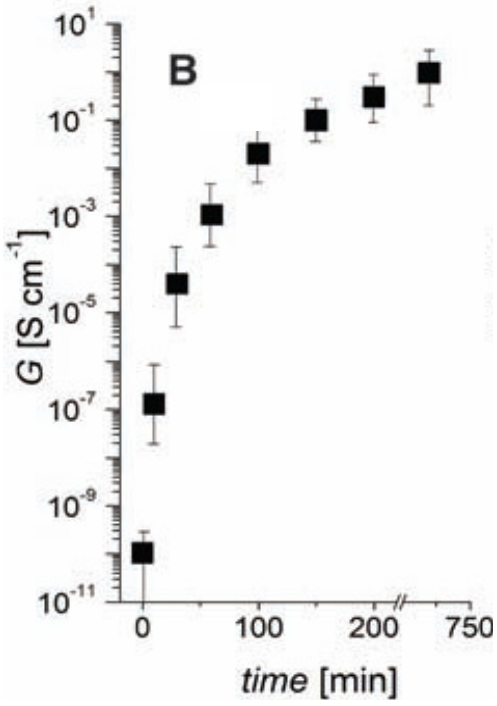

Figure 1-2. Conductance of a PbSe NC film versus exposure time to hydrazine. Adapted from [15].

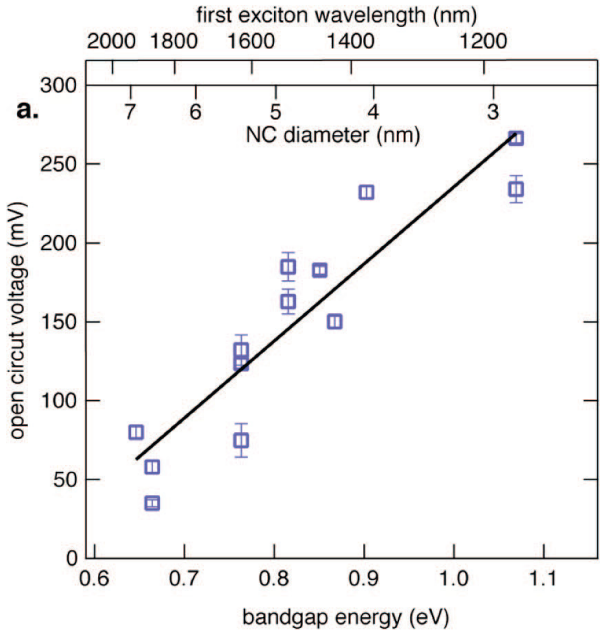

Figure 1-3. Decreasing PbSe NC diameter results in an increase in solar cell open-circuit voltage. Adapted from [18].

1.3 The case for germanium

Most of the progress made in the field of quantum dot devices has involved group II-VI or group IV-VI materials. There is significant interest in reproducing this work with non-toxic and abundant materials such as Si and Ge. Unfortunately, development of similar quantum confined films of group IV NCs has been slowed by difficulties synthesizing spherical NCs with narrow size distributions and dispersing them into solution. The standard synthesis technique for II-VI and IV-VI NCs such as CdSe and PbTe produces colloidal solutions which provide a convenient starting point for film formation.[12] However, an analogous solution synthesis route does not exist for group VI materials because of their high crystallization temperatures resulting from the covalent

nature of their bonds.[19] Researchers have devised alternative synthesis methods and produced quantum confined Si and Ge NCs in solution,[20-24] but reports of films of NCs remain limited.

Germanium is often overlooked in favor of Si because of the narrow bandgap and poor oxide of bulk Ge, and the brilliantly successful history of Si in electronic devices. However, Ge quantum dots may be better candidates for multi-junction solar cell applications than Si quantum dots. Germanium absorbs light better than Si because of its near-direct bandgap. In addition, although the bandgap of bulk Ge is narrow, theoretical and experimental work suggests that the Ge bandgap is very sensitive to crystallite size reductions—more sensitive than Si—because of its large Bohr exciton radius (Fig. 1-4). According to theoretical calculations by Nesher et al.[25] and Takagahara et al.,[26] and absorption measurements by Wilcoxon et al.,[24] Takeoka et al.,[27] and Lee et al.[28] 2 nm Ge NCs are predicted to have a bandgap of ~2 eV. As a result, it should be possible to tune the absorption edge of Ge NCs from the IR across the visible wavelengths without requiring unfeasibly small crystallites.

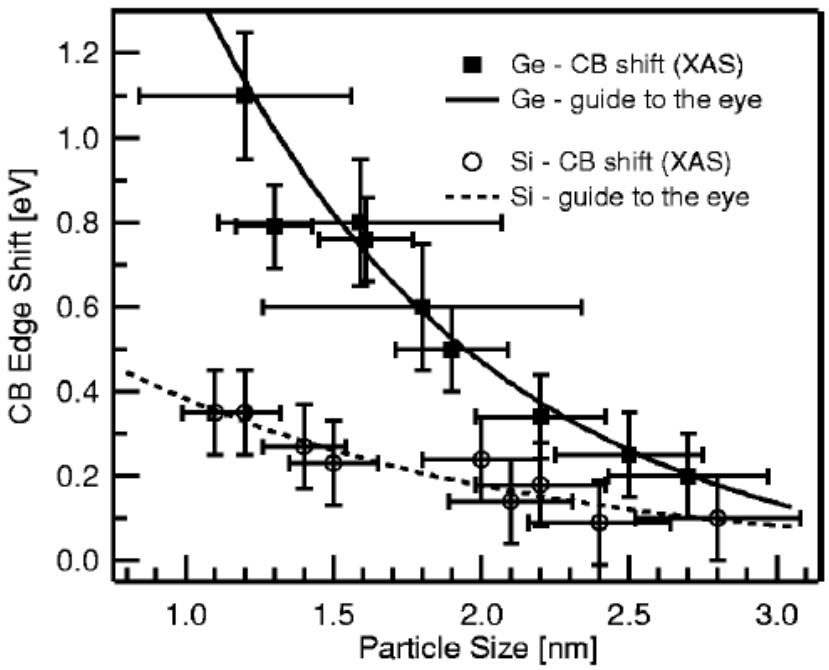

Figure 1-4. Shift of the conduction band edge of Si and Ge quantum dots as a function of NC size, showing the sensitivity of Ge to size reductions. Adapted from [29].

1.4 Status of germanium nanocrystal research

For solar cell applications, the ideal quantum dot synthesis route would produce freestanding, monodisperse NCs (for tunable absorption) in large yields (~5 g is needed for a 1 m^3 solar cell). Many Ge NC synthesis techniques have previously been reported. Liquid-phase Ge NC synthesis techniques are convenient for subsequent liquid-phase surface-functionalization reactions,[24,30-33] but these synthetic routes are often time consuming, have low material yields, and sometimes produce Ge NCs with broad size and shape distributions. Germanium NCs can also be precipitated in the solid phase,[34-37] which leaves Ge NCs embedded in a matrix material such as SiO_2 that, in many cases,

passivates the surfaces very well. However, the range of possible surface treatments for embedded Ge NCs is limited, as is the flexibility of using embedded NCs for device applications. Gas-phase synthesis[38,39] produces freestanding Ge NCs with surfaces are easily accessible for functionalization.[21,40,41] Unfortunately, uncontrollable particle agglomeration is present in most gas-phase processes. Such agglomeration makes it challenging to synthesize NCs with a narrow size distribution, and may cause loss of quantum confinement.[42]

In addition to the plasma synthesis route described here, two reported techniques are particularly impressive. Wilcoxon *et al.* grew Ge NCs inside surfactant aggregates, known as inverse micelles.[24] The surfactants are placed in an oil-based solvent so that their hydrophobic tails extend into the solvent and their hydrophilic heads aggregate to create nanometer-sized hydrophilic volumes, the exact size of which can be varied. Germanium salt, which is completely insoluble in the oily solvent, is then dissolved in the interior volume of the inverse micelles. Finally, a metal hydride is added to reduce the Ge salt, and Ge NCs nucleate and grow to fill the volume of the inverse micelles. The authors found that the absorption and photoluminescence spectra of an ensemble of quantum dots, which are characteristic of the dots' bandgap and therefore their size, can be finely tuned by changing the size of the inverse micelle interior. Transmission electron microscope (TEM) images showing spherical, crystalline quantum dots 2 and 4 nm in diameter (from different reactions) corroborate this finding, and high-resolution chromatography indicates narrow size distributions.

In 2008, Stoldt *et al.* reported a gas-phase synthesis route in which an organic Ge precursor, tetrapropylgermane, is nebulized and the resulting droplets are then passed through a series of furnaces where the precursor is thermally decomposed and Ge NCs are condensed.[39] This technique, known as ultrasonic aerosol pyrolysis, produces spherical, unagglomerated, and relatively monodisperse Ge-NCs with diameters which can be tuned from 3-11 nm by adjusting the precursor concentration. The authors collected the Ge NCs by bubbling them through a solvent, although it is unclear whether or not the colloid was stable and why agglomeration is avoided.

Despite recent advances in synthesizing Ge NCs, we are not aware of any publications reporting thin films of freestanding Ge NCs, let alone films with tunable absorption and favorable electronic properties as would be needed for the multi-junction quantum dot solar cells previously envisioned. Devices based on films of Ge NCs, of course, are also yet to be realized.

1.5 Scope of this dissertation

This dissertation is concerned with the development of thin films of Ge NCs for use in future solar cells. Five years ago, I envisioned fabricating working photovoltaic devices with power conversion efficiencies >1% by the end of my degree. The realities of research, however, have dictated that my work almost exclusively be dedicated to developing Ge NCs as a potential electronic material rather than making solar cells. Fortunately, the results of this research provide much of the necessary foundation for future students to begin constructing devices, and the scientific phenomena and

processing techniques discovered along the way are of interest to a much broader audience.

Four processes occur in every solar cell: exciton generation upon light absorption, exciton dissociation, charge carrier transport, and charge carrier collection at the electrodes. The second and fourth processes depend on the interfaces and energetic alignment between two or more materials (e.g., carrier separation in the built-in electric field generated when *p*- and *n*-type materials are brought into contact, or the collection of electrons at a metal-semiconductor junction), but the first and third processes happen within each material, independent of the others. Efficient light absorption—and in the case of NC solar cells, *tunable* light absorption—and carrier transport are thus prerequisites for consideration for use in solar cells. Studying and improving these properties in thin films of Ge NCs is the focus of this dissertation.

Chapters 2-7 are presented as modified manuscripts which have either been published or submitted for publication. The synthesis of high-quality Ge NCs using a nonthermal plasma is described in Chapter 2. The effects of plasma power, plasma geometry, plasma pressure, and gas flow rates on the resulting Ge NCs are investigated in detail. Adjusting these parameters allow for intimate control of NC size, crystallinity, and surface chemistry. Some of this chapter has been published as Ryan Gresback, Zachary Holman, and Uwe Kortshagen, "Nonthermal plasma synthesis of size-controlled, monodisperse, freestanding germanium nanocrystals," *Applied Physics Letters* **91**, 093119 (2007).

Chapter 3 has been published as Zachary Holman and Uwe Kortshagen, "Solution-processed germanium nanocrystal thin films as materials for low-cost optical and electronic devices," *Langmuir* **25**, 11883 (2009). This chapter describes the formation of Ge NC colloidal solutions via the reaction of Ge NC powder with alkene molecules and subsequent suspension of the functionalized NCs in non-polar solvents. Provided the right solvent is chosen, uniform thin films may be cast from these solutions. Unfortunately, the films are electrically insulating prior to annealing treatments at temperatures of 250 °C or higher. A study reveals that the alkene ligands which were required for solubility prevent charge carrier transfer between NCs, and the films only become semiconducting after these molecules decompose during annealing.

In Chapter 4, an alternative method for forming Ge NC colloids is presented, in which no ligands or reactions are required. With careful solvent choice, "bare" Ge NCs form a stable, transparent colloid. The stabilization mechanism is not yet understood, but we hypothesize that it either involves a reduction in the van der Waals forces that cause agglomeration due to Hamaker constant matching, or electrostatic repulsion. We demonstrate that the non-interacting Ge NCs in these solvents demonstrate quantum confinement, and we present results on the quality of spun films. A manuscript based on this chapter is in preparation as Zachary Holman and Uwe Kortshagen, "Nanocrystal inks without ligands."

Chapter 5 presents field-effect transistors (FETs) using the thin Ge NC films developed in Chapter 4. FETs are a useful tool for gauging the electronic quality of materials under consideration for photovoltaic applications since charge carrier mobilities

can be easily extracted. Germanium NC FETs exhibit *n*-type behavior for annealing temperatures between 200 and 400 °C, and *p*-type behavior for temperatures above 600 °C. Mobilities as large as 0.02 cm^2/Vs were measured, which approach the mobilities in amorphous Si and common semiconducting polymers. We observe that device behavior strongly depends on the state of the NC surfaces, which presents both opportunities and challenges for future device design. This chapter has been published as Zachary Holman, Chin-Yi Liu, and Uwe Kortshagen, "Germanium and silicon nanocrystal thin-film field-effect transistors from solution," *Nano Letters* **10**, 2661 (2010).

Chapter 6 investigates a gas-phase method for depositing NC films, and has been published as Zachary Holman and Uwe Kortshagen, "A flexible method for depositing dense nanocrystal thin films: Impaction of germanium nanocrystals," *Nanotechnology* **21**, 335302 (2010). Germanium NCs are accelerated through a slit-shaped orifice directly downstream of the synthesis plasma, and are impacted onto a rastered substrate. The density of an impacted film increases with increasing pressure ratio across the orifice and an appropriate distance between the orifice and substrate. Films that are greater than 50% of the density of bulk Ge are reproducibly achieved for a variety of NC sizes, approaching the random packing limit for monodisperse hard spheres.

The absorption spectra of impacted Ge NC films are presented in Chapter 7, and blue-shift with decreasing NC size. Approximate bandgaps for the films are extracted and compared to the peak photoluminescence energy (reported by others) for isolated Ge NCs. The comparison indicates that there is little, if any, loss of quantum confinement during the transition from individual, non-interacting Ge NCs to dense films of NCs in

direct contact. This is promising for future multijunction photovoltaics based exclusively on films of Ge NCs. Chapter 7 has been submitted for publication as Zachary Holman and Uwe Kortshagen, "Quantum confinement in germanium nanocrystal thin films."

Chapter 8 presents measurements of preliminary solar cells which use thin films of Ge NCs. These devices confront new issues which arise when Ge NC films are used in conjunction with other materials (e.g., energy level alignment). A shortage of time prevented proper investigation and resolution of these matters; I recommend future experiments which might prove illuminating.

1.6 References

[1] J. Goldemberg and T. B. Johansson, *World Energy Assessment Overview: 2004 Update*, www.undp.org, (2004).

[2] M.I. Hoffert, K. Caldeira, A.K. Jain, E.F. Haites, L.D.D. Harvey, S.D. Potter, M.E. Schlesinger, S.H. Schneider, R.G. Watts, T.M.L. Wigley, and D.J. Wuebbles, *Nature* **395**, 881 (1998).

[3] N.S. Lewis, *MRS Bull.* **32**, 808 (2007).

[4] T. Surek, *J. Cryst. Growth* **275**, 292 (2005).

[5] D. Poponi, *Sol. Energy* **74**, 331 (2003).

[6] D. Poponi, J. Byrne, and S. Hegedus, *Energy Studies Review* **14**, 104 (2006).

[7] M. Rogol, in *Photon International*, January, 84 (2008).

[8] R.G. Little and M.J. Nowlan, *Prog. Photovoltaics* **5**, 309 (1997).

[9] C.C. Grosjean and A. Devos, *J. Phys. D: Appl. Phys.* **14**, 883 (1981).

[10] W. Shockley and H.J. Queisser, *J. Appl. Phys.* **32**, 510 (1961).

[11] M.A. Green, K. Emery, Y. Hishikawa, and W. Warta, *Prog. Photovoltaics* **16**, 61 (2008).

[12] C.B. Murray, D.J. Norris, and M.G. Bawendi, *J. Am. Chem. Soc.* **115**, 8706 (1993).

[13] W.U. Huynh, J.J. Dittmer, and A.P. Alivisatos, *Science* **295**, 2425 (2002).

[14] I. Gur, N.A. Fromer, M.L. Geier, and A.P. Alivisatos, *Science* **310**, 462 (2005).

[15] D.V. Talapin and C.B. Murray, *Science* **310**, 86 (2005).

[16] K.W. Johnston, A.G. Pattantyus-Abraham, J.P. Clifford, S.H. Myrskog, D.D. Macneil, L. Levina, and E.H. Sargent, *Appl. Phys. Lett.* **92**, 151115 (2008).

[17] G.I. Koleilat, L. Levina, H. Shukla, S.H. Myrskog, S. Hinds, A.G. Pattantyus-Abraham, and E.H. Sargent, *ACS Nano* **2**, 833 (2008).

[18] J.M. Luther, M. Law, M.C. Beard, Q. Song, M.O. Reese, R.J. Ellingson, and A.J. Nozik, *Nano Lett.* **8**, 3488 (2008).

[19] J.R. Heath and J.J. Shiang, *Chem. Soc. Rev.* **27**, 65 (1998).

[20] J.D. Holmes, K.J. Ziegler, R.C. Doty, L.E. Pell, K.P. Johnston, and B.A. Korgel, *J. Am. Chem. Soc.* **123**, 3743 (2001).

[21] D. Jurbergs, E. Rogojina, L. Mangolini, and U. Kortshagen, *Appl. Phys. Lett.* **88**, 233116 (2006).

[22] S. Sato and M.T. Swihart, *Chem. Mater.* **18**, 4083 (2006).

[23] B.R. Taylor, S.M. Kauzlarich, G.R. Delgado, and H.W.H. Lee, *Chem. Mater.* **11**, 2493 (1999).

[24] J.P. Wilcoxon, P.P. Provencio, and G.A. Samara, *Phys. Rev. B* **64**, 035417 (2001).

[25] G. Nesher, L. Kronik, and J.R. Chelikowsky, *Phys. Rev. B* **71**, 035344 (2005).

[26] T. Takagahara and K. Takeda, *Phys. Rev. B* **46**, 15578 (1992).

[27] S. Takeoka, M. Fujii, S. Hayashi, and K. Yamamoto, *Phys. Rev. B* **58**, 7921 (1998).

[28] D.C. Lee, J.M. Pietryga, I. Robel, D.J. Werder, R.D. Schaller, and V.I. Klimov, *J. Am. Chem. Soc.* **131**, 3436 (2009).

[29] C. Bostedt, T. Van Buuren, T.M. Willey, N. Franco, L.J. Terminello, C. Heske, and T. Moller, *Appl. Phys. Lett.* **84**, 4056 (2004).

[30] D. Gerion, N. Zaitseva, C. Saw, M.F. Casula, S. Fakra, T. Van Buuren, and G. Galli, *Nano Lett.* **4**, 597 (2004).

[31] J.R. Heath, J.J. Shiang, and A.P. Alivisatos, *J. Chem. Phys.* **101**, 1607 (1994).

[32] X.M. Lu, B.A. Korgel, and K.P. Johnston, *Chem. Mater.* **17**, 6479 (2005).

[33] B.R. Taylor, S.M. Kauzlarich, H.W.H. Lee, and G.R. Delgado, *Chem. Mater.* **10**, 22 (1998).

[34] W.K. Choi, H.G. Chew, V. Ho, V. Ng, W.K. Chim, Y.W. Ho, and S.P. Ng, *J. Cryst. Growth* **288**, 79 (2006).

[35] M. Fujii, S. Hayashi, and K. Yamamoto, *Jpn. J. Appl. Phys., Part 1* **30**, 687 (1991).

[36] T.P. Leervad Pedersen, J.S. Jensen, J. Chevallier, O. Hansen, J.M. Jensen, B.B. Nielsen, and A.N. Larsen, *Appl. Phys. A* **81**, 1591 (2005).

[37] J.G. Zhu, C.W. White, J.D. Budai, S.P. Withrow, and Y. Chen, *J. Appl. Phys.* **78**, 4386 (1995).

[38] C. Bostedt, T. Van Buuren, J.M. Plitzko, T. Moller, and L.J. Terminello, *J. Phys.: Condens. Matter* **15**, 1017 (2003).

[39] C.R. Stoldt, M.A. Haag, and B.A. Larsen, *Appl. Phys. Lett.* **93**, 043125 (2008).

[40] Y.C. Liao and J.T. Roberts, *J. Am. Chem. Soc.* **128**, 9061 (2006).

[41] A.M. Nienow and J.T. Roberts, *Chem. Mater.* **18**, 5571 (2006).

[42] C. Bostedt, T. Van Buuren, T.M. Willey, and L.J. Terminello, *Appl. Phys. Lett.* **85**, 5334 (2004).

2

Synthesis and characterization of germanium nanocrystals[*]

2.1 Outline

This chapter discusses the synthesis of monodisperse germanium nanocrystals via a nonthermal plasma approach which allows for precise control of the nanocrystal size. Germanium crystals are synthesized from germanium tetrachloride and hydrogen entrained in an argon background gas. The crystal size can be varied between 4-50 nm by changing the residence times of crystals in the plasma between ~30-440 ms. Adjusting the plasma power enables one to synthesize fully amorphous or fully crystalline particles with otherwise similar properties.

[*] Reproduced in part with permission from Ryan Gresback, Zachary Holman, and Uwe Kortshagen, "Nonthermal plasma synthesis of size-controlled, monodisperse, freestanding germanium nanocrystals," *Applied Physics Letters* **91**, 093119 (2007). Copyright 2007 American Institute of Physics.

2.2 Introduction

Semiconductor nanocrystals have received significant attention in recent years due to their size-dependent optical and electronic properties. Most of the attention given to group IV semiconductor nanocrystals has focused on silicon nanocrystals (Si NCs), due to their efficient and tunable light emission.[1-5] However, germanium nanocrystals (Ge NCs) may be more interesting than Si NCs for device applications that require a small bandgap material, a material that exhibits stronger quantum confinement than Si, or a material that absorbs light better than Si. In particular, Ge NCs may be well suited for photovoltaic applications since both theoretical[6,7] and experimental[8-10] studies have shown that the bandgap of Ge NCs can be tuned across the solar spectrum from the bulk Ge bandgap of ~0.7 eV, to ~2 eV for crystals 2 nm in diameter.

Many synthesis techniques have previously been reported in which Ge NCs are precipitated in the solid phase,[11-14] grown in solution,[8,9,15-18] or nucleated in the gas phase.[19,20] Germanium NCs are nucleated in the solid phase upon annealing films of co-sputtered Ge and SiO_2.[11-14] Unfortunately, this method gives little control over NC size, shape, placement, and future manipulation, and the Ge NC-embedded films are of little interest for device applications which require charge carriers to pass between NCs.

Solution syntheses are most common and involve the reduction of germanium tetrachloride ($GeCl_4$) or germanium diiodide (GeI_2) by a strong reducing agent such as an alkyllithium.[8,9,15-18] The idea is to mimic the approach used in the colloidal synthesis of II-VI and IV-VI NCs in which a nucleation burst is initiated in a heated solvent by the injection of suitable precursor reagents. The reagents cool the solution sufficiently to

almost immediately suppress nucleation, allowing for the temporal separation of NC nucleation and growth necessary for narrow size distributions. Subsequent growth is obtained by heating the solution to a much lower temperature at which atoms diffuse and bond to the NC surfaces. As Heath and Shiang observed, this scheme becomes difficult as bond covalency increases for two reasons.[21] First, bare group IV atoms are not stable, and the complexed precursors which must therefore be used require high temperatures to dissociate. Consequently, nucleation and growth occur at similar temperatures and are not easily separated. Broad NC size and shape distributions result and can be seen in many reports of colloidal Ge NCs. Second, group IV materials have higher crystallization temperatures than other semiconductors, so that long reactions at high temperature are required to produce crystalline particles. Germanium NC syntheses often take several hours or even days at temperatures up to 300 °C, with low yields.

Gas-phase syntheses are based on either evaporation and condensation of a Ge melt or aerosol pyrolysis of a liquid Ge precursor.[19,20] These techniques produce NCs with the cleanest surfaces but are susceptible to the formation of hard agglomerates which prevents further manipulation and may result in loss of quantum confinement. Stoldt et al. demonstrated that agglomeration was substantially suppressed in ultrasonic aerosol pyrolysis of tetrapropylgermane, but this may be due to the formation of an (undesirable) carbonaceous shell around each NC.[20]

Previously, Mangolini et al. reported a nonthermal plasma technique with large material yields for the synthesis of freestanding Si NCs.[22] Three aspects of the plasma environment make the approach particularly amenable to the synthesis of group IV

NCs.[23] First, the flow-through reactor design and finite plasma length mean that the NC growth time can be controlled by altering the residence time of the NCs in the plasma zone. Although detailed studies have not been performed, the narrow size distributions of synthesized Si NCs indicate that each NC must nucleate near the top of the plasma, likely due to the high concentration of precursors. Each NC is then swept through the remaining plasma region in approximately the same time as its neighbors by the gas flow, and the NCs grow by condensation to their final size. Consequently, nucleation and growth are effectively separated and the growth time can be controlled.

Second, surfaces—including NC surfaces—tend to become negatively charged in nonthermal plasmas.[24-28] There is a large discrepancy between the temperatures of the light electrons and massive positive ions in nonthermal plasmas, and the much more mobile electrons must accumulate on surfaces to make the electron and ion fluxes equal in steady state. Consequently, NCs repel each other and the agglomeration problems which afflict other gas-phase processes are not present.[24,27,28] As the reactor walls also charge, this phenomenon also helps confine NCs to the plasma, preventing losses and encouraging uniform residence times among NCs.

Finally, nanosized particles in nonthermal plasmas are selectively heated by electron-ion recombination and exothermic chemical reactions at their surfaces. Although the gas temperature in nonthermal plasmas is approximately room temperature, Mangolini, Thimsen, Galli, and Kortshagen have shown that the instantaneous temperature of Si NCs less than 10 nm in diameter in the plasma can exceed the gas temperature by several hundred Kelvin.[22,24,29] This provides the necessary energy for

crystallization of particles of high melting point materials like Si and Ge, and provides a distinct advantage over solution synthesis methods.

In this chapter, we describe the adaptation of the plasma synthesis approach to the synthesis of nearly monodisperse, freestanding Ge nanoparticles which can be produced to be either crystalline or amorphous, and to have mean diameters from 4-50 nm. The plasma parameters also allow for control of the NC surface chemistry, but this discussion is reserved for Chapter 3.

2.3 Experimental

A flow-through, nonthermal plasma reactor similar to that described in [22] was used to synthesize Ge NCs. As sketched in Fig. 2-1, the reactor consists of a 25 mm outer diameter quartz tube through which precursor gases are passed. The reactor is evacuated using a roughing pump, and the pressure in the reactor is controlled with a downstream valve. Typical operating pressure is 1–10 Torr. Radiofrequency power of 50-250 W at 13.56 MHz is applied to a copper ring electrode pair wrapped around the tube, resulting in a 5-15 cm long plasma that causes precursor dissociation and subsequent NC formation. The NCs are collected downstream of the plasma on transmission electron microscope (TEM) grids or stainless steel filter meshes.

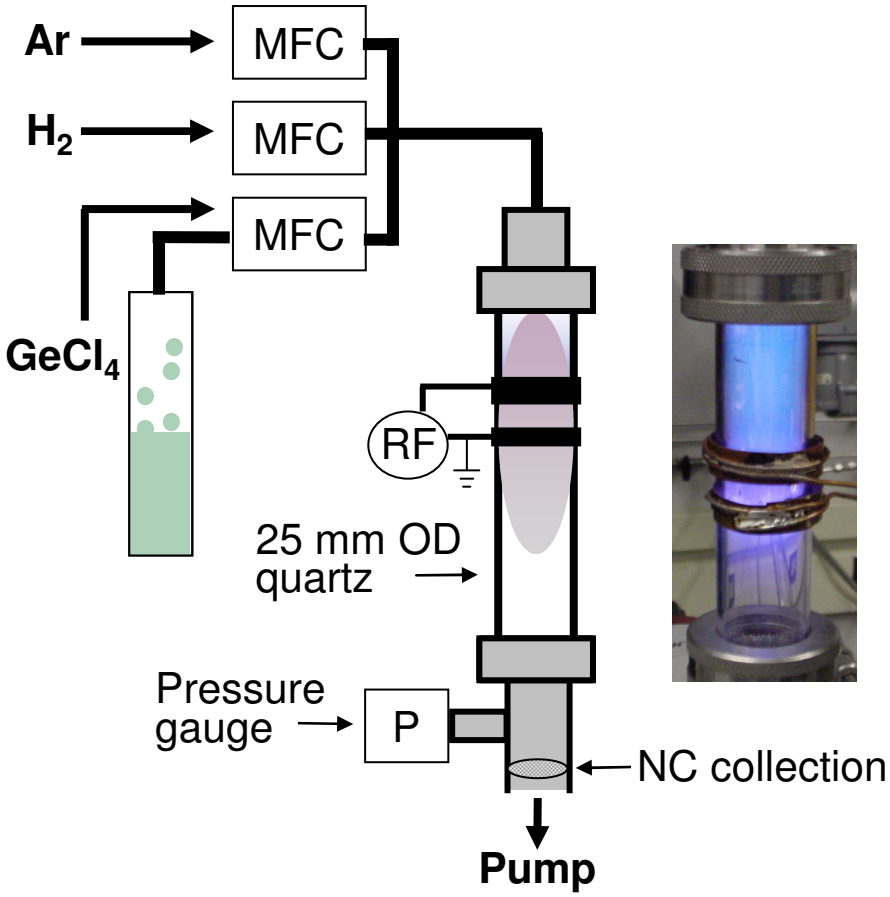

Figure 2-1: Schematic and photograph of the experimental setup.

Germanium tetrachloride ($GeCl_4$) and hydrogen gas (H_2) are used as Ge NC precursors; H radicals serve to scavenge Cl produced in the dissociation of $GeCl_4$, allowing Ge NCs to nucleate. Argon is used as a background gas to sustain the plasma. Germanium tetrachloride is a liquid at room temperature with a vapor pressure of 76 Torr, and is introduced into the reactor either using a custom built low pressure mass flow controller (MKS Instruments, Inc.) or by bubbling Ar through a $GeCl_4$-containing bubbler held at 1,500 Torr so that the gas mixture entering the reactor has a $GeCl_4$:Ar ratio of 5:95. For the studies presented here, the Ar:H_2:$GeCl_4$ gas flow ratios were 220:20:1 or 21:15:1; other ratios are investigated in Chapter 3.

2.4 Results and discussion

Residence time and NC size. The NC residence time in the plasma zone is the primary parameter affecting NC size,[22] with longer times leading to larger NCs. The residence time can be controlled by changing the gas flow rates, the plasma pressure, or the plasma geometry, with all other parameters held constant. We first consider the total gas flow rate. Figure 2-2 shows TEM images of Ge NCs collected on TEM grids downstream of the plasma for 1 min. The Ar:H_2:$GeCl_4$ gas flow ratio was held constant at 220:20:1 while the total flow rate was varied from 121 sccm to 7.5 sccm, and thus the residence time from ~27 ms to ~440 ms. It is clearly seen that the Ge NCs are rather monodisperse under all conditions and that longer residence times lead to larger crystals. The effect of residence time on NC size is quantitatively summarized in Fig. 2-3. The mean particle diameter changes by about a factor of ten when the residence time is adjusted throughout the above range, indicating the versatility of this synthesis technique.

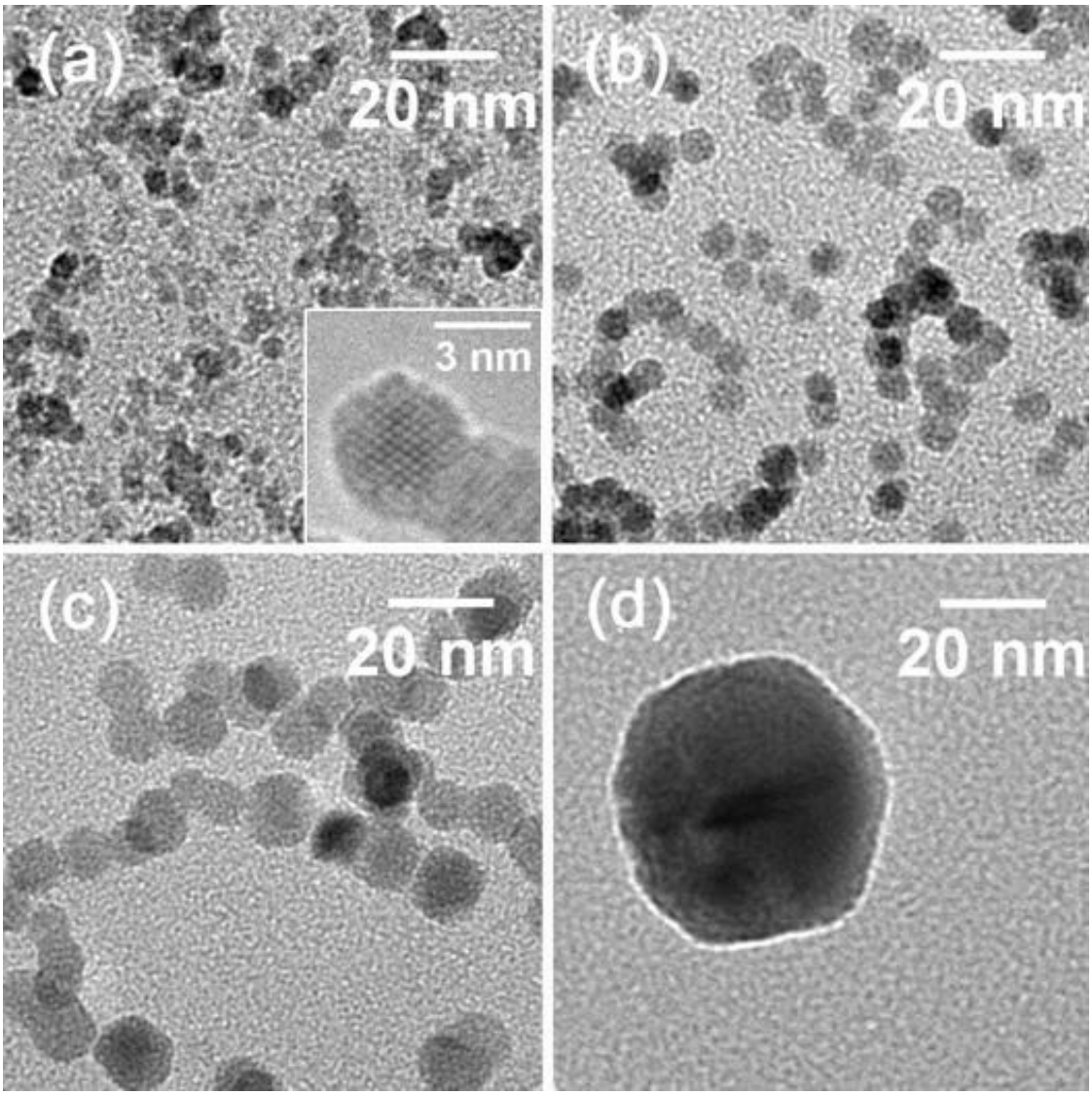

Figure 2-2: Plasma synthesized Ge NCs for various residence times in the plasma. Precursor flow rates were: (a) 110 sccm Ar, 10 sccm H_2, and 0.5 sccm $GeCl_4$ (inset shows high resolution); (b) 55 sccm Ar, 5 sccm H_2, and 0.25 sccm $GeCl_4$; (c) 27.5 sccm Ar, 2.5 sccm H_2, and 0.13 sccm $GeCl_4$; (d) 6.9 sccm Ar, 0.63 H_2, and 0.03 sccm $GeCl_4$. All depositions were for ~1 min at 80 W power.

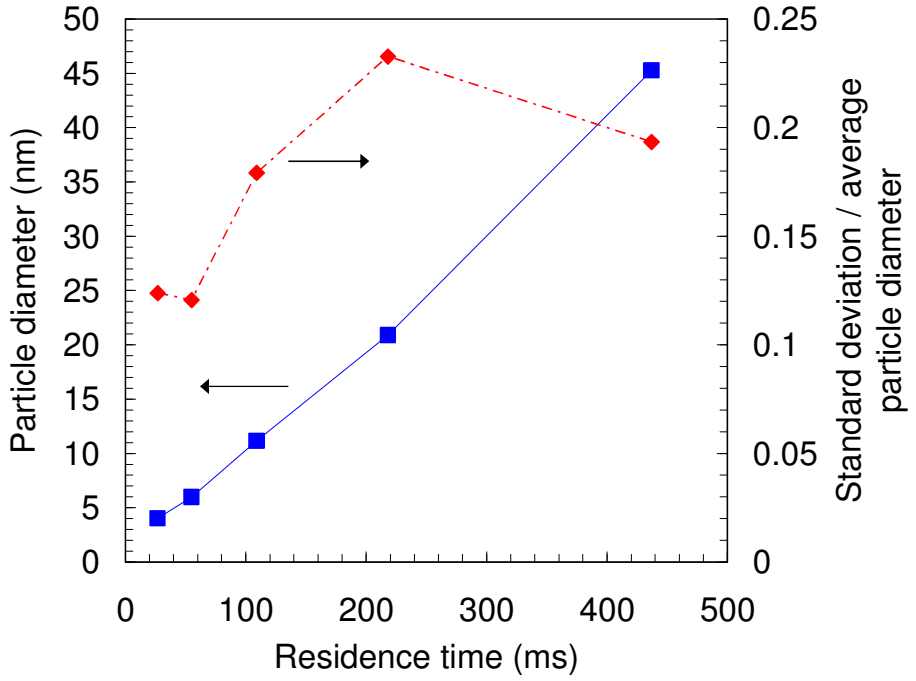

Figure 2-3: NC mean diameter and standard deviation of the NC size distribution as a function of the NC residence time in the reactor. Plasma conditions were as in Fig. 2-2.

Compared to Ge NCs synthesized using many of the techniques previously reported in the literature, the size and shape distributions of our NCs are narrow, though the distributions broaden with increasing particle size (Fig. 2-3). For 5 nm Ge NCs, standard deviations (determined by measurement of >50 NCs from TEM images) of 10-15% are typical. The particles are nearly uniformly spherical at small sizes, but some shape deviation is introduced at larger sizes and faceting can be seen. Size and shape uniformity are very important for both fundamental studies of nanosize phenomena and device applications since the signatures of size-dependent properties (e.g., absorption) will broaden with increasing polydispersity.

In addition, the particles do not fuse together to form “hard” agglomerates. Rather, the boundaries between particles are easily distinguishable and, as we will show

in a different paper, NCs that may appear to be "stuck together" are easily separated during liquid-phase chemical reactions used to terminate the NC surfaces. As was previously reported for Si NCs,[22] the plasma environment effectively inhibits agglomeration by dispensing a unipolar negative charge on the NCs. Non-agglomerated, monodisperse particles such as the Ge NCs reported here are required for many device processing steps such as the formation of densely packed or superlattice films from NC colloidal solutions.[30,31]

Unfortunately, there is a disadvantage that is hidden in Fig. 2-3 to controlling the NC size with gas flow rate: The residence time is inversely proportional to the flow rate. The data from Fig. 2-3 is plotted again in Fig. 2-4 as a function of the total gas flow rate—the parameter that is actually controlled during experiments. The NC size is highly nonlinear with the gas flow rate, and two problems become clear. It is evident that one reason (other factors also play a role) that we have not successfully synthesized Ge NCs with diameters smaller than 3.5 nm is that the required gas flow rates become very large—larger than we have yet investigated. In addition, the gas flow rates must be diminishingly small to make large NCs. The mass of material produced is proportional to the amount of $GeCl_4$ used so that the NC yield per time decreases with increasing NC size.

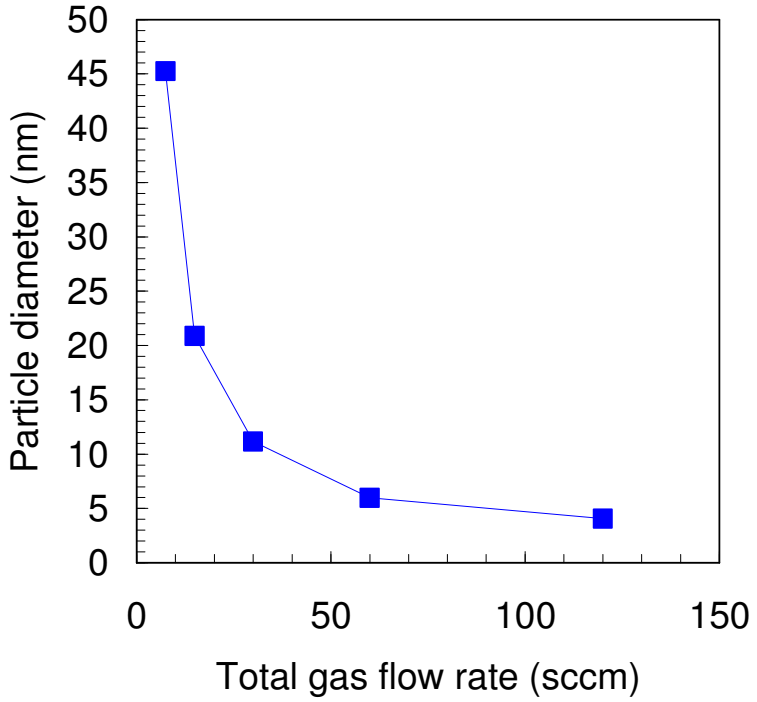

Figure 2-4: Germanium NC mean diameter as a function of the total gas flow rate (same data as in Fig. 2-3). Plasma conditions were as in Fig. 2-2.

By contrast, residence time is proportional to plasma volume and pressure. Figure 2-5 shows photographs of plasmas of different lengths and a plot of the resulting NC sizes determined from Debye-Scherrer fits to X-ray diffraction (XRD) spectra. Although the NC size increases monotonically with plasma length, the dependence is not strong. Consequently, it is impractical to synthesize a wide range of NC sizes by changing the plasma length.

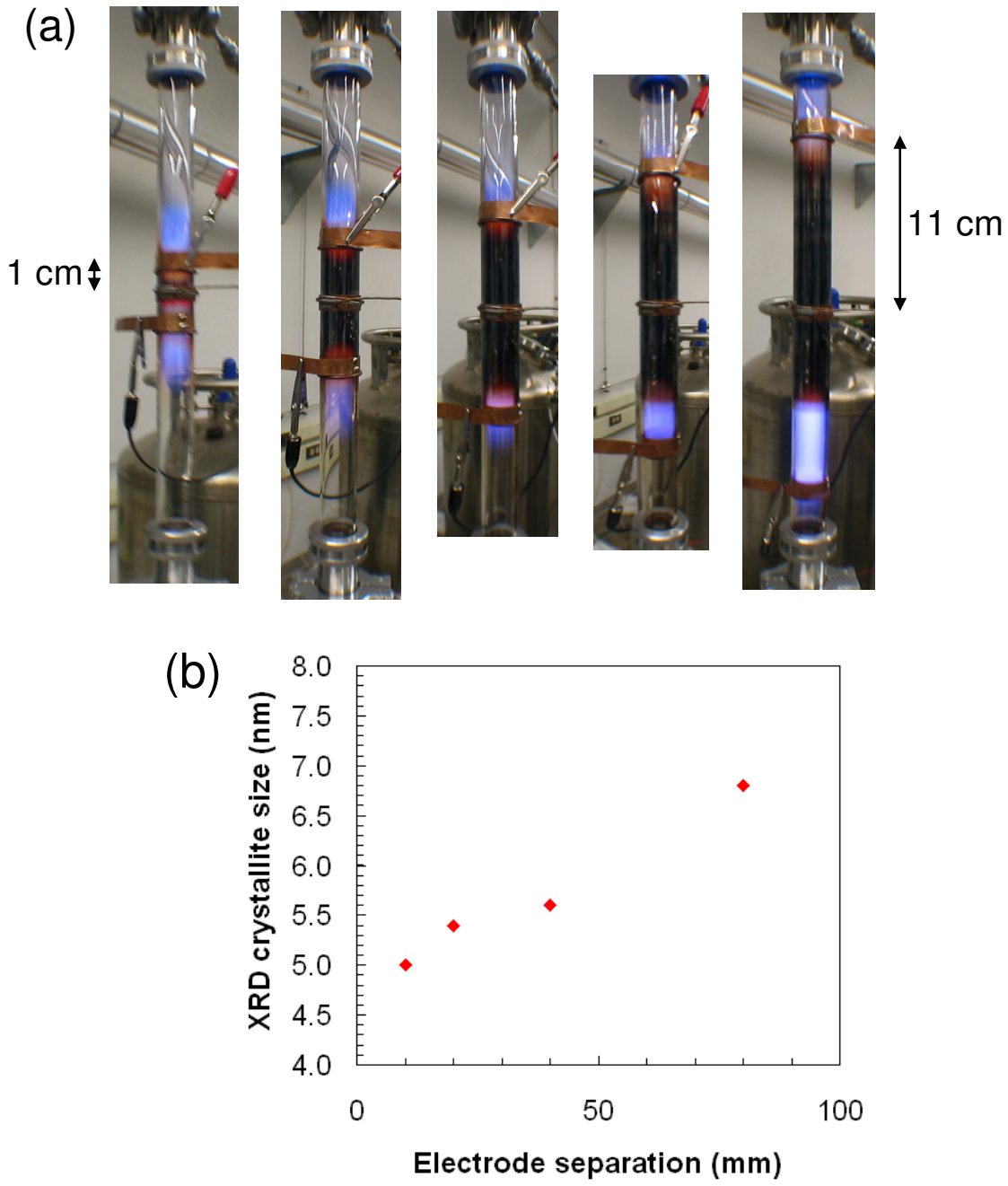

Figure 2-5: (a) Photographs of plasmas used to synthesize Ge NCs using electrode separations of 1-11 cm. A three-electrode setup was used in which the middle electrode was powered and the outer two were grounded. The reported electrode separation is the distance between the powered electrode and one grounded electrode (nominally half the plasma length). (b) Germanium NC size determined from XRD as a function of the electrode separation. The gas flow rates were 45 sccm Ar, 32 sccm H_2, and 2 sccm $GeCl_4$, the pressure was 2.2 Torr, and powers of 125–200 W were used.

Changing the plasma pressure affords the most control over Ge NC size without compromising material yield. Figure 2-6 displays NC size (again determined from XRD peak broadening) as a function of pressure in Torr. The dependence is near-linear with a slope of roughly 0.6, indicating that Ge NCs with a wide range of mean diameters can be synthesized with a relatively narrow range of pressures. The dependence likely breaks down for pressures less than 1 Torr and greater than a few tens of Torr due to changes in the plasma. Fortunately, Ge NCs larger than ~10 nm have properties similar to those of bulk Ge and are of little interest, and NCs smaller 3–10 nm in diameter are synthesized using 1-10 Torr.

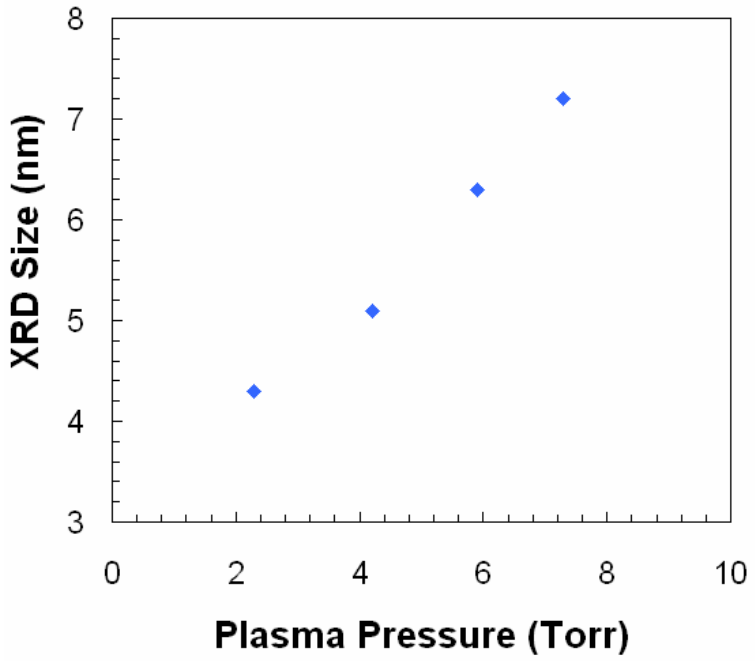

Figure 2-6: Germanium NC mean diameter determined from XRD as a function of the plasma pressure. The gas flow rates were 80 sccm Ar, 56 sccm H_2, and 2 sccm $GeCl_4$, and powers of 150–250 W were used.

Plasma power and NC crystallinity. Mangolini and coworkers demonstrated that electron-ion recombination and exothermic chemical reactions at the surface of particles are responsible for their crystallization.[22] The species that participate in these reactions are generated by the radiofrequency excitation. Consequently, the amount of power coupled to the plasma provides an effective handle on the particle crystallinity without altering the particle size or mass yield.[24] Figure 2-7 compares XRD and TEM results for samples synthesized with 60 and 90 W power, and otherwise identical conditions. Two broad features characteristic of amorphous material are seen in the XRD pattern of the low power sample, while the (111), (220), (311), (400), and (331) reflections of diamond cubic Ge are clearly visible for the high power sample. Selected-area diffraction (SAD) performed in the TEM corroborates these results; rings corresponding to the (111), (220), and (311) reflections are present in the SAD pattern of the high power sample but not the low power sample. Crystallinity aside, Ge nanoparticles synthesized with 60 and 90 W are similar in both their shape and size, as seen in the TEM images shown in Fig. 2-7. The transformation from amorphous to crystalline can be seen more clearly in Fig. 2-8, which shows Raman spectra of Ge NCs. As the power is increased from 60–125 W, the broad band at 275 cm^{-1} from amorphous Ge disappears and is replaced with the crystalline Ge peak at 300 cm^{-1}.

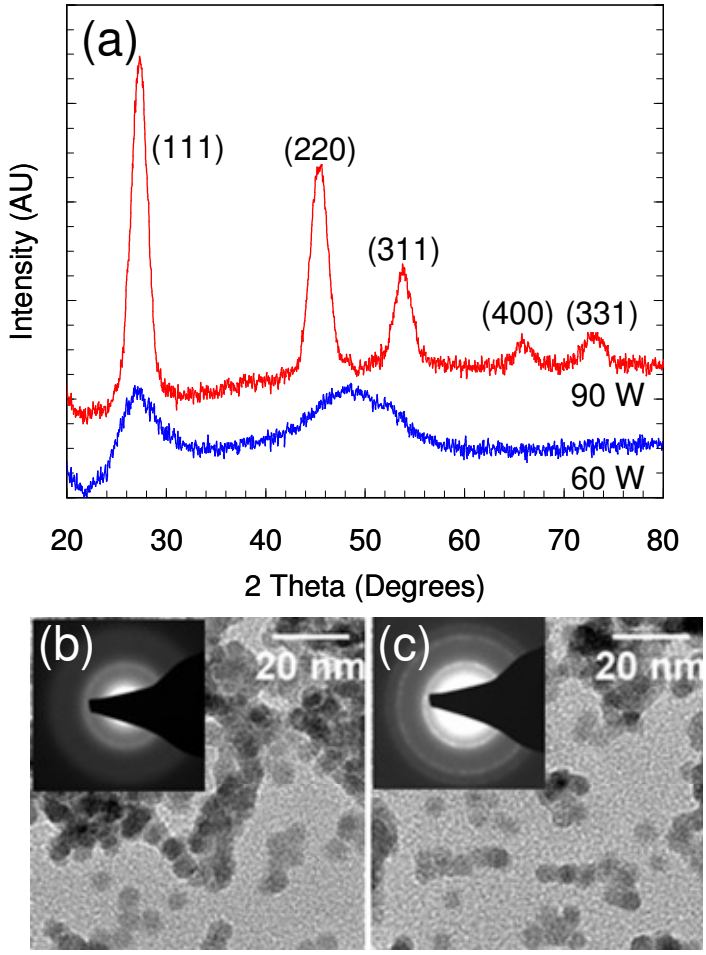

Figure 2-7: (a) X-ray diffraction patterns of particles synthesized with 60 and 90 W power. Both samples were deposited for 20 mins using 60 sccm Ar, 15 sccm H_2, and 0.5 sccm $GeCl_4$. Transmission electron micrographs and selected area diffraction patterns of particles deposited for 1 min with the above flow rates using (b) 60 W and (c) 90 W power.

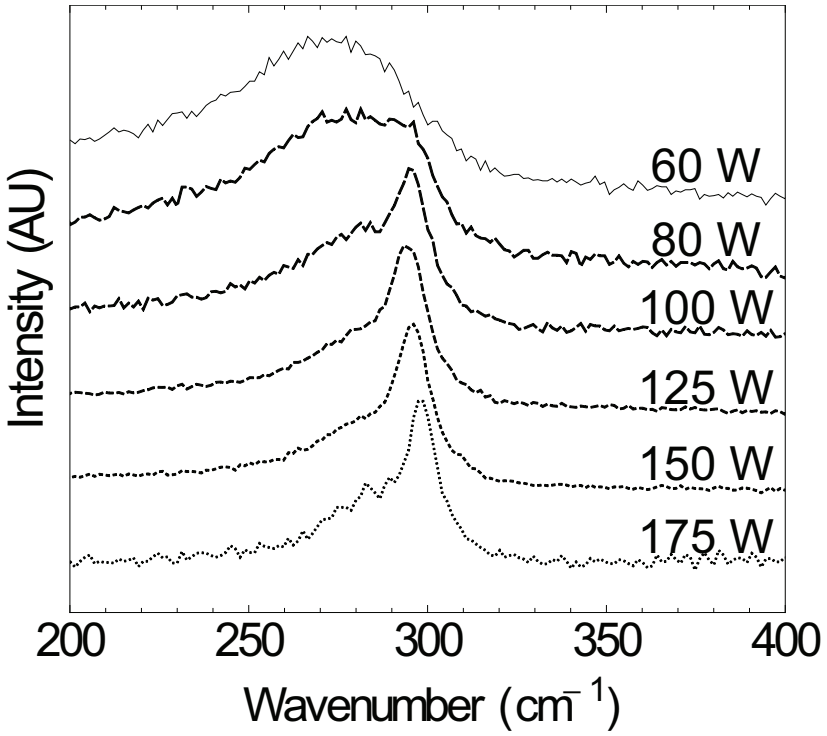

Figure 2-8: Raman spectra of 4.5 nm Ge NCs synthesized using 46 sccm Ar, 32 sccm H_2, 2 sccm $GeCl_4$, and 60–175 W power at 2.2 Torr. The fraction of NCs that are crystalline can be determined from the ratio of areas under the amorphous and crystalline Ge peaks at 275 and 300 cm^{-1}, respectively. The spectra have been normalized and offset for clarity.

The power required to synthesize crystalline particles changes dramatically with gas composition. Figure 2-9 shows how the crystallinity of Ge nanoparticles changes as a function of plasma power and ratio of H_2 and Ar flow rates. This experiment was intended to provide a practical guide for power selection given a gas mixture, so samples were either deemed "mostly crystalline" or "mostly amorphous" based on qualitative evaluations of Raman spectra like those in Fig. 2-8. The optimal power range is highlighted in green—at lower power the samples are amorphous, and at higher power the material yield decreases—and increases from ~75 to ~200 W as the H_2/Ar gas flow rate ratio varies from 0.1 to 1.8. Changes in the NC surface chemistry occur as the H_2/Ar

ratio is altered (discussed in Chapter 3), and this is the motivation for changing this parameter. The primary reason that additional power is required to make crystalline NCs at large H_2 fractions is that dissociation of H_2 acts as a power sink.

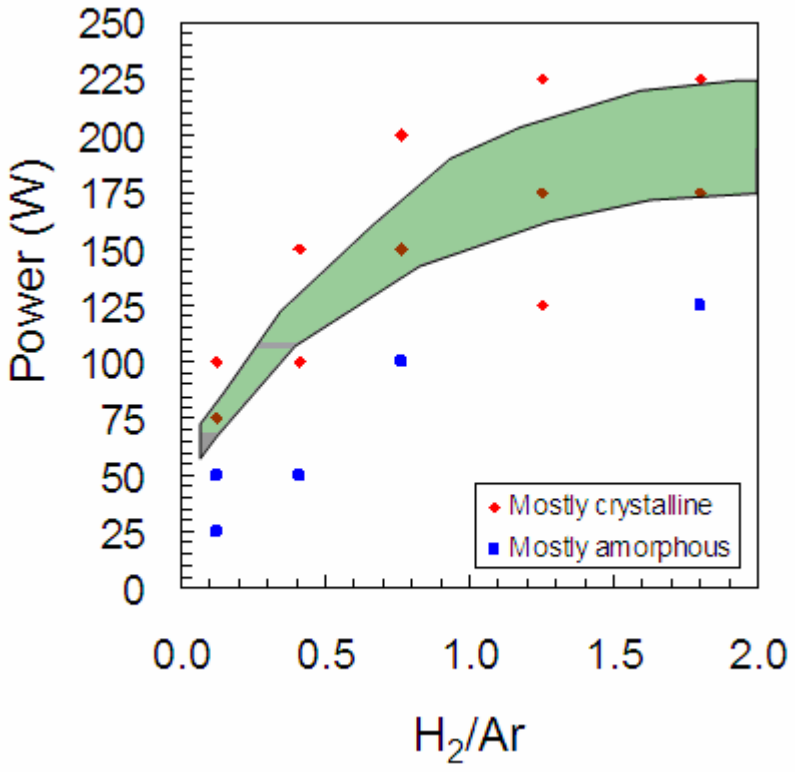

Figure 2-9: Qualitative crystallinity of Ge nanoparticles as a function of the input power and H_2/Ar gas flow rate ratio. The highlighted green area is a guide to selecting the optimal power given a H_2/Ar ratio. Samples were made with 50–82 sccm Ar, 10–90 sccm H_2, and sccm $GeCl_4$ at a pressure of 2.2 Torr.

While crystalline materials are generally preferred for their superior electronic properties, certain applications may favor amorphous materials and it is convenient to be able to easily synthesize both crystalline and amorphous Ge nanoparticles. For example, a nanoporous polycrystal could be made by depositing a few crystalline NC seeds in a porous film of amorphous Ge particles so that, upon annealing, the amorphous particles adopt the crystallographic orientation of the NC seeds to form extended, porous crystals.

Gas composition and NC yield, chemistry, and photoluminescence. Gas flow ratios other than 220:20:1 or 21:15:1 Ar:H_2:$GeCl_4$ may be used to alter NC production. In particular, simultaneously increasing the $GeCl_4$ and H_2 flows results in greater mass yield—with yields as high as hundreds of milligrams per hour—but does not significantly affect the NC size since the larger Ar flow is the dominant factor in determining the residence time. Changing the $GeCl_4$:H_2 ratio alters both the NC size and yield, with more H_2 leading to larger Ge NCs and too little H_2 resulting in no NC formation. We believe that H radicals prevent the fast recombination of Cl with fragments of dissociated $GeCl_4$ so that Ge atoms have a chance to bond with other Ge atoms, leading to Ge NC nucleation. We suspect that, in the absence of H_2 gas, Cl radicals reattach to Ge atoms to re-form $GeCl_4$ before Ge NC nucleation can occur. With increasing H_2, less Cl is present to hinder Ge NC growth, leading to larger particles. Importantly, the $GeCl_4$:H_2 ratio also changes the chemistry of the Ge NC surfaces. This is investigated in Chapter 3.

Nanocrystalline Ge with feature sizes smaller than ~6 nm have been reported by others to exhibit visible photoluminescence (PL).[8,32-37] The source of this PL is controversial, with some authors claiming that it is intrinsic to the NCs and is blue-shifted due to quantum confinement,[8,32,33] and others claiming it is extrinsic and results from oxides and defects.[34-37] We believe that the majority of reports of visible PL—and certainly all of those for NCs larger than ~3 nm—result from radiative recombination at surface states. It is predicted that Ge NCs larger than ~4 nm will emit in the infrared (IR) since the PL peak wavelength must approach the bulk Ge bandgap of 0.7 eV as the NC size increases,[6,7] but there are only two reports of IR PL from Ge NCs.[9,10] No PL was

observed from the Ge NCs reported here, independent of their size and oxidation state, although careful investigations in the IR region were not conducted. We suspect that this is a result of Cl on the NC surfaces, since halogens have been observed to quench PL in porous Si,[38] and the groups that have successfully observed IR PL in Ge NCs did not use $GeCl_4$ as a precursor.

2.5 Conclusions

In summary, we have demonstrated the synthesis of freestanding Ge NCs using a nonthermal plasma technique which allows control of the NC properties. Nearly monodisperse NCs with mean diameters of 4-50 nm have been synthesized with mass yields as high as hundreds of milligrams per hour by changing the NC residence time in the plasma zone. The nanoparticle crystallinity can be controlled independent of other particle properties by varying the plasma power. As the plasma synthesis approach produces Ge NCs without any surfactants, the NC surfaces are available for many post-processing modification schemes, making them suitable for a wide range of applications.

2.6 Future work

The synthesis of Ge NCs using the plasma reactor described above is relatively well understood, but additional research in four areas may prove fruitful. First, online feedback and improved reactor stability would save time and give additional control over the resulting NCs. Replacement of the $GeCl_4$ bubbler delivery system with a specially

designed mass flow controller (MFC) and development of the impaction system described in Chapter 6 were significant improvements to the reactor that greatly improved sample reproducibility and made NC handling easier. Additional desirable modifications include an accurate measurement of the power coupled to the plasma (not just the power read at the matchbox, as reported here) and integrated Raman and FTIR instruments for in-situ analysis of NC crystallinity and surface chemistry. We have observed that the power needed to make crystalline particles varies by as much as 30% with the condition of the electrodes and matchbox, so that frequent recalibration of the optimum power is necessary. Accurate power measurement and in-situ Raman would alleviate this problem and ensure that every sample is deposited with the intended crystalline fraction. As demonstrated in the following chapters, the chemistry at the surfaces of NCs often dominates their behavior. Consequently, an in-situ FTIR apparatus that allows the user to monitor the surfaces of Ge NCs both during synthesis and in post-synthesis experiments (e.g., controlled oxygen exposure) would be invaluable. Holm and Roberts have demonstrated the power of such a setup.[39-41]

Experiments to further control NC growth via manipulation of the plasma would also be useful. While the Si and Ge NCs reported by the Kortshagen group have narrower size distributions than Si and Ge NCs synthesized by other methods, they are broader than the ~5% standard deviation obtainable in, e.g., PbTe and CdSe NC ensembles after size-selective precipitation. Narrow size distributions are critical for resolving size-dependent properties such as excitonic peaks, and NC superlattices that may have interesting physics have been demonstrated using nearly monodisperse NCs.[31] While the

Kortshagen group has carefully modeled NC charging, heating, and coagulation in plasmas, we do not yet understand the spatio-temporal evolution of the NCs. For example, does all nucleation happen within the first 1 cm of the plasma? 1 mm? What is the critical concentration of $GeCl_x$ monomers for nucleation? What is the profile of the reactive Ge species along the plasma length? Answering questions like these is critical to understanding—and further controlling—NC nucleation and growth, and therefore the NC size distribution. Ideally, the operator would be able partition the amount of $GeCl_4$ consumed in nucleation and condensation growth, and finely tune the amount of volume in which each occurs. The use of magnetic fields would help to limit the plasma volume by confining electrons without also confining the much more massive NCs. An alternative approach to obtaining narrower size distributions is to segregate NCs based on charge to mass ratio NCs after synthesis. Cernetti demonstrated this using an electromagnetic lens, but the process was not scaled up to produce useful quantities of powder.[42]

We suspect that the lack of PL from our Ge NCs is related to their surface passivation, and perhaps the presence of residual Cl. Lee et al. are one of two groups that have reported IR PL from Ge NCs, and they used germanium(II) iodide (GeI_2) as a precursor (the other group co-sputtered Ge and SiO_2 and nucleated Ge NCs in the SiO_2 matrix). GeI_2 is a crystalline solid which decomposes to Ge and GeI_4 upon melting, and it sublimates when heated to 240 °C in vacuum.[43] Reaction of I radicals in the plasma would result in hydroiodic acid (HI) similar to the formation of HCl when $GeCl_4$ is used, but it is unknown what will be left at the NC surfaces and how I behaves as a surface

passivant. Other Ge halides may also be of interest as precursors, including germanium bromide ($GeBr_2$ or $GeBr_4$). Minimal apparatus alterations are required to try these molecules. Unfortunately, most are more expensive than $GeCl_4$. Ryan Gresback has also experimented with using GeH_4 as a precursor and successfully synthesized Ge NCs. The surface and properties of these samples have not yet been thoroughly investigated.

The final topic for potential future work in the area of Ge NC synthesis is the intentional introduction of dopants into the synthesis reactor. Pi et al. have demonstrated that small concentrations of phosphine or diborane gas in a Si NC plasma reactor generate Si NCs with controllable densities of P or B dopants.[44] It is expected that Ge NCs could be similarly doped. If the dopants are electrically active, they will donate excess electrons or holes to the NCs, and devices such as *p-n* junctions can be made. Interestingly, we have seen *p*- and *n*-type behavior from Ge NCs that were synthesized intrinsic (see Chapter 5). If this apparent doping by post-synthesis surface adsorption can be controlled, there may not be a need to add dopant atoms during NC synthesis. If it cannot, doping with e.g, P and B must be explored if Ge NCs are to find use in semiconductor devices.

2.7 References

[1] A.G. Cullis and L.T. Canham, *Nature* **353**, 335 (1991).

[2] J.P. Wilcoxon, G.A. Samara, and P.N. Provencio, *Phys. Rev. B* **60**, 2704 (1999).

[3] J.D. Holmes, K.J. Ziegler, R.C. Doty, L.E. Pell, K.P. Johnston, and B.A. Korgel, *J. Am. Chem. Soc.* **123**, 3743 (2001).

[4] X.G. Li, Y.Q. He, S.S. Talukdar, and M.T. Swihart, *Langmuir* **19**, 8490 (2003).

[5] D. Jurbergs, E. Rogojina, L. Mangolini, and U. Kortshagen, *Appl. Phys. Lett.* **88**, 233116 (2006).

[6] T. Takagahara and K. Takeda, *Phys. Rev. B* **46**, 15578 (1992).

[7] G. Nesher, L. Kronik, and J.R. Chelikowsky, *Phys. Rev. B* **71**, 035344 (2005).

[8] J.P. Wilcoxon, P.P. Provencio, and G.A. Samara, *Phys. Rev. B* **64**, 035417 (2001).

[9] D.C. Lee, J.M. Pietryga, I. Robel, D.J. Werder, R.D. Schaller, and V.I. Klimov, *J. Am. Chem. Soc.* **131**, 3436 (2009).

[10] S. Takeoka, M. Fujii, S. Hayashi, and K. Yamamoto, *Phys. Rev. B* **58**, 7921 (1998).

[11] M. Fujii, S. Hayashi, and K. Yamamoto, *Jpn. J. Appl. Phys., Part 1* **30**, 687 (1991).

[12] J.G. Zhu, C.W. White, J.D. Budai, S.P. Withrow, and Y. Chen, *J. Appl. Phys.* **78**, 4386 (1995).

[13] W.K. Choi, H.G. Chew, V. Ho, V. Ng, W.K. Chim, Y.W. Ho, and S.P. Ng, *J. Cryst. Growth* **288**, 79 (2006).

[14] T.P. Leervad Pedersen, J.S. Jensen, J. Chevallier, O. Hansen, J.M. Jensen, B.B. Nielsen, and A.N. Larsen, *Appl. Phys. A* **81**, 1591 (2005).

[15] J.R. Heath, J.J. Shiang, and A.P. Alivisatos, *J. Chem. Phys.* **101**, 1607 (1994).

[16] B.R. Taylor, S.M. Kauzlarich, H.W.H. Lee, and G.R. Delgado, *Chem. Mater.* **10**, 22 (1998).

[17] D. Gerion, N. Zaitseva, C. Saw, M.F. Casula, S. Fakra, T. Van Buuren, and G. Galli, *Nano Lett.* **4**, 597 (2004).

[18] X.M. Lu, B.A. Korgel, and K.P. Johnston, *Chem. Mater.* **17**, 6479 (2005).

[19] C. Bostedt, T. Van Buuren, J.M. Plitzko, T. Moller, and L.J. Terminello, *J. Phys.: Condens. Matter* **15**, 1017 (2003).

[20] C.R. Stoldt, M.A. Haag, and B.A. Larsen, *Appl. Phys. Lett.* **93**, 043125 (2008).

[21] J.R. Heath and J.J. Shiang, *Chem. Soc. Rev.* **27**, 65 (1998).

[22] L. Mangolini, E. Thimsen, and U. Kortshagen, *Nano Lett.* **5**, 655 (2005).

[23] U. Kortshagen, *J. Phys. D: Appl. Phys.* **42**, 113001 (2009).

[24] F. Galli and U.R. Kortshagen, *IEEE Trans. Plasma Sci.* **38**, 803 (2010).

[25] M. Gatti and U. Kortshagen, *Phys. Rev. E* **78**, 046402 (2008).

[26] J. Goree, *Plasma Sources Sci. Technol.* **3**, 400 (1994).

[27] T. Matsoukas and M. Russell, *J. Appl. Phys.* **77**, 4285 (1995).

[28] U. Kortshagen and U. Bhandarkar, *Phys. Rev. E* **60**, 887 (1999).

[29] L. Mangolini and U. Kortshagen, *Phys. Rev. E* **79**, 026405 (2009).

[30] C.P. Collier, T. Vossmeyer, and J.R. Heath, *Annu. Rev. Phys. Chem.* **49**, 371 (1998).

[31] C.B. Murray, C.R. Kagan, and M.G. Bawendi, *Annu. Rev. Mater. Sci.* **30**, 545 (2000).

[32] Y. Maeda, *Phys. Rev. B* **51**, 1658 (1995).

[33] B.R. Taylor, S.M. Kauzlarich, G.R. Delgado, and H.W.H. Lee, *Chem. Mater.* **11**, 2493 (1999).

[34] S. Miyazaki, K. Sakamoto, K. Shiba, and M. Hirose, *Thin Solid Films* **255**, 99 (1995).

[35] M. Zacharias and P.M. Fauchet, *Appl. Phys. Lett.* **71**, 380 (1997).

[36] G. Kartopu, S.C. Bayliss, V.A. Karavanskii, R.J. Curry, R. Turan, and A.V. Sapelkin, *J. Lumin.* **101**, 275 (2003).

[37] H.P. Wu, M.Y. Ge, C.W. Yao, Y.W. Wang, Y.W. Zeng, L.N. Wang, G.Q. Zhang, and J.Z. Jiang, *Nanotechnology* **17**, 5339 (2006).

[38] J.M. Buriak, *Chem. Rev.* **102**, 1271 (2002).

[39] J. Holm and J.T. Roberts, *Langmuir* **23**, 11217 (2007).

[40] J. Holm and J.T. Roberts, *J. Am. Chem. Soc.* **129**, 2496 (2007).

[41] J. Holm and J.T. Roberts, *J. Vac. Sci. Technol., A* **28**, 161 (2010).

[42] P. Cernetti, Ph.D. Thesis, University of Minnesota, 2006.

[43] O.H. Johnson, *Chem. Rev.* **51**, 431 (1952).

[44] X.D. Pi, R. Gresback, R.W. Liptak, S.A. Campbell, and U. Kortshagen, *Appl. Phys. Lett.* **92**, 123102 (2008).

3

Solution-processed germanium nanocrystal thin films[*]

3.1 Outline

Solution-processed nanocrystal films have attracted significant interest as potential semiconductor materials with size-tunable optical and electronic properties that can be deposited with low-cost printing and coating techniques. Significant progress has been reported with II-VI and IV-VI nanocrystal films, since the electrically-insulating ligands that solubilize the nanocrystals can be easily exchanged or removed after film deposition. While progress to date has been slow for group IV silicon and germanium nanocrystal films, this chapter reports solution-processed germanium nanocrystal films with promising electrical conductivities. Stable germanium nanocrystal colloids are

[*] Reproduced in part with permission from Zachary C. Holman and Uwe R. Kortshagen, "Solution-processed germanium nanocrystal thin films as materials for low-cost optical and electronic devices," *Langmuir* **25**, 11883 (2009). Copyright 2009 American Chemical Society.

produced via nonthermal plasma synthesis and subsequent alkene surface functionalization. Electrical characterization of drop-cast germanium nanocrystal films reveals that the films are insulating as deposited, but have conductivities as large as 10^{-6} S/cm and 5×10^{-4} S/cm after annealing at 250 °C and 500 °C, respectively. Mass spectrometry, thermogravimetric analysis, and infrared spectroscopy indicate that the increase in conductivity coincides with the decomposition and departure of the alkyl ligands from the films.

3.2 Introduction

Semiconductor nanocrystals (NCs) embedded in matrices and dissolved in solution have garnered much attention for their size-dependent optical properties; however, in order to be used in traditional thin film devices, NC films with tunable properties must be designed. The most commonly employed method involves the self-assembly of drop- or spin-cast colloidal NCs into dense films on substrates.[1-11] This approach dates to 1995 when Murray et al. demonstrated the formation of colloidal crystals and superlattice thin films of nearly monodisperse CdSe NCs.[7] More recently, researchers have cast NC films of several II-VI and IV-VI materials and begun constructing electronic devices including transistors,[10] solar cells,[2-4,6] and photodetectors.[8] One of the advantages of this film deposition technique is its low cost and simplicity since colloidal NCs are typically synthesized in a beaker and films are cast with a pipette. More importantly, there have been several reports that the excitonic electronic structure of monodisperse NCs remains largely intact during film

formation;[7,10,11] films have properties that are similar, if not identical, to their constituent NCs. This opens the door for decoupling a film's optical properties from the material of which it is composed.

Casting films from colloidal suspensions of II-VI and IV-VI NCs has been successful primarily because, for these materials, a solution synthesis method exists which produces spherical, monodisperse NCs with functionalized surfaces.[12] There is significant interest in replicating this work with the non-toxic and abundanat group IV materials Si and Ge. Unfortunately, making a stable colloid of high quality Si or Ge NCs remains an obstacle. Finding precursors that are suitable for the rapid-injection-in-a-coordinating-solvent method commonly used to grow compound NCs has proved challenging, and other solution-based approaches for synthesizing group IV materials often yield particles with broad size and shape distributions and generate unwanted byproducts.[13-15] Recent progress in solution-phase Ge NC synthesis has begun to overcome these challenges.[16]

We previously reported a gas-phase method for synthesizing nearly monodisperse Si[17] and Ge[18] NCs using a nonthermal plasma. These NCs, which are collected as a powder, do not go into solution as produced since the van der Waals attraction between NCs causes agglomeration and flocculation. However, Jurbergs et al. have demonstrated that the attachment of long alkyl groups to the surface of Si NCs using a hydrosilylation reaction provides sufficient steric stabilization to allow the NCs to be solubilized in common organic solvents.[19] A similar functionalization scheme is reported in this paper for the formation of Ge NC colloids. While most of the attention given to Group IV NCs

has focused on Si, both theoretical[20,21] and experimental[22] reports in the literature indicate that the bandgap of Ge is more sensitive to reductions in NC size than the bandgap of Si. As a result, a broad range of optical properties should be accessible for a relatively narrow range of Ge NC sizes, making them particularly attractive for applications such as multi-junction photovoltaics.

This paper also describes the formation of dense, uniform films from Ge NC colloids and the electrical properties of these films. One challenge faced by nearly all researchers who have cast NC films from colloids is that the films are insulating as deposited due to the bulky surface ligands which afford solubility. This is clearly unsuitable for device applications. Promising results have been obtained, however, after thermal or chemical treatments intended to remove the ligands.[1,5,9] For example, Talapin and Murray reported an impressive 10 orders of magnitude increase in the conductance of PbSe NC films following hydrazine treatment.[10] Thermal treatments of Ge NC films are explored toward the end of this chapter.

3.3 Experimental

Plasma synthesis of germanium nanocrystals. As described in detail elsewhere,[18] Ge NCs were synthesized in a flow-through plasma reactor via the decomposition of germanium tetrachloride ($GeCl_4$). Briefly, $GeCl_4$ (Acros Organics, 99.99%, used as received) entrained in Ar gas was passed through a 25 mm outer diameter quartz tube around which a pair of copper ring electrodes were wrapped. H_2 gas and additional Ar background gas were also fed through the tube. Radiofrequency power

of 50–125 W was applied to the electrode pair at 13.56 MHz, resulting in a plasma roughly 5 cm in length. The reactor was operated at 2 Torr and typical total flow rates for producing 5 nm Ge NCs were 0.75 sccm $GeCl_4$, 5–30 sccm H_2, and 40–65 sccm Ar. Nanocrystal formation occurred in the plasma following the dissociation of $GeCl_4$ and subsequent clustering of Ge atoms (H radicals served to scavenge the Cl atoms). The crystals were collected in the form of a powder downstream of the plasma on stainless steel meshes or substrates placed on meshes.

The surface chemistry of as-produced Ge NC powder collected on meshes was studied using a Nicolet Fourier transform infrared (FTIR) spectrometer operated in the diffuse reflectance mode. The presence of Cl on the NCs was studied using a Physical Electronics Industries Auger electron spectrometer (AES) since the Ge-Cl bond is not easily probed with IR spectroscopy. For AES, Ge NCs were collected on Au-coated Si substrates so as to avoid sample charging. In all cases, samples were removed from the plasma reactor directly into a N_2-purged glove bag and sealed in containers for transport. Total air exposure, which was unavoidable during sample loading prior to measurement, was thus limited to ~1 min for each sample.

Hydrogermylation of Ge-H_x surfaces. Roughly 2 mg of Ge NCs were synthesized using H_2-rich conditions (0.75 sccm $GeCl_4$, 30 sccm H_2, and 42 sccm Ar) and collected on a mesh for approximately 5 mins. The mesh was removed to a glove bag as described above and sealed inside a test tube, which was then removed from the bag and placed on a Schlenk line. All subsequent steps were carried out on the Schlenk line and all transfers were done air-free via cannula transfer. A solution of 5:1 mesitylene:1-

dodecene (Aldrich) was dried with molecular sieves and degassed by bubbling N_2 through it for at least 20 mins. Mesitylene was chosen for its boiling point, which is slightly lower than that of 1-dodecene and therefore allows the solution to reflux without evaporating the 1-dodecene. The concentration of 1-dodecene in the solution is not particularly important; 3:1 and 10:1 solutions have been successfully used as well. Approximately 10 mL of solution was added to the Ge NCs and the resulting mixture was sonicated for 5 mins to form a turbid solution. The solution was then added to a reaction flask attached to a condenser tube, where it was refluxed near the solvent boiling point (165° C) for 3 hrs under vacuum and N_2 flow. Solutions typically became clear after ~15 mins. After cooling, the solution was dried under vacuum and N_2 flow overnight (no heat), and redispersed in dried, degassed mesitylene or another solvent of choice. The solution was finally moved (air-free) into a glove box and filtered through a 0.2 μm PTFE filter to remove any sediment.

The surface chemistry of functionalized Ge NCs was studied with a Nicolet FTIR spectrometer operated in the attenuated total reflection (ATR) mode. Drops of solution were placed on a clean Ge or ZnSe ATR crystal in the glove box and allowed to dry overnight prior to measurement.

Nanocrystal film formation and characterization. Germanium NC films were formed on transmission electron microscopy (TEM) grids, Au-coated Si wafer chips, and Corning 1737 glass substrates patterned with electrodes. The latter substrates were made by a lift-off photolithographic process which yielded 1 cm × 1 cm substrates each with three sets of 100 nm thick Au or Al electrodes separated by gaps of 5, 10, and 100 μm

(Fig. 3-1). Films were formed by placing enough drops of solution on each substrate to completely cover the substrate surface. In the case of TEM grids, the grids were placed on glass substrates which were then covered with solution. The substrates were next placed in a glass petri dish, covered, and placed on a Boekel rocking table set on a low speed where they were allowed to dry overnight. Mulitple coatings were sometimes applied to build up thicker films, with each layer allowed to dry before additional applications (although previous layers were redispersed in the solvent of subsequent layers). All steps were carried out in the glove box.

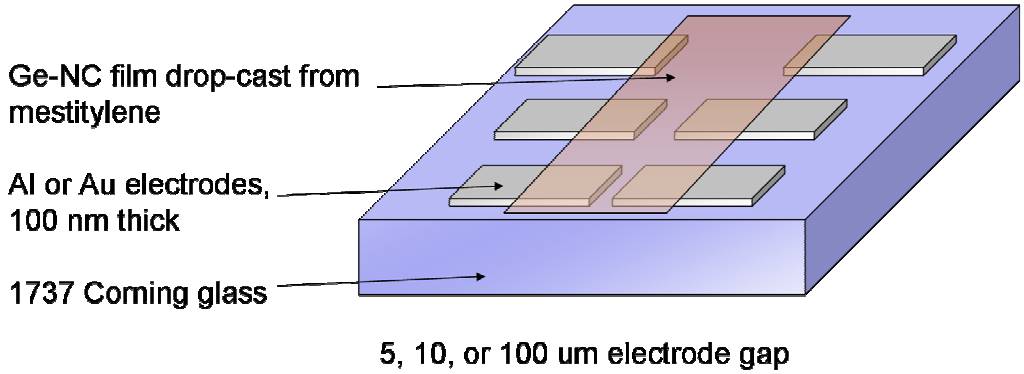

Figure 3-1. Schematic of the device architecture used to measure current-voltage characteristics of Ge NC films.

The morphology of Ge NC films deposited on TEM grids was studied with a Tecnai T12 transmission electron microscope. Films deposited on Au-Si wafer chips—which prevent charge build-up under an electron beam—were imaged using a JEOL 6500 field-emission scanning electron microscope. X-ray diffraction (XRD) measurements were performed on thick (~1 μm) films on glass using a Bruker Microdiffractometer. Current-voltage characteristics were recorded in vacuum (~10^{-5} Torr) using a Desert probe station with Keithley 237 and 6517A electrometers. Conductivities were then

determined from the slope of the low-field current-voltage characteristic, the measured thickness of the film, and the known electrode geometry. All current-voltage measurements were performed on Ge NC films deposited on the previously described glass substrates patterned with electrodes. Thermogravimetric analysis was performed using a PerkinElmer TG/DTA 6300. A thick Ge NC film was deposited in the sample pan and heated to 500 °C at a ramp rate of 5 °C/min.

Film annealing up to 500 °C was performed in a home-built rapid thermal annealing chamber maintained at 200 mTorr with N_2 gas flowing, except for experiments using an SRS RGA100 residual gas analyzer, which were performed at ~10^{-6} Torr with no gas flowing. Samples were placed on a Si wafer which was illuminated from the underside using a tungsten halogen lamp. A thermocouple in contact with the wafer provided temperature feedback to a Watlow temperature controller which controlled the lamp power. The ramp-up rate was roughly 100 °C/min, and the ramp-down rate was much slower. For temperatures higher than 500 °C, a Modular Process Technology Corporation RTP-600S commercial rapid thermal annealing chamber capable of reaching higher temperatures was used. This system was operated at atmospheric pressure with 10 slm N_2 gas flow, including 3 mins of gas flow to purge the chamber prior to sample annealing. Annealing times in this system were limited to 2 mins because of the increased temperatures.

3.4 Results and discussion

Plasma synthesis of germanium nanocrystals. Germanium NCs were synthesized using a nonthermal plasma technique in which germanium tectrachloride ($GeCl_4$) and molecular hydrogen (H_2) are dissociated in an Ar plasma, resulting in nucleation of Ge NCs. As we have shown previously, it is possible to alter the size and crystallinity of plasma-synthesized Ge NCs by tuning the particle residence time in the plasma and the plasma power.[18] For the sake of keeping some variables constant, all particles synthesized in this work were roughly 5 nm in diameter and crystalline (as verified by transmission electron microscopy and selected area electron diffraction). The standard deviation of the NC size distribution was 10-15% of the mean NC diameter, or roughly 0.5 nm.[18] To achieve consistent particle size across samples, the total gas flow rate (and therefore the particle residence time in the plasma) was kept constant at 72 sccm. However, the ratios of the precursor gases were varied, and the resulting effects on Ge NC surface chemistry were studied. In particular, the H_2 flow rate was varied from 5 sccm to 30 sccm while holding the $GeCl_4$ flow constant at 0.75 sccm, and adjusting the Ar flow to meet the balance. This resulted in three noticeable changes in the Ge NC powder. First, increasing the H_2 content increased the particle mass yield, which is to be expected since H radicals must scavenge dissociated Cl in order for Ge NC nucleation to occur. Second, the amount of plasma power required to produce crystalline particles increased with increasing H_2. This may be due to several factors including increased diffusion losses and an altercation of the particle heating mechanisms, but the majority of the effect is likely due to energy lost to dissociation of the additional H_2. Finally, and

most importantly for this study, the species present at the surfaces of the Ge NCs was observed to vary with the H_2 flow.

Figure 3-2 shows Auger electron spectroscopy (AES) derivative spectra for Ge NCs synthesized using 5, 7, and 9 sccm H_2. The peak-to-peak height of each feature is proportional to the measured atomic concentration of the element associated with that feature through a sensitivity factor. The spectra indicate the presence of Ge, Cl, and a small amount of O and C likely due to the short air exposure during sample transfer. The non-Ge species are presumed to be surface species since their AES signals are observed to change as the Ge NCs oxidize and high-resolution transmission electron microscopy (TEM) studies show single crystal diamond cubic Ge lattice fringes. Hydrogen, which may also be present on the surface, is not detectable with AES since Auger processes require two electrons. The spectra have been normalized to the Ge peak, and offset from each other to provide clarity. With 5 sccm H_2, the ratio of the Cl and Ge atomic concentrations is 0.11. This ratio rapidly decreases as the H_2 gas flow is increased, and is only 0.02 for 9 sccm H_2. With 30 sccm H_2, the Cl peak is no longer detectable.

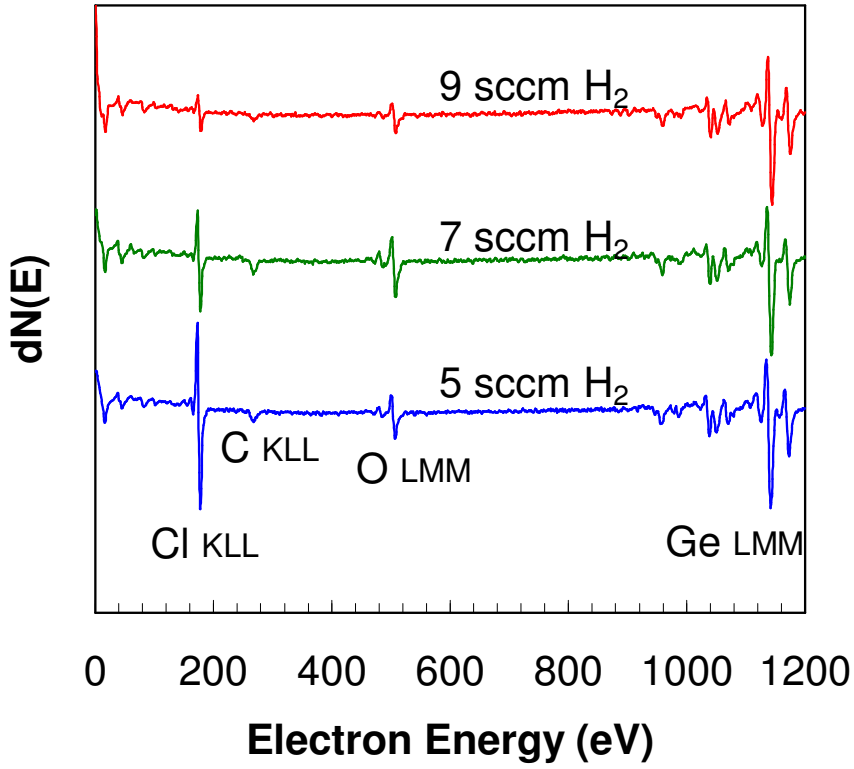

Figure 3-2. AES derivative spectra of three Ge NC powder samples synthesized with 0.75 sccm $GeCl_4$, 5-9 sccm H_2, and 62-66 sccm Ar. Spectra are normalized to the Ge LMM peak and offset for clarity.

As the presence of Cl at the Ge NC surfaces decreases, the presence of H increases. In Fig. 3-3, Fourier transform infrared (FTIR) spectra of Ge NC powder synthesized using 7, 13, and 20 sccm H_2 are displayed (the Ar flow was again varied to maintain a total flow of 72 sccm). The band at 2000 cm^{-1} is attributed to the stretching of Ge-H_x where the H species are located at the surface, and is seen to increase in intensity as additional H_2 is added to the plasma until it dominates the high wavenumber region of the spectrum.[23] Simultaneously, the lower frequency vibrations of Ge-H_x sharpen with increasing H_2 content, and the 575 cm^{-1}, 760 cm^{-1}, and 830 cm^{-1}peaks that arise from the bending modes of Ge-H and Ge-H_2 are clearly visible when 20 sccm H_2 is introduced

into the reactor.[23] Fang et al. have previously shown that for a-Ge:H the integrated intensity of the 575 cm^{-1} bend/wag peak is proportional to the hydrogen content in the material.[24] The peak at 1610 cm^{-1} and the broad feature above 3000 cm^{-1} arise from the bending and stretching of O-H_2. The presence of water at low H_2 flow rates may arise during sample transfer from increased reactivity with the atmosphere due to the presence of Cl on the Ge NC surfaces. There is little signature of water when the H_2 flow has reached 20 sccm or more. The Ge-O-Ge stretch at 860 cm^{-1} is not seen in these spectra because of the limited sample exposure to air prior to measurement; fresh Ge NCs are seen to oxidize in FTIR over the course of a few days.

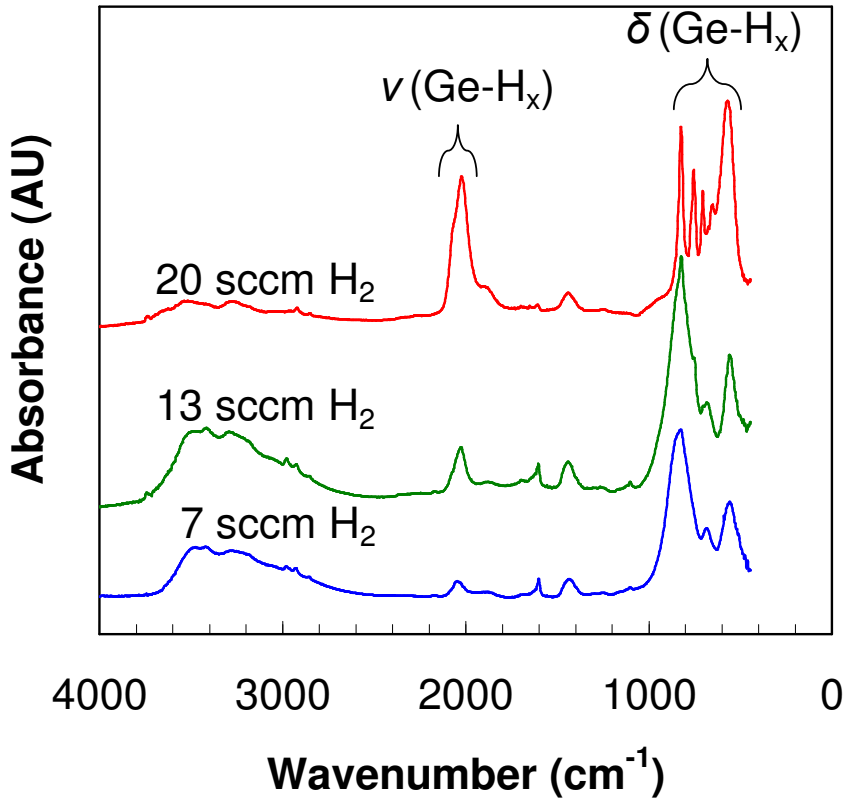

Figure 3-3. Diffuse reflectance FTIR spectra of three Ge NC powder samples synthesized with 0.75 sccm $GeCl_4$, 7-30 sccm H_2, and 64-41 sccm Ar. Spectra are offset for clarity.

Taken together, the AES and FTIR data give a complete picture of the evolution of the Ge NC surface species as the precursor gas ratios are varied. Using H_2-lean conditions, the as-synthesized particle surfaces are primarily Cl-terminated, while the termination is almost exclusively H under H_2-rich conditions. The surface chemistry may be tuned between these two extremes by choosing an appropriate H_2 flow rate.

Hydrogermylation of Ge-H_x surfaces. Thermally initiated hydrogermylation reactions were used to functionalize the surfaces of Ge NCs with alkyl molecules that solubilize the NCs in non-polar solvents. Hydrogermylation, which is directly analogous to the well-known hydrosilylation reaction, involves the insertion of an unsaturated bond into a Ge-H_x group. Choi and Buriak first demonstrated this reaction in 2000 by reacting alkenes and alkynes with H-terminated Ge(100) surfaces to leave attached alkyl and alkenyl groups.[25] The reaction has since been performed on nanowires[26] and nanoparticles[27] in addition to bulk Ge.

Germanium NCs were synthesized using 30 sccm H_2 in order to produce H-terminated particles suitable for hydrogermylation (Fig. 3-4). 1-dodecene was chosen for the reaction, and the attenuated total reflection (ATR) FTIR spectrum of neat 1-dodecence shown in Fig. 3-4 has the expected signature bands at 3010 cm^{-1}, 1640 cm^{-1}, 990 cm^{-1}, and 910 cm^{-1} arising from the alkene group. Following hydrogermylation, the dried, redispersed reaction product shows no IR activity where the Ge-H_x and C=C-H_2 bands were previously observed. However, C-H_x stretching (2850 cm^{-1}–3000 cm^{-1}) and bending (e.g., 1470 cm^{-1}, 1380 cm^{-1}, and 1300 cm^{-1}) bands are visible, indicating that the reaction successfully grafted alkyl chains to the particle surfaces. Furthermore, the

initially turbid solution became optically transparent, indicating that the attached ligands offer sufficient steric stabilization to solubilze the Ge NCs. Reactions with longer and shorter alkene chains were tried; we found that for chains with fewer than 10 carbon atoms the Ge NCs agglomerated and precipitated out of solution despite the presence of the ligands. After drying, Ge NCs reacted with 1-dodecene were successfully redispersed in alkanes such as hexane and octane, alkylbenzenes such as toluene and mesitylene, and trihalomethanes such as chloroform. The colloids were typically stable for months, with no signs of flocculation.

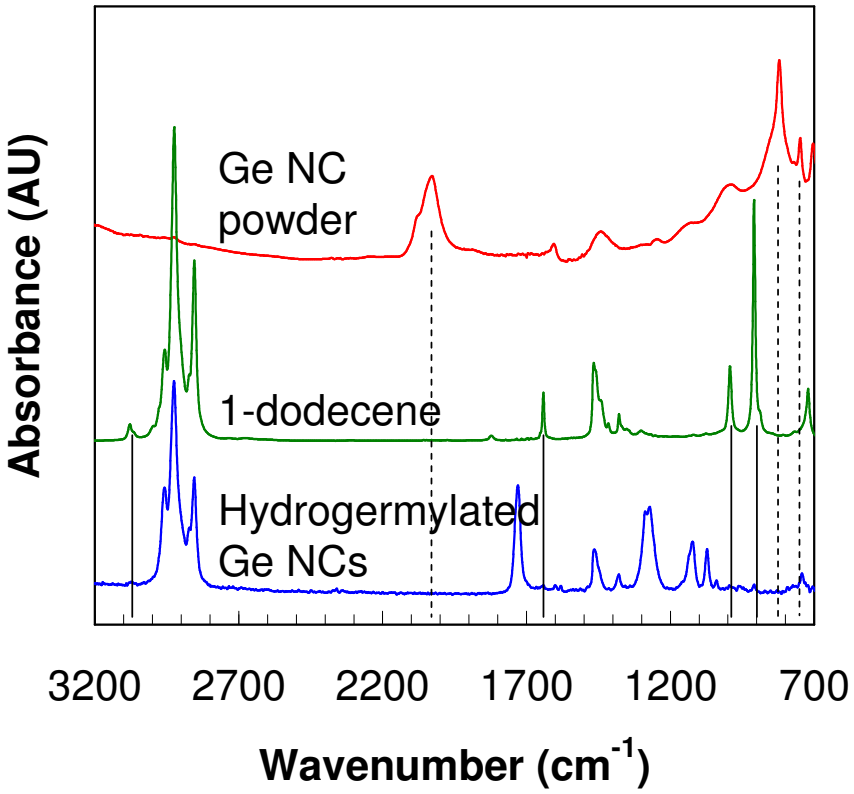

Figure 3-4. FTIR spectra of Ge NC powder (recorded in diffuse reflectance mode), neat 1-dodecene (recorded in ATR mode), and the reaction product after hydrogermylation of Ge NCs (recorded in ATR mode). The dotted lines indicate bands arising from Ge-H_x while the solid lines show bands from C=C-H_2.

Nanocrystal film formation and characterization. Films formed by drop-casting functionalized Ge NCs onto substrates exhibited very different morphologies depending on the solvents used. It is well known that solvent choice is important in the deposition of NCs from solution. For example, either random or superlattice arrangements of NCs have been obtained by controlling particle flocculation during drying via proper solvent choice.[28] In this work, solvents with low boiling points, such as chloroform and hexanes, did not allow the Ge NCs ample time to find their equilibrium positions during drying and resulted in films that were visibly rough. Scanning electron microscopy (SEM) revealed discontinuous film coverage and significant particle agglomeration. Slow drying alkanes, such as octane and nonane produced films that were locally uniform, but exhibited macroscopic thickness variations akin to coffee ring stains. Alkylbenzenes, particularly mesitylene and to a lesser degree xylenes, performed the best and produced films that were uniform both on microscopic and macroscopic scales. Figure 3-5 shows glassy films (unordered arrangements of Ge NCs) drop-cast from mesitylene at several magnifications. Size-selection techniques were not employed in this work; the monodispersity of the particles observed in Fig. 3-5 is therefore testimony to the success of the plasma synthesis method.

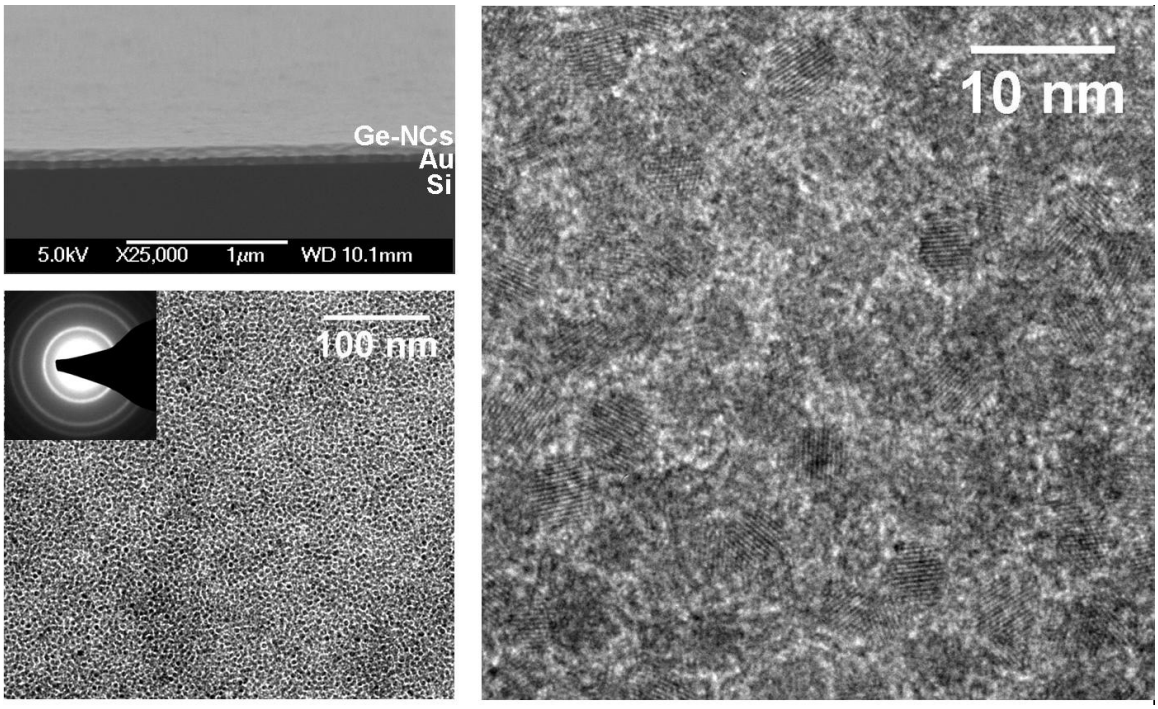

Figure 3-5. Cross-sectional SEM, top-view TEM (selected-area diffraction shown in inset), and top-view high-resolution TEM images of 5 nm Ge NCs reacted with 1-dodecene, dispersed in mesitylene, and drop-cast onto Au-coated Si or TEM grids. Each dark circle in the TEM images is an NC.

Figure 3-6 shows current-voltage measurements performed on Ge NC films drop-cast on glass substrates pre-patterned with electrodes where a log-log scale has been used for clarity. For sufficiently small applied biases, ohmic behavior was observed in all samples across all electrode gaps. However, the voltage range over which this linear behavior was seen was small for the 5 and 10 μm gaps because of contact effects. Consequently, all results reported here were measured over the 100 μm gap, for which the contact resistance was negligible compared to the film resistance, yielding linear curves across much larger voltage ranges. The films were initially insulating with conductivities of approximately 10^{-9} S/cm or smaller. This is consistent with reports for other untreated NC systems and is commonly attributed to the insulating nature of the

bulky ligands which allow the particles to be solubilized.[1,5,9,10] For 12-carbon-long 1-dodecene molecules, the minimum interparticle spacing expected assuming fully interlocking chains on neighboring NCs is on the order of 1.5 nm. This gap between crystals presents a significant barrier to charge transport by physically separating viable charge carrier states until there is no wavefunction overlap, leading to Mott insulator behavior.[29,30] Only with appreciably small interparticle distances can the exchange coupling energy become large enough to overcome the energy required to add an additional charge to a particle.[31,32]

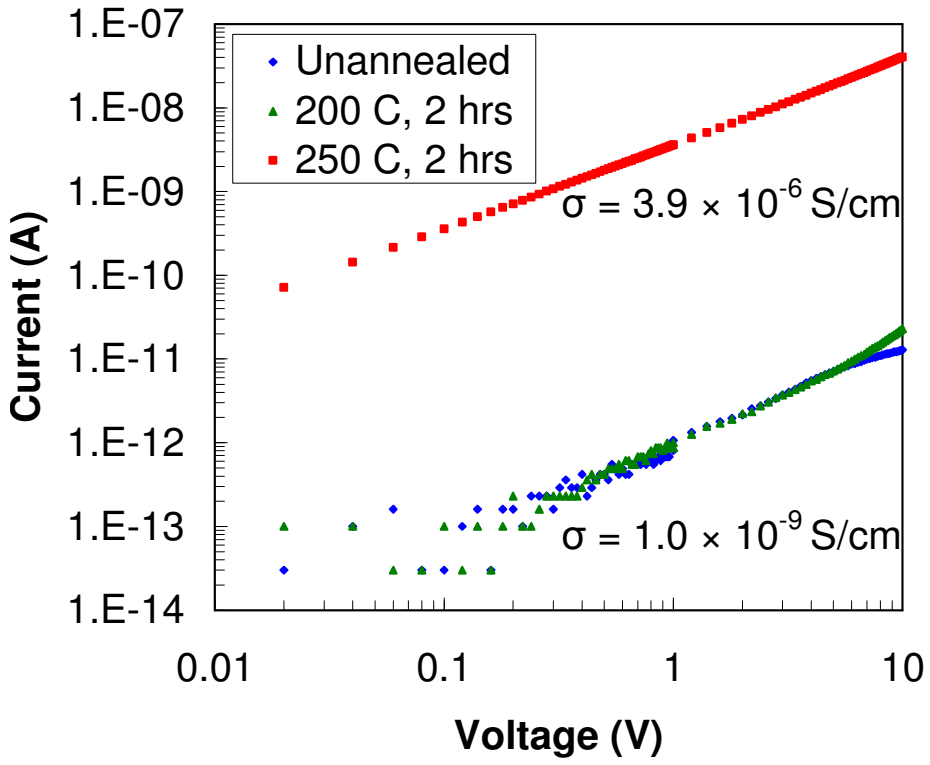

Figure 3-6. Current-voltage characteristics for Ge NC films as-deposited and annealed at 200 °C and 250 °C for 2 hours. These samples were prepared on glass pre-patterned with pairs of electrodes. A log-log scale is used for convenience because the data spans several orders of magnitude. Conductivities were calculated from the measured film thicknesses and known electrode geometry.

For films of 8 nm diameter PbSe NCs, Talapin and Murray observed that the conductivity increased by 10 orders of magnitude as the interparticle spacing decreased from 1.1 nm to 0.3 nm, although doping effects were also present.[10] The effect of decreasing the interparticle spacing is not expected to be as spectacular for Ge NCs as for PbSe NCs because the unusually large PbSe dielectric constant (~200 for bulk) means that the charging energy of a PbSe NC is roughly one-tenth that of a similarly sized Ge NC. However, treating a 5 nm Ge NC as a simple charged conducting sphere with potential $V = e / (4\pi\varepsilon_m\varepsilon_0 r)$ yields charging energies of 50-100 meV, which is still comparable to the thermal energy available at room temperature. Here, r is the NC radius and ε_m is the dielectric constant of the medium around the Ge NC (roughly one-third to two-thirds the bulk value of 16 depending on the interparticle spacing).

In an attempt to improve electrical performance, films were subjected to annealing treatments at various temperatures. A residual gas analyzer utilizing a mass spectrometer was attached to the annealing chamber during a series of experiments in order to monitor any gaseous species leaving the Ge NC films. Figure 3-7a displays mass spectra for a control experiment in which no sample was present in the chamber, and Fig. 3-7b shows the results of an identical experiment in which a Ge NC film was annealed. In all spectra, peaks from H_2, H_2O, N_2, O_2, Ar, and CO_2 can be seen at 2 amu, 18 amu, 28 amu, 32 amu, 40 amu, and 44 amu, respectively, due to residual air in the chamber. In the control experiment, little change is seen as the temperature is increased and these peaks remain the most prominent features at all temperatures. However, when a Ge NC film is in the chamber, broad peaks centered around 42 amu, 56 amu, 70 amu, 84 amu,

and 98 amu emerge at elevated temperature and grow as the temperature is increased. These signals are not due to the removal of solvent trapped in the film; FTIR spectra of dry films show no aromatic stretching or bending bands that would indicate residual mesitylene. Rather, the features, which are separated by intervals equal to the mass of CH_2, arise from gaseous hydrocarbon species C_yH_x which leave the Ge NC film upon decomposition of the dodecane chains. CH_x and C_2H_x are also present, and appear as a broadening of the H_2O and N_2 peaks with which they overlap. We note that the presence of gaseous hydrocarbons of all lengths indicates that alkyl chains bonded to the Ge NC surfaces do not simply detach; they decompose and likely leave carbonaceous residue behind.

In a similar experiment, a Ge NC film was annealed at 400˚ C and mass spectra were recorded in time (Fig. 3-7c). Hydrocarbon peaks dominate the initial spectrum, but they decrease in intensity much more quickly than the peaks that arise from residual air, such as H_2 and H_2O. After 5 mins at 400 °C, there are actually fewer gaseous hydrocarbon species present than if the sample had been annealed for the same time at 300 °C. Apparently, the rate of decomposition of the alkyl chains is accelerated with increasing temperature, and 400 °C is sufficient to remove the finite supply in just a few minutes.

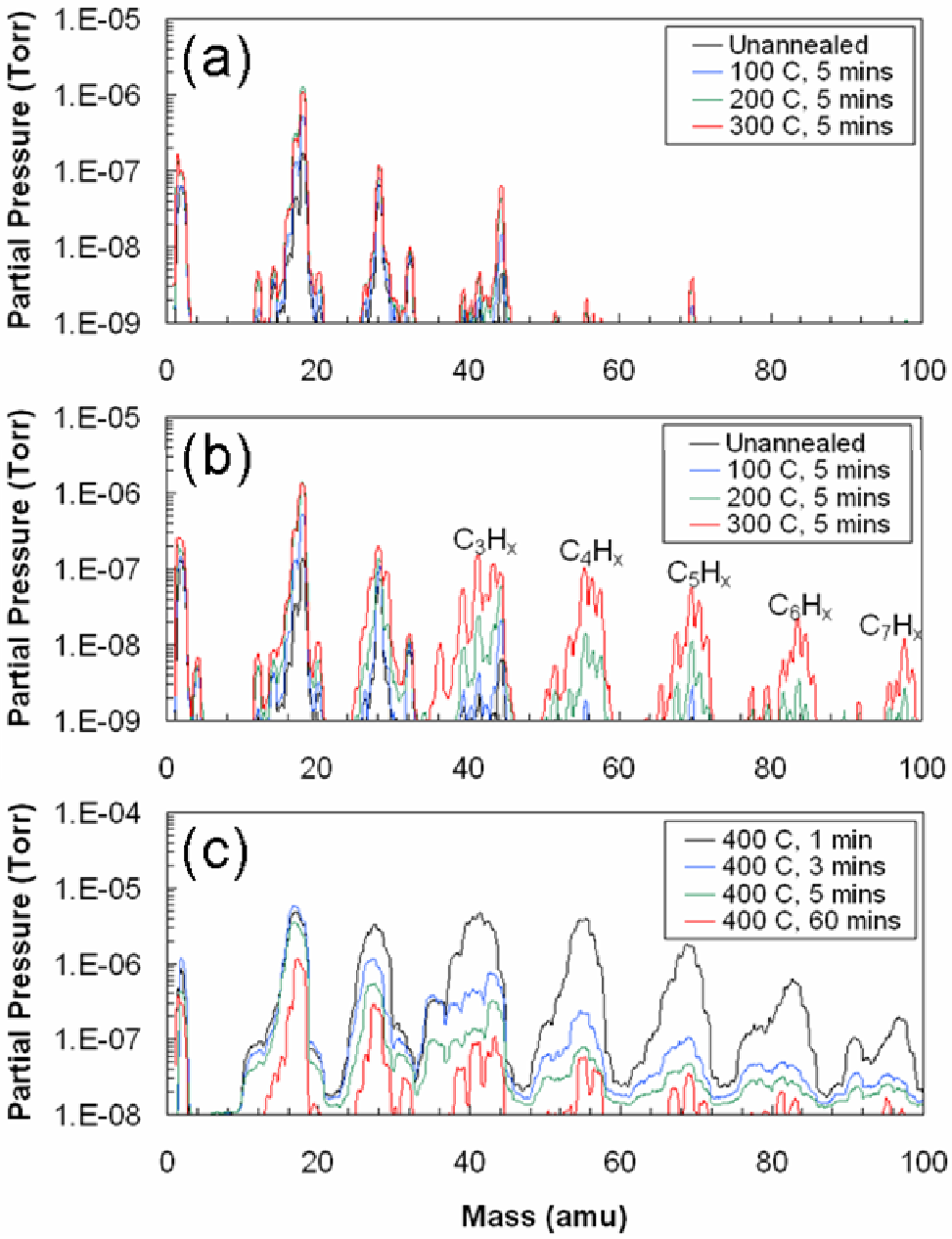

Figure 3-7. Mass spectra recorded in vacuum using a residual gas analyzer. Spectra for (a) a control sample (no film) and (b) a Ge NC film cast from a colloidal solution recorded at room temperature and annealing temperatures up 300 °C. (c) Spectra recorded in time for a Ge NC film held at 400 °C.

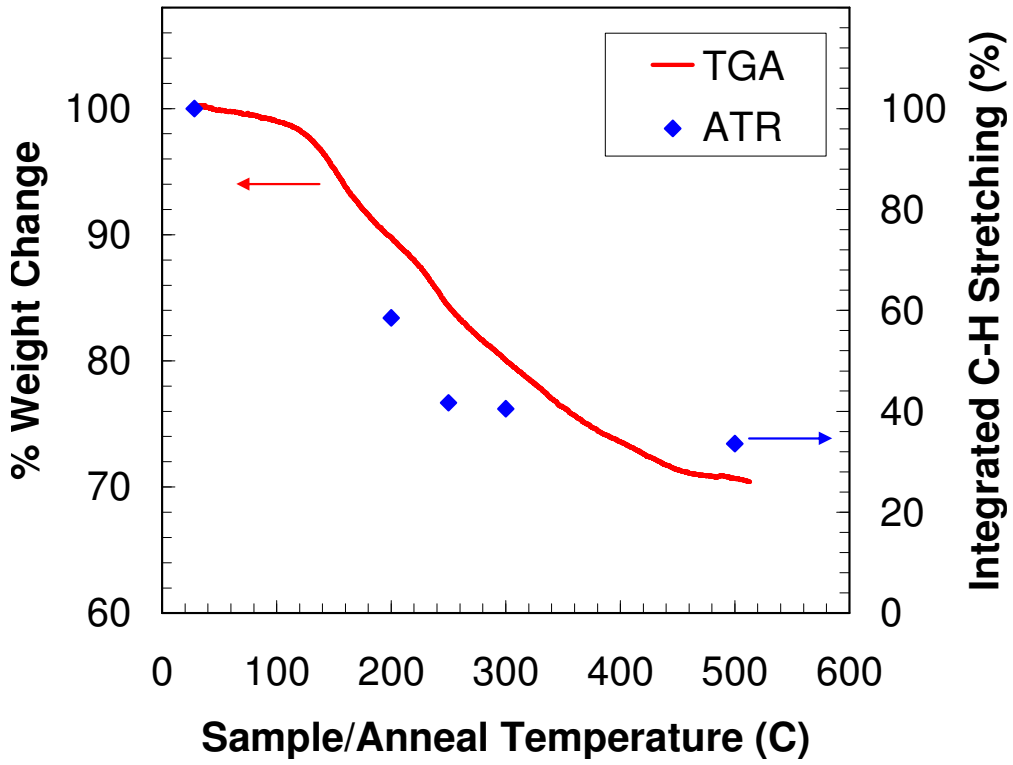

Figure 3-8. TGA fractional weight change (left axis) and ATR FTIR integrated intensity of the C-H_x stretching bands (right axis) of Ge NC films cast from solution and heated (TGA) or annealed (FTIR) at temperatures up to 500° C. A 1 hour annealing time was used for each temperature for the FTIR data.

ATR FTIR and Thermogravimetric analysis (TGA) corroborate these results; Fig. 3-8 shows the reduction in the integrated FTIR intensity of the C-H_x stretching region and the fractional weight loss for Ge NC films versus annealing temperature. The C-H_x stretch signal decreases with increasing annealing temperature as hydrocarbons are released from the sample and more than a two-fold reduction is seen by 250 °C. The TGA data shows the same trend and the film weight—given by the sum of the NC weight and the weight of the alkyl molecules—decreases to roughly two-thirds its original value by 500 °C. Both sets of data show that, above some threshold temperature (~130 °C for the TGA data), incremental increases in temperature yield diminishing improvement in

hydrocarbon removal. Consistent with the mass spectrometry findings that the alkyl chains do not cleave off at the NC surfaces, some C-H_x stretching signal is still present after annealing for 1 hr at 500 °C.

No significant changes in electrical behavior were seen in our films for annealing temperatures up to 200 °C (Fig. 3-6), despite some loss of insulating hydrocarbons. However, a dramatic increase in performance occurs when the temperature is raised to 250 °C. After 2 hours of annealing at 250 °C, conductivities on the order of 10^{-6} S/cm have been measured, an increase of three orders of magnitude. In addition, cracking has been observed in thick (~1 μm) films via SEM after annealing treatments at temperatures above 250 °C, indicating decreases in film volume and interparticle spacing. This suggests that there is a threshold annealing temperature near 250 °C, beyond which enough carbonaceous material has been removed to allow electronic coupling between neighboring Ge NCs. Indeed, we have observed that above 250 °C the conductivity continues to increase with increasing annealing temperature, up to 5×10^{-4} S/cm for samples annealed at 500 °C. There is only marginal improvement in conductivity as the annealing time is extended from 1 to 3 hrs. This is expected since mass spectrometry indicates that the characteristic time of ligand decomposition is less than 1 hr for temperatures greater than 250 °C.

When annealing NCs with large surface energies at elevated temperatures, there is a concern that the particles will sinter together. Thus, XRD spectra were recorded for thick Ge NC films on glass annealed up to 500 °C for 1 hr to ensure that the observed improvements in conductivity were not due to sintering of NCs. In Fig. 3-9, the spectra

are displayed and the diamond cubic Ge peaks are labeled. The average crystallite grain size was determined from the peak broadening using the Debye-Scherrer equation, and a constant Ge NC size of roughly 5 nm was obtained for all samples up to 500 °C. Samples were also heated to 600 °C, 700 °C, and 800˚ C in a commercial rapid thermal annealing chamber capable of reaching higher temperatures than our home-built chamber. For these three samples, the commercial annealing chamber was operated at atmospheric pressure with 10 slm N_2 flow. Sintering of the NCs was not observed until 800 °C, at which point the film began to flake and the average grain size extrapolated from the XRD measurement varied from 8 nm to ~25 nm across the sample depending on whether the beam was focused on a flaking area or not (Fig. 3-9). We found it surprising that such high temperatures were required for sintering, particularly because similar annealing experiments performed with bare (H-terminated) Ge NC powder show sintering and grain growth beginning at 500-600 °C. We presume that the hydrocarbon residue left in the films of 1-dodecene-terminated Ge NCs is responsible for delaying sintering to higher temperatures. High-resolution SEM studies of films corroborate the XRD findings and show no observable sintering for annealing temperatures below 500 °C, but clear evidence of both grain and void growth at 800 °C (Fig. 3-10). Hence, increases in electrical conductivity cannot be attributed to grain growth for annealing temperatures below 500 °C, but instead results from increased electronic coupling of distinct Ge NCs as the insulating 1-dodecene ligands that separate them decompose.

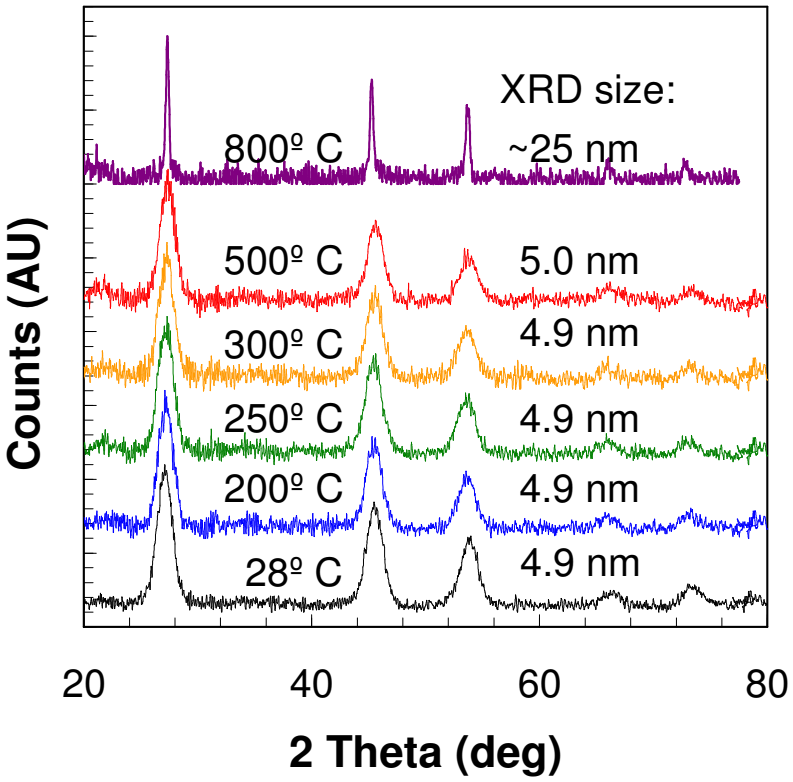

Figure 3-9. XRD spectra of thick (~ 1 μm) Ge NC films cast from solution and annealed up to 800 °C. The samples annealed at 500 °C and lower were annealed for 1 hr in the home-built rapid thermal annealing chamber described in the Experimental section. The sample annealed at 800 °C was annealed for only 2 mins in a similar, commercial system operated at atmospheric pressure with 10 slm of N_2 flow. Samples were also annealed at 600 °C and 700 °C (not shown) in this system, but no grain growth was observed at these temperatures. Crystallite sizes were calculated from the peak widths using the Debye-Scherrer equation.

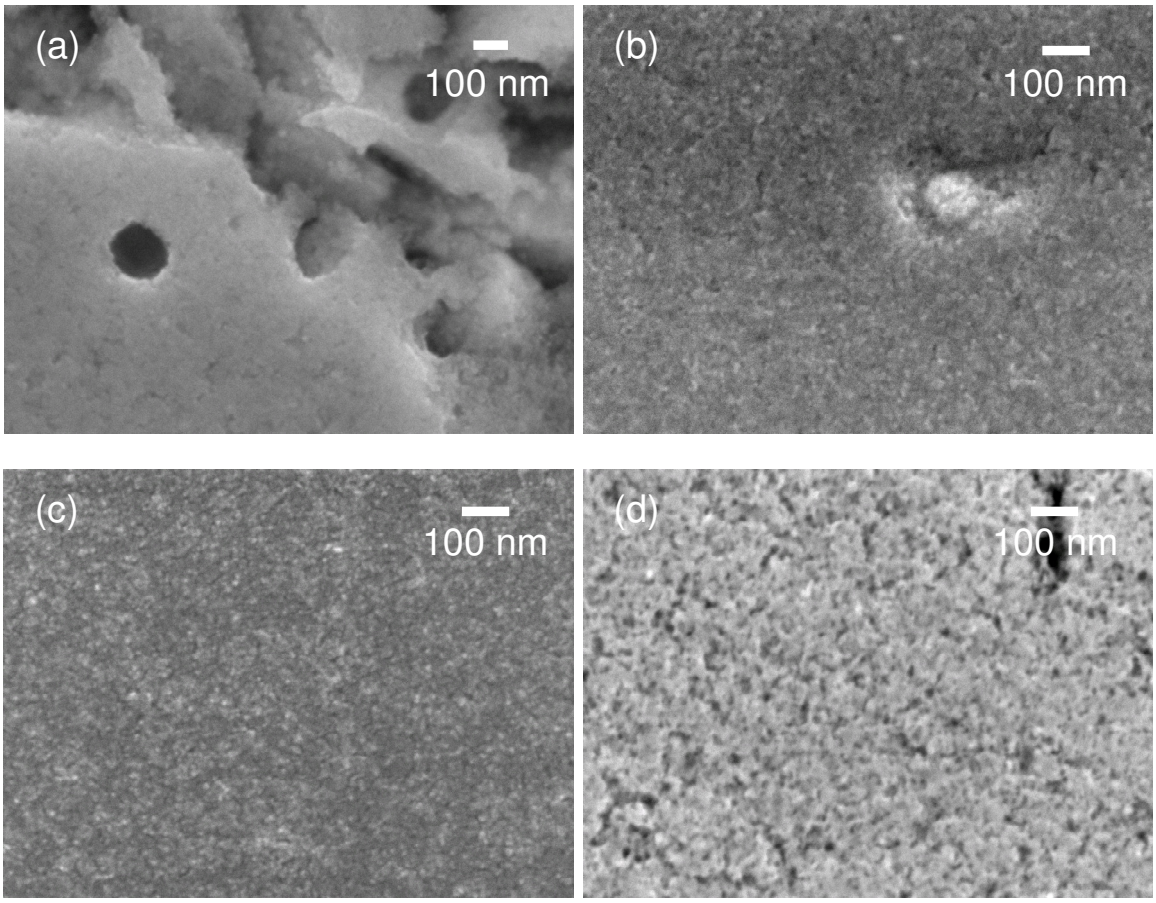

Figure 3-10. High resolution SEM images of (a) an unannealed Ge NC film and films annealed at (b) 250 °C for 1 hr, (c) 500 °C for 1 hr, and (d) 800 °C for 2 mins. No observable sintering is seen in (b) and (c), but both grain and void growth are clearly seen in (d). Note that it is challenging to image unannealed films like (a) under an electron beam at high resolution because their insulating nature causes them to charge. As a result, (a) is at slightly lower magnification than (b), (c), and (d), and a defect in the film was found to provide contrast.

3.5 Conclusions

Progress in group IV NC electronic devices has been slowed by difficulties synthesizing Si and Ge NCs in solution. Here, we have bypassed this barrier by synthesizing Ge NCs using a gas-phase method and then transferring them into solution

after functionalizing the surfaces with long-chain alkene molecules. Provided they are sufficiently long, the molecules provide enough steric stabilization in non-polar solvents to counteract the van der Waals attractions between NCs and prevent agglomeration. Dense films of Ge NCs that are uniform over several square centimeters are formed by drop-casting the colloid onto substrates.

After film deposition, the alkyl molecules that were key to stabilizing the Ge NC colloid become a nuisance since they physically separate neighboring NCs and inhibit charge transport between them. One key difference between our Ge NCs and II-VI and IV-VI NCs is that the former form strong covalent bonds with the alkyl molecules on their surfaces whereas the latter form coordination complexes with ligands which are more easily severed. Consequently, ligand exchange reactions which work for II-VI and IV-VI NCs are not successful with alkyl-terminated Ge NCs. In addition, the attachment between Ge NCs and the alkyl molecules is so strong that the molecules decompose upon heating rather than fracturing from the surface of the NCs.

At annealing temperatures greater than 250 °C, enough hydrocarbon material is removed to open conduction pathways between NCs, resulting in an increase in the electrical conductivity of initially insulating films. Conductivities as large as 10^{-6} S/cm have been measured for Ge NC films annealed at 250 °C for 2 hours, and the conductivity continues to rise at higher annealing temperatures. While these conductivities are modest compared to those in bulk semiconductors, Schottky-barrier solar cells with power conversion efficiencies of 2.1% were recently reported using PbSe NC thin films with measured conductivities of 5×10^{-5} S/cm.[6] In light of this work, the

Ge NC films presented here are promising candidates for NC photovoltaic devices including future multi-junction solar cells.

3.6 Future work

The attachment of alkene molecules to Ge NCs via hydrogermylation in solution yields very nice colloids and subsequent thin films, but is neither amenable to scale-up nor desirable for device applications. The reaction in solution is slow and is performed in batches, although Mangolini et al. demonstrated a plasma-initiated hydrosilylation scheme in which alkene vapor is injected into a low power plasma downstream of a Si NC synthesis plasma.[33] This approach has the advantage of being quick, simple, and continuous, although the resulting alkene termination was apparently not as complete as when attachment was performed in solution. We have successfully tried this approach with Ge NCs as well; however, there is currently no motivation to functionalize Ge NCs with alkenes, even if doing so is easy. Silicon NCs exhibit dramatically improved photoluminescence (PL) after hydrosilylation and have been recently incorporated into light-emitting diodes,[34] but our Ge NCs do not show any PL either before or after hydrogermylation. Furthermore, all devices we have made with functionalized Ge or Si NCs have been insulating as deposited. Similar to the two-contact devices for conductivity measurements reported in this chapter, field-effect transistors (FETs) fabricated with dodecene-passivated Ge NCs only begin to perform after they are annealed at temperatures in excess of 300 °C. We have found an alternative method to make superior Ge NC FETs from solution (see Chapter 5), so it is not clear that there is a

future for hydrogermylated Ge NCs in devices. Perhaps another reaction will be discovered which attaches more useful molecules (e.g., conductive polymer) to the NC surfaces.

3.7 References

[1] M. Drndic, M.V. Jarosz, N.Y. Morgan, M.A. Kastner, and M.G. Bawendi, *J. Appl. Phys.* **92**, 7498 (2002).

[2] I. Gur, N.A. Fromer, M.L. Geier, and A.P. Alivisatos, *Science* **310**, 462 (2005).

[3] K.W. Johnston, A.G. Pattantyus-Abraham, J.P. Clifford, S.H. Myrskog, D.D. Macneil, L. Levina, and E.H. Sargent, *Appl. Phys. Lett.* **92**, 151115 (2008).

[4] G.I. Koleilat, L. Levina, H. Shukla, S.H. Myrskog, S. Hinds, A.G. Pattantyus-Abraham, and E.H. Sargent, *ACS Nano* **2**, 833 (2008).

[5] M. Law, J.M. Luther, O. Song, B.K. Hughes, C.L. Perkins, and A.J. Nozik, *J. Am. Chem. Soc.* **130**, 5974 (2008).

[6] J.M. Luther, M. Law, M.C. Beard, Q. Song, M.O. Reese, R.J. Ellingson, and A.J. Nozik, *Nano Lett.* **8**, 3488 (2008).

[7] C.B. Murray, C.R. Kagan, and M.G. Bawendi, *Science* **270**, 1335 (1995).

[8] D.C. Oertel, M.G. Bawendi, A.C. Arango, and V. Bulovic, *Appl. Phys. Lett.* **87**, 213505 (2005).

[9] H.E. Romero and M. Drndic, *Phys. Rev. Lett.* **95**, 156801 (2005).

[10] D.V. Talapin and C.B. Murray, *Science* **310**, 86 (2005).

[11] J.J. Urban, D.V. Talapin, E.V. Shevchenko, and C.B. Murray, *J. Am. Chem. Soc.* **128**, 3248 (2006).

[12] C.B. Murray, D.J. Norris, and M.G. Bawendi, *J. Am. Chem. Soc.* **115**, 8706 (1993).

[13] H.W. Chiu and S.M. Kauzlarich, *Chem. Mater.* **18**, 1023 (2006).

[14] D. Gerion, N. Zaitseva, C. Saw, M.F. Casula, S. Fakra, T. Van Buuren, and G. Galli, *Nano Lett.* **4**, 597 (2004).

[15] X.M. Lu, B.A. Korgel, and K.P. Johnston, *Chem. Mater.* **17**, 6479 (2005).

[16] D.C. Lee, J.M. Pietryga, I. Robel, D.J. Werder, R.D. Schaller, and V.I. Klimov, *J. Am. Chem. Soc.* **131**, 3436 (2009).

[17] L. Mangolini, E. Thimsen, and U. Kortshagen, *Nano Lett.* **5**, 655 (2005).

[18] R. Gresback, Z. Holman, and U. Kortshagen, *Appl. Phys. Lett.* **91**, 093119 (2007).

[19] D. Jurbergs, E. Rogojina, L. Mangolini, and U. Kortshagen, *Appl. Phys. Lett.* **88**, 233116 (2006).

[20] G. Nesher, L. Kronik, and J.R. Chelikowsky, *Phys. Rev. B* **71**, 035344 (2005).

[21] T. Takagahara and K. Takeda, *Phys. Rev. B* **46**, 15578 (1992).

[22] J.P. Wilcoxon, P.P. Provencio, and G.A. Samara, *Phys. Rev. B* **64**, 035417 (2001).

[23] M. Cardona, *Phys. Status Solidi B* **118**, 463 (1983).

[24] C.J. Fang, K.J. Gruntz, L. Ley, M. Cardona, F.J. Demond, G. Muller, and S. Kalbitzer, *J. Non-Cryst. Solids* **35-6**, 255 (1980).

[25] K. Choi and J.M. Buriak, *Langmuir* **16**, 7737 (2000).

[26] T. Hanrath and B.A. Korgel, *J. Am. Chem. Soc.* **126**, 15466 (2004).

[27] E. Fok, M.L. Shih, A. Meldrum, and J.G.C. Veinot, *Chem. Commun.* **4**, 386 (2004).

[28] C.B. Murray, C.R. Kagan, and M.G. Bawendi, *Annu. Rev. Mater. Sci.* **30**, 545 (2000).

[29] C.P. Collier, R.J. Saykally, J.J. Shiang, S.E. Henrichs, and J.R. Heath, *Science* **277**, 1978 (1997).

[30] N.F. Mott, *Metal-Insulator Transitions* (Taylor & Francis, London, 1990).

[31] F. Remacle, *J. Phys. Chem. A* **104**, 4739 (2000).

[32] F. Remacle, K.C. Beverly, J.R. Heath, and R.D. Levine, *J. Phys. Chem. B* **107**, 13892 (2003).

[33] L. Mangolini and U. Kortshagen, *Adv. Mater.* **19**, 2513 (2007).

[34] K.Y. Cheng, R. Anthony, U.R. Kortshagen, and R.J. Holmes, *Nano Lett.* **10**, 1154 (2010).

4

Bare germanium nanocrystals in solution

4.1 Outline

Colloidal nanocrystals typically have ligands attached to their surfaces which afford solubility in common solvents but hinder charge transport in nanocrystal films. Here, an alternative route is explored in which bare germanium nanocrystals are solubilized by select solvents to form stable colloids without the use of ligands. A survey of candidate solvents shows that germanium nanocrystals completely dissolve in benzonitrile, likely because of electrostatic stabilization and reduced van der Waals forces. Films cast from these dispersions are uniform, dense, and smooth, making them suitable for device applications. In addition, molar absorptivities are calculated from absorption spectra of colloidal germanium nanocrystals, and the quantum-confinement-induced shifts of the E_0 and E_1 transition energies are measured as a function of nanocrystal size.

4.2 Introduction

Semiconductor nanocrystals (NCs) or quantum dots have received increasing attention in the past 15 years for their potential use in new optical and electronic devices. Colloidal NCs are particularly interesting, as they promise a new era in inorganic semiconductor processing in which quantum-confined thin films are inexpensively printed. Methods have been developed to synthesize high quality II-VI and IV-VI NCs in solution with ligands such as trioctylphosphine/trioctylphosphine oxide or oleic acid on their surfaces.[1-6] The ligands provide steric stabilization in non-polar solvents—compression of the ligands as two NCs approach each other decreases the entropy of the system and consequently increases the Gibbs free energy—so that aggregation of NCs due to van der Waals forces is suppressed. Unfortunately, the ligands also hinder charge carrier transport between NCs after films casting, and as-deposited films are insulating.[7-10] While the ligands may be exchanged in solution for shorter molecules that reduce the interparticle spacing in films,[5,11] shorter molecules provide less steric stability, encouraging flocculation. An alternative approach is to reduce the ligand length *after* depositing films. Excellent electronic properties have been obtained in PbSe NC films treated with hydrazine and 1,2-ethanedithiol, but the films crack after the treatments.[10,12]

Depositing conductive thin films from group IV colloidal NCs is even more difficult. Silicon and Ge have comparatively large crystallization temperatures because of their covalent bonds, making solution synthesis challenging.[13] Furthermore, once ligands have been attached either during solution synthesis or via grafting to gas-phase synthesized NCs, they do not come off. Attempts to exchange ligands in solution or

chemically treat films after deposition are ineffectual, again because of the covalent bonds formed. We previously reported that Ge NC films fabricated by synthesizing Ge NCs in a plasma, functionalizing their surfaces with 1-dodecene, and casting them from solution were electrically insulating until annealed at 250 °C or higher.[14] At these temperatures, the dodecene molecules still did not cleave from the NC surfaces; they decomposed instead.

Steric stabilization is not the only way to prevent flocculation of colloids. Colloidal particles may acquire charge at their surfaces in polar or ionic solutions, resulting in the formation of electrical double layers which repel each other upon approach. The potential at the surface of shear outside each particle—the zeta potential—provides an indication of the degree of stabilization and the sign of the accumulated charge. Additionally, van der Waals attractions may be reduced by proper solvent choice. The van der Waals force between two identical spheres in a medium disappears if the Hamaker constant of the medium is the same as that for the spheres, and no repulsive force is required between the spheres to inhibit aggregation. Nanocrystal colloids which are stabilized via one of these mechanisms instead of with bulky ligands offer new opportunities for NC handling and device fabrication.

In previous publications (Chapter 5 of this thesis), we reported that "bare" Si and Ge NCs are relatively stable in 1,2-dichlorobenzene (DCB).[15,16] The NCs are synthesized as powders with a plasma process that produces H-terminated surfaces for Si NCs, and H- and Cl-terminated surfaces for Ge NCs. The Ge NCs form particularly nice colloids that are optically transparent and yield uniform thin films when spun, and

respectable field-effect transistors have been demonstrated using these films.[15] In this chapter, we investigate the solubility of Ge NCs in nearly 20 solvents that are similar to DCB, and probe the mechanism responsible for stability of the colloids.

One solvent, benzonitrile, is found to perfectly solubilize Ge NCs. This represents an important step in NC processing; additionally, it allows for new fundamental studies of the optical properties of Ge NCs. Most reports of quantum confinement in Ge NCs have relied on photoluminescence (PL) measurements,[17-25] which are complicated by the apparent presence of radiative defect states. Visible PL has been repeatedly reported, and the literature is divided as to whether its source is the NC core,[19,22,23] or oxide or surface states.[18,20,24,25] Although the PL energy is expected to approach the bulk Ge bandgap of 0.7 eV as the NC size increase, we are aware of only two reports of IR PL in Ge NCs.[17,21] Interpretation of absorption data is less complicated and yields more information about band structure, but it is difficult to know the concentration of NCs accurately if they are synthesized in solution with ligands attached. Consequently, absorption spectra of Ge NCs of different sizes are typically normalized when compared.[17,23,26] In fact, extinction coefficients have been measured for relatively few NC materials systems because of this limitation. Molar absorptivities calculated from absorption spectra of colloids of known concentration are presented here for bare Ge NCs of various sizes in benzonitrile.

4.3 Experimental

Germanium NCs were synthesized in powder form using a nonthermal plasma process described elsewhere.[27] Briefly, $GeCl_4$ and H_2 were used as precursors in a flow-through, radiofrequency plasma reactor to nucleate Ge NCs with H- and Cl-terminated surfaces.[14,15] Nanocrystals 3.9–10.7 nm in diameter were produced by varying the residence time of the NCs in the plasma via the reactor pressure. Nanocrystals were collected air-free and transferred to a N_2-purged glove box, where the mass of the samples were measured (~10 mg average, 5 mins deposition). A variety of solvents (Aldrich, degassed) were added to vials containing Ge NCs and the mixtures were ultra-sonicated for 5 mins outside of the glove box. The resulting dispersions were returned to the glove box and filtered through 0.2 μm PTFE filters (Pall).

Absorption measurements were performed using an Ocean Optics UV-Vis spectrometer (for solvent comparison) or a Cary UV-Vis-NIR spectrophotometer (for measuring molar absorptivity). Air exposure was limited to ~1 min for all samples prior to measurement to prevent oxidation, and measurements were taken within 30 mins of sonnication. For some samples, zeta potential was measured with a Brookhaven Instruments Corporation ZetaPlus instrument. Nanocrystal diameters were determined from Debye-Scherrer fits to X-ray diffraction (XRD) spectra of powder or films cast from concentrated NC solutions. For two samples, the accuracy of the XRD sizes was confirmed using transmission electron microscopy. The variation in mean size was found to be less than 10%. Some films were imaged using a JEOL 6500 field-emission scanning

electron microscope (SEM) and a Digital Instruments Nanoscope III atomic force microscope (AFM) operated in tapping mode.

4.4 Results and discussion

Survey of solvents. The stability of 6 nm diameter Ge NCs in a variety of solvents was studied by comparing the concentration of Ge NCs that remained suspended after filtering the dispersions through a 0.2 μm filter to the initial concentration. Solvents were chosen for their similarity to DCB in dielectric constant, Hansen Solubility Parameters, or chemical structure. The solvents are shown in Fig. 4-1, and primarily consist of molecules with halogens or nitrile groups. Common solvents such as water, toluene, and hexanes were also tried, but Ge NCs were found to rapidly flocculate in all very polar or very non-polar solvents. Germaniums NCs remained in powder form at the bottom of their vials upon addition of all solvents except benzonitrile and acetonitrile, and ultrasonication was required to break up the powder and suspend the NCs. Benzonitrile, and to a lesser extent acetonitrile, solubilized bare Ge NCs upon contact and an optically transparent colloid was formed with a brief shake. The process is visually similar to the addition of non-polar solvents to dried Ge NCs that have been functionalized with 1-dodecene.

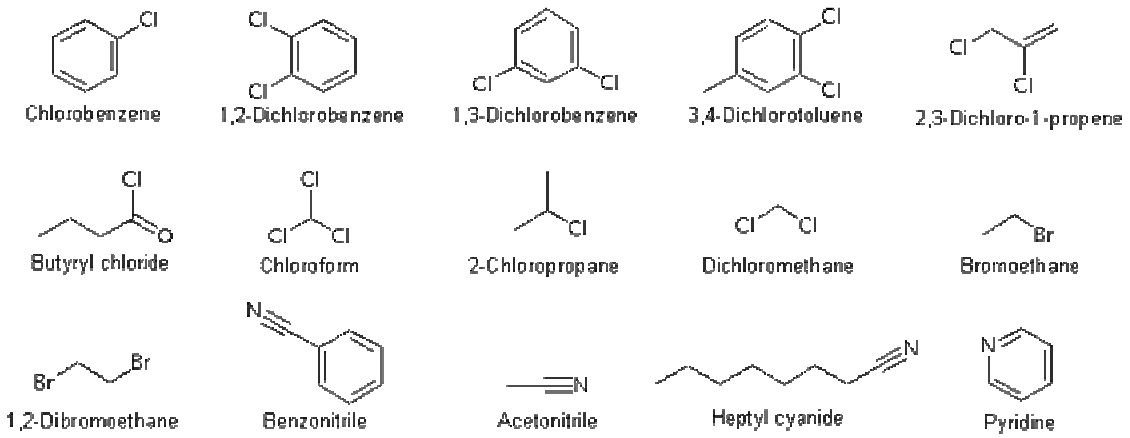

Figure 4-1. Names and chemical structure of solvents used in this study.

0.25 mg ml^{-1} dispersions were prepared for each solvent, and UV-Vis absorption measurements were recorded before and after filtration. Scattering from agglomerates dominated the spectra for most suspensions before filtration, and many samples looked like pristine solvent after filtration. Germanium NCs in these solvents, which include 2-chloropropane, heptyl cyanide, 1,2-dibromoethane, bromoethane, dichloromethane, pyridine, 1,3-dichlorobenzene, chloroform are unstable and quickly form aggregates larger than the filter pore size. The absorption spectra of Ge NCs in benzonitrile, by contrast, were identical before and after filtration, indicating small (or no) aggregates. Because scattering is not an issue in these samples, the Beer-Lambert Law can be used to correctly relate absorption to concentration, which in this case is the same before and after filtering and is known. Consequently, the absorption of Ge NCs in benzonitrile was used as a reference to determine the unknown concentrations of Ge NCs remaining in other solvents after filtration. The ratio of absorbances was calculated using absorbance data at 500 nm, although the result was nearly wavelength-independent. Figure 4-2 displays the relative concentrations after filtration for all solvents that had non-zero post-

filtration concentrations. Also shown is a photograph of Ge NC colloids in several solvents after filtration; these samples had the same initial concentration.

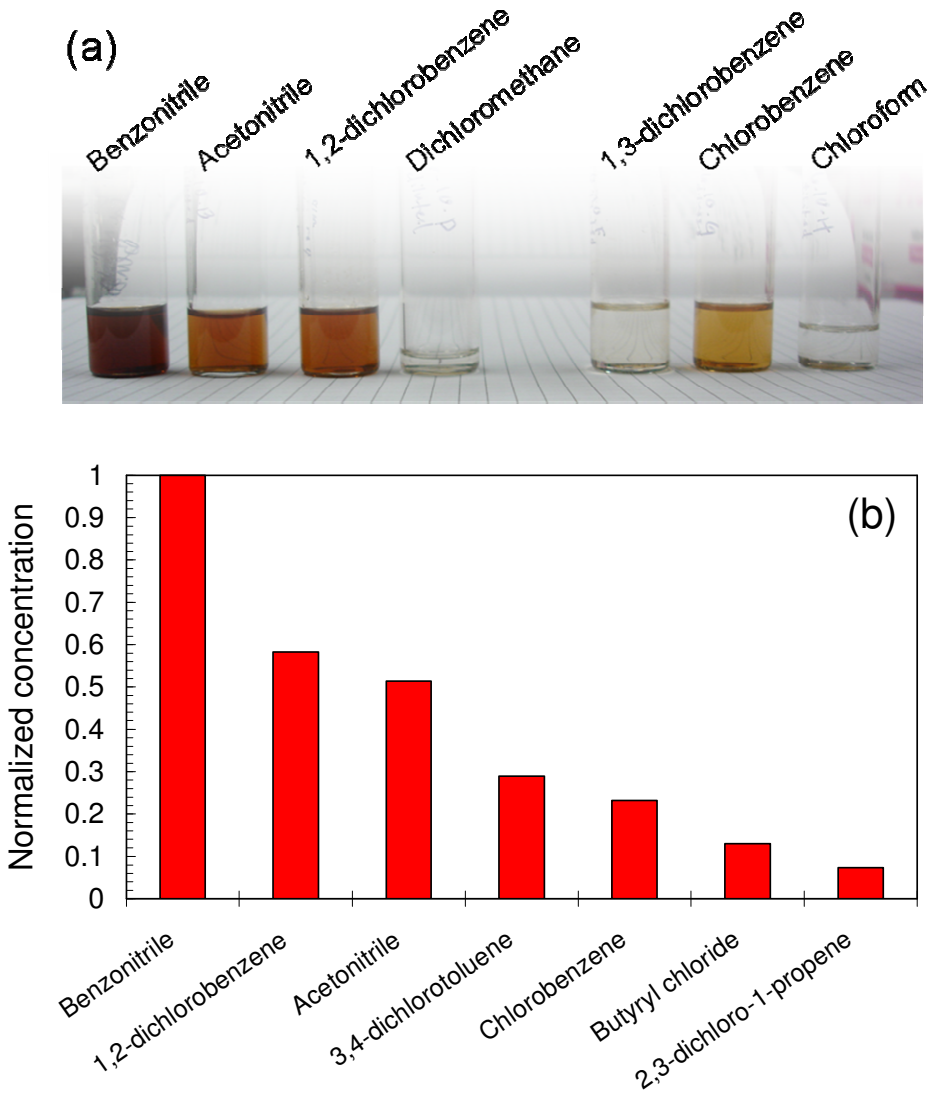

Figure 4-2. (a) Photograph of Ge NCs in various solvents after passing through a 0.2 µm filter. All samples started at the concentration of the benzonitrile sample at the left. (b) Concentration of Ge NCs in solvents after filtration, normalized to pre-filtration concetration. Solvents not plotted had concentrations of 0.

These data represent a metric for colloidal stability, albeit a somewhat unusual one. While techniques such as dynamic light scattering (DLS) are more commonly

employed to characterize colloids, they do not easily measure the quantities desired here. From a device applications perspective, an ideal NC colloid has a minimum flocculation time of a month and produces homogeneous films when cast. Dynamic light scattering gives the size distribution of colloidal particles. However, DLS data may indicate that the "best" sample is one with 99% of the material precipitated at the bottom of the cuvette, provided the 1% remaining suspended consists of isolated NCs. We would like to find solvents that have the fewest agglomerates larger than a few hundred nanometers (as these are sure to either precipitate or ruin film morphology), and filtration measures this.

What is the mechanism by which Ge NCs are stabilized in select solvents? Steric stabilization plays no role since there are no ligands on the NC surfaces. We note as well that, in the majority of cases, we believe chemical reactions do not occur. X-ray diffraction spectra of Ge NC powder and films cast from three solvents (benzonitrile, 1,2-dichlorobenzene, and chlorobenzene) show no change in crystal grain size after the NCs are put into solution, indicating that, e.g., the Ge does not dissolve. In addition, Fourier transform infrared spectroscopy and Rutherford backscattering measurements show no significant changes in the H and Cl species at the NC surfaces after Ge NCs are solubilized in DCB.[15]

The measured zeta potential on colloidal Ge NCs in benzonitrile is -23 ± 5 mV, indicating that the NC surfaces are negatively charged. Zeta potentials of either sign greater than 25 or 30 mV are generally accepted as being large enough to provide long-term electrostatic stability. Surface charging mechanisms for particles in solution include preferential adsorption of ions of one charge from solution, and ionization or dissociation

of surface species. We do not yet understand Ge NC charging, but note that the concentration of ions in benzonitrile or the other solvents studied here should be near zero, and no electrolyte was added. However, others have reported electrical double layer formation for colloids in polar solvents with no electrolyte addition.[28] Dissociation of H on Ge NC surfaces could account for their negative potential.

If electrostatic repulsion is the dominant force in stabilizing Ge NC colloids, stability is expected to be correlated with ion concentration (not investigated here) and solvent dielectric constant.[28] The degree to which van der Waals attractions are reduced by particle-solvent matching should also be correlated with solvent dielectric constant. Dispersion forces vanish when the solvent and colloidal particles have equal Hamaker constants, and the Hamaker constant is approximately proportional to polarizability squared, which in turn depends on dielectric constant. The relative concentration of Ge NC colloids after filtering is plotted in Fig. 4-3 as a function of solvent static dielectric constant. Nanocrystals only passed through the filter in solvents with dielectric constants between 5 and 38 and while there may be a trend with the optimal dielectric constant being ~20, there is too little data to know. It is clear, however, that dielectric constant alone is not sufficient to predict colloid stability. Germanium NCs in several solvents with dielectric constants of 9–14 were completely removed by filtration. A complication in interpreting this data in terms of stability mechanism is that Fig. 4-3 plots static dielectric constant, but an accurate treatment of the Hamaker constant considers the frequency-dependence of the dielectric constant. Further experiments are required to parse the details of Ge NC stabilization.

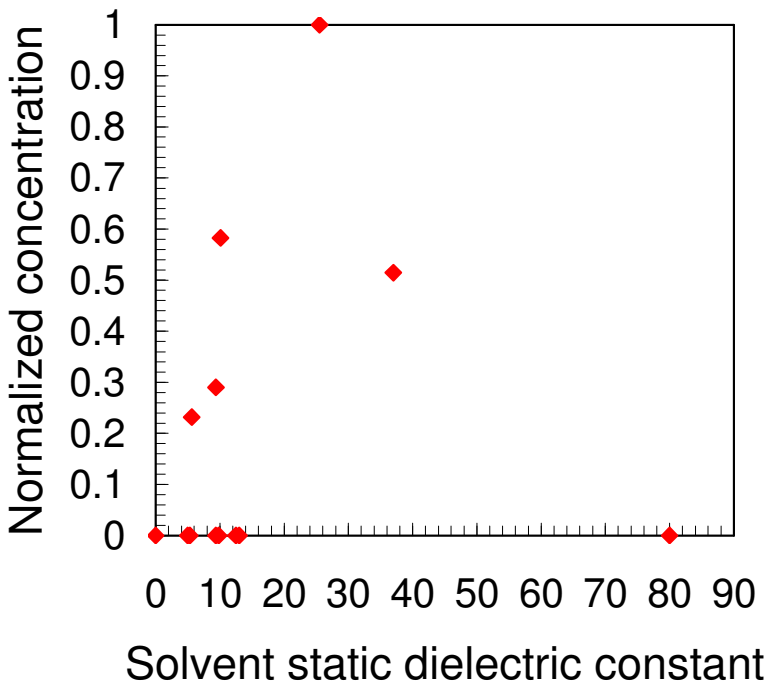

Figure 4-3. Concentration of Ge NCs after filtration vs. solvent static dielectric constant.

The post-filtration concentration data is plotted again in Fig. 4-4 as a function of solvent Hansen Solubility Parameters (HSP). HSP quantify the thermodynamic properties of molecules using three parameters to describe the energy in dispersion (δD), polar (δP), and hydrogen bonds (δH). Each molecule is assigned a location in three-dimensional Hansen space based on its HSP, and molecules which are closer together in this space are more likely to dissolve one another. We have observed that benzonitrile fully solubilizes Ge NCs; consequently, solvents with similar HSP may as well. As with dielectric constant, the predictive power of HSP appear limited. Although all solvents that "work" are within a relatively small range of HSP (the range that is plotted—water and hexanes would be far off the plot), not all solvents in this range "work".

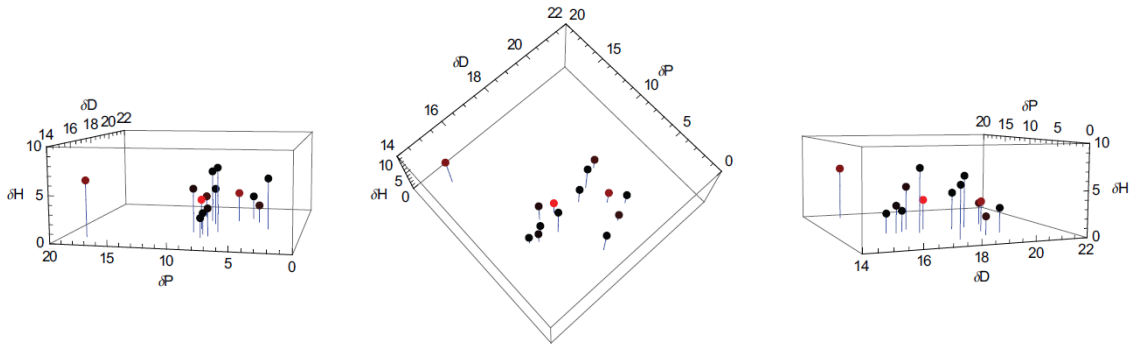

Figure 4-4. Concentration of Ge NCs after filtration vs. HSP parameters. Concentrations are indicated by the color of each data point, with red and black corresponding to final relative concentrations of 1 and 0, respectively. The plot is shown from three angles for clarity, and blue lines are drawn from each point to the bottom plane of the plot to aid the eye.

Films spun from Ge NC dispersions decrease in roughness as the size of the aggregates decreases. Nanocrystals in, e.g., chloroform produce films that are discontinuous and mountainous. Thin (< 100 nm) films from benzonitrile colloids are uniform and continuous with an RMS surface roughness of 8 nm, as determined from tapping-mode AFM. Figure 4-5 shows cross-sectional SEM images of thin and thick Ge NC films cast from benzonitrile. Films of similar quality are obtainable with DCB, and we have reported Ge NC field-effect transistors (FETs) based on such films (Chapter 5).[15] Transistors have also been made from films cast from benzonitrile; the sample in Fig. 4-5a is a fractured FET and the drain electrode is visible. These devices have the same behavior both before and after annealing as FETs from DCB, indicating that device performance is not solvent-dependent.

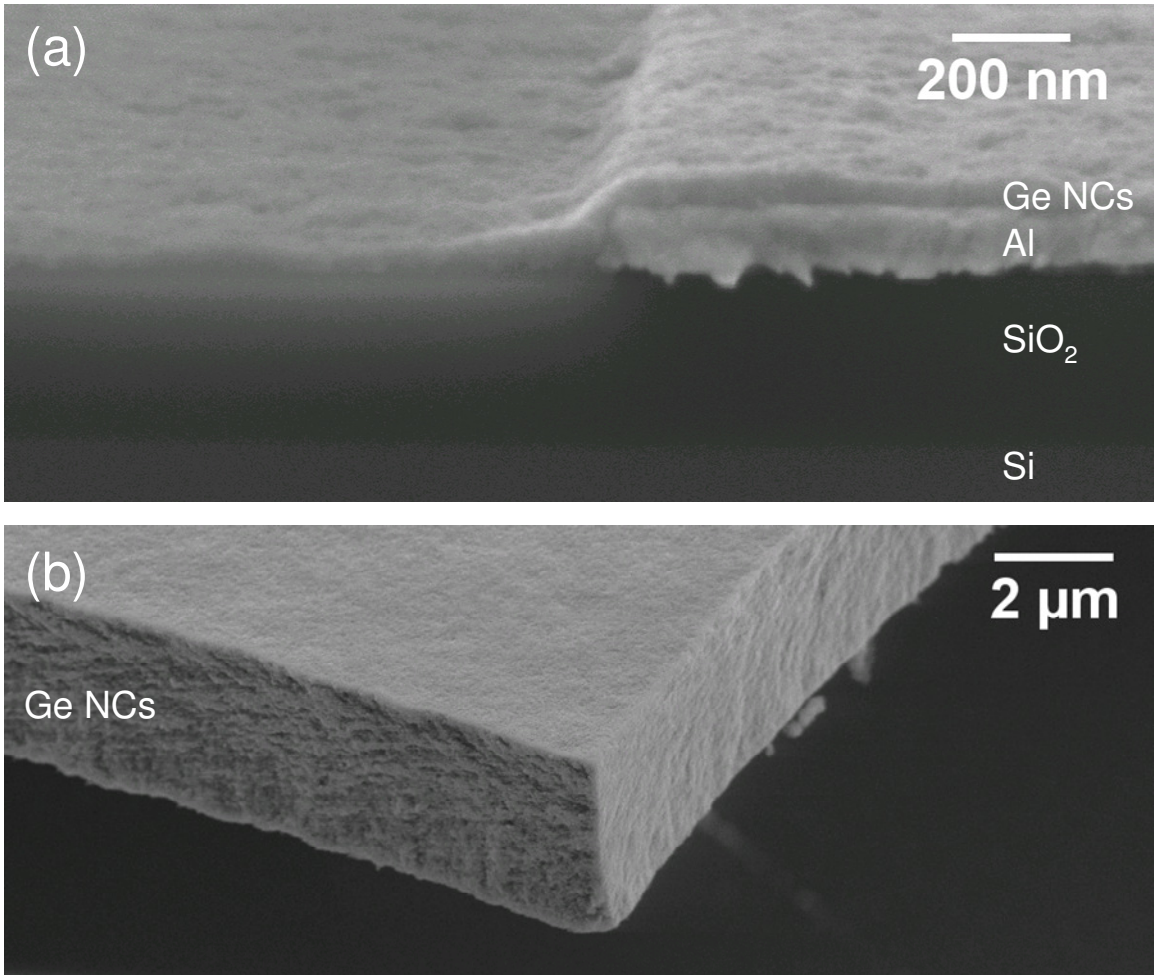

Figure 4-5. Cross-sectional SEM images of Ge NC films cast from benzonitrile. (a) The edge of an FET channel in which a 50 nm thick Ge NC film was deposited after source and drain contact evaporation. (b) A 3 µm thick Ge NC film flake that has detached from the substrate. Both images were taken at a 5° tilt from normal.

Optical properties versus nanocrystal size. The perfect solubility of bare Ge NCs in benzonitrile allows for the precise determination of Ge NC extinction coefficients. Absorption spectra were recorded for colloidal Ge NCs of several mean sizes in benzonitrile. Spectra of 1 and 0.04 mg ml^{-1} solutions were then overlaid for each NC size to yield spectra that are accurate across a large range of photon energies. Molar absorptivities calculated from these spectra using the Beer-Lambert Law are plotted in

Fig. 4-6, along with the absorption coefficient of bulk Ge on the second y-axis. The absorptivities are per mole of Ge atoms, not per mole of NCs.

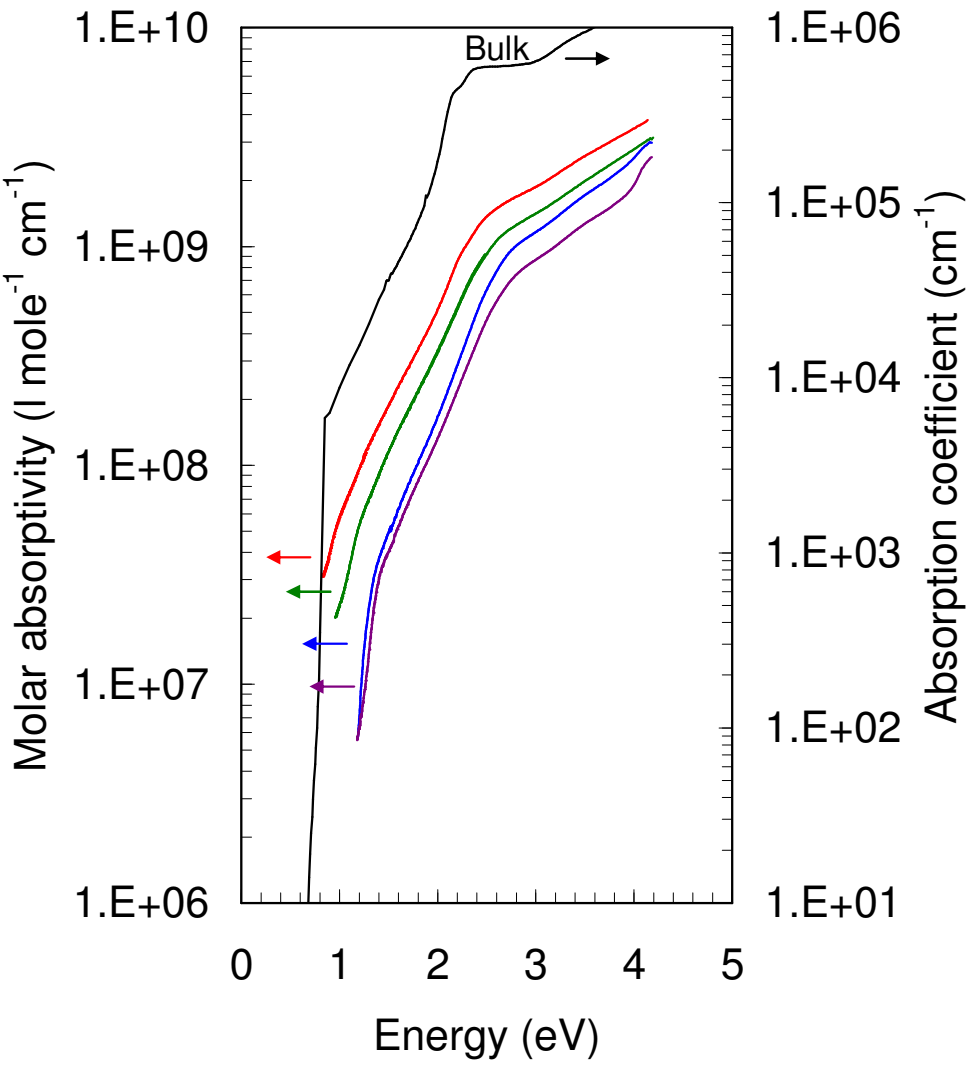

Figure 4-6. Molar absorptivity (per mole NC) of Ge NCs in benzonitrile. The red, green, blue, and purple curves correspond to 10.7, 6.0, 4.1, and 3.9 nm diameter Ge NCs, as measured using XRD. The absorption coefficient of bulk Ge from [29] is plotted on the second y-axis.

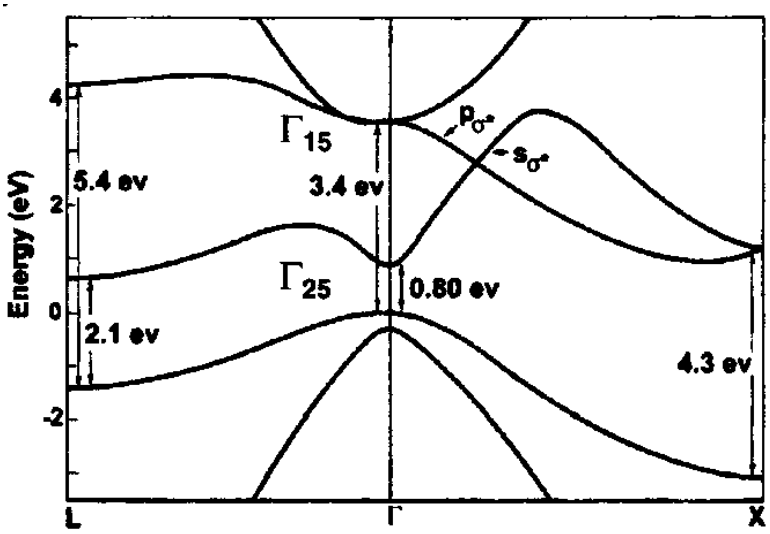

Figure 4-7. Energy band diagram of bulk Ge. Adapted from [23].

The features in the bulk Ge spectrum can be interpreted in terms of the energy band diagram shown in Fig. 4-7. From low to high energy there is the indirect Γ-L transition at E_g = 0.67 eV, the strong absorption at E_0 = 0.80 eV and subsequent shoulder from the direct transitions at Γ, and the large shoulder above E_1 = 2.1 eV from direct transitions near L.[30] These same features are present in the spectra of Ge NC colloids, although they are not as sharp due to the small degree of polydispersity in our samples. The features shift to both larger energies and lower absorptivities with decreasing NC size as the NCs become increasingly quantum confined. The change in absorption in the visible region of the spectrum can be seen with the unaided eye; Fig. 4-8 is a photograph of three colloids that have the same Ge concentration (0.04 mg ml^{-1}) but different sizes of NCs.

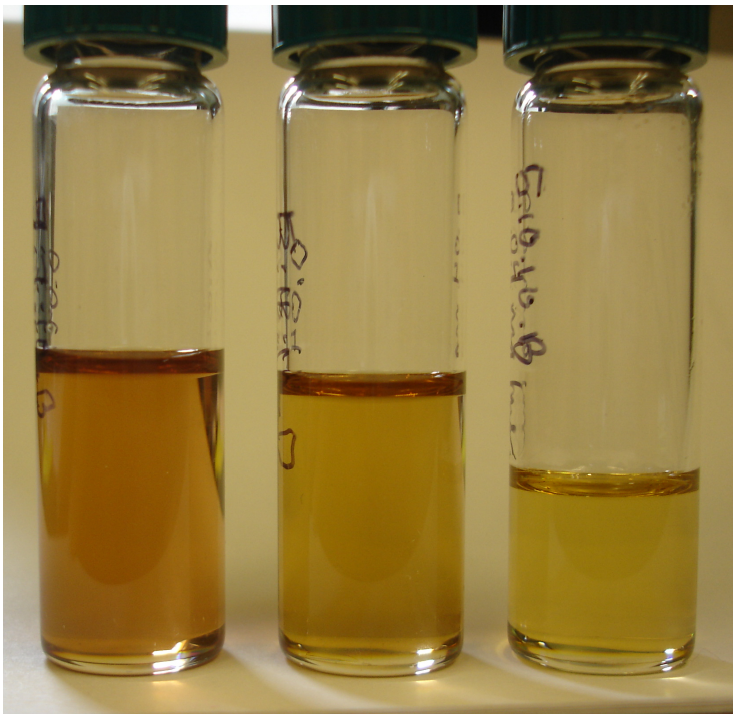

Figure 4-8. Photograph of colloidal Ge NCs in benzonitrile with mean NC sizes of (left to right) 10.7, 6.0, and 3.9 nm. The solutions have the same Ge concentration (0.04 mg ml^{-1}).

Unfortunately, we were unable to obtain sufficient scatter-free signal at long wavelengths to monitor the change in the E_g transition with NC size. However, the location of the shoulders associated with the E_0 and E_1 transitions are plotted in Fig. 4-9 as a function of NC size. A stronger dependence on NC size is observed for the E_0 transition than for the E_1 transition, although the difference between the bulk and 10.7 nm NC values is larger for the E_1 transition. This is expected because the band curvature at Γ is larger than at L, making the E_0 transition more sensitive to quantum confinement.[26] Small blue-shifts are seen in the features associated with the E_0 and E_1 transitions for 10.7 nm Ge NCs, consistent with the large Bohr exciton radius.[31] Optical transitions in colloidal Ge NCs have been studied experimentally by Heath et al. and Wilcoxon et al.

previously.[23,26] Contrary to our findings, neither group reported observable shifts in the E_1 energy for NCs larger than 4 nm.

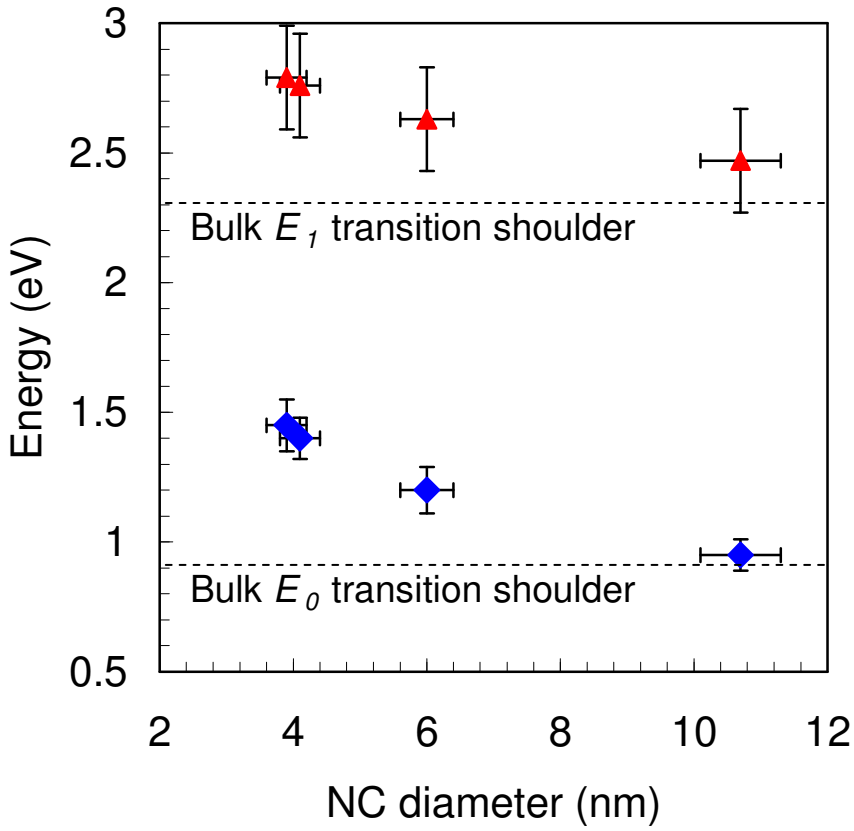

Figure 4-9. Energy of the absorption shoulders associated with the E_0 (blue diamonds) and E_1 (red triangles) transitions vs. NC mean diameter.

4.5 Conclusions

Germanium NCs synthesized as a powder in a plasma have been put into solution without further surface functionalization. The NCs are most stable in benzonitrile, DCB, and acetonitrile, with 50–100% of the initial NCs passing through a 0.2 µm filter. The detailed stabilization mechanism remains to be determined, but zeta potential

measurements indicate that the surfaces of Ge NCs in benzonitrile acquire a negative charge. High-quality films have been cast from the dispersions, demonstrating the potential of these solutions for use in future optical and electronic devices. Germanium NCs in benzonitrile are quantum confined, and we have measured that the E_0 transition energy blue-shifts by more than 0.5 eV compared to bulk Ge for 4 nm Ge NCs. Quantitative absorption coefficients have been reported in the form of molar absorptivities for the first time for Ge NCs, and show that the band structure of Ge NCs as small as 4 nm is similar to that of bulk Ge.

4.6 Future work

Although this chapter appears early in this thesis, the work described in it is the most recent. Many interesting investigations were never begun or were left incomplete. It is very important that the stabilization mechanism of Ge NCs in select solvents be further studied and understood so that the principles may be applied to other material systems (e.g., Si NCs). The zeta potential of Ge NC dispersions should be measured for all the solvents investigated here and correlated with the post-filtration concentration. The effects of salts, acids, and bases should be studied, as the stability of electrostatically stabilized colloids is a function of the ion concentration. We suspect that NC surface chemistry is critical, and experiments in which the H/Cl ratio is varied (as demonstrated in Chapter 3) should be undertaken.

High-quality films for device applications are the real goal of this work, and we have only just touched on this. What is the density of films of bare NCs cast from

solution? How do their optical and electronic properties compare to films of alkene-terminated NCs (Chapter 3)? Impacted NCs (Chapter 6)? Can size-selection techniques be used successfully in solution to narrow the size distribution of Ge NCs in cast films? If so, can NC superlattice films be obtained? Can polymer be dissolved in the same solvents that solubilize NCs, so that hybrid films with unagglomerated NCs can be cast? An additional Ph.D. thesis could be spent studying these questions!

4.7 References

[1] M.A. Hines and P. Guyot-Sionnest, *J. Phys. Chem. B* **102**, 3655 (1998).

[2] O.I. Micic, S.P. Ahrenkiel, D. Bertram, and A.J. Nozik, *Appl. Phys. Lett.* **75**, 478 (1999).

[3] O.I. Micic, J.R. Sprague, C.J. Curtis, K.M. Jones, J.L. Machol, A.J. Nozik, H. Giessen, B. Fluegel, G. Mohs, and N. Peyghambarian, *J. Phys. Chem.* **99**, 7754 (1995).

[4] J.E. Murphy, M.C. Beard, A.G. Norman, S.P. Ahrenkiel, J.C. Johnson, P.R. Yu, O.I. Micic, R.J. Ellingson, and A.J. Nozik, *J. Am. Chem. Soc.* **128**, 3241 (2006).

[5] C.B. Murray, D.J. Norris, and M.G. Bawendi, *J. Am. Chem. Soc.* **115**, 8706 (1993).

[6] C.B. Murray, S.H. Sun, W. Gaschler, H. Doyle, T.A. Betley, and C.R. Kagan, *IBM J. Res. Dev.* **45**, 47 (2001).

[7] M. Drndic, M.V. Jarosz, N.Y. Morgan, M.A. Kastner, and M.G. Bawendi, *J. Appl. Phys.* **92**, 7498 (2002).

[8] M. Law, J.M. Luther, O. Song, B.K. Hughes, C.L. Perkins, and A.J. Nozik, *J. Am. Chem. Soc.* **130**, 5974 (2008).

[9] H.E. Romero and M. Drndic, *Phys. Rev. Lett.* **95**, 156801 (2005).

[10] D.V. Talapin and C.B. Murray, *Science* **310**, 86 (2005).

[11] C.B. Murray, C.R. Kagan, and M.G. Bawendi, *Science* **270**, 1335 (1995).

[12] J.M. Luther, M. Law, Q. Song, C.L. Perkins, M.C. Beard, and A.J. Nozik, *ACS Nano* **2**, 271 (2008).

[13] J.R. Heath and J.J. Shiang, *Chem. Soc. Rev.* **27**, 65 (1998).

[14] Z.C. Holman and U.R. Kortshagen, *Langmuir* **25**, 11883 (2009).

[15] Z.C. Holman, C.-Y. Liu, and U.R. Kortshagen, *Nano Lett.* **10**, 2661 (2010).

[16] C.Y. Liu, Z.C. Holman, and U.R. Kortshagen, *Nano Lett.* **9**, 449 (2009).

[17] D.C. Lee, J.M. Pietryga, I. Robel, D.J. Werder, R.D. Schaller, and V.I. Klimov, *J. Am. Chem. Soc.* **131**, 3436 (2009).

[18] G. Kartopu, S.C. Bayliss, V.A. Karavanskii, R.J. Curry, R. Turan, and A.V. Sapelkin, *J. Lumin.* **101**, 275 (2003).

[19] Y. Maeda, *Phys. Rev. B* **51**, 1658 (1995).

[20] S. Miyazaki, K. Sakamoto, K. Shiba, and M. Hirose, *Thin Solid Films* **255**, 99 (1995).

[21] S. Takeoka, M. Fujii, S. Hayashi, and K. Yamamoto, *Phys. Rev. B* **58**, 7921 (1998).

[22] B.R. Taylor, S.M. Kauzlarich, G.R. Delgado, and H.W.H. Lee, *Chem. Mater.* **11**, 2493 (1999).

[23] J.P. Wilcoxon, P.P. Provencio, and G.A. Samara, *Phys. Rev. B* **64**, 035417 (2001).

[24] H.P. Wu, M.Y. Ge, C.W. Yao, Y.W. Wang, Y.W. Zeng, L.N. Wang, G.Q. Zhang, and J.Z. Jiang, *Nanotechnology* **17**, 5339 (2006).

[25] M. Zacharias and P.M. Fauchet, *Appl. Phys. Lett.* **71**, 380 (1997).

[26] J.R. Heath, J.J. Shiang, and A.P. Alivisatos, *J. Chem. Phys.* **101**, 1607 (1994).

[27] R. Gresback, Z. Holman, and U. Kortshagen, *Appl. Phys. Lett.* **91**, 093119 (2007).

[28] H.K. Christenson and R.G. Horn, *Chem. Phys. Lett.* **98**, 45 (1983).

[29] S. Adachi, *Optical Constants of Crystalline and Amorphous Semiconductors: Numerical Data and Graphical Information* (Springer, 1999).

[30] M.L. Cohen and J.R. Chelikowsky, *Electronic Structure and Optical Properties of Semiconductors*, 2nd ed (Springer, New York, 1989).

[31] Y. Maeda, N. Tsukamoto, Y. Yazawa, Y. Kanemitsu, and Y. Masumoto, *Appl. Phys. Lett.* **59**, 3168 (1991).

5

Germanium and silicon nanocrystal thin-film field-effect transistors[*]

5.1 Outline

Germanium and silicon have lagged behind more popular II-VI and IV-VI semiconductor materials in the emerging field of semiconductor nanocrystal thin film devices. We report germanium and silicon nanocrystal field-effect transistors fabricated by synthesizing nanocrystals in a plasma, transferring them into solution, and casting thin films. Germanium devices show *n*-type, ambipolar, or *p*-type behavior depending on annealing temperature, with electron and hole mobilities as large as 0.02 and 0.006 $cm^2 V^{-1} s^{-1}$, respectively. Silicon devices exhibit *n*-type behavior without any post-deposition treatment, but are plagued by poor film morphology.

[*] Reproduced in part with permission from Zachary C. Holman, Chin-Yi Liu, and Uwe R. Kortshagen, "Germanium and silicon nanocrystal thin-film field-effect transistors from solution," *Nano Letters* (2010). Copyright 2010 American Chemical Society.

5.2 Introduction

Thin films of semiconductor nanocrystals (NCs) or quantum dots hold promise for both cheap conventional optoelectronic devices and novel devices which capitalize on quantum confinement. Colloidal NCs are particularly attractive from a processing perspective, since large-area or patterned films can be printed or cast from solution. An ongoing challenge in the infant field of nanocrystal devices is obtaining films which are of high quality both morphologically and electronically. Films cast from colloidal solutions of NCs are often insulating as deposited because of the ligands which stabilize the NCs in solution, and post-treatments are necessary to improve charge carrier transport.[1-4]

Field-effect transistors (FETs) are convenient devices for evaluating the electronic quality of NC thin films since the mobility and sign of the charge carriers can be extracted from current-voltage characteristics. The first nanocrystal FETs were reported by Ridley et al. in 1999 using sintered CdSe NCs,[5] and Talapin and Murray reported the first unsintered NC FETs in 2005 using PbSe NCs terminated with oleic acid.[4] They found that the films were initially insulating due to the capping groups, but that *n*-type behavior was induced upon treatment with hydrazine (N_2H_4), and *p*-type behavior resulted upon desorption of the hydrazine. Group IV materials are of great importance and, while FETs have been reported using Si and Ge nanowires,[6-8] Si and Ge liquid precursors,[9,10] and large (~70 nm) Si particles,[11] progress with Si and Ge NC films lags behind model materials like PbSe. This is in large part because the comparatively high crystallization temperatures of Si and Ge make the solution synthesis of high-quality Si

and Ge NCs challenging.[12] In this letter we report the first Ge and Si NC FETs fabricated by using NCs that are synthesized in a plasma, transferred into solution, and cast as thin films.

Previously, we demonstrated the synthesis of high-quality, nearly monodisperse Si and Ge NCs using a plasma.[13,14] As in other gas-phase approaches, the NCs are synthesized as a powder with "bare" (H- or Cl-terminated, in this case) surfaces that allow, but do not require, further functionalization.[15,16] Unique to our process, the NCs do not form hard agglomerates because of unipolar charging in the plasma, and they may therefore be solubilized with relative ease.[17] We, and others, have performed hydrosilylation and hydrogermylation reactions to functionalize the NC surfaces with alkene molecules which afford solubility in a wide range of non-polar solvents.[15,16,18-20] However, as is the case for other colloidal NCs that are synthesized with ligands, the films are insulating as deposited and do not become conductive until the ligands are decomposed.[16] Here, we demonstrate a different route in which films are cast from bare NCs suspended in a solvent that is specially suited to stabilize the NCs.

5.3 Experimental

NC synthesis. Ge and Si NCs were synthesized in plasma reactors described in detail elsewhere.[13,14] Briefly, precursor gases were passed through a quartz tube around which two copper electrodes were wrapped. A 13.56 MHz RF voltage applied to the electrodes sustained a plasma in the tube, and NCs nucleated after precursor dissociation. For 6 nm Ge NC synthesis, 42 sccm Ar, 30 sccm H_2, and 2 sccm $GeCl_4$ were used. The

plasma pressure was 2.2 Torr and 150 W of RF power was applied to the ring electrode pair. A 2 mm diameter circular orifice placed downstream of the plasma accelerated the NCs towards a piece of stainless steel mesh where they were deposited as a powder. For 10-20 nm Si NCs, 35 sccm 5% SiH_4 (balance He) and 25 sccm Ar were used. The plasma pressure was 3.5 Torr and 175 W of power was applied. Silicon NCs were also collected on mesh.

FET fabrication. Approximately 50 mg of NC powder was collected for each sample and transferred air-free to a glove box with O_2 and H_2O concentrations less than 5 ppm. 1,2-dichlorobenzene (DCB)(Aldrich, degassed) was added to the powder in a vial to bring the NC concentration to 10, 25, or 50 mg ml^{-1}. The vials were then sealed and sonicated for 5 mins to suspend the NCs. We have observed previously that DCB inhibits flocculation of Si NCs so that a stable—though not optically transparent—suspension is formed.[21] This may be due to electrostatic stabilization caused by NC charging or a reduction in the van der Waals attraction between NCs due to similar Hamaker constants of the NCs and DCB, and is currently under investigation. Germanium NCs behave differently and form a stable, optically transparent solution when sonicated in DCB, indicating that the size of flocs is less than a few hundred nanometers. Germanium NC colloids were filtered through a 0.45 μm PTFE filter, which removed any large agglomerates and consequently slightly reduced the concentration. Silicon NC suspensions were not filtered; the aggregate size is sufficiently large in these suspensions that all NCs are removed by a 0.45 μm filter. Bottom-gate FETs were fabricated by spinning Ge and Si NC suspensions onto substrates in a glove box. The substrates were

heavily doped p-type Si wafers (SVM ,<100>, 0.007–0.009 Ω cm) with a 300 nm thermal oxide grown on top and a Au back contact formed by evaporating 15 nm Al followed by 75 nm Au, and rapid thermal annealing at 500 °C. The NC films were annealed after drying (details below), and then source and drain contacts were deposited on top by evaporating either Au or Al through a thin Si shadow mask. A large channel length of 200 μm was used to minimize contact effects. Figure 5-1a shows a schematic of a completed device.

Characterization. Device current-voltage characteristics were recorded at ambient temperature in vacuum (~10^{-5} Torr) using a Desert probe station with Keithley 236, 237, and 6517A electrometers. Sweep speeds of 3 V s^{-1} were used. Sample air exposure was limited to < 20 min from NC synthesis to device characterization, depending on the annealing method used (details below). Film morphology, NC size, and NC surface chemistry were investigated using a JEOL 6500 field-emission SEM, Bruker Microdiffractometer, and Nicolet FTIR spectrometer operated in the attenuated total reflection (ATR) mode, respectively. Ion beam analysis (RBS and FRES) was performed on Ge NC films on Si wafers using a 2 MeV He^{2+} beam in a NEC accelerator with a sample angle of 75°. 5-10 μC of charge were collected in each experiment and beam currents ranged from 10-20 nA.

Annealing. Sample annealing was performed on a hot plate in a glove box (N_2 atmosphere), in a custom-built rapid thermal annealing (RTA) chamber (vacuum with <100 sccm N_2 flow), and in a Modular Process Technology Corporation RTP-600S commercial RTA system operated at atmospheric pressure with 10 slm of N_2 gas flow,

including 3 mins of gas flow to purge the chamber prior to sample annealing. Annealing times were 1 hour for the hot plate and custom-built RTA, but were limited to 5 mins for the commercial RTA. Typical air exposure times prior to measurement caused by sample loading and unloading in the annealing apparatuses were 20, 2, and 0 mins for devices annealed in the commercial RTA, custom-built RTA, and glove box, respectively. For TPD measurements, a turbomolecular pump and SRS RGA 100 quadropole mass spectrometer were attached to the custom-built RTA and mass spectra were recorded every 10 °C. The chamber base pressure was 2×10^{-7} Torr and the temperature ramp rate was 10 °C/min.

5.4 Results and discussion

The spin speed used to deposit NC films was adjusted to produce films of the desired 10–50 nm thickness. For 25 mg ml^{-1} Ge NCs, the optimal speed was 2000 rpm, while 700 rpm was used for 10 mg ml^{-1} Si NCs. Cross-sectional scanning electron microscopy (SEM) reveals that films of 6 nm Ge NCs processed with these conditions are 30 nm thick and continuous, with a surface roughness of approximately 10 nm (Fig. 5-1c). These films are not as smooth as films we reported previously using Ge NCs with alkene-functionalized surfaces.[16] They are, however, surprisingly uniform for bare NCs. Films of Si NCs 4 and 7 nm in diameter are non-uniform, discontinous, and visibly rough (Fig. 5-1d). The difference in film quality between Ge and Si NCs is attributable to their respective solubilities in DCB. Using larger (10-20 nm) Si NCs we were able to fabricate

continuous films and make devices (Fig. 5-1b), but micron-sized aggregates were still visible in SEM.

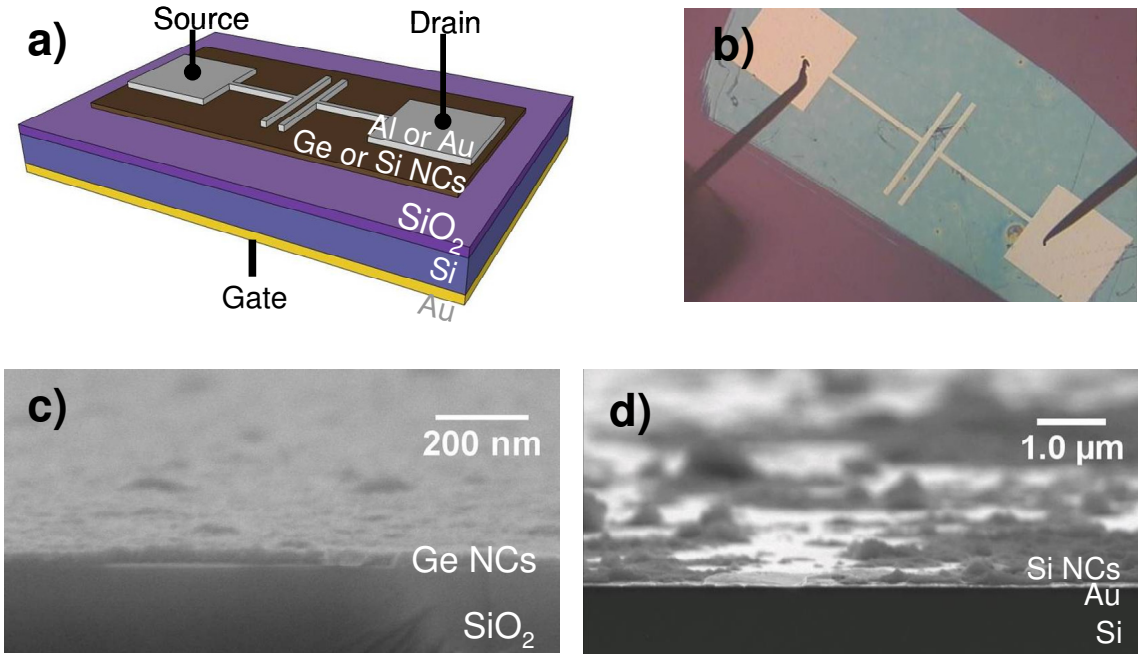

Figure 5-1. a) FET device schematic. The channel dimensions are 200 × 2000 μm and the source was grounded during operation. b) A photograph of a 10–20 nm Si NC FET in operation. Cross-sectional SEM images of c) 6 nm diameter Ge NC and d) 7 nm diameter Si NC films. c) shows an actual FET device fractured in half, while a Au-coated Si wafer was used as a substrate in d) for convenient imaging.

As-deposited Ge NC films have conductivites of 10^{-8} S cm^{-1} in the dark and an order of magnitude higher under illumination, but show no gating. Consequently, three different annealing treatments were explored after spin coating and prior to contact evaporation in order to alter the electronic behavior of the films. For temperatures below 500 °C, samples were annealed either on a hot plate in a glove box (N_2 atmosphere) or in a custom-built rapid thermal annealing (RTA) chamber operated in vacuum with a small N_2 flow (<100 sccm). For temperatures between 300 and 700 °C, samples were annealed

in a commercial RTA system operated at atmospheric pressure with 10 slm of N_2 gas flow.

After annealing at 200 °C, *n*-type behavior is observed in Ge NC films. As the annealing temperature is increased to 300 °C the devices show improved gating, and devices annealed at 400 °C are either better, worse, or the same, as those at 300 °C, depending on which annealing apparatus is used. The transfer and output characteristics of a device made under the best conditions—annealing in the commercial RTA at 400 °C—are shown in Figs. 5-2a and 5-2b. The transfer curve shows electron conduction only, with a turn-on voltage of approximately -40 V and an on-to-off ratio of over three orders of magnitude. We have observed on-to-off ratios of four orders of magnitude in some devices, comparable to the best NC FETs in the literature.[4] The electron saturation field-effect mobility determined from the slope of the square root of the transfer curve is 0.02 $cm^2\ V^{-1}\ s^{-1}$. While this is five orders of magnitude smaller than that of bulk Ge, it rivals some organic semiconductors and is respectable for a solution-cast NC film. We suspect that the strongly shifted turn-on voltage and small hysteresis in the transfer curve are indicative of unintentional doping and slow charging and discharging, respectively.

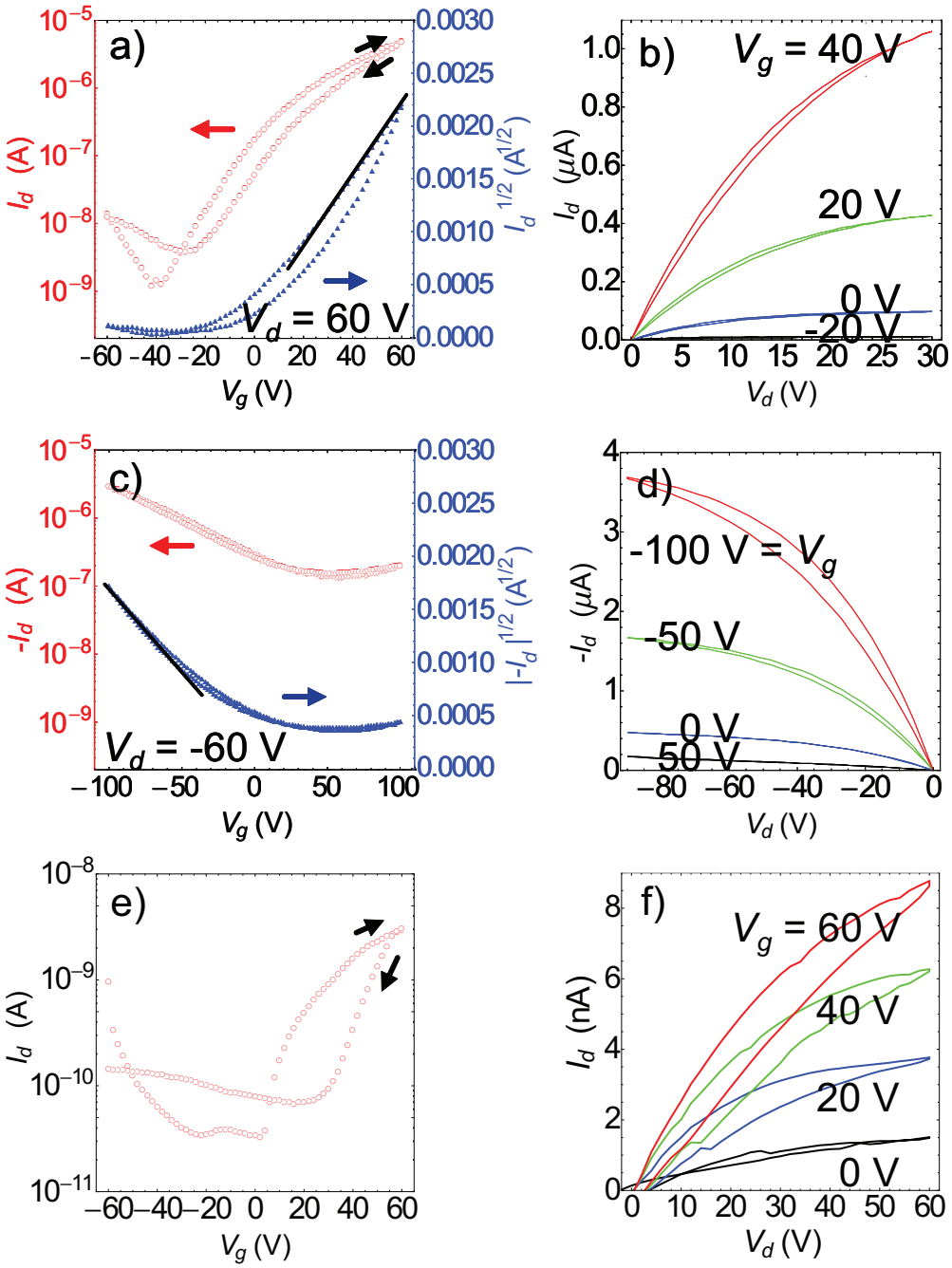

Figure 5-2. Drain current (I_d)-gate voltage (V_g) and drain current (I_d)-drain voltage (V_d) characteristics for a) and b) a 6 nm Ge NC FET annealed at 400 °C in the commercial RTA, c) and d) a 6 nm Ge NC FET annealed at 600 °C in the commercial RTA, and e) and f) two different 10–20 nm as-deposited Si NC FETs. For a) and c), the square root of I_d is plotted on the second y-axis and the fit from which the saturation mobility was determined is shown.

Distinct changes are observed for annealing temperatures of 500 °C and greater. The electron mobility decreases after annealing at 500 °C, and devices annealed in the commercial RTA at this temperature exhibit ambipolar behavior. For temperatures of 600 °C and 700 °C, which are attainable only in the commercial RTA, the FETs show strictly *p*-type behavior with hole saturation mobilities approaching 0.01 $cm^2\ V^{-1}\ s^{-1}$. Transfer and output characteristics for a typical device annealed at 600 °C are displayed in Figs. 5-2c and 5-2d. The Ge NC films clearly become more conductive when annealed above 500 °C; the off-current in Fig. 5-2c is two orders of magnitude larger than that in Fig. 5-2a and resistor-like behavior is seen in Fig. 5-2d for a gate voltage V_g = 50 V. The field-effect mobilities of annealed Ge NC devices are summarized in Fig. 5-3. Note that the same temperature-dependent trends are seen with each annealing procedure, and the results are very repeatable. More than five devices were made for each condition over the course of several months using different batches of NCs, and the extracted mobilities did not typically vary by more than 50%.

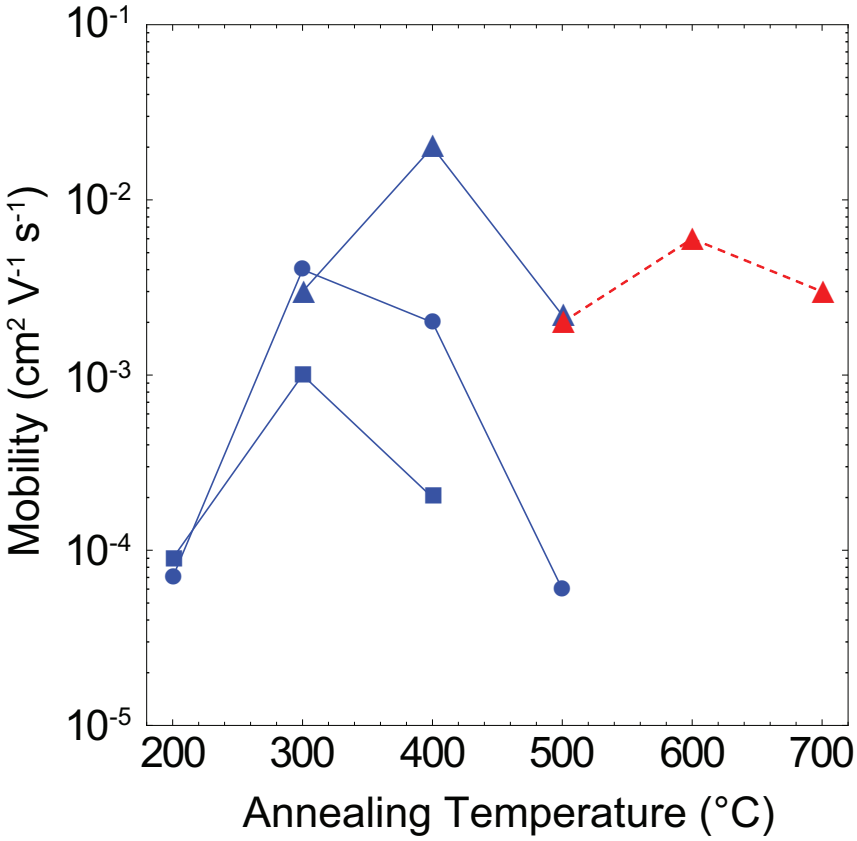

Figure 5-3. Summary of the saturation field-effect mobilities for Ge NC FETs annealed under various conditions. Data represented by squares, circles, and triangles correspond to samples annealed in the custom-built RTA, on the hot plate in the glove box, and in the commercial RTA, respectively. Electron mobilities are represented by blue data points connected by solid blue lines, while hole mobilities are represented by red data points connected by dashed red lines. Both electron and hole mobilities were measured for samples annealed at 500 °C in the commercial RTA because these devices are ambipolar.

Transistors fabricated with 10–20 nm Si NCs behaved very differently than Ge NC devices. As seen in Figs. 5-2e and 5-2f, as-deposited films exhibit *n*-type behavior. We believe this may be the first report of NC thin films deposited from solution which show gating without any post-deposition treatment, regardless of NC material. However, the performance is relatively poor. The on-to-off ratio is approximately two orders of magnitude and the transfer curve shows significant hysteresis, likely arising from trapped

charge. The electron mobility cannot be determined accurately from the square root of the transfer curve, but is on the order of 10^{-5}–10^{-6} cm^2 V^{-1} s^{-1}. Unlike Ge NC FETs, Si NC devices do not show significant changes when annealed at temperatures up to 300 °C. We note that nanocrystalline Si thin films deposited using plasma-enhanced chemical vapor deposition (CVD) with electron and hole mobilities as large as 150 and 0.2 cm^2 V^{-1} s^{-1} have recently been demonstrated.[22,23] This alternative technology sets the benchmark for electrical performance of Si NC films, although films of freestanding, spherical NCs cast from solution offer additional functionality (e.g., tunable absorption and emission) compared to CVD films with nanocrystalline grains.

Surfaces are of acute importance in devices based on NC films—we estimate that the surface area of randomly-packed 6 nm NCs in an FET channel is an order of magnitude larger than for a thin film of the same dimension—and we have studied the surfaces of Ge and Si NC films to understand the FET behavior. Researchers have shown that atoms or molecules adsorbed onto the surface of NCs can effectively dope NC films,[22] and surfaces therefore dominate the behavior of FETs based on such films.[4] While SiH_4 plasmas always produce Si NCs with H-terminated surfaces, the more complex chemistry of $GeCl_4/H_2$ plasmas can result in either Cl-, H-, or Cl- and H-terminated surfaces depending on the precursor ratios.[16] It is challenging to study surface H and Cl with a single technique, since many elemental techniques cannot detect H. We have used ion beam analysis to determine atomic concentrations of H and Cl in Ge NC films from forward recoil spectrometry (FRES) and Rutherford backscattering (RBS) signals. For the synthesis conditions used in this work, as-deposited Ge NC films spun

from DCB have H and Cl atomic fractions of 26 ± 6% and 8 ± 4%, respectively. Note that Fourier transform infrared (FTIR) spectroscopy of Si and Ge NC powder and spun films show that the NC surface chemistry remains unchanged during suspension in DCB and film casting (Fig. 5-4).

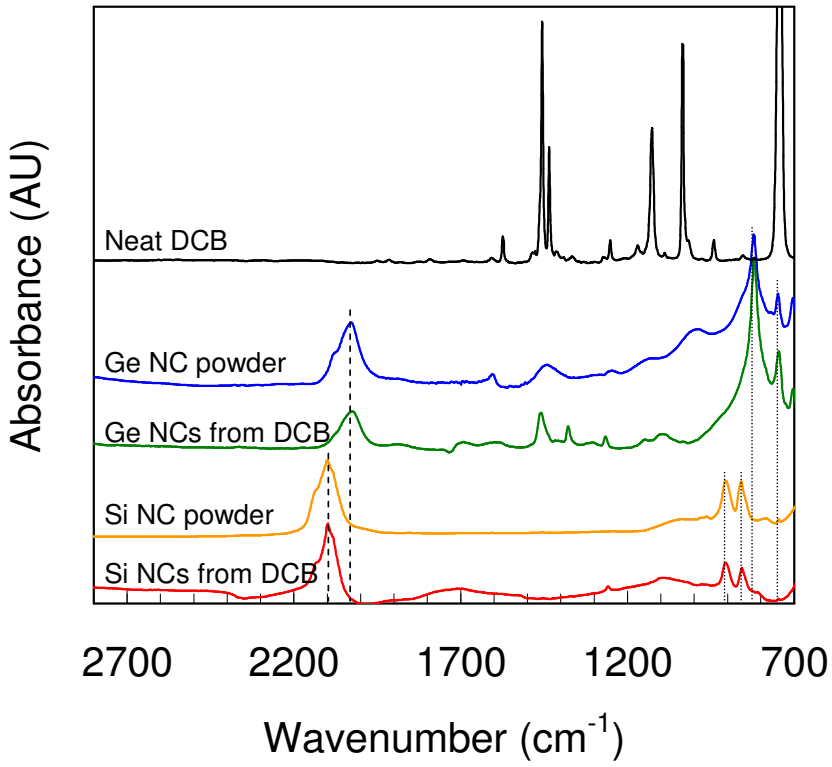

Figure 5-4. FTIR spectra of neat DCB, Ge and Si NC powder, and Ge and Si NC films cast from DCB. The vertical dashed lines indicate the locations of the Ge-H_x and Si-H_x stretching bands, while the dotted lines indicate the bending and wagging modes.

Hydrogen is known to be an effective amphoteric passivant of surface states (dangling bonds) in Si,[23] but H in Ge is surprisingly different. Recent theoretical work has found that H in Ge creates states which are *below* the valence band edge, so that H is always in the negative charge state.[24,25] Chlorine, of course, is similarly electron-withdrawing.[26] Calculations have also revealed that dangling bonds in Ge generate states

that are near (and perhaps below) the valence band edge rather than mid-gap,[25,27,28] so that these also are negatively charged and are not passivated by H. Consequently, the surfaces of H- and Cl-terminated Ge NCs are expected to have fixed negative charge, and the core of the NCs will acquire a corresponding positive charge so that each NC acts as a radially-oriented depletion region. This immobile charge will be insensitive to the application of a gate voltage, leading to the behavior we observe for as-deposited Ge NC FETs. Because of the dissimilar behavior of H in Si (and the absence of Cl), Si NCs will not suffer from the same charging. This is consistent with the behavior shown in Fig. 5-2e in which as-cast Si NC FETs turn on near V_g = 0 V. Ambipolar behavior would be expected ideally; perhaps hole-traps prevent this.

Figure 5-5 displays the evolution of H and Cl on Ge NC surfaces as a function of annealing temperature on the glove box hot plate, as determined from FRES and RBS. The removal of Cl over the same temperature range for which Ge NC films become gate-sensitive is striking, and reinforces the notion of a causal relationship between NC surface chemistry and device performance. While it appears that H is more resistant to desorption, this is misleading. FRES yields no information about bonding and cannot distinguish between H bonded to Ge, and H in water or hydrocarbons that may have adsorbed after annealing during sample loading in air. FTIR spectra of Ge NC films are shown in Fig. 5-6. The Ge-H_x stretching mode near 2000 cm^{-1} decreases drastically in intensity after annealing at 200 °C on the glove box hot plate for one hour, and has disappeared by 300 °C. A large OH stretching band near 3500 cm^{-1} develops in its place (likely during the ~5 mins of air exposure prior to measurement), and this accounts for

the “extra” H seen in FRES at higher annealing temperatures. To confirm our RBS and FTIR findings, we attached a turbomolecular pump and residual gas analyzer to the custom-built RTA to perform temperature programmed desorption (TPD) measurements. H_2 and HCl are the prominent desorbing species observed for temperatures up to 500 °C, with peak partial pressures at 277 and 306 °C, respectively (Fig. 5-7). These results are in excellent agreement with the findings of D’Evelyn et al. for dissociatively adsorbed HCl on bulk Ge(100),[29] and are consistent with the temperatures at which Ge-H_x bond breaking is seen in FTIR and Cl removal is observed in RBS.

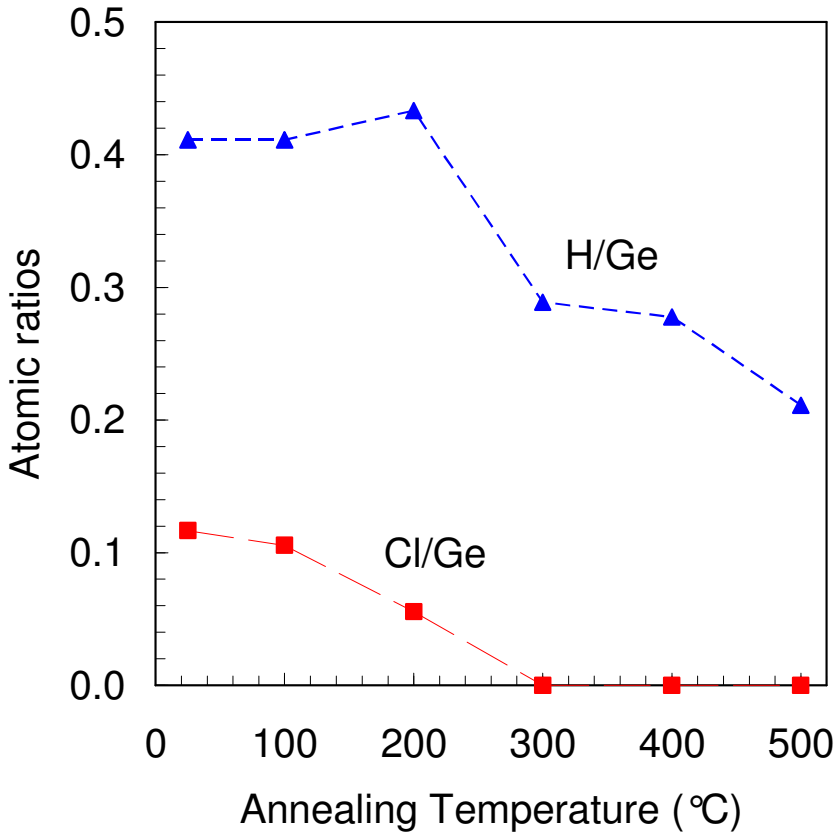

Figure 5-5. Ratios of the atomic concentrations of H (blue data) and Cl (red data) to Ge in Ge NC films as a function of annealing temperature. Atomic concentrations were determined from fitting to FRES and RBS data. All samples were annealed on the hot plate in the glove box for 1 hour.

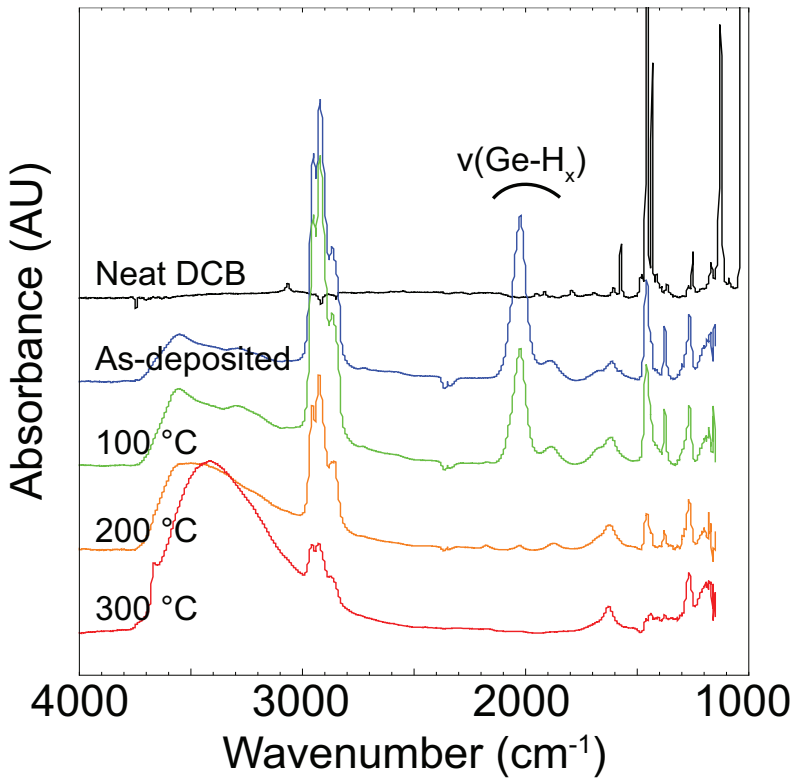

Figure 5-6. ATR-FTIR spectra of neat DCB and a Ge NC film as deposited (after drying) and annealed on the hot plate in the glove box up to 300 °C. Note that the spectra are all recorded on the same film and are not normalized, although they are offset for clarity. The dry, as-deposited film shows no signal from DCB but does exhibit a band near 2000 cm^{-1} arising from stretching of Ge-H_x formed on the NC surfaces in the plasma. This band nearly disappears after annealing at 200 °C. Signal from hydrocarbons (e.g., 2800-3000 cm^{-1}) is due to adsorbed contamination from solvents used in the glove box.

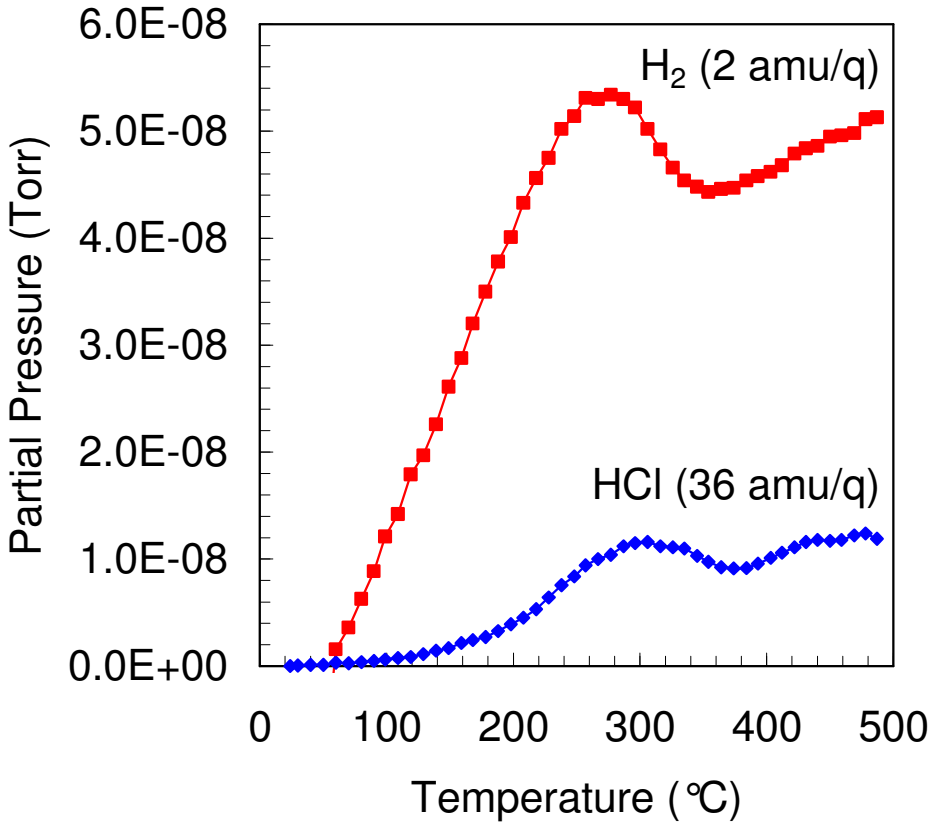

Figure 5-7. TPD curves for H_2 (2 amu/q) and HCl (36 amu/q) desorbing from a Ge NC film. The total pressure in the chamber increased by a factor of ~10 over the course of heating, and all gases besides H_2 and HCl (e.g., H_2O, N_2, Ar, etc) showed a corresponding monotonic increase in partial pressure. The H_2 and HCl TPD curves have an upward slanting background as a result of the total pressure increase, but the peaks at 277 and 306 °C resulting from desorption from the Ge NC film are clearly distinguishable.

Removal of H and Cl surface species may relieve the charge separation previously discussed, but we are not certain what is left behind on the Ge NC surfaces after annealing, and why *n*-type behavior with a strongly shifted turn-on voltage is observed. Most likely, O or OH species adsorb onto the Ge NC surfaces in place of desorbed H and Cl during sample transfer in air after annealing but before measurement, and act as donors. This hypothesis is supported by the fast formation of an OH stretching band in FTIR spectra of samples that are annealed and exposed to air for ~5 mins during

measurement. We also observe surprising performance stability in these devices for air exposures up to 100 hours (Fig. 5-8), consistent with O- or OH-related doping. In 1953, Clarke reported that the conductance of high-resistivity bulk Ge permanently increased by a factor of 10 after heating a crystal in vacuum at 450 °C, cooling it back to room temperature or 197 K, and subsequently exposing it to O_2 gas.[30] This procedure is remarkably similar to two of the annealing procedures used here. Clarke later confirmed that the conductance was *n*-type,[31] and subsequent studies determined that a shallow thermal donor is formed in Ge intentionally doped with O (see Ref. [32] for a review). Typical O doping concentrations are 10^{16}-10^{18} cm^{-3} in bulk samples in which O thermal donors are observed, and O concentrations greater than 10^{18} cm^{-3} are anticipated for our samples if each Ge NC has a single O atom on its surface. Another possible dopant is OH, which is observed to act as a shallow donor in bulk Ge when a complex is formed between a substitutional O atom and an interstitial H atom.[33] OH was also repeatedly observed to act as a donor at the *surface* of bulk Ge in the 1950's. Placing thin Ge samples in wet environments created an *n*-type surface and shifted the surface potential positive by as much as 0.5 V (see Ref. [34] for a review). Note that the formation of O- or OH-related donor states may explain why the highest electron mobilities are obtained using the dirtiest annealing technique—typical air exposure times prior to measurement are 20, 2, and 0 mins for devices annealed in the commercial RTA, custom-built RTA, and glove box, respectively.

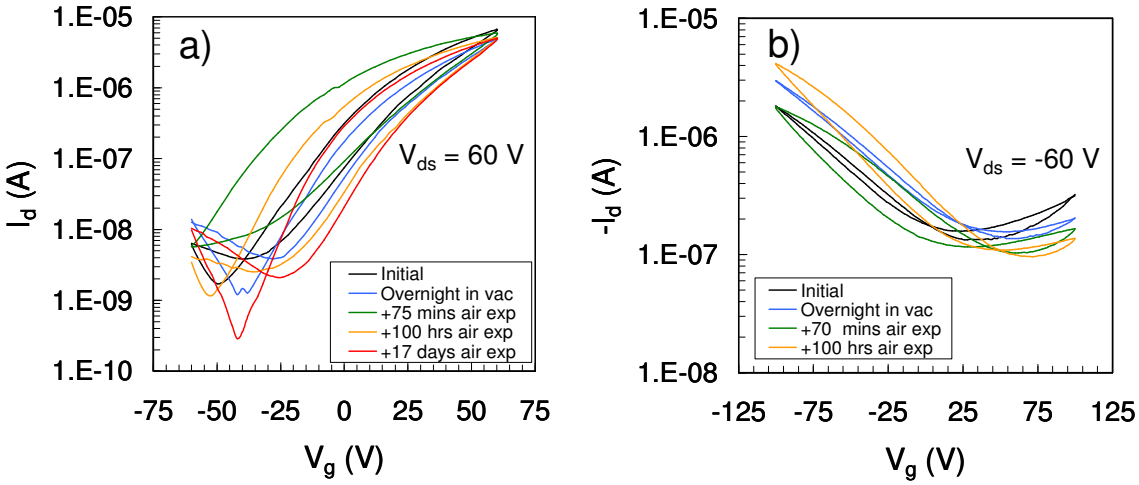

Figure 5-8. Drain current (I_d)-gate voltage (V_g) characteristics for Ge NC FETs annealed at a) 400 and b) 600 °C in the commercial RTA. Characteristics are shown for the devices in their as-made state, after sitting in vacuum (~10^{-5} Torr) overnight, and after exposure to air for various lengths of time. These characteristics are for the same devices shown in Fig. 5-2. Notably, hysteresis is reduced in both devices after sitting in vacuum overnight, but no improvement in mobility or on-to-off ratio is observed. The devices are surprisingly stable in air, and the device annealed at 600 °C actually performs better after 100 hours of air exposure than it did initially.

Improved FET performance and corresponding electron mobility cannot be attributed to NC coalescence for the lower temperatures investigated. We have studied sintering of Ge NC films and observed that the grain sizes determined from Scherrer fits of X-ray diffraction (XRD) spectra do not increase below annealing temperatures of 400 °C when annealed in the glove box for 1 hour or of 500 °C when annealed in the commercial RTA for 5 mins (Fig. 5-9). However, for temperatures of 500 °C and above, the sintering of Ge NCs leads to the observed increase in conductivity (FET off-current) and it is difficult to know if surface chemistry still dominates device characteristics. The transition from *n*-type to ambipolar to *p*-type behavior at these temperatures is not yet understood. The variability in electron mobility with annealing treatment at temperatures of 400 and 500 °C is correlated with the onset of NC sintering. Surprisingly, a decrease in

electron mobility occurs at the same temperatures at which grain growth is first observed in XRD, and the onset temperature is near 400 °C for samples annealed for 1 hour but is delayed to 500 °C for samples annealed in the commercial RTA for 5 mins.

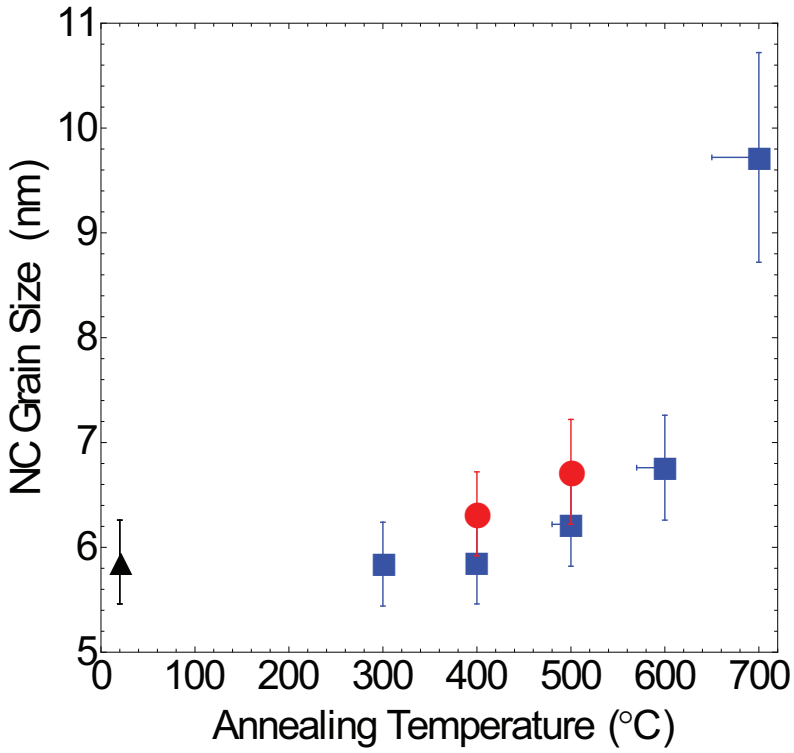

Figure 5-9. Nanocrystal grain sizes extracted from Scherrer fits to XRD spectra of films of bare Ge NCs cast from DCB and annealed at 300–700 °C. The black triangle, blue squares, and red circles correspond to samples that were unannealed, annealed in the commercial RTA system for 5 mins, and annealed on the hot plate in the glove box for 1 hour, respectively.

For bulk Si(100) surfaces, desorption of H_2 occurs at higher temperatures (~400 °C) than for Ge(100) surfaces.[35,36] Holm and Roberts recently studied the surface chemistry of H-terminated Si NCs using in-situ FTIR during annealing in a tube furnace.[37] They observed no changes in the Si-H bonding below 450 °C, and found that the Si-H stretch intensity does not significantly decrease until 650 °C. Silicon NC FETs were annealed only up to 300 °C in our experiments, and the insensitivity of device

behavior to annealing is thus reasonable given the relative chemical stability of H-terminated Si NC surfaces at these temperatures. We believe Si NC FET performance is at this point severely limited by film morphology, and discovery of a solvent that is as good for H-terminated Si NCs as DCB is for H- and Cl-terminated Ge NCs may dramatically improve the devices.

5.5 Conclusions

In summary, we have fabricated Ge and Si NC FETs using plasma-synthesized NCs suspended in DCB and cast as thin films. Germanium NC FETs exhibit promising performance with electron and hole mobilities on the order of 10^{-2} cm^2 V^{-1} s^{-1} and on-to-off ratios better than 10^3. Annealing-induced removal of H and Cl surface species is required to activate the devices, and the annealing temperature determines whether n-type, ambipolar, or p-type behavior is observed. Silicon NC FET performance is hindered by non-uniform film morphology, but the devices show gating without any post-deposition treatment. Further studies to find solvents which optimally solubilize bare NCs and to understand the effects of NC surface chemistry on the electronic properties of films are necessary. If solution-processed Si and Ge NC films with mobilities on the order of 1 cm^2 V^{-1} s^{-1} can be fabricated without high-temperature annealing, they may compete with materials such as organic semiconductors and amorphous Si in flexible thin-film devices.

5.6 Future work

There are several exciting routes to follow in future research on Ge and Si NC FETs. First, the role of NC surface chemistry in device behavior needs to be studied in greater detail. Is the removal of *both* H and Cl from Ge NC surfaces necessary before *n*-type behavior is observed? Must they be removed so that the proposed dopants (O or OH) can attach, or do O and OH attach upon air exposure without annealing, but the H or Cl species act as traps that prevent transport of the donated electrons? Why do the devices become ambipolar or *p*-type after annealing at higher temperatures? Is the mechanism also related to air exposure? Are surface species diffusing into the Ge NCs at these temperatures? Surface studies will help answer some of these questions. X-ray photoelectron spectroscopy (XPS) should be particularly helpful since it yields both elemental composition and bonding information. Unfortunately, H cannot be studied with XPS. The Kortshagen group obtained an FTIR instrument to put in a glove box, which will be helpful since we have never studied Ge NC surfaces without any air exposure. A vacuum chamber in which FET performance can be measured in situ while controllably dosing with gases would also be instructive. For example, Rivillon et al. reported that Si surfaces can be chlorinated via exposure to chlorine gas (Cl_2) in vacuum.[38] Would annealed Ge NC FETs continue to work after Cl_2 exposure? As-deposited Si NC FETs? How would their behavior change?

Once the cause of Ge NC doping is better understood, it may be possible to achieve *n*-type, ambipolar, or *p*-type films without annealing. A dosing chamber would also be useful for these studies. Do Ge NC films become *n*-type upon exposure to water

vapor without first annealing? Can films be made ambipolar or p-type with other gas exposures? In a review of studies on bulk Ge surfaces performed in the 1950's, Kingston reported that the Ge surface potential could be shifted by as much as 0.5 V in either direction by exposing Ge to a variety of environments (Table 8-I).[34] It would be nice to repeat these experiments using Ge NC FETs. Nanocrystal films have orders of magnitude more surface area than bulk samples, so we would expect Ge NC films to be particularly sensitive to surface doping. If changes are observed, are the reversible? New devices (e.g., sensors) may be possible with semiconductor films for which the carrier type and conductivity can be modulated chemically instead of electronically.

Table 5-I. Germanium surface Fermi level vs ambient. Adapted from [34].

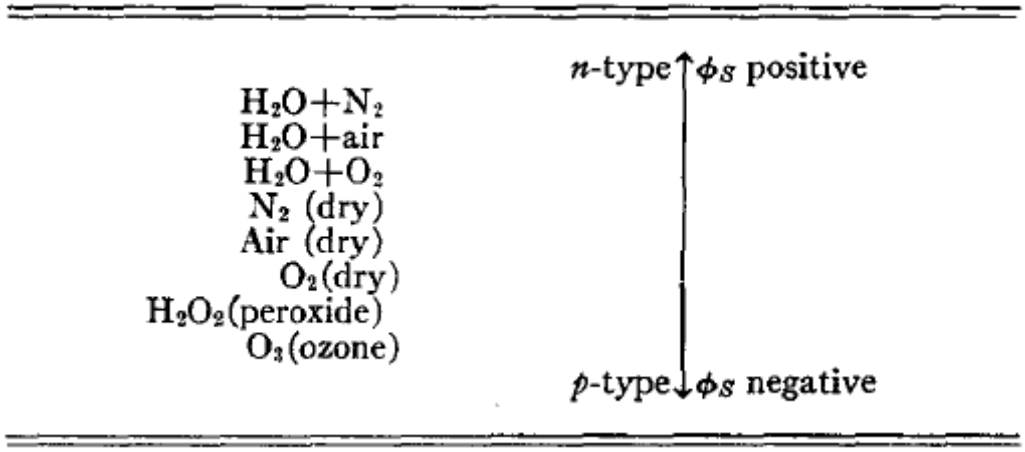

Finally, Si is in many ways a superior electronic material than Ge, and Si NC FETs that perform as well or better as the Ge NC FETs reported in this chapter would generate a lot of interest. We feel that the morphology of Si NC films limits FET performance at this point, and the research proposed in Chapter 4 to solubilize bare Si NCs is critically important. Also, the role of Si NC surface chemistry in FET

performance has not yet been studied. We do not know why H-termination results in *n*-type behavior, and what effects other terminations may have.

5.7 References

[1] M. Drndic, M.V. Jarosz, N.Y. Morgan, M.A. Kastner, and M.G. Bawendi, *J. Appl. Phys.* **92**, 7498 (2002).

[2] H.E. Romero and M. Drndic, *Phys. Rev. Lett.* **95**, 156801 (2005).

[3] M. Law, J.M. Luther, O. Song, B.K. Hughes, C.L. Perkins, and A.J. Nozik, *J. Am. Chem. Soc.* **130**, 5974 (2008).

[4] D.V. Talapin and C.B. Murray, *Science* **310**, 86 (2005).

[5] B.A. Ridley, B. Nivi, and J.M. Jacobson, *Science* **286**, 746 (1999).

[6] X.F. Duan, C.M. Niu, V. Sahi, J. Chen, J.W. Parce, S. Empedocles, and J.L. Goldman, *Nature* **425**, 274 (2003).

[7] A.B. Greytak, L.J. Lauhon, M.S. Gudiksen, and C.M. Lieber, *Appl. Phys. Lett.* **84**, 4176 (2004).

[8] D.W. Wang, Q. Wang, A. Javey, R. Tu, H.J. Dai, H. Kim, P.C. Mcintyre, T. Krishnamohan, and K.C. Saraswat, *Appl. Phys. Lett.* **83**, 2432 (2003).

[9] T. Shimoda, Y. Matsuki, M. Furusawa, T. Aoki, I. Yudasaka, H. Tanaka, H. Iwasawa, D.H. Wang, M. Miyasaka, and Y. Takeuchi, *Nature* **440**, 783 (2006).

[10] A. Watanabe, F. Hojo, and T. Miwa, *Appl. Organomet. Chem.* **19**, 530 (2005).

[11] M. Harting, J. Zhang, D.R. Gamota, and D.T. Britton, *Appl. Phys. Lett.* **94**, 193509 (2009).

[12] J.R. Heath and J.J. Shiang, *Chem. Soc. Rev.* **27**, 65 (1998).

[13] L. Mangolini, E. Thimsen, and U. Kortshagen, *Nano Lett.* **5**, 655 (2005).

[14] R. Gresback, Z. Holman, and U. Kortshagen, *Appl. Phys. Lett.* **91**, 093119 (2007).

[15] D. Jurbergs, E. Rogojina, L. Mangolini, and U. Kortshagen, *Appl. Phys. Lett.* **88**, 233116 (2006).

[16] Z.C. Holman and U.R. Kortshagen, *Langmuir* **25**, 11883 (2009).

[17] U. Kortshagen and U. Bhandarkar, *Phys. Rev. E* **60**, 887 (1999).

[18] L.H. Lie, M. Duerdin, E.M. Tuite, A. Houlton, and B.R. Horrocks, *J. Electroanal. Chem.* **538**, 183 (2002).

[19] F.J. Hua, M.T. Swihart, and E. Ruckenstein, *Langmuir* **21**, 6054 (2005).

[20] E. Fok, M.L. Shih, A. Meldrum, and J.G.C. Veinot, *Chem. Commun.* **4**, 386 (2004).

[21] C.Y. Liu, Z.C. Holman, and U.R. Kortshagen, *Nano Lett.* **9**, 449 (2009).

[22] D. Yu, C.J. Wang, and P. Guyot-Sionnest, *Science* **300**, 1277 (2003).

[23] N.M. Johnson, C. Doland, F. Ponce, J. Walker, and G. Anderson, *Physica B* **170**, 3 (1991).

[24] C.G. Van De Walle and J. Neugebauer, *Nature* **423**, 626 (2003).

[25] J.R. Weber, A. Janotti, P. Rinke, and C.G. Van De Walle, *Appl. Phys. Lett.* **91**, 142101 (2007).

[26] D. Troost, L. Koenders, L.Y. Fan, and W. Monch, *J. Vac. Sci. Technol., B* **5**, 1119 (1987).

[27] P. Broqvist, A. Alkauskas, and A. Pasquarello, *Phys. Rev. B* **78**, 075203 (2008).

[28] P. Tsipas and A. Dimoulas, *Appl. Phys. Lett.* **94**, 012114 (2009).

[29] M.P. Develyn, Y.M.L. Yang, and S.M. Cohen, *J. Chem. Phys.* **101**, 2463 (1994).

[30] E.N. Clarke, *Phys. Rev.* **91**, 756 (1953).

[31] E.N. Clarke, *Phys. Rev.* **95**, 284 (1954).

[32] P. Clauws, *Mater. Sci. Eng., B* **36**, 213 (1996).

[33] E.G. Haller, W.L. Hansen, and F.S. Goulding, *Adv. Phys.* **30**, 93 (1981).

[34] R.H. Kingston, *J. Appl. Phys.* **27**, 101 (1956).

[35] M.C. Flowers, N.B.H. Jonathan, Y. Liu, and A. Morris, *J. Chem. Phys.* **99**, 7038 (1993).

[36] K. Sinniah, M.G. Sherman, L.B. Lewis, W.H. Weinberg, J.T. Yates, and K.C. Janda, *J. Chem. Phys.* **92**, 5700 (1990).

[37] J. Holm and J.T. Roberts, *J. Phys. Chem. C* **113**, 15955 (2009).

[38] S. Rivillon, F. Amy, Y.J. Chabal, and M.M. Frank, *Appl. Phys. Lett.* **85**, 2583 (2004).

6

Impaction of germanium nanocrystals

6.1 Outline

Nanomaterials are exciting candidates for use in new optical and electronic devices ranging from solar cells to gas sensors. However, to reach their full potential, nanomaterials must be deposited as dense thin films on flexible substrates using inexpensive processing technologies such as roll-to-roll printing. We report a new, flexible technique for depositing aerosolized nanocrystals that lends itself to roll-to-roll processes. Germanium nanocrystals produced in a plasma are accelerated through a slit orifice by a supersonic gas jet and are impacted onto a translated substrate. A uniform nanocrystal film is quickly deposited over large areas, and features as small as 2 μm can then be patterned using conventional lift-off photolithography. The density of the deposited films depend on the pressures upstream and downstream of the orifice, their ratios, and the distance between the orifice and the substrate. Nanocrystal film densities

exceeding 50% the density of bulk germanium are routinely achieved with several sizes of nanocrystals, approaching the theoretical limit for randomly packed spheres. A simple model is presented which shows that the calculated nanocrystal velocity upon impaction is strongly correlated with the resulting film density.

6.2 Introduction

As nanomaterials research matures, the emphasis is shifting from synthesis to application. Nanomaterials show particular promise for inclusion in semiconductor devices, creating a growing need for high-quality thin films of semiconductor nanocrystals (NCs) or quantum dots. Any technique suitable for depositing NCs as a film must ensure—as a prerequisite—that the unique NC properties are not compromised during deposition. The ideal deposition method would go further, and make dense, uniform films with NCs of any size, shape, and composition on any substrate. The method would also be suitable for large-area deposition as well as microscopic patterning, so that NC films could be deposited for solar cells and transistors alike.

Solution-based deposition methods are popular, in large part because many NC synthesis techniques are solution based.[1-6] Spin-coating, drop-casting, and dip-coating are all common techniques for depositing colloidal NCs such as CdSe and PbSe.[7-9] Large areas can be covered with roll-to-roll printing, and recent work has demonstrated that small features can be patterned with conventional photolithography[7] or new lithographic techniques in which functionalized NCs themselves take on the role of the resist.[8-10] However, NC-solvent and solvent-substrate interactions can make working

with solutions limiting. Proper solvent choice is critical to control drying kinetics and create thin films which are macroscopically and microscopically uniform. In addition, NCs usually require ligands on their surfaces to dissolve in solution; these ligands limit the packing density of NCs in the film and are often detrimental to film performance.[11-14] Finally, there are many NC materials which are not amenable to solution synthesis or are commonly synthesized with gas-phase techniques. While it may be possible to put these NCs into solution and cast films,[14,15] it is not ideal.

Most common of the gas-phase deposition methods are those that charge NCs and accelerate them with an electric field. This family of techniques can accommodate NCs in almost any form: both NC colloids and NC powders can be aerosolized, charged, and deposited via electrostatic precipitation. Recent work has demonstrated the assembly of NCs into sub-micron features using nanoxerography with contact[16-18] and non-contact[20-22] charging, and large scale deposition is possible with conventional xerography. Nevertheless, electrostatic precipitation is constrained by the requirement that the NCs and substrate must be charged. The techniques demonstrated to-date require either a conducting[20,21] or insulating[16,17] substrate; no single technique works with both. The NC beam flux is limited by the rates of substrate charging and NC ionization, and deposition may be slowed or distorted by the buildup of space charge. In addition, most methods use a single substrate charging event so that deposition ceases once enough NCs have arrived to neutralize the substrate (usually a monolayer or less). Recent work has begun to address this with continuous substrate charging.[19] Finally, NCs cannot be accelerated to large speeds under the usual deposition conditions of a nearly stagnant gas

at atmospheric pressure. According to a simple electric field–gas drag force balance calculation, a singly-charged 5 nm NC will reach a terminal velocity of roughly 1 m s^{-1} in a 10^5 V cm^{-1} electric field. Low velocities result in fluffy films, and this can be seen in much of the published work.[16,18-20] Improvements should be possible at lower pressure.

Another approach that has not been thoroughly explored is the deposition of NC films using impaction. Supersonic or hypersonic gas jets have been shown to accelerate NCs to velocities of 1 km s^{-1},[21,22] and NCs as small as 2 nm have been deposited.[23,24] Supersonic impaction research to date has concentrated primarily on focusing and size classification of aerosols. However, the technique is well suited to depositing NC films since the substrate material is inconsequential, favorable conditions exist for NCs of nearly any shape, size, and composition, the NC impaction speed is controllable and large enough to give dense films, and the NCs do not need to be charged or have special surface chemistry. A few researchers have recognized the potential of impaction for NC films,[22,25,26] but previous work has been limited to deposition of NCs through circular orifices or nozzles. The circular geometry yields towers on stationary substrates and lines on substrates translated in one dimension. The feature sizes are on the order of tens to hundreds of microns,[22,27] which are unfortunately neither small enough to be of interest for microelectronics nor large enough to be of interest for coatings. Substrates can of course be rastered in two dimensions, but this is slow and produces non-uniform films.

Here, we introduce a new NC thin film deposition scheme which uses a slit-shaped orifice to produce a one-dimensional beam or curtain of NCs traveling at high speeds. One-dimensional translation of a substrate perpendicular to the curtain produces a

highly uniform film over large areas, such as is required for solar cells. Plasma-synthesized Ge NCs are used as a model system to explore the key parameters in NC impaction, although we emphasize that the technique is not limited to the material Ge or our plasma synthesis approach. We demonstrate that, in combination with standard lift-off photolithographic techniques, features as small as 2 um can be patterned, with the possibility of <500 nm features with improved lithography. A simple model is used to explain and inform the experimental results.

6.3 Background

Pioneering experimental work in NC supersonic impactors using circular orifices was conducted by Fernandez de la Mora et al.,[26,27,31] and there are a few reports of complimentary simulation.[32-34] In an impactor (Fig. 6-1), a pressure drop is established across an orifice or nozzle through which gas flows. Provided the pressure drop is larger than a critical pressure drop (~2, depending on the gas), the gas reaches sonic velocity at the throat of the orifice and a supersonic jet emanates into the downstream chamber. The gas density decreases as the jet expands, but—in the absence of a substrate—collapses to the background pressure in a strong shock known as the Mach disk. The Mach disk location for a "free jet" is a simple function of the pressure ratio across the orifice. The gas velocity increases until the shock, and can accelerate NCs in the process. The larger the pressure ratio, the longer the jet, the higher the terminal gas velocity, and the higher the NC velocity. However, the pressure *ratio* is not the only important variable; the absolute pressures upstream (P_{up}) and downstream (P_{down}) of the orifice also matter. A

pressure ratio of 100 with P_{up} = 1 atm will accelerate NCs to higher velocities than the same ratio with P_{up} = 1 Torr because the larger gas density results in greater transfer of the gas velocity to the NCs via collisions. In short, the pressure ratio determines the gas velocity profile, but the absolute pressures determine how strongly the gas and NC velocities are coupled.

To deposit NCs, a substrate must be inserted into the gas flow. If the substrate is placed upstream of the free jet Mach disk location x_M, the jet will be perturbed and the shock will move to remain upstream of the substrate. If the substrate is placed downstream of x_M, the jet retains its substrate-free structure. In either case, the NCs find themselves moving much faster than the gas flow once the shock has occurred, and they slow by gas drag. Depending on the gas density, drag will cause NCs smaller than a particular cut size to follow the streamlines around the substrate. Larger NCs will cross the streamlines and impact. The literature often portrays the pressure ratio across the orifice as the critical variable in determining the impaction cut size, but this is misleading. It is actually the gas density downstream of the Mach disk which determines whether small NCs will impact, as demonstrated by Jurcik et al.[28] Consequently, a pressure ratio of only 3 can cause 4 nm Ge NCs to impact, provided P_{up} = 2 Torr. In this case, the gas density downstream of the Mach disk is not large enough to deflect 4 nm NCs before impaction, unless the substrate is far from the shock. The situation is much different for a pressure ratio of 3 with P_{up} = 1 atm.

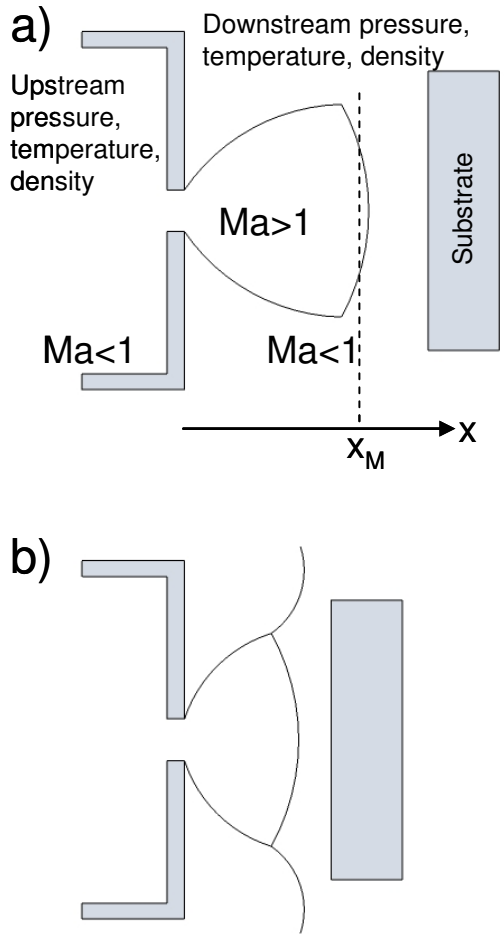

Figure 6-1. Cartoon of a supersonic impactor in which the substrate is placed a) downstream and b) upstream of the free jet Mach disk location x_M.

There are limited studies on supersonic jets with or without NCs emanating from slit-shaped orifices,[35-37] and to the best of our knowledge, there are no reports of NCs deposited as thin films. We are also unaware of any studies evaluating the density of films of NCs deposited via supersonic impaction through orifices of any shape as a function of operating conditions and NC size.

6.4 Experimental

Nanocrystal film deposition. We previously reported the synthesis of Si and Ge NCs using a nonthermal plasma approach.[38,39] For Ge NCs, $GeCl_4$ and H_2 are used as precursors and are dissociated with Ar background gas in a radiofrequency flow-through plasma reactor. Nanocrystals nucleate in the plasma and grow by condensation of reactive Ge species, so that the size of the NCs can be controllably tuned from 4-50 nm by adjusting the residence time of the NCs in the plasma zone.

In earlier work, NCs were collected by diffusion to a mesh filter placed downstream of the plasma. In this work, the plasma synthesis technique was coupled with the deposition technique described here by placing a slit-shaped orifice directly downstream of the plasma (Fig. 6-2a). The gas and Ge NCs were accelerated through the orifice, and the orifice dimensions determined the plasma or upstream pressure P_{up} for a given gas flow rate. P_{up} was maintained between 1-10 Torr in these experiments since these are the conditions for NC synthesis with which we are most familiar. The pressure far downstream of the office, P_{down}, was determined by the gas flow rate and the pumping speed of the system. In most experiments, a roughing pump was used with an angle control valve to control the pumping speed and achieve pressure ratios across the orifice P_{up}/P_{down} of 2-10. A 230 l s^{-1} turbo pump was added when larger pressure ratios were needed, so that the full range of P_{down} explored was 0.05-2 Torr. The temperature both upstream of the orifice and downstream of the Mach disk is roughly room temperature. Note that the conditions just described are very different from conditions commonly used

for hypersonic impactors, in which P_{up} = 1 atm, P_{up}/P_{down} >100, and there may be significant temperature gradients.[21,29]

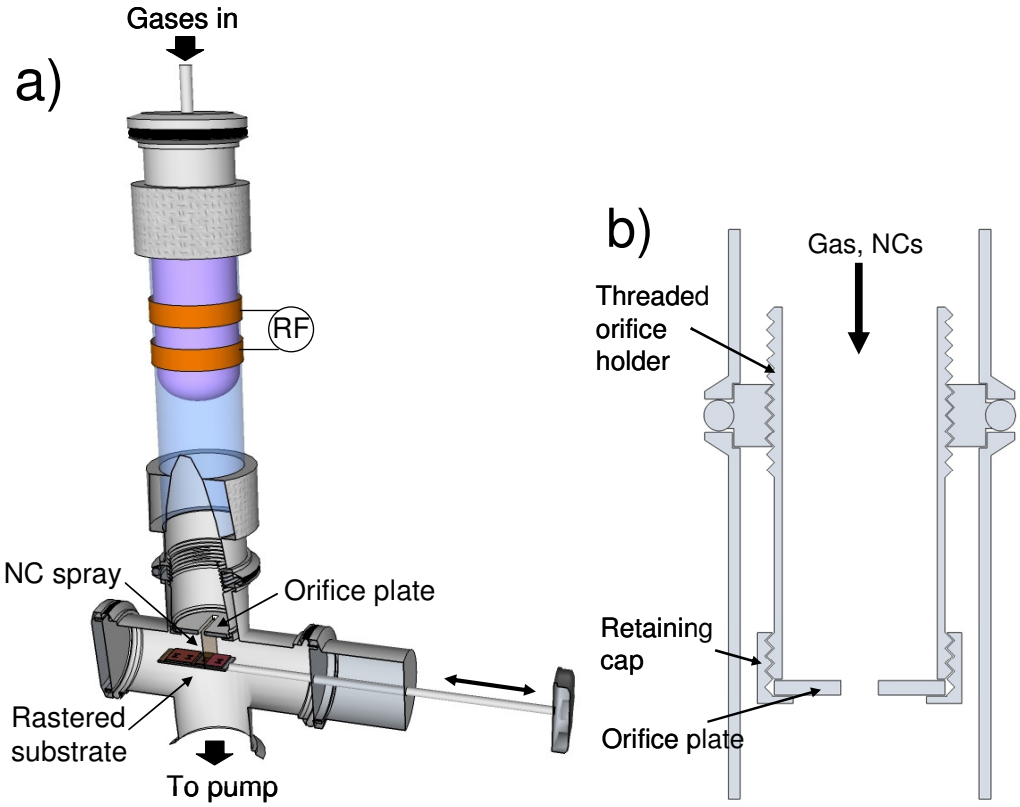

Figure 6-2. a) Cut-away schematic of the experimental apparatus. Precursor gases enter the top of the reactor and are dissociated in the radiofrequency plasma. The NCs which nucleate are accelerated through a slit-shaped orifice and impacted on a substrate rastered under the beam. b) Schematic of the orifice holder design. The retaining cap can be unthreaded to allow for quick-changing of the orifice plate, and the threaded holder allows the orifice to be moved closer or further from the substrate downstream.

The orifice holder (Fig. 6-2b) was designed to allow for quick changing of the orifice plates and control over the orifice-substrate standoff distance. We used both thin (0.3 mm) PEEK plastic orifice plates and a much thicker (6.4 mm) metal orifice plate. The PEEK orifice plates were cut with a CO_2 laser and had orifice lengths of 10 mm and widths ranging from 0.20-0.70 mm. The metal orifice plate was constructed from two

half cylinders separated by a gap, the length of this orifice was 12 mm, and its width could be adjusted from 0-0.97 mm with a screw. All orifices were square-edged. The orifice holder has a threaded body which allows the user to adjust its distance from the substrate, and the range of standoff distances accessible was increased by adding additional vacuum straight tubes to the system.

Substrates were mounted on a push-rod linear motion feedthrough and translated by hand in the direction perpendicular to the NC curtain emanating from the orifice for the duration of the deposition. The orifice-substrate standoff distance was varied from 3-100 mm. Most depositions were ~1 min long, resulting in films a few hundreds of nm thick.

Nanocrystal films were patterned using a standard lift-off procedure in which the metal evaporation step was replaced by NC deposition. A lift-off resist (LOR 3A, Microchem) was spun onto a Si wafer at 5000 rpm following cleaning and pre-baking. The wafer was then soft-baked at 190 °C for 2 mins, which sets the LOR undercut rate during development. Positive resist (S1813, Shipley) was spun on top of the LOR at 5000 rpm and soft-baked at 115 °C for 2 mins. The thickness of the LOR and positive resist layers were 0.2 and 1.2 μm, respectively. After exposure for 4 secs, a two-step development process was used in which the wafer was developed in CD-26 (Shipley) for 45 secs, baked at 125 °C for 2 mins, and then developed in CD-26 for an additional 15 secs. Baking after the first development step hardens the positive resist and creates a greater disparity in etch rate between the positive resist and LOR, thereby allowing formation of the undercut. The wafer was cut into pieces and Ge NC films of thicknesses

less than the LOR thickness were deposited onto the pieces. Finally, the resist was lifted off by soaking the pieces in 1165 Stripper (Shipley).

Film characterization. Film densities were determined using a little-known technique based on Rutherford backscattering (RBS). In RBS, the number of incident ions that are reflected and detected at a given energy is $A = \sigma\Omega N_s Q$, where σ is the average scattering cross section of the atoms in the sample, Ω is the detector solid angle, N_s is the number of atoms per square centimeter, and Q is the number of incident ions. Consequently, the intensity of the RBS signal at a given energy is proportional to the areal atomic density, and the thickness of the film can be determined if the (volumetric) atomic density is known, or vice versa. In addition, peak widths in RBS contain information about sample thickness and density. Ions which are reflected from atoms in the film's interior lose energy to excitation, ionization, etc. on the way in and out, so that ions which penetrate deeper into the film before scattering are detected with less energy. This gives RBS peaks their widths, and film thickness can be determined since the energy loss as a function of distance is known for each material. Note that, if the atomic density of bulk Ge is used in conjunction with peak height, or the energy loss function of bulk Ge is used in conjunction with peak width, the thickness determined will be the "equivalent thickness"—the thickness of the film if it were fully dense. The real density of the film is then found from the ratio of actual film thickness (measured separately) to the equivalent thickness. The same result is obtained if the actual film thickness is used as the independent variable and the density is calculated from the peak height and width, but this is not as convenient with commercial RBS software.

For our experiments, Ge NC films were deposited on Si wafers and irradiated with a 2 MeV He^{2+} beam in a NEC accelerator. Silicon works well as a substrate since it is relatively conductive and has a smaller kinematic factor than Ge, so that the substrate and film peaks are separated in energy space. 5-10 μC of charge were collected in each experiment and beam currents ranged from 10-20 nA. The samples were then fractured and cross-sectional scanning electron microscopy (SEM) performed with a JEOL 6500F was used to measure actual film thicknesses. For some samples (deposited on glass), X-ray diffraction (XRD) spectra were recorded with a Bruker-AXS microdiffractometer and NC sizes were determined from Debye-Scherrer fits. Raman spectroscopy using a Witec confocal Raman microscope was also performed on select samples.

6.5 Model description

A simple model was written using Mathematica to approximate the impaction process. First, the gas flow was calculated for all positions downstream of the orifice on the slit centerline, and then spherical NCs were introduced. The model only considers gas drag on the NCs—gravitational forces, electrostatic forces, and thermophoretic forces were deemed unimportant, and Brownian motion was also neglected because of the low temperature and pressure downstream of the orifice. This is a common assumption in similar models built by others.[28,30] We assumed that the gas was ideal and the NCs were sufficiently dilute so as not to affect the gas or interact with each other. For each point in time, the NC acceleration due to drag was calculated and assumed constant over a small

time step. The time was then advanced, the new NC position and velocity were calculated using the kinematic equations, and the acceleration was reevaluated.

The slit jet flow field has been calculated previously.[35,36,40] Raju and Kurian measured the Mach number of slit free jets along their center lines for slits of several aspect ratios, and found that slits with aspect ratios of 10 or greater had Mach number profiles that agreed very well with the theoretical profile of an infinitely long slit calculated using a two-dimensional method of characteristics.[31] Sulkes et al. also used a method of characteristics analysis to calculate the Mach number profiles of infinite slits for gases with heat capacity ratios of 5/3, 7/5, and 9/7.[32] The profiles were fit with equations of the form

$$M(x) = A \cdot (x - x_0)^{\frac{\gamma-1}{2}} - B \cdot (x - x_0)^{-\frac{\gamma-1}{2}}, \qquad (6\text{-}1)$$

where M is the Mach number, x is the distance downstream of the orifice along the centerline, γ is the heat capacity ratio, and A, B, and x_0 are fitting parameters.

The minimum slit aspect ratio used in our experiments was 14. We therefore expect the Mach number profile calculated for an infinite slit to be a good approximation based on the results of Raju and Kurian. We made use of the fits obtained by Sulkes et al., and interpolated between the fitting parameters for gases with γ = 5/3 and 7/5 since our gas mixture is 60% Ar and 40% H_2. This interpolation is not strictly accurate, but the deviation between the Mach number profiles for γ = 5/3 and 7/5 gases is small for Mach numbers less than 4, and the interpolation is sufficient for our present purposes. Note also that we neglected changes in heat capacity ratio with temperature. The fitting parameters we obtained are A = 3.22, B = 1.27, x_0 = -0.0984, and γ = 1.56.

The gas temperature T and density ρ in the jet were calculated from the Mach number profile. Assuming isentropic flow,

$$T(x) = T_0 \left\{ 1 + \frac{(\gamma - 1) \cdot M^2(x)}{2} \right\}^{-1}, \tag{6-2}$$

$$\rho(x) = \rho_0 \left\{ 1 + \frac{(\gamma - 1) \cdot M^2(x)}{2} \right\}^{-\frac{1}{\gamma - 1}}, \tag{6-3}$$

where T_0 and ρ_0 are the upstream stagnation temperature and density, respectively.[33] Finally, the gas velocity was calculated with knowledge of the Mach number and temperature using the ideal gas expression for the speed of sound. In this calculation, as with all others, we used calculated values for the properties of the gas mixture.

The derived expressions for the gas properties only apply to the free jet region upstream of the Mach disk. For a slit-shaped orifice, the free jet Mach disk location x_M is found from:

$$\frac{x_M}{w} = 1.23 \left(\frac{P_{up}}{P_{down}} \right)^{0.775}, \tag{6-4}$$

where w is the orifice slit width.[34] The jet collapses suddenly at the Mach disk, and we make the simplifying assumption that the velocity, temperature, and density take on their constant downstream values at the Mach disk location using a Heaviside function. The downstream velocity is determined by the measured gas flow rate, measured downstream pressure, and 1" tube diameter, the temperature is 298 K, and the density is calculated using the ideal gas law. The discontinuous treatment of the properties at the Mach disk is not unreasonable (see for example Chang et. al[30]); the strong shock and low gas density

mean that the NCs experience few collisions in the transition region between the jet and the downstream flow. The gas properties are plotted as a function of position in Fig. 6-3 for three different pressure ratios and corresponding jet lengths.

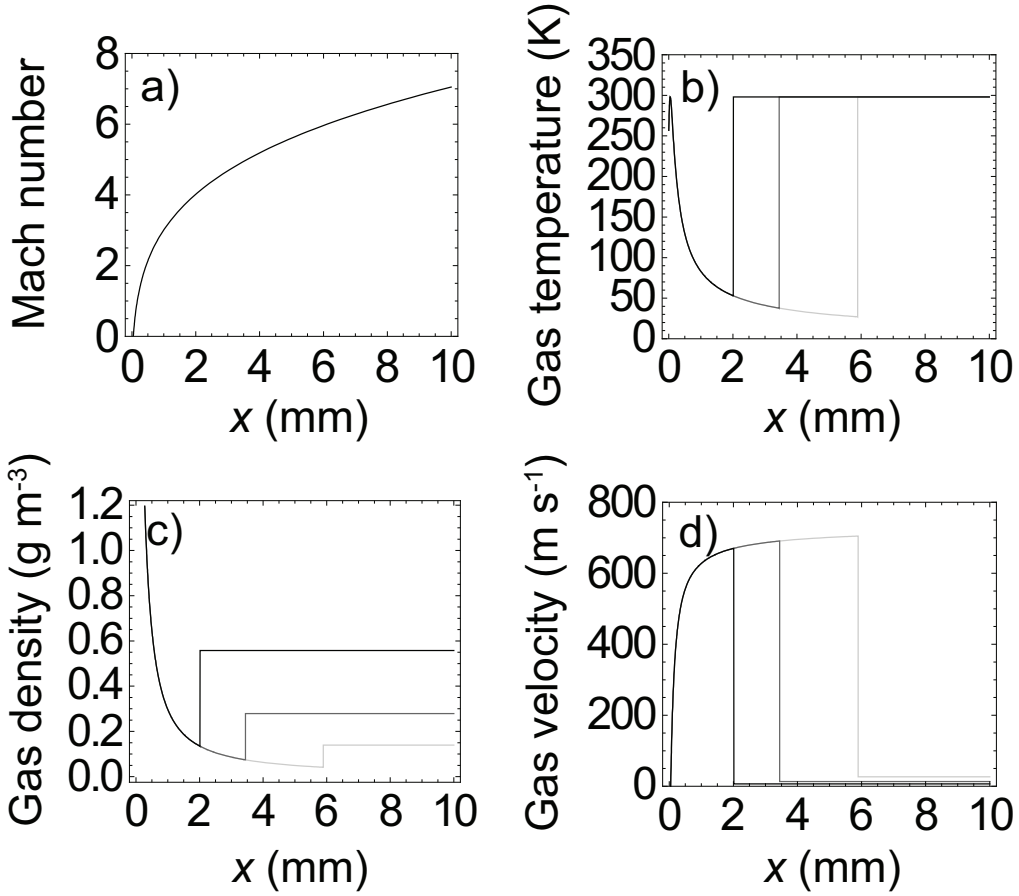

Figure 6-3. Profiles of the gas a) Mach number, b) temperature, c) density, and d) velocity downstream of the orifice for P_{up}/P_{down} = 5 (black), 10 (gray), and 20 (light gray). Except for the Mach number profile (which is given for an infinite jet), the profiles collapse to their downstream values at the Mach disk, the location of which varies with the pressure ratio. For this calculation, P_{up} = 2.2 Torr, the total flow rate was 113 sccm, and the orifice slit width was 0.47 mm.

Nanocrystals were introduced in the flow at the orifice exit plane (x = 0). The NCs were given the same initial velocity as the gas, Mach 1 or 410 m/s. This initial velocity assumes that the NCs have ample time upstream to equilibrate with the flow. A

calculation using the formalism described here in which an NC at rest is placed in a constant Mach 1 flow reveals that a 4.5 nm Ge NC attains 90% of its final velocity after 14.0, 4.7 and 1.6 mm for gas pressures of 1, 3, and 9 Torr, respectively. A 7.0 nm Ge NC requires 21.8, 7.3, and 2.4 mm under the same conditions. If the orifice plate thickness is greater than the velocity equilibration length, the NCs will certainly reach Mach 1 by the exit plane. If the orifice plate thickness is smaller, the quality of the initial velocity assumption will depend on the details of the flow upstream of the orifice. For particularly thin orifices (such as the PEEK orifices used here), the assumption will be poor at low pressures. We encounter this situation later.

The NC position, velocity, and acceleration were calculated recursively using Newton's 2nd law for gas drag and the kinematic equations:

$$x(n) = x(n-1) + v(n-1)\cdot t + \frac{1}{2}a(n-1)\cdot t^2, \tag{6-5}$$

$$v(n) = v(n-1) + a(n-1)\cdot t, \tag{6-6}$$

$$a(n) = \frac{1}{m_{NC}} f(x(n))\cdot\{u(x(n)) - v(n)\}, \tag{6-7}$$

Here, x, v, a, and m_{NC} are the NC position, velocity, acceleration, and mass, respectively. The time step t is taken to be 1 or 10 ns, n is the step number, and u is the gas velocity. Changing the time step does not affect the model so long as the gas properties are approximately constant over the time step. We use an expression derived from kinetic theory for the friction coefficient f,[35] since the NCs are deep in the free molecule regime:

$$f(x) = \frac{2}{3}d^2\rho(x)\sqrt{\frac{2\pi kT(x)}{m_g}}\cdot\left(1+\frac{\alpha\pi}{8}\right), \tag{6-8}$$

Here, d is the NC diameter, k is the Boltzmann constant, m_g is the molecular mass of the gas, and α is the so-called accommodation coefficient, taken to be 0.9 in our calculations.[36] Similar results are obtained if the friction coefficient is calculated using the Stokes expression with the Cunningham slip correction factor. Note that f and u have to be reevaluated at each time step since the gas properties vary as the NC moves downstream. The code is typically run up to $n = 2\times10^5$ (0.2 or 2 ms), which is enough time for the NCs to travel to the substrate for reasonable orifice-substrate standoff distances.

6.6 Results and discussion

Large-area films. Germanium NCs are accelerated through the orifice via collisions with the expanding gas, generating a one-dimesional beam or curtain of NCs with a cross-section similar to the dimensions of the orifice. When a substrate is rastered under the beam, a film is deposited that has the width of the NC curtain, arbitrary length, and thickness proportional to the deposition rate and speed with which the substrate passes under the curtain. This design is conducive to large-area roll-to-roll processing of, e.g., thin film nanocrystal solar cells, in which a flexible substrate passes under an orifice that is perhaps a meter in width.

By rastering a substrate under the curtain multiple times, we have deposited films with thickness from 20 nm (<1 sec) to 20 μm (~10 mins). Photographs of three Ge NC films on glass with widths of ~12 mm and thicknesses from 200-800 nm are shown in

Fig. 6-4. The films are macroscopically uniform, with some thickness variation observable in the thinnest film near the edges of the NC beam.

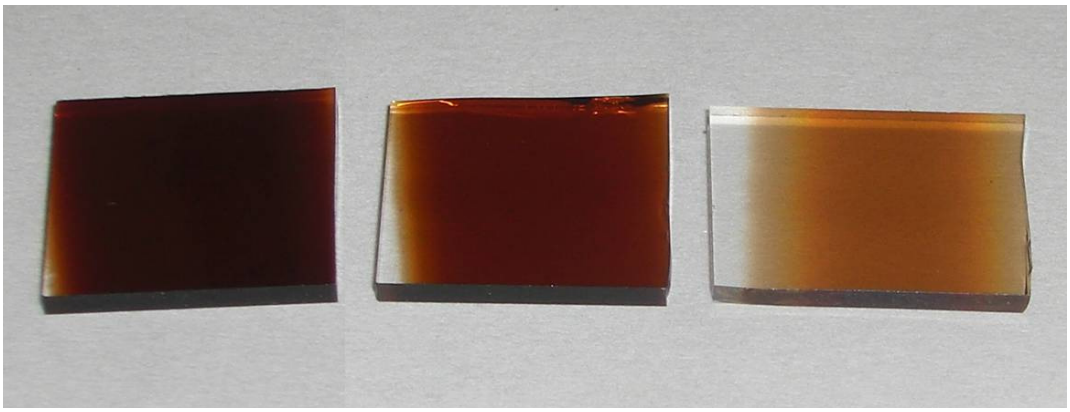

Figure 6-4. Photograph of impacted Ge NC films of varying thicknesses deposited on glass. The films are uniform, with some thickness variation visible at the curtain edges.

Film patterning. In order to investigate the potential of NC impaction for patterned microelectronics, we used the technique in conjunction with standard lift-off processing, with the metal deposition step replaced by NC impaction. Figure 6-5a shows a cross-sectional SEM image of a sample prior to the final lift-off step, where the Ge NC film is clearly discontinuous at the feature edges due to the undercut LOR. Figures 6-5b and 6-5c show cross-sectional and top-view SEM images of the 2 μm line after lift-off. The Ge NC film is uniform and the feature edges are well-defined, with side-wall widths of less than 200 nm for these 230 nm thick films. The resolution limit here is imposed by the photolithography and not the deposition process; we believe 200 nm features are possible for thin films (< 100 nm) using electron beam lithography. Figure 6-5d shows an optical microscope image of a patterned Ge NC film with UMN lettering of several sizes. The NC films were remarkably robust during the processing and did not suffer damage

when squirted directly with water or solvents, or soaked in an NMP-based stripper. Exposure to solvents may, however, alter the NC surface chemistry.

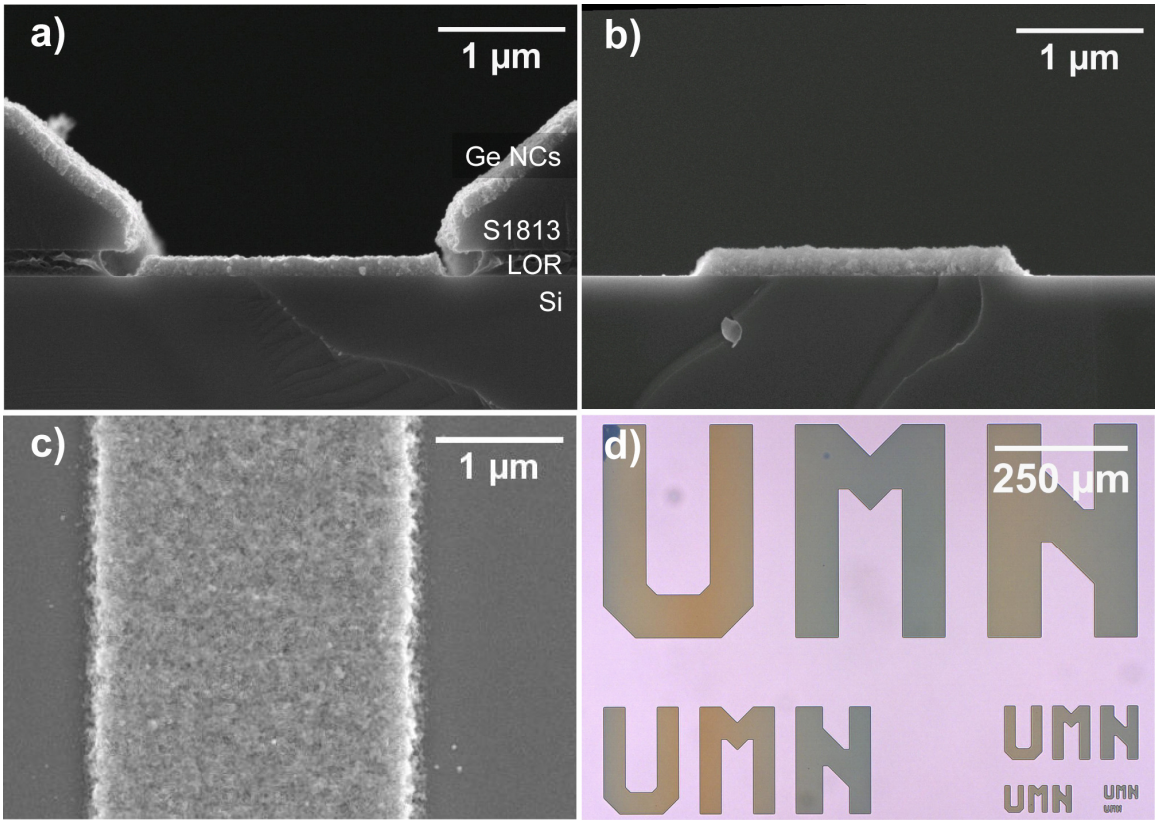

Figure 6-5. Cross-sectional SEM images of a 2 µm wide Ge NC film on Si patterned using conventional lift-off photolithography a) before and b) after lifting off the resist. c) Top-view SEM image of the patterned film in b). Note the sharp features, film uniformity, and low surface roughness. d) Optical microscope image of a Ge NC film on glass patterned into UMN lettering of several sizes.

Investigation of deposition parameters. The morphology—in particular, the density—of impacted films is observed to vary across a wide range as the deposition parameters are altered, as shown in the cross sectional SEM images of Fig. 6-6. The Ge NC sample in Fig. 6-6a is fluffy and highly porous like a powder. The sample in Fig. 6-6b is dense and film-like, as demonstrated by the propagation of a crack from the substrate. While porous films find use in certain applications such as gas-sensing and

catalysis, they are clearly unsuitable for use in semiconductor devices in which charge carriers must pass between neighboring NCs. Thus, the factors determining film density must be understood and controlled in order to tailor NC films to their intended applications.

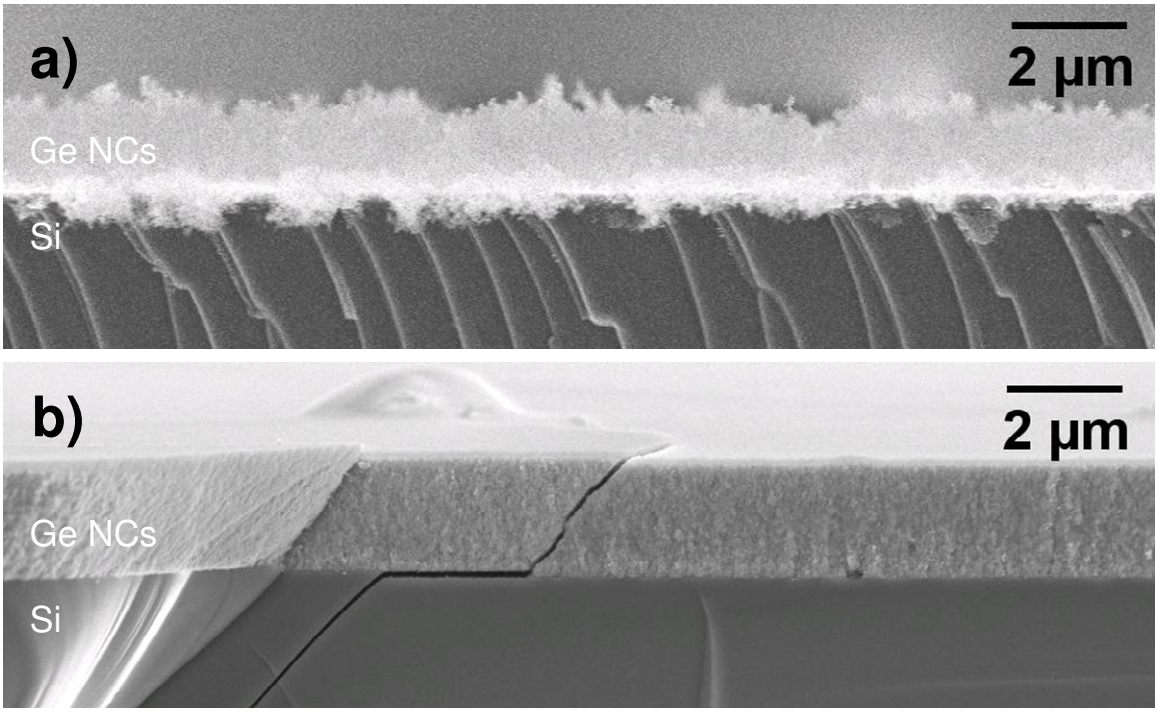

Figure 6-6. Cross-sectional SEM images of Ge NC films on Si substrates showing a) a fluffy, porous sample, and b) a dense film.

We have found that the density of impacted NC films varies with the pressure ratio across the orifice P_{up}/P_{down}, the orifice-substrate standoff distance x_s, and the absolute value of P_{up} or P_{down}. We experimentally investigated each of these parameters in detail, although their significance is clear from intuition alone. At $P_{up}/P_{down} \approx 2$, gas flow through the orifice becomes sonic. The supersonic jet emanating from the orifice increases in length as the pressure ratio is further increased, allowing the gas to reach lower densities and higher velocities as it expands. P_{up} and P_{down} determine the disparity

between the gas and NC velocities, since the gas velocity is coupled to the NC velocity through the gas density (via collisions). Finally, the substrate position relative to the jet structure—in particular, its proximity to the collapse of the jet at the Mach disk—determines how much energy the NCs have lost to collisions with the near-stationary gas prior to impaction. Other considerations, such as orifice design, can also be important, but are outside the scope of this work.

The densities of Ge NC films deposited with pressure ratios of 2-51 are displayed in Fig. 6-7. P_{up} was held constant for each data set and the ratio was varied by changing P_{down} using a valve downstream of the system. The open-circles data correspond to 4.5 nm Ge NCs (determined from XRD), while the filled-squares data are for films of 7.0 nm Ge NCs. The reported film densities are those measured using RBS and cross-sectional SEM, but we have checked the results against those obtained using the more common N_2 adsorption-desorption technique for one sample and found less than 10% deviation. No deposition is observed for pressure ratios less than 2 for 4.5 nm Ge NCs, and 4 for 7.0 nm Ge NCs. For larger pressure ratios, the film density increases rapidly, then saturates near 50% the density of bulk Ge.

It is not clear from Fig. 6-7 why the two different sizes of Ge NCs have different onset values of P_{up}/P_{down} for impaction. Is this the result of the NC sizes, or are the different values of orifice size, P_{up}, and P_{down} (given in the Fig. caption) the cause? One drawback of our current experimental apparatus is that the synthesis conditions are coupled with the deposition conditions through the orifice. The orifice size not only determines the pressure ratio for impaction, but it also controls the NC residence time in

the plasma and thus the NC size. Consequently, 7.0 nm Ge NCs cannot be impacted under identical conditions to 4.5 nm Ge NCs because they cannot be synthesized under identical conditions. Our model, however, allows us to separate the effects of each parameter when it is hard to do so experimentally.

Simulation results for the NC velocity v_{NC} at the substrate position (x_s = 8 mm) of NCs impacted under the above conditions are shown in Fig. 6-8. Although we have chosen to plot v_{NC}, it is not obvious that velocity—or any other fundamental quantity—is an appropriate proxy for film density. The impaction of all but the first monolayer of NCs is complicated, with subsequent NCs landing on a porous, malleable surface of formerly deposited NCs which deforms and compresses with their impact. Nonetheless, the simulated velocities exhibit the same trends as the experimental film densities, with similar onset values and curvature. This suggests that there is a near-linear relationship between v_{NC} and film density, at least for low velocities. The trend cannot hold at high velocities of course, since the film density must saturate at the bulk Ge density while v_{NC} can, in principle, increase indefinitely. The importance of particle velocity (as opposed to, e.g., momentum) has been pointed out for other sprayed coatings. In cold gas-dynamic spraying of 1-50 μm metal particles at P_{down} = 1 atm the particle velocity has been found to be the critical parameter in determining coating porosity.[37,38]

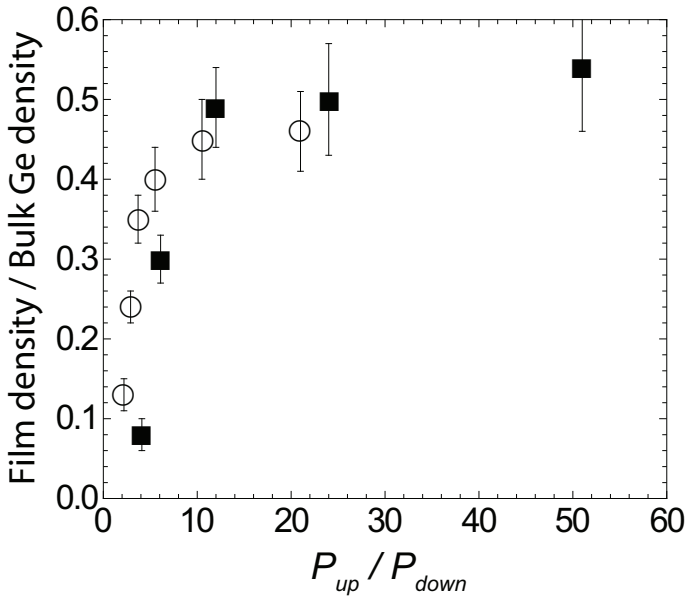

Figure 6-7. Measured relative film densities as a function of the pressure ratio across the orifice. The open circles correspond to films of 4.5 nm Ge NCs impacted through a PEEK 10 mm × 0.47 mm orifice with P_{up} = 2.2 Torr and a total flow rate of 113 sccm. The filled squares correspond to films of 7.0 nm Ge NCs impacted through a PEEK 10 mm × 0.20 mm orifice with P_{up} = 7.2 Torr and a total flow rate of 139 sccm. In both cases the standoff distance was 8 ± 3 mm and the pressure ratio was varied by controlling P_{down}.

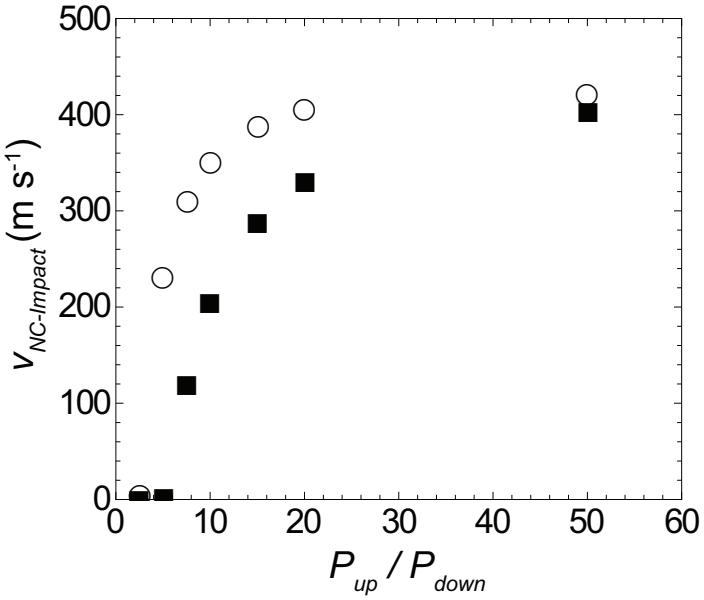

Figure 6-8. Modeled Ge NC impaction v_{NC} for the same conditions as in Fig. 6-7.

Figure 6-9 shows simulated v_{NC} versus centerline position x for three pressure ratios (2.5, 7.5, and 15) for the same conditions as in Figs. 6-7 and 6-8. Note that for x_s = 8 mm the substrate is downstream of the free jet Mach disk location x_M (visible as the kink in v_{NC} at its maximum) for all pressure ratios investigated. x_M is smaller for the 7.0 nm NCs for equivalent pressure ratios because of the reduced orifice width (see (6-4)). It is now apparent that 7.0 nm NCs are not impacted for pressure ratios less than 4 because they lose all of their velocity to gas drag before traveling the 8 mm to the substrate. Simulations altering one parameter at a time reveal that the excess drag is not due to the increased NC size—larger NCs accelerate slower from drag, all conditions the same—but from the high downstream gas density (as reported in the caption of Fig. 6-7, in these depositions P_{up} is over three times larger for the 7.0 nm Ge NCs than the 4.5 nm NCs). The model is also instructive with regard to the saturation of the film density at pressure ratios larger than 20. For $P_{down} < 0.2$ Torr, the downstream gas density is sufficiently low that the coupling between the gas and NC velocities is too weak to either further accelerate the NCs in the tail of the free jet or decelerate the NCs downstream of the Mach disk. Consequently, lowering P_{down} further alters the gas flow field but not the NC behavior.

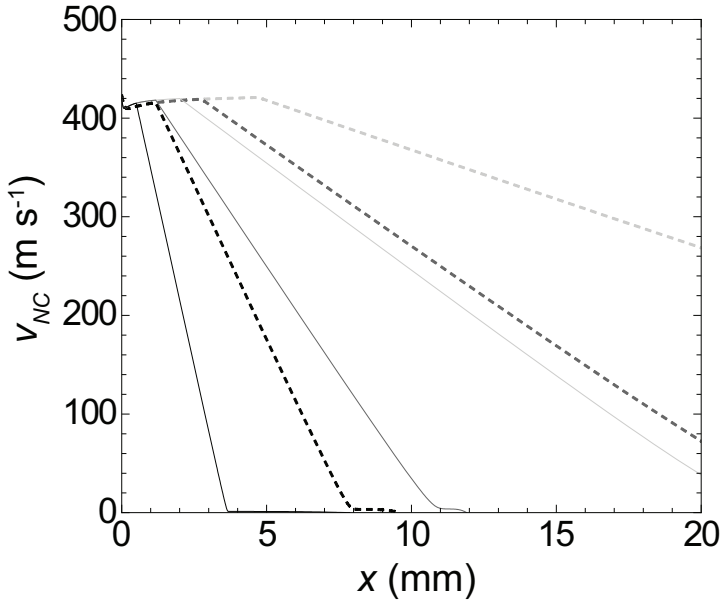

Figure 6-9. Modeled v_{NC} as a function of position x (the orifice exit plane is at $x = 0$) for the same conditions as in Fig. 6-7. The dashed and solid lines correspond to the 4.5 and 7.0 nm Ge NCs, respectively, and the black, gray, and light gray curves are for P_{up}/P_{down} = 2.5, 7.5, and 15, respectively. The Mach disk location is visible as the kink in the profiles at which the maximum velocity occurs.

Figure 6-9 also indicates how v_{NC}, and consequently film density, depend on x. We investigated this experimentally for two different conditions by threading the orifice holder in or out to adjust x_s (Fig. 6-10), and simulated the same conditions with our model (Fig. 6-11). The filled-squares (solid line in Fig. 6-11) data correspond to 5.5 nm Ge NCs deposited with P_{up}/P_{down} = 10, while the open-circles (dashed line in Fig. 6-11) data correspond to 4.3 nm Ge NCs deposited with P_{up}/P_{down} = 20. For both data sets, Fig. 6-10 indicates that film density remains roughly constant for small x_s, and falls rapidly after some threshold value. For the sample at 100 mm, the NCs deposited by diffusion alone and the film looked like that in Fig. 6-6a. Close to the orifice, a large discrepancy is observed between the film densities of the two data sets. The difference in pressure ratio may contribute to this, although Fig. 6-7 suggests this is a small effect at these ratios.

More likely, the low value of P_{up} combined with the thin PEEK orifice results in inadequate upstream coupling of the gas and NC velocities so that the NCs represented by the filled-squares data are not accelerated to Mach 1 before entering the free jet. The model does not take this into account and assumes that v_{NC} = 410 m s^{-1} at x = 0 in all cases. Consequently, the solid curve in Fig. 6-11 should be shifted to lower velocities.

Nonetheless, the agreement between the *shapes* of the film density curves in Fig. 6-10 and the calculated v_{NC} curves in Fig. 6-11 is quite good. However, there is more structure in Fig. 6-11 than can be made out in Fig. 6-10. In particular, Fig. 6-11 shows that NC acceleration in the free jet should yield films of slightly increasing density for standoff distances up to x_M. This trend may be visible in the filled-squares data of Fig. 6-10, but it is clearly not for the open-circles data. One reason may be that v_{NC} is large enough that proportionality with film density is lost; we have not produced films denser than 56% the density of bulk Ge, suggesting that a limit is approached. Additionally, our model does not account for the relocation of the shock when a substrate is placed upstream of x_M, and the gas flow field is thus inaccurate for small orifice-substrate standoff distances. It is also interesting to note that Fig. 6-11 predicts a linear decrease in v_{NC} with increasing x downstream of the free jet. There is not enough data to resolve this trend in the film densities. Finally, Fig. 6-11 reveals that the optimal substrate location for producing dense films is just downstream of the Mach disk location x_M. Here, the NCs capitalize on the entire length of the accelerating free jet, yet experience little drag after the shock.

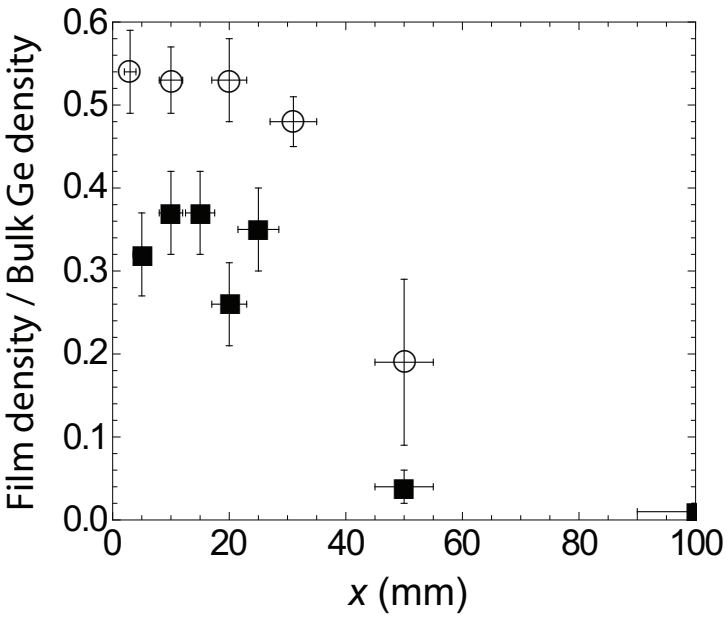

Figure 6-10. Measured relative film densities as a function of substrate position x_s. The open circles correspond to films of 4.3 nm Ge NCs impacted through the metal adjustable orifice plate with an orifice width of 0.85 mm using P_{up} = 3.0 Torr, P_{down} = 0.15 Torr (ratio = 20), and a total flow rate of 185 sccm. The filled squares correspond to films of 5.5 nm Ge NCs impacted through a PEEK 10 mm × 0.40 mm orifice with P_{up} = 1.7 Torr, P_{down} = 0.17 Torr (ratio = 10), and a total flow rate of 74 sccm.

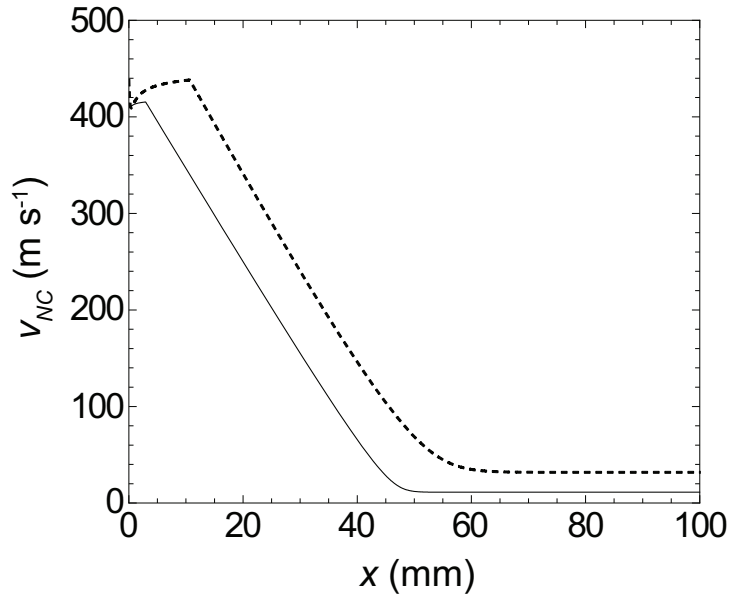

Figure 6-11. Simulated v_{NC} as a function of position x for the same conditions as in Fig. 6-10. The dashed and solid lines correspond to the 4.3 and 5.5 nm Ge NCs, respectively.

We investigated the pressure ratio through P_{down} above; now we address the effects of changing P_{up}. This is challenging to do experimentally without altering the NCs because the plasma synthesis method is sensitive to the pressure. Three films deposited with P_{up} = 1.0, 3.0, and 6.0 Torr and a constant pressure ratio of 20 at a standoff distance of 10 mm had relative densities of 29, 53, and 56%, respectively. The enhancement with increasing P_{up} is expected and is attributable to greater coupling of the gas and NC velocities both upstream of the orifice and in the free jet. However, it is difficult to make quantitative judgments from this data because XRD and Raman spectroscopy reveal that one sample was amorphous and the other two contained crystalline NCs of different sizes. This is a limitation of our synthesis approach, not the impaction apparatus.

Methods to increase film density. The model shows that with increasing P_{up}, the gas and NCs are more strongly coupled and v_{NC} approaches the gas velocity in the supersonic jet. Consequently, increasing P_{up} is one way to further increase film density. Ideally, P_{down} would be held constant. In this case, increasing the pressure ratio (by raising P_{up}) beyond 20 would continue to increase v_{NC}, and the resulting film density may not saturate at ~50% as in Fig. 6-7. Figure 6-12 compares simulated v_{NC} values for P_{up} = 1, 5, and 25 Torr, with P_{down} = 0.1 Torr held constant and all other conditions identical. With P_{up} = 25 Torr, v_{NC} is approximately 30% larger than for 1 Torr and the Mach disk is much farther downstream. However, reaching pressure ratios greater than 100 can be difficult in practice, depending on orifice size and pumping capability. It is still advantageous to increase P_{up} even if P_{down} rises, within limits. In this case, the NCs decelerate more quickly after the shock because of the increased downstream gas density,

so the substrate must be placed carefully. In addition, small NCs will more closely follow the streamlines at higher downstream gas densities so that the impaction cut size will increase.

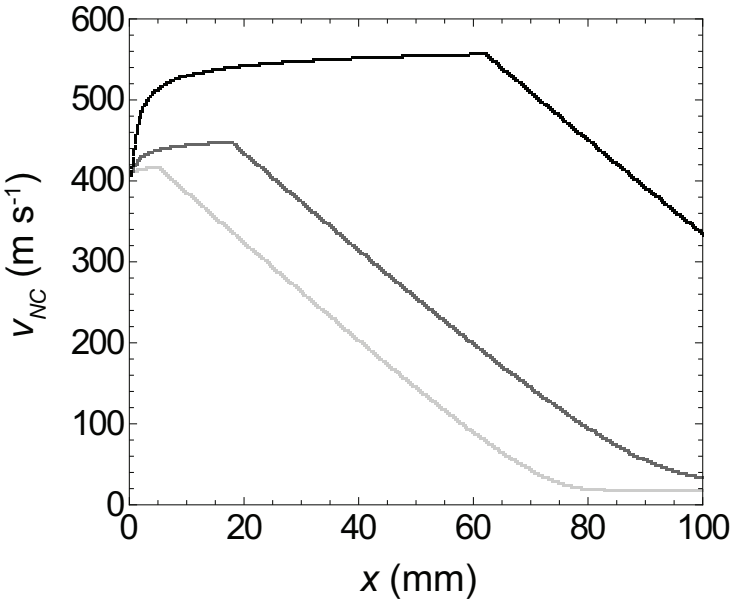

Figure 6-12. Modeled v_{NC} as a function of position x for P_{up} = 25 (black), 5 (gray), and 1 (light gray) Torr. All other parameters were held constant: P_{down} = 0.1 Torr, 5 nm Ge NCs, 100 sccm total flow rate, and 0.7 mm width orifice.

v_{NC} is determined not only by the coupling between the gas and NCs, but also by the gas velocity profile. Figure 6-3 shows that the gas temperature drops very rapidly in the free jet, causing the sonic velocity to decrease. Preheating the gas prior to expansion through the orifice would increase the gas velocity and subsequently v_{NC}, promoting additional film densification. Figure 6-13 shows simulated v_{NC} profiles for upstream gas temperatures of 298, 500, and 700 K. The improvement per degree of temperature increase is modest, but the maximum v_{NC} is ~30% larger at 700 K. Higher temperatures would risk melting Ge NCs.

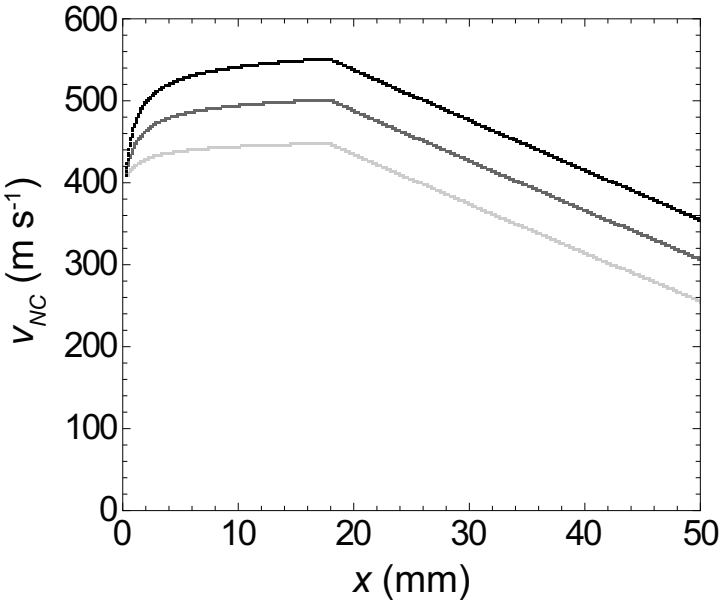

Figure 6-13. Modeled v_{NC} as a function of position x for upstream temperatures of 700 (black), 500 (gray), and 298 (light gray) K. All other parameters were held constant: P_{up} = 5 Torr, P_{down} = 0.1 Torr, 5 nm Ge NCs, 100 sccm total flow rate, and 0.7 mm width orifice.

Changing the gas composition also dramatically affects the gas velocity profile since lower molecular weight gases have higher sonic velocities. Our model indicates that changing the Ar in our experiments to He, which should not significantly alter the NC plasma synthesis process, would increase the maximum v_{NC} by nearly a factor of two. Using He in conjunction with higher upstream pressures and temperatures, v_{NC} exceeding 1000 m s^{-1} are predicted. Preheated He is commonly used in cold gas-dynamic spraying of micron-sized metal particles,[39] and initial experiments that we conducted with Ge NCs in He yielded film densities that were consistently higher than equivalent films using Ar (Fig. 6-14).

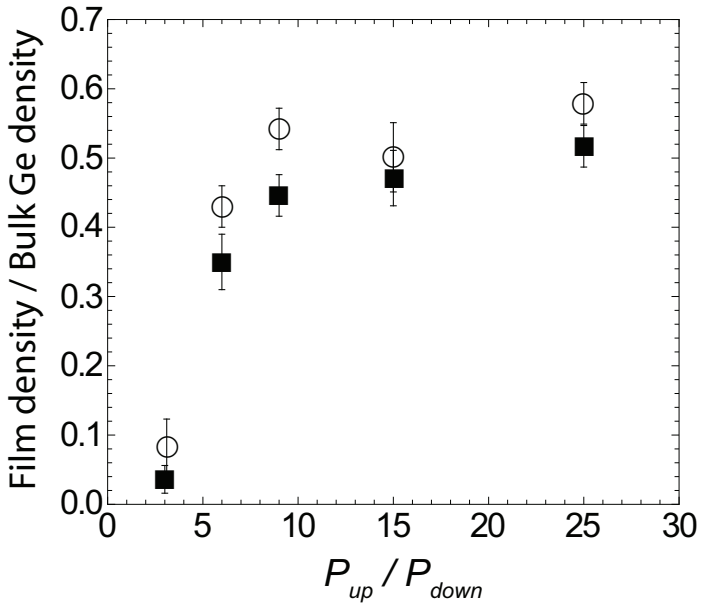

Figure 6-14. Measured relative film densities as a function of the pressure ratio across the orifice for Ge NCs synthesized with He and Ar. The open circles correspond to films of 3.9 nm Ge NCs synthesized with He with a total flow rate of 266 sccm. The filled squares correspond to films of 4.9 nm Ge NCs synthesized with Ar with a total flow rate of 151 sccm. For both data sets, Ge NCs were impacted through the metal adjustable orifice plate with an orifice width of 0.85 mm, the standoff distance was 8 ± 3 mm, P_{up} = 3.2 Torr, and the pressure ratio was varied by controlling P_{down}. Note that although the films deposited with He are denser than those deposited with Ar, identical deposition conditions could not be achieved for both gases at each pressure ratio (e.g., P_{up} is the same, but the flow rates and NC sizes are not).

A trade-off: Film density and quantum confinement. In striving to optimize film morphology, it must be remembered that it is possible to achieve NC impact velocities that are *too* large. To realize their potential, semiconductor NCs must maintain their unique size-dependent optical and electronic properties after film formation. The maximum random packing density of hard, monodisperse spherical NCs is 64%;[40] randomly deposited NC films with this density or higher have likely lost quantum confinement because of deformation, sintering, or amorphization. We have repeatedly measured densities that are 55% that of bulk Ge under optimized conditions (e.g., Fig. 6-

10), which approaches this limit. Our model indicates that the corresponding NC impaction velocity is ~400 m s^{-1}. Valentini and Dumitrica have performed molecular dynamics simulation of Si NCs impacted onto a Si substrate.[41] They found that 5 nm Si NCs impacted at room temperatures with velocities of 546 m s^{-1} undergo elastic deformation and experience a temperature rise to about 400 K. Impacts beyond ~1000 m s^{-1}, on the other hand, result in significant structural changes. Although this situation is not identical to ours, it suggests that the Ge NC velocity should be further increased cautiously.

We performed XRD on the most dense Ge NC films we could make using a variety of NC sizes. The spectra are displayed in Fig. 6-15 along with the crystallite sizes extracted from Debye-Scherrer fits. Figure 6-15 shows that we have successfully impacted Ge NCs 4–14 nm in diameter—the size range of interest for devices based on quantum confined NCs. There is no observed increase in the crystallite size after impaction; samples deposited under identical conditions but with significantly increased orifice-substrate standoff distances (not shown) have the same size crystal grains. This is not sufficient evidence to prove that the NCs retain quantum confinement even up to relative film densities of 55%, but it is reassuring. Further studies are presented in the following chapter.

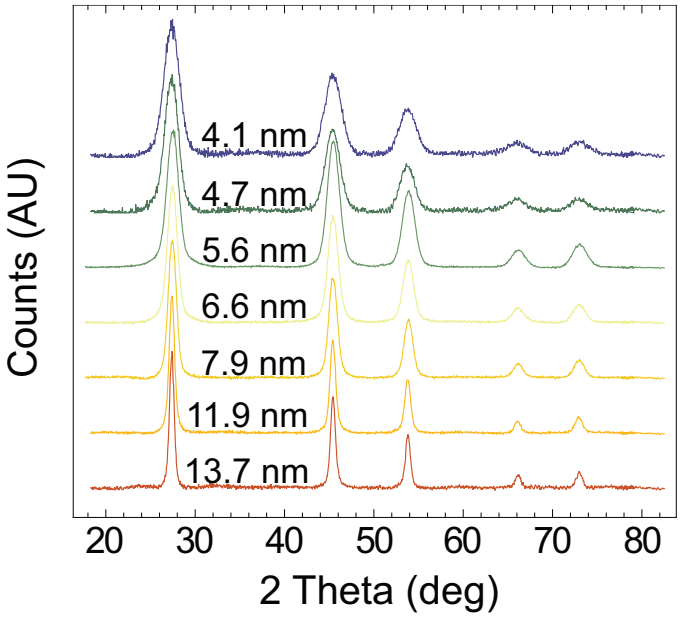

Figure 6-15. XRD spectra of films of impacted diamond-cubic Ge NCs. Decreasing crystallite size is visible as a broadening of the peaks, and the NC size was extracted using the Debye-Scherrer equation. Spectra are normalized and shifted for clarity.

Note that 55% relative density is significantly better than is achievable for colloidal NCs with ligands cast from solution. For 5 nm diameter Ge NCs with 1 nm long ligands, the maximum packing is reduced to 23% (random) or 27% (hexagonal) because of the volume occupied by the ligands. Recent work in NC colloidal films involves replacing longer ligands with shorter molecules after casting films,[11,12] but even for 0.3 nm molecules the maximum density is 46% (random) or 53% (hexagonal).

6.7 Conclusions

We have demonstrated a new technique for depositing thin films of NCs using a supersonic gas jet to accelerate and impact the NCs. Ge NC films were synthesized in a nonthermal plasma, accelerated through a slit-shaped orifice, and impacted onto

substrates rastered perpendicularly to the NC beam. Uniform films were deposited over areas as large as several cm^2, and lift-off photolithographic techniques produced patterned features as small as 2 μm. The densities of the NC films varied from 1–55% the density of bulk Ge, with larger pressure ratios, smaller orifice-substrate standoff distances, and larger upstream pressures resulting in denser films. Films of Ge NCs 4–14 nm in diameter were deposited without post-deposition crystallite growth, although proof that NC quantum confinement remains intact remains to be shown.

This deposition technique, like all others, has limitations. Low downstream pressures (<1 Torr) are necessary to overcome diffusion and deposit small NCs. The upstream pressure cannot be too small (<2 Torr), else the NCs will need an exceptionally long time to equilibrate with the gas flow. With the 60% Ar, 40% H_2 gas mixture used in this study, the NC maximum velocity is limited to ~600 m s^{-1}. Finally, with the setup used here, NC synthesis and deposition were coupled through the orifice so that the impaction parameters were to some extent dictated by the synthesis parameters.

However, we believe this deposition technique holds great promise, in large part because of its flexibility. It is relatively material independent: this study used Ge NCs only, but we have also successfully deposited films of Si NCs and InP NCs synthesized with the same plasma processes. The NCs we deposited were plasma synthesized, but the technique should accommodate any other aerosolized NCs, including those synthesized in the gas phase, and powders and liquids that have been aerosolized. In some cases, special care will be required to understand the nature of the impacting particles, since agglomerates of NCs or liquid droplets containing NCs will require deposition conditions

that are appropriate to their size. Depositing agglomerates could be advantageous, since higher pressures could be used throughout the system without fear of diffusion. We have deposited on Si, glass, Al foil, plastic, and paper without any noticeable difference in the films, demonstrating the substrate-independent nature of the process. We concentrated on maximizing the density of our films without grain growth in this work, but other researchers may want to use the technique to controllably deposit films of high porosity, or increase the NC velocity until sintering occurs upon impact. Finally, while the feature sizes investigated here ranged from 1 cm to 2 μm, these are not the limits of the technique. The one-dimensional nature of this technique makes it natural for roll-to-roll processing with meter-wide films. With electron beam lithography, we are confident that NC films can be reproducibly patterned with feature sizes on the order of 200 nm.

6.8 Future work

The impaction scheme demonstrated in this chapter works well for the impaction of Ge NCs of various sizes. Future improvements to the design would likely focus on the orifice design—a long, nozzle-like entrance and a tapered exit would disrupt the gas flow less and allow the gas to expand in a controlled fashion downstream—and decoupling the synthesis parameters from the impaction parameters. The latter problem is challenging, but may be overcome by adapting the synthesis plasma to run at higher pressures (>10 Torr, preferably).

We would like to see the impaction apparatus used in conjunction both with other materials synthesized with the plasma approach used here, and with NCs synthesized

using other methods. We and others in the Kortshagen laboratory have successfully impacted Si and InP NCs, but detailed studies to verify that the three parameters identified in this chapter also govern deposition in other materials systems have not been conducted. Preliminary studies using the impaction scheme in conjunction with lift-off photolithography to pattern luminescent Si NCs appear exciting (Fig. 6-16). The impaction scheme was also used successfully with the in-flight plasma-initiated hydrosilylation apparatus described by Mangolini et al. to deposit dense films of hydrosilylated Si NCs. This may prove to be important, as exciting new LEDs using hydrosilylated Si NC films (spun from solution) and polymer were recently reported.[42]

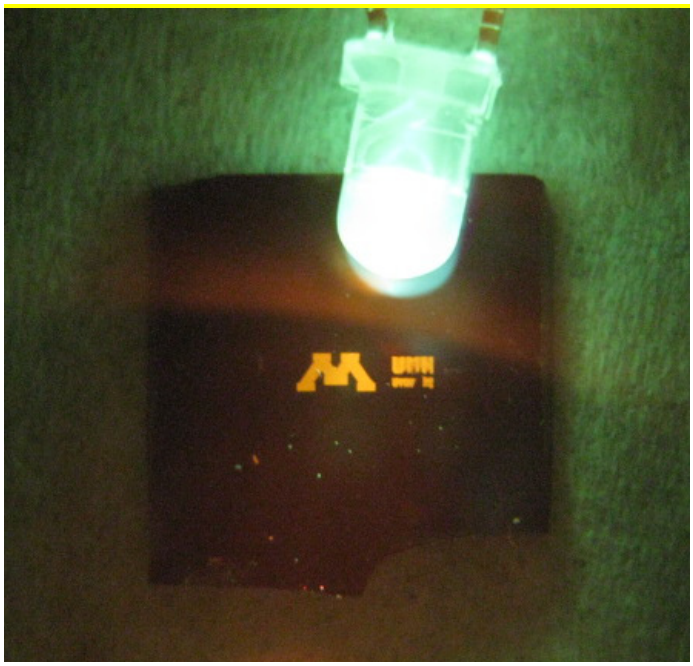

Figure 6-16. Photograph of a patterned impacted Si NC film on a Si wafer. The NCs glow orange under UV illumination from an LED (a long-pass filter between the sample and camera blocks the UV light from the LED from reaching the camera). The film was patterned using the same mask as the Ge NC film in Fig. 6-5d. This work was done with Rebecca Anthony.

6.9 References

[1] C.B. Murray, D.J. Norris, and M.G. Bawendi, *J. Am. Chem. Soc.* **115**, 8706 (1993).

[2] O.I. Micic, J.R. Sprague, C.J. Curtis, K.M. Jones, J.L. Machol, A.J. Nozik, H. Giessen, B. Fluegel, G. Mohs, and N. Peyghambarian, *J. Phys. Chem.* **99**, 7754 (1995).

[3] M.A. Hines and P. Guyot-Sionnest, *J. Phys. Chem. B* **102**, 3655 (1998).

[4] O.I. Micic, S.P. Ahrenkiel, D. Bertram, and A.J. Nozik, *Appl. Phys. Lett.* **75**, 478 (1999).

[5] C.B. Murray, S.H. Sun, W. Gaschler, H. Doyle, T.A. Betley, and C.R. Kagan, *IBM J. Res. Dev.* **45**, 47 (2001).

[6] J.E. Murphy, M.C. Beard, A.G. Norman, S.P. Ahrenkiel, J.C. Johnson, P.R. Yu, O.I. Micic, R.J. Ellingson, and A.J. Nozik, *J. Am. Chem. Soc.* **128**, 3241 (2006).

[7] S.H. Huh, D.H. Riu, Y. Naono, Y. Taguchi, S. Kawabata, and A. Nakajima, *Appl. Phys. Lett.* **91**, 093118 (2007).

[8] S. Jun, E.J. Jang, J. Park, and J. Kim, *Langmuir* **22**, 2407 (2006).

[9] L. Martiradonna, T. Stomeo, M. De Giorgi, R. Cingolani, and M. De Vittorio, *Microelectron. Eng.* **83**, 1478 (2006).

[10] W.J. Kim, S.J. Kim, K.S. Lee, M. Samoc, A.N. Cartwright, and P.N. Prasad, *Nano Lett.* **8**, 3262 (2008).

[11] D.V. Talapin and C.B. Murray, *Science* **310**, 86 (2005).

[12] J.M. Luther, M. Law, Q. Song, C.L. Perkins, M.C. Beard, and A.J. Nozik, *ACS Nano* **2**, 271 (2008).

[13] M. Drndic, M.V. Jarosz, N.Y. Morgan, M.A. Kastner, and M.G. Bawendi, *J. Appl. Phys.* **92**, 7498 (2002).

[14] Z.C. Holman and U.R. Kortshagen, *Langmuir* **25**, 11883 (2009).

[15] F.J. Hua, F. Erogbogbo, M.T. Swihart, and E. Ruckenstein, *Langmuir* **22**, 4363 (2006).

[16] T.J. Krinke, H. Fissan, K. Deppert, M.H. Magnusson, and L. Samuelson, *Appl. Phys. Lett.* **78**, 3708 (2001).

[17] H.O. Jacobs, S.A. Campbell, and M.G. Steward, *Adv. Mater.* **14**, 1553 (2002).

[18] C.R. Barry, J. Gu, and H.O. Jacobs, *Nano Lett.* **5**, 2078 (2005).

[19] J.J. Cole, E.C. Lin, C.R. Barry, and H.O. Jacobs, *Appl. Phys. Lett.* **95**, 113101 (2009).

[20] F. Otten, U. Auer, F.E. Kruis, W. Prost, F.J. Tegude, and H. Fissan, *Mater. Sci. Technol.* **18**, 717 (2002).

[21] S.L. Girshick, *J. Nanopart. Res.* **10**, 935 (2008).

[22] C. Huang, W.T. Nichols, D.T. O'brien, M.F. Becker, D. Kovar, and J.W. Keto, *J. Appl. Phys.* **101**, 064902 (2007).

[23] J.F. Delamora and A. Schmidtott, *J. Aerosol Sci.* **24**, 409 (1993).

[24] S. Ude and J.F. De La Mora, *J. Aerosol Sci.* **34**, 1245 (2003).

[25] N.P. Rao, N. Tymiak, J. Blum, A. Neuman, H.J. Lee, S.L. Girshick, P.H. Mcmurry, and J. Heberlein, *J. Aerosol Sci.* **29**, 707 (1998).

[26] P. Milani, P. Piseri, E. Barborini, A. Podesta, and C. Lenardi, *J. Vac. Sci. Technol., A* **19**, 2025 (2001).

[27] F. Di Fonzo, A. Gidwani, M.H. Fan, D. Neumann, D.I. Iordanoglou, J.V.R. Heberlein, P.H. Mcmurry, S.L. Girshick, N. Tymiak, W.W. Gerberich, and N.P. Rao, *Appl. Phys. Lett.* **77**, 910 (2000).

[28] B.J. Jurcik, J.R. Brock, and I. Trachtenberg, *J. Aerosol Sci.* **20**, 701 (1989).

[29] J.F. Delamora, S.V. Hering, N. Rao, and P.H. Mcmurry, *J. Aerosol Sci.* **21**, 169 (1990).

[30] P.S. Chang, J.R. Brock, and I. Trachtenberg, *J. Aerosol Sci.* **24**, 31 (1993).

[31] C. Raju and J. Kurian, *Vacuum* **46**, 389 (1995).

[32] M. Sulkes, C. Jouvet, and S.A. Rice, *Chem. Phys. Lett.* **87**, 515 (1982).

[33] A.S. Shapiro, *The Dynamics and Thermodynamics of Compressible Fluid Flow* (Ronald Press, New York, 1957).

[34] G. Dupreyat and S.S. Fischer, *Rarefied Gas Dynamics, Part II* (AIAA, New York, 1981).

[35] P.S. Epstein, *Phys. Rev.* **23**, 710 (1924).

[36] S.K. Friedlander, *Smoke, Dust, and Haze*, 2nd ed (Oxford University Press, New York, 2000).

[37] D.L. Gilmore, R.C. Dykhuizen, R.A. Neiser, T.J. Roemer, and M.F. Smith, *J. Therm. Spray Technol.* **8**, 576 (1999).

[38] G. Bae, S. Kumar, S. Yoon, K. Kang, H. Na, H.J. Kim, and C. Lee, *Acta Mater.* **57**, 5654 (2009).

[39] A. Papyrin, V. Kosarev, S. Klinkov, A. Alkhimov, and V. Fomin, *Cold Spray Technology* (Elsevier, Amsterdam, 2007).

[40] J.L. Finney, *Proc. R. Soc. London, Ser. A* **319**, 479 (1970).

[41] P. Valentini and T. Dumitrica, *Phys. Rev. B* **75**, 224106 (2007).

[42] K.Y. Cheng, R. Anthony, U.R. Kortshagen, and R.J. Holmes, *Nano Lett.* **10**, 1154 (2010).

7

Quantum confinement in germanium nanocrystal thin films

7.1 Outline

Thin films of semiconductor nanocrystals that exhibit tunable optical properties are promising materials for new device applications, but progress has been slow for group IV materials. We report absorption measurements near the absorption edge of thin films of germanium nanocrystals synthesized in a plasma and impacted onto substrates. Bandgaps extracted from the absorption data vary from the near-bulk value of 0.73 eV for 9.0 nm nanocrystals to over 1.0 eV for 4.7 nm nanocrystals. These values are comparable to those reported for isolated, non-interacting germanium nanocrystals, indicating minimal loss of quantum confinement upon dense film formation.

7.2 Introduction

Semiconductor nanocrystals (NCs) in solution exhibit tunable optical properties due to quantum confinement.[1] Recent work in the II-VI and IV-VI NC communities has demonstrated that films assembled from colloidal nanocrystals approximately adopt the optical properties of their constituent particles.[1-3] Consequently, the absorption and photoluminescence spectra of the films can be varied by changing the NC size, effectively decoupling the films' optical properties from their other material properties. Nanocrystal thin films thus offer exciting new opportunities for applications in which optical constraints severely limit materials selection, such as solar cells, photodetectors, and light-emitting diodes.

Development of quantum confined films of group IV NCs such as Si and Ge has lagged behind that of other materials systems, in large part due to difficulties synthesizing NCs with narrow size and shape distributions and dispersing them into solution. The standard synthesis technique for II-VI and IV-VI NCs such as CdSe and PbTe produces colloidal solutions that provide a convenient starting point for film formation.[4] However, an analogous solution synthesis route does not exist for group VI materials because of their comparatively large crystallization temperatures.[5] Researchers have devised alternative synthesis methods and produced quantum confined Si and Ge NCs in solution,[6-11] but reports of films of NCs remain limited.

We previously reported the synthesis of high-quality Si[12] and Ge[13] NCs in powder-form using a nonthermal plasma apparatus. These NCs have been transferred into solution,[7,14] and cast as thin films.[14,15] We have also demonstrated an alternative

approach to NC thin film formation in which NCs are deposited via impaction directly downstream of the plasma.[16] In this chapter, we report quantum confinement in impacted films of Ge NCs, and investigate the dependence of the film bandgap on NC size. The impaction deposition method is unique in that NCs are deposited with the surface chemistry established in the plasma; there are no ligands on the NC surfaces since stabilization in solution is unnecessary. As a result, the measurements we report correspond to films of NCs that are in direct contact with each other and not separated by organic molecules.

7.3 Experimental

Germanium NCs were synthesized using a nonthermal flow-through plasma reactor described in detail elsewhere.[13] Briefly, in this approach germanium tetrachloride ($GeCl_4$), H_2, and Ar are passed through a quartz tube maintained between 1–10 Torr, around which electrodes are wrapped. A radio frequency power of ~100 W applied to the electrodes causes the precursors to dissociate and allows nanometer-sized Ge NCs to nucleate. The NCs are relatively monodisperse (standard deviations of 10–20% the mean size) and the mean size can be adjusted by changing the residence time of the NCs in the plasma.

Dense, uniform films of NCs were deposited by placing a slit-shaped orifice downstream of the plasma and translating glass substrates under the “curtain” of NCs emanating from the orifice.[16] The pressure downstream of the orifice was several times lower than the upstream pressure so that the gas flow was choked at the orifice and the

resulting supersonic gas jet accelerated the NCs towards the substrate. We demonstrated previously that films of Ge NCs with mean NC sizes of 4–14 nm and densities as large as 55% of the density of bulk Ge can be deposited in this manner.[16] For each NC size investigated, four films with thicknesses varying from 100 nm to 4 μm were deposited. Thicknesses were measured using scanning electron microscopy and NC sizes were determined from Debye-Scherrer fits of X-ray diffraction spectra. Figure 7-1 displays representative images of the Ge NCs and films.

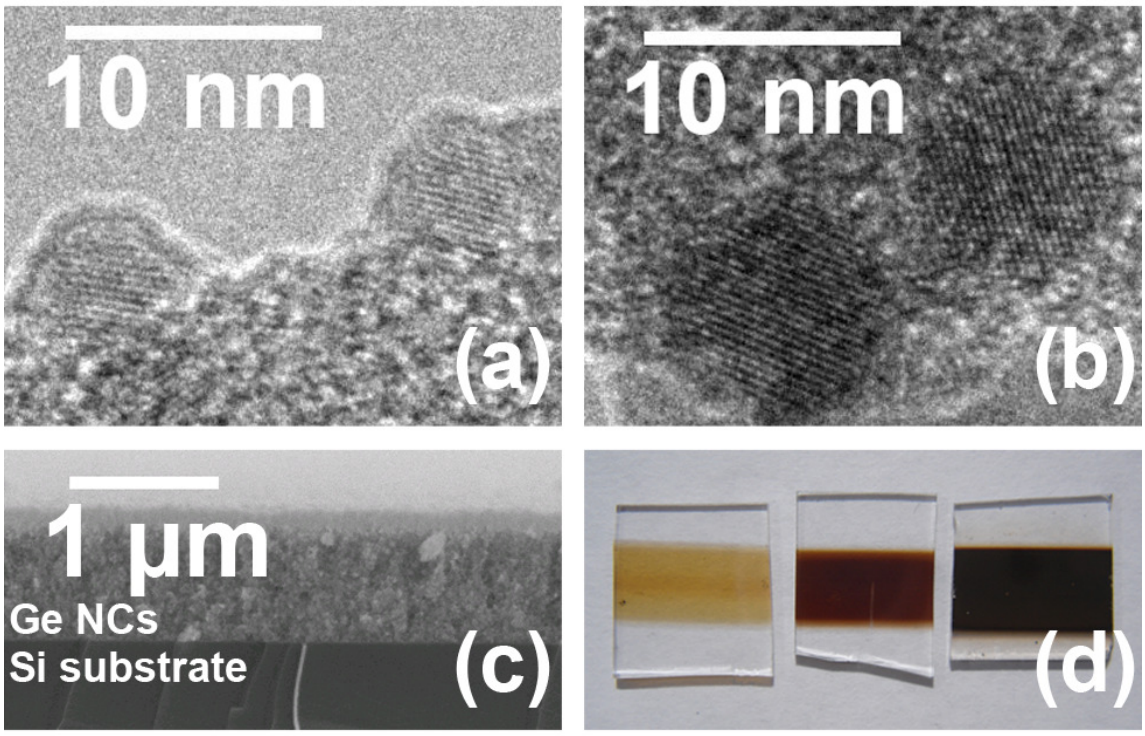

Figure 7-1. Transmission electron micrographs of (a) 4 nm and (b) 9 nm Ge NCs synthesized in the plasma. (c) Scanning electron micrograph of a 1 μm thick Ge NC film cross-section, showing the thickness uniformity obtained. (d) Photograph of three Ge NC films of various thicknesses impacted on glass substrates.

The easiest way to study the optical properties of Ge NC films is to measure the peak photoluminescence (PL) wavelength. However, while visible PL believed to be caused by oxide states is commonly observed,[17] only two groups have reported infrared PL that likely comes from the NC core.[8,18] We do not see PL from our Ge NCs and instead performed absorption measurements on each film using a Cary UV-Vis-NIR spectrophotometer. Refractive indices were determined from interference fringes in the absorption spectra at long wavelengths and the measured film thicknesses. The refractive indices of the films depend on their densities and are not equal to that of bulk Ge since they are not fully dense. It is noteworthy that interference fringes are only obtainable for films that are uniform in thickness over the spot size of the incident beam (several mm diameter), which is testimony to the uniformity of the films. For a few samples, film densities were measured using Rutherford backscattering (see ref. [16]) and refractive indices were calculated with an alternative technique using the Lorentz-Lorentz expression.[19] These values were within 10% of those determined from interference fringes. We assumed for simplicity that the calculated refractive indices were dispersion-free; the refractive index of bulk Ge varies by only 15% across the energies of interest (0.5–1.5 eV),[20] and we expect that the dispersion in the films is similar.

7.4 Results and discussion

Absorption coefficients α were calculated for each film at each measured wavelength using the method described by Essick and Mather.[21] The absorption coefficients of films of various thicknesses containing Ge NCs of the same size were then

overlaid. It is necessary to compile data from films of several thicknesses since any single film only gives meaningful absorption data for the range of wavelengths for which the absorbance is between roughly 0.1 and 2, and that wavelength range depends on film thickness. Data points for which the absorbance fell outside of the above range were discarded. Absorption coefficients for bulk Ge[20] and films of Ge NCs 3.9–9.1 nm in diameter are plotted in Fig. 7-2a. The features clearly blue-shift with decreasing NC size, indicating that the NCs retain (at least some) quantum confinement after film deposition. The absorption coefficient at each wavelength is smaller in magnitude for the Ge NC films than for bulk Ge. This occurs both because the NC film spectra are shifted to higher energy and because the films are less dense than bulk Ge. The density of the NC films in this study varied from 20-50% of the density of bulk Ge, with films of smaller NCs being denser.

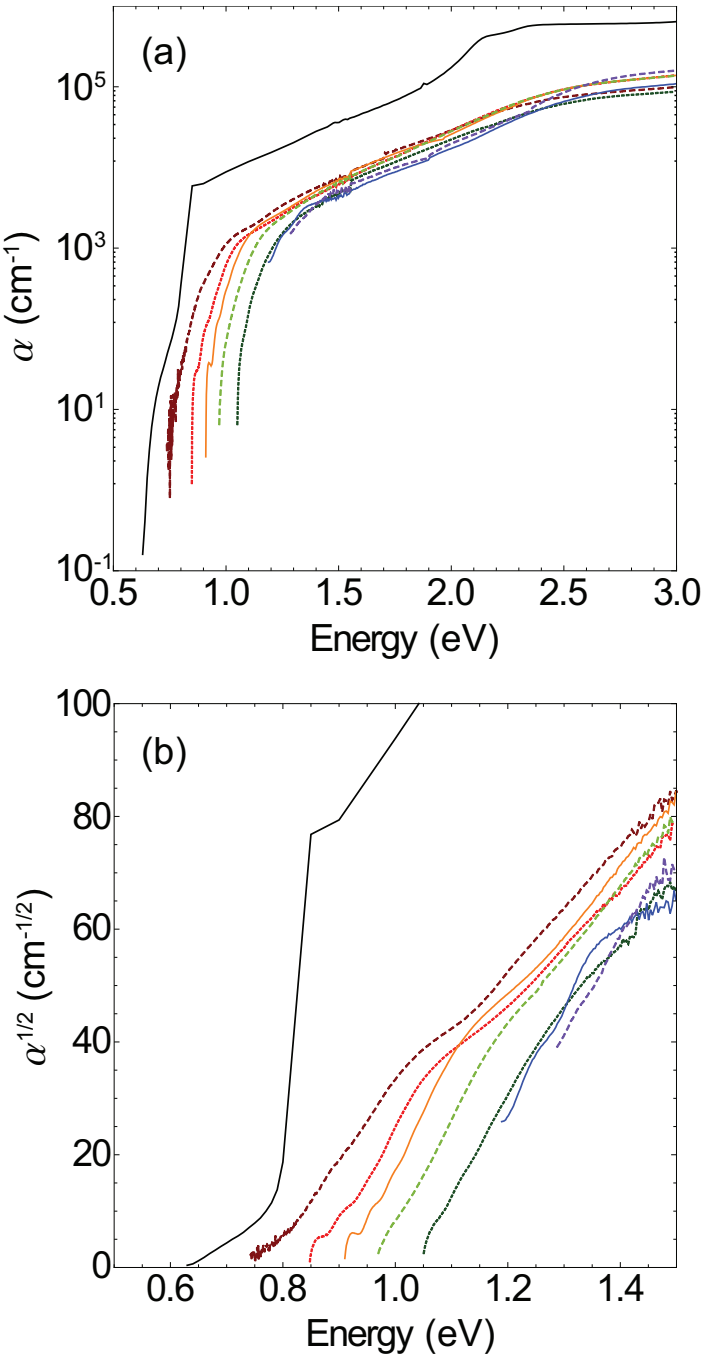

Figure 7-2. a) Absorption coefficient and b) square-root of the absorption coefficient of bulk Ge and Ge NC films. Plotted from left to right are bulk Ge taken from ref. [20] (black, solid) and films of Ge NCs 9.1 nm (maroon, dashed), 7.0 nm (red, dotted), 6.2 nm (orange, solid), 5.5 nm (light green, dashed), 4.7 nm (dark green, dotted), 4.4 nm (blue, solid), and 3.9 nm (purple, dashed) in diameter. The noise in the data near 1.5 eV arises from a detector change in the spectrometer.

In Fig. 7-2b, the square root of the absorption coefficient $\alpha^{1/2}$ is shown. For the bulk Ge spectrum, absorption at the indirect bandgap can be seen as a linear "foot" below 0.8 eV. The film of 9.1 nm Ge NCs displays this same feature indicating that an indirect gap still exists for NCs of this size. Unfortunately, our data is too noisy near the band edge absorption of the other films to determine if the gap becomes direct for the smallest NCs, as has been proposed.[22] For the 4.4 and 3.9 nm samples, we were not able to deposit sufficiently thick crack-free films to accurately measure absorption near the band edge, but absorption in these films is shifted to even higher energy.

For indirect gap materials, the optical bandgap is given by the *x*-intercept of $\alpha^{1/2}$ to within a phonon energy. Neglecting the contributions of (relatively low-energy) phonons, approximate optical bandgaps E_g were extracted from the absorption data and are shown in Fig. 7-3 (filled black circles) as a function of NC size. The bandgap of Ge NC films can be varied from bulk-like values for large NCs to over 1 eV for 4.7 nm NCs. Consistent with the large Bohr exciton radius of Ge (24.3 nm),[23] films of Ge NCs as large as 9.1 nm exhibit confinement-induced bandgap widening.

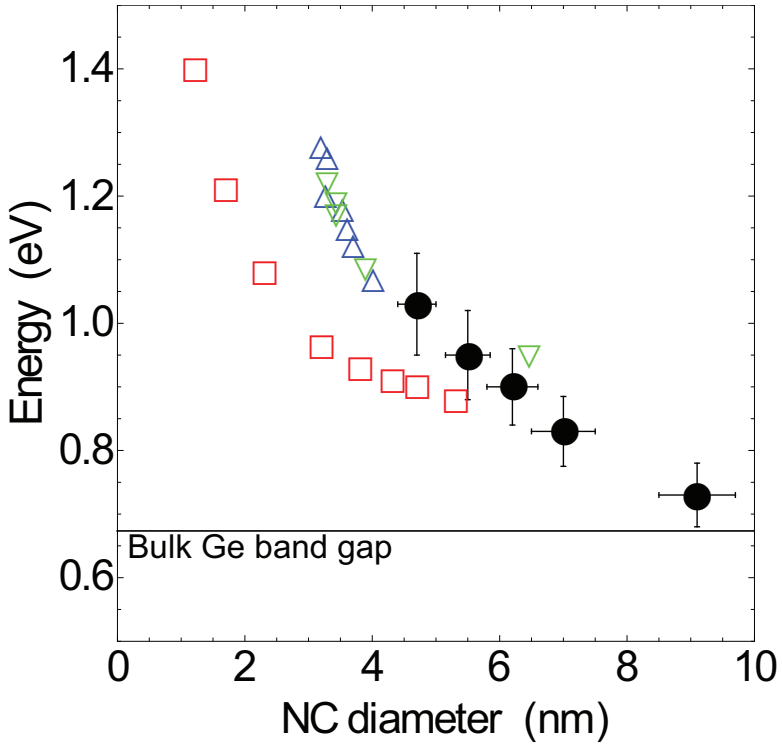

Figure 7-3. Approximate optical bandgap extracted from absorption measurements of Ge NC films as a function of constituent NC size (filled black circles). Digitized data points from ref. [8] for the PL peak (empty blue triangles) and absorption onset (empty, inverted green triangles) of functionalized Ge NCs in solution are plotted as empty blue triangles and empty, inverted green triangles, respectively. Digitized data points from ref. [18] for the PL peak of Ge NCs embedded in SiO_2 are plotted as empty red squares.

Also plotted in Fig. 7-3 are data recorded by Lee et al. for the infrared PL peak and absorption onset of functionalized Ge NCs in solution,[8] and data recorded by Takeoka et al. for the infrared PL peak of Ge NCs embedded in SiO_2.[18] These data represent the approximate optical bandgaps of *isolated, non-interacting* Ge NCs in solvent and oxide host matrices. While there is little overlap in the ranges of NC sizes studied, our data falls between that of Lee et al. and Takeoka et al. This suggests that there is minimal loss of quantum confinement as isolated Ge NCs are brought into contact with one another during the deposition of dense films. For other NC material

systems (e.g., CdSe, PbS), a small red-shift in the peak PL wavelength is commonly reported after film casting and is attributed to exciton transfer from smaller NCs to neighboring larger NCs.[1]

Bulk Ge's large mobilities make it attractive for device applications, but its use is limited by its poor quality oxide and small bandgap. We have demonstrated that the latter obstacle can be overcome by depositing films of NCs, and the bandgap can be tuned smoothly up to greater than 1 eV by changing the NC size. Germanium NC films with tunable absorption (and, ideally, tunable and efficient emission) are of particular interest for infrared detectors and solar cells. However, NC films bring with them new properties—including a dramatically increased number of surface states—which may hinder charge carrier transport and reduce the mobility to unacceptable levels.

Two-probe current-voltage measurements reveal that as-deposited dense films of Ge NCs have dark conductivities on the order of 10^{-7} S/cm and conductivities an order of magnitude higher under solar-simulating light. This is small, but not insignificant. In nearly all other reports, NC films are insulating as-deposited due to the bulky ligands required for colloidal stability, and chemical treatments are required before semiconductor behavior is observed.[14,24-27] We have also fabricated Ge NC field-effect transistors like those reported in Chapter 5 (ref. [15]) using impacted films of 4.3 nm NCs, and found that the devices become *n*-type with electron mobilities as large as 10^{-3} cm^2/Vs after annealing at 300 °C. Additional research is necessary to understand and control the surfaces of the NCs in order to further increase the mobility.

7.5 Conclusions

In summary, we have demonstrated that quantum confinement is retained in Ge NCs after deposition of NC thin films. Plasma-synthesized Ge NCs were impacted onto substrates to form thin films in which the NCs were in direct contact. The absorption spectra of the films blue-shift with decreasing NC size, indicating that the optical properties of the films are similar to the properties of the individual NCs of which they are composed. The bandgap can be smoothly tuned from the bulk value of 0.67 eV to over 1 eV for 4.7 nm Ge NCs. Electronic transport through the films was possible, even for films of small NCs that displayed the strongest confinement.

7.6 Future work

The quest for NC films that both display both quantum confinement and behave electronically like semiconductors is a recurring theme in this thesis. While as-deposited impacted Ge NC films have tunable bandgaps and non-zero electrical conductivities, they do not exhibit gating in FETs until they are annealed above 200 °C (Fig. 7-4). No sintering occurs at such low temperatures, but we have not yet verified that the onset of FET performance after annealing is not accompanied by a loss of quantum confinement caused by changes at the NC surfaces. An interesting study would be to measure the absorption of films of various sizes of Ge NCs as a function of annealing temperature up to 700 °C, and correlate the changes with chemical and structural transformations in the films.

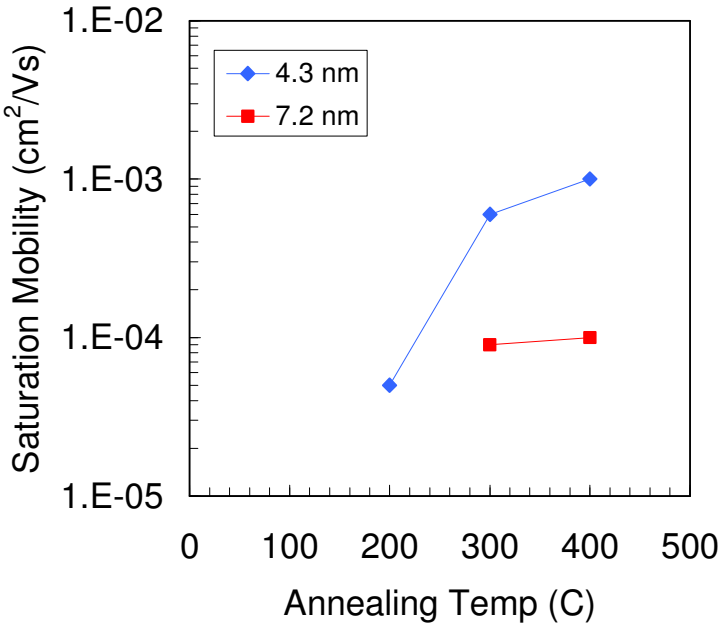

Figure 7-4. Field-effect saturation mobility of electrons in impacted films of 4.3 and 7.2 nm Ge NCs annealed up to 400 °C in the glove box on a hot plate. No gating is seen for unannealed films, and the trend with temperature is the same as for Ge NC films spun from DCB.

An alternative approach is to try to find conditions for which impacted Ge NC films are gate-sensitive and have large mobilities without annealing. We have performed preliminary two-probe conductivity measurements on as-deposited impacted Ge NC films synthesized with varying plasma power (Fig. 7-5), gas composition (Fig. 7-6), and film density (Fig. 7-7). Some of the behavior observed was expected (dense Ge NC films are more conductive than fluffy films) and some was surprising (films of crystalline NCs conduct better than films or amorphous NCs in the light, but worse in the dark). Further studies to understand and improve these results, as well as to test the films' performance in the more informative FET structure are important.

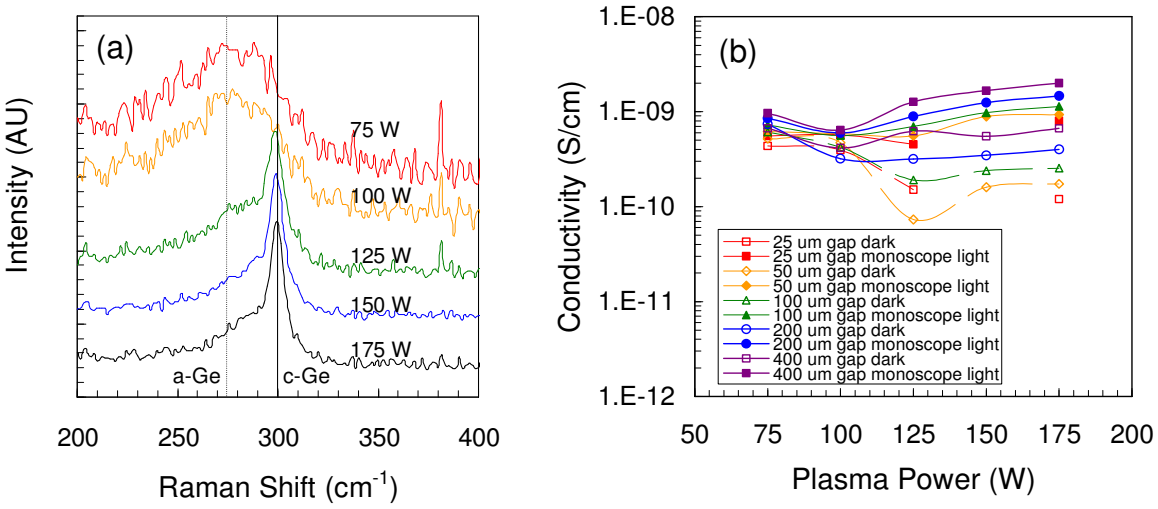

Figure 7-5. (a) Normalized, offset Raman spectra of Ge NCs synthesized with 75-175 W showing the transition from amorphous to crystalline at ~125 W, and (b) conductivities of Ge NC films synthesized using the same powers as in (a). Data points for several electrode spacings (25–400 µm) are plotted, and the samples were measured both in the dark and under a monoscope light.

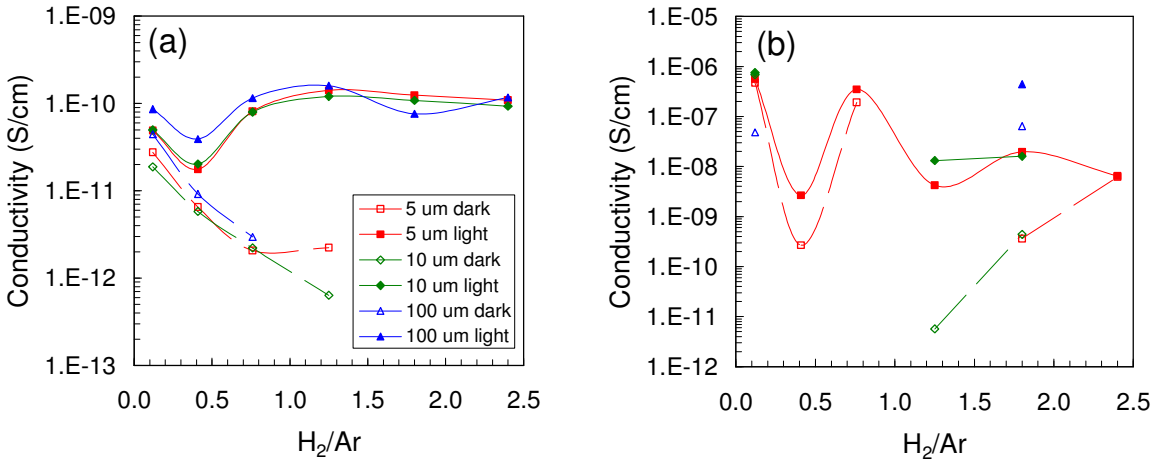

Figure 7-6. (a) Conductivites of Ge NC films deposited with H_2/Ar flow rate ratio ranging from 0.1–2.4. Measurements were taken air-free in a glove box in the dark and under a monoscope light. While the light conductivity remains roughly constant, the dark conductivity falls with increasing hydrogen coverage. (b) The same films measured in air, showing erratic behavior.

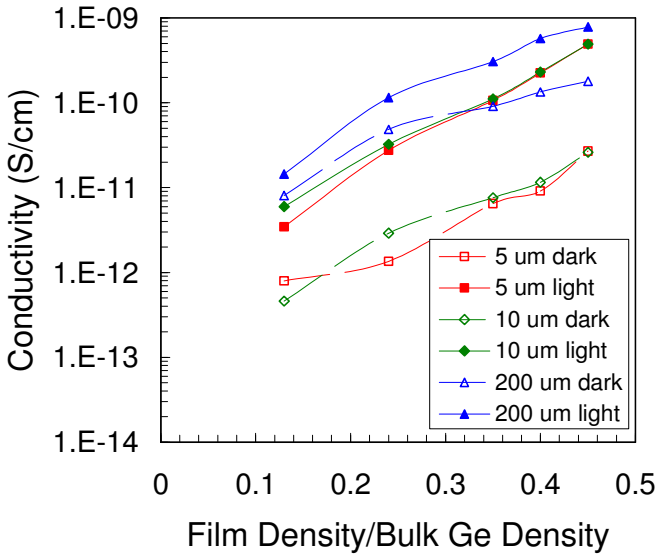

Figure 7-7. Conductivites of Ge NC films with densities of 0.14–0.45 the density of bulk Ge, measured across three electrode gaps both in the dark and under a monoscope light.

Finally, determining the absolute position of the conduction and valence band edges of Ge NC films would be of both fundamental interest and practical use. The bandgap evolution with NC size in itself does not allow device engineers to design junctions between two materials; the band edge energies must be known. For the more popular Si NC system it has been reported that the valence band shift is twice that of the conduction band shift,[28] and approximate band edge positions can be determined from the quantum confined bandgap using this empirical trend. A similar rule of thumb does not yet exist for Ge NCs, although Bostedt et al. have measured the conduction band edge shift of Ge NCs using synchrotron radiation X-ray absorption spectroscopy (XAS).[29] The Ge NCs used in this study were sufficiently different from our Ge NCs that the results are not necessarily applicable to our Ge NC films. We previously initiated

collaboration with the group at Lawrence Livermore National Laboratory that performs XAS measurements, and it would be beneficial to send them more samples.

7.7 References

[1] C.B. Murray, C.R. Kagan, and M.G. Bawendi, *Annu. Rev. Mater. Sci.* **30**, 545 (2000).

[2] C.B. Murray, C.R. Kagan, and M.G. Bawendi, *Science* **270**, 1335 (1995).

[3] J.J. Urban, D.V. Talapin, E.V. Shevchenko, and C.B. Murray, *J. Am. Chem. Soc.* **128**, 3248 (2006).

[4] C.B. Murray, D.J. Norris, and M.G. Bawendi, *J. Am. Chem. Soc.* **115**, 8706 (1993).

[5] J.R. Heath and J.J. Shiang, *Chem. Soc. Rev.* **27**, 65 (1998).

[6] J.D. Holmes, K.J. Ziegler, R.C. Doty, L.E. Pell, K.P. Johnston, and B.A. Korgel, *J. Am. Chem. Soc.* **123**, 3743 (2001).

[7] D. Jurbergs, E. Rogojina, L. Mangolini, and U. Kortshagen, *Appl. Phys. Lett.* **88**, 233116 (2006).

[8] D.C. Lee, J.M. Pietryga, I. Robel, D.J. Werder, R.D. Schaller, and V.I. Klimov, *J. Am. Chem. Soc.* **131**, 3436 (2009).

[9] S. Sato and M.T. Swihart, *Chem. Mater.* **18**, 4083 (2006).

[10] B.R. Taylor, S.M. Kauzlarich, G.R. Delgado, and H.W.H. Lee, *Chem. Mater.* **11**, 2493 (1999).

[11] J.P. Wilcoxon, P.P. Provencio, and G.A. Samara, *Phys. Rev. B* **64**, 035417 (2001).

[12] L. Mangolini, E. Thimsen, and U. Kortshagen, *Nano Lett.* **5**, 655 (2005).

[13] R. Gresback, Z. Holman, and U. Kortshagen, *Appl. Phys. Lett.* **91**, 093119 (2007).

[14] Z.C. Holman and U.R. Kortshagen, *Langmuir* **25**, 11883 (2009).

[15] Z.C. Holman, C.-Y. Liu, and U.R. Kortshagen, *Nano Lett.* **10**, 2661 (2010).

[16] Z.C. Holman and U.R. Kortshagen, *Nanotechnology* **21**, 335302 (2010).

[17] M. Zacharias and P.M. Fauchet, *Appl. Phys. Lett.* **71**, 380 (1997).

[18] S. Takeoka, M. Fujii, S. Hayashi, and K. Yamamoto, *Phys. Rev. B* **58**, 7921 (1998).

[19] A. Feldman, E.N. Farabaugh, W.K. Haller, D.M. Sanders, and R.A. Stempniak, *J. Vac. Sci. Technol., A* **4**, 2969 (1986).

[20] S. Adachi, *Optical Constants of Crystalline and Amorphous Semiconductors: Numerical Data and Graphical Information* (Springer, 1999).

[21] J.M. Essick and R.T. Mather, *Am. J. Phys.* **61**, 646 (1993).

[22] T. Takagahara and K. Takeda, *Phys. Rev. B* **46**, 15578 (1992).

[23] Y. Maeda, N. Tsukamoto, Y. Yazawa, Y. Kanemitsu, and Y. Masumoto, *Appl. Phys. Lett.* **59**, 3168 (1991).

[24] M. Drndic, M.V. Jarosz, N.Y. Morgan, M.A. Kastner, and M.G. Bawendi, *J. Appl. Phys.* **92**, 7498 (2002).

[25] M. Law, J.M. Luther, O. Song, B.K. Hughes, C.L. Perkins, and A.J. Nozik, *J. Am. Chem. Soc.* **130**, 5974 (2008).

[26] H.E. Romero and M. Drndic, *Phys. Rev. Lett.* **95**, 156801 (2005).

[27] D.V. Talapin and C.B. Murray, *Science* **310**, 86 (2005).

[28] T. Van Buuren, L.N. Dinh, L.L. Chase, W.J. Siekhaus, and L.J. Terminello, *Phys. Rev. Lett.* **80**, 3803 (1998).

[29] C. Bostedt, T. Van Buuren, T.M. Willey, N. Franco, L.J. Terminello, C. Heske, and T. Moller, *Appl. Phys. Lett.* **84**, 4056 (2004).

8

Germanium nanocrystal solar cells

8.1 Outline

This chapter discusses our progress in fabricating photovoltaic devices based on thin films of germanium nanocrystals. Four device architectures were investigated, including Schottky junctions and heterojunctions with polymer, silicon nanocrystals, and silicon wafers. The best performance was observed from thin, as-deposited films of germanium nanocrystals on *p*-type silicon wafers. These devices had open-circuit voltages as large as 0.3 V and short-circuit currents of nearly 4 mA cm^{-2}. The nanocrystal/metal junctions were problematic in all devices, and more research is needed to understand these interfaces.

8.2 Introduction

Semiconductor nanocrystals (NCs) present both new opportunities and new challenges when incorporated into photovoltaic devices. Their tunable absorption, low-cost synthesis, and solution-processability promise a new paradigm in cheap multi-junction solar cells. However, the performance of high-efficiency solar cells currently on the market is limited by electron-hole recombination, primarily at interfaces. Nanocrystal films are full of interfaces—for 5 nm NCs, half of the atoms lie at the NC surface—threatening to severely restrict the performance of NC devices. The mobility of charge carriers in NC films is reduced compared to those in the bulk, further increasing the probability of recombination during diffusion to the electrodes. Finally, the stability of NC films in ambient conditions is a concern for nearly all materials systems.

Many properties of NC films pertinent to solar cell performance can be explored and improved by studying individual films on substrates. However, other processes and properties (e.g., exciton dissociation, open-circuit voltage) depend on the relationships *between* materials, and photovoltaic test devices must be constructed to understand them. Several device structures based on NC films are imaginable, including Schottky junctions, NC/NC *p-n* junctions or heterojunctions, and NC/polymer junctions. Examples from the literature of each of these architectures are given in Fig. 8-1.

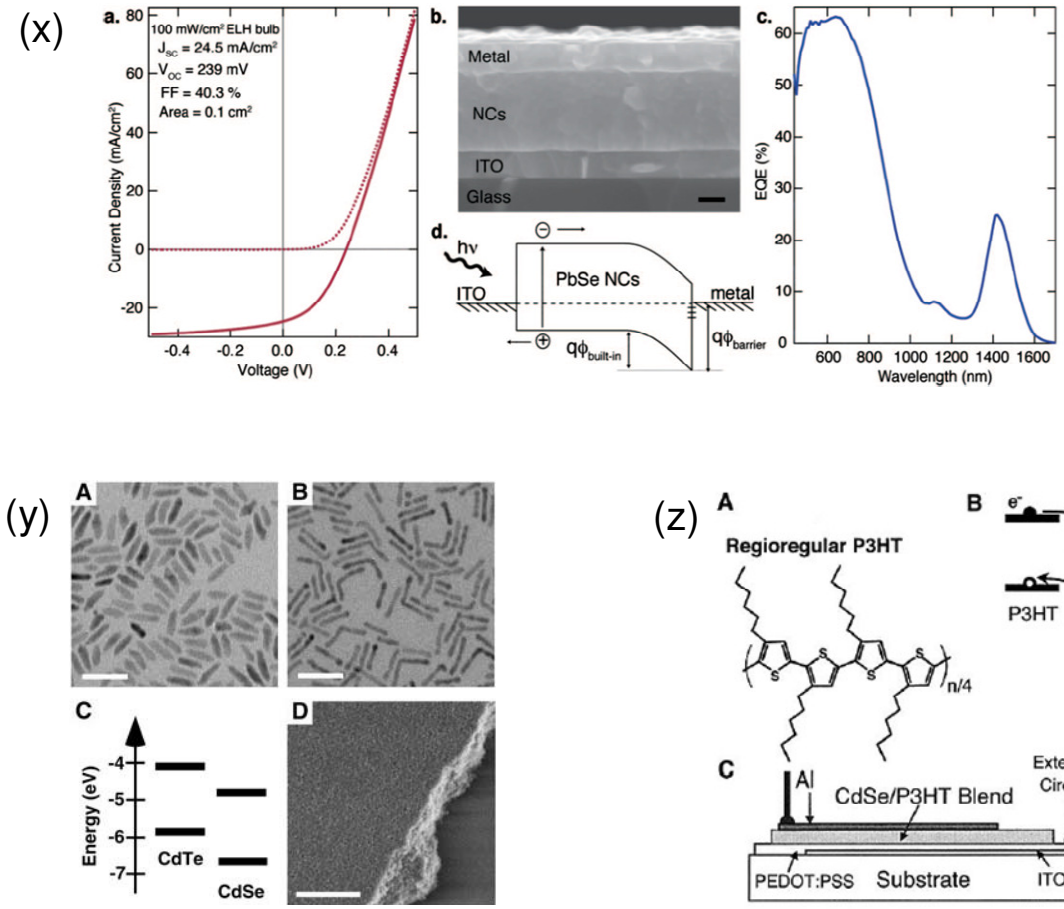

Figure 8-1. Examples of three solar cell architectures using NC thin films. (x) A PbSe NC Schottky device which is driven by the built-in field at the NC/metal junction. Adapted from [1]. (y) A solar cell based on a CdTe NC/CdSe NC heterojunction. Adapted from [2]. (z) A polymer/inorganic NC hybrid device using a blend of poly-3-hexylthiophene (P3HT) and CdSe NCs. Adapted from [3].

This chapter reports on solar cell structures that incorporate Ge NC films. The results are preliminary, incomplete, and rather unimpressive, as the large majority of research performed in completing this thesis was spent developing Ge NC films, and not solar cells using them. However, it is appropriate to disclose what little work has been done, as photovoltaic applications motivated much of this thesis and future students may use these findings as a starting point. Four device architectures are discussed: Ge NC

Schottky devices, and bilayer devices in which a junction is formed between a Ge NC film and poly-3-hexylthiophene (P3HT) polymer, Si NCs, or a Si wafer.

Schottky barriers are the simplest of photovoltaic devices since only a single semiconductor layer is required. There are only two junctions in a Schottky device (the electrode semiconductor interfaces), and one must be Ohmic while the other is blocking. The built-in field at the blocking or Schottky contact drives photogenerated carriers to their respective electrodes, and the voltage output of the device is given by the barrier height. Ideally, this height depends linearly on the metal work function with a slope of one, but this is often not seen experimentally because of Fermi-level pinning at interface states.[4] Such pinning occurs near the valence band of bulk Ge, resulting in Ohmic contacts (zero barrier height) in *p*-type Ge regardless of metal choice and Schottky barriers of nearly constant height in *n*-type Ge independent of electrode material.[5] The barrier heights associated with Ge NC (intrinsic, *p*-, or *n*-type)/metal junctions are not known. To this point in this thesis, the effects of contacts have been largely ignored. This is reasonable for devices for which the resistance of the film is large compared to the contact resistances (e.g., long channel FETs like those in Chapter 5). However, the geometry of thin film solar cells is such that contact effects may easily dominate device behavior (that is the goal in Schottky devices, in fact).

In a bilayer device, three junctions are present: one between the semiconductors, and one between each semiconductor and the closest electrode. The semiconductor/metal junctions should both be Ohmic, as the device is driven by the difference in the Fermi levels of the semiconductors. In a traditional *p*-*n* junction, free charge carriers diffuse

across the interface until the chemical potential is continuous at the interface, and in doing so create a built-in electric field. For many polymer and nanocrystals solar cells, it has been argued that a *p-n* junction is not formed due to a dearth of free charge carriers.[2,6] In these so-called excitonic solar cells, there remains a discontinuity in the chemical potential at the interface of the semiconductors, and excitons which diffuse to this interface are dissociated by the energetic gain that occurs when one carrier crosses the junction.

8.3 Experimental

Germanium and Si NCs were synthesized using a nonthermal plasma reactor discussed in detail in Chapter 2 and elsewhere.[6,7] For all devices except Ge NC/Si wafer devices, glass substrates with indium tin oxide (ITO) patterned electrodes were used. Nanocrystals were deposited either by spin-coating from 1,2-dichlorobenzene (DCB) solutions (as in Chapter 5) or by impaction (as in Chapter 6). For Ge NC/P3HT devices, P3HT films were spun from DCB prior to NC deposition, and a Poly(3,4- ethylenedioxy thiophene)/poly(styrenesulfonate) (PDOT:PSS) underlayer was spun before the P3HT. Gold or Al electrodes were evaporated on top of the films to complete the devices (shown schematically in Fig. 8-2).

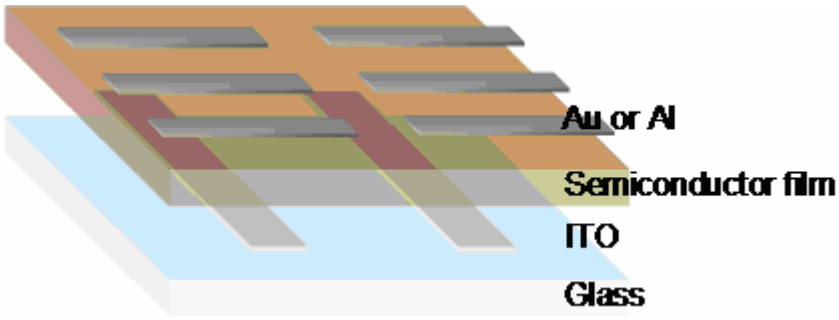

Figure 8-2. Schematic of devices deposited on ITO-coated glass

For Ge NC/Si wafer devices, heavily doped *p*-type Si wafer chips (SVM, Boron, 0.007-0.009 Ω cm) coated with a 300 nm thick thermal oxide were used as substrates. The oxide on the back of the wafers was removed and Al/Au back contacts were deposited via evaporation. The front of the wafers were patterned using conventional photolithography and the oxide was etched in buffer oxide etch (BOE) to expose 300 µm × 300 µm squares of the underlying wafer. The wafers were cut so that there was one exposed square per wafer chip, and the chips were then used as substrates with the exposed square serving as the device active area. Germanium NCs were impacted on the substrates and formed junctions with the wafer in the exposed areas (Fig. 8-3). Finally, Al or Au was evaporated on top in a comb pattern to form electrodes that both allowed 50% of the incident light to reach the device and collected at least some of the generated charge carriers (Fig. 8-4). Alternatively, 100 nm of ITO was sputtered on top of the films. For all devices, all steps were carried out air-free (including measurement) except when ITO had to be sputtered on top. Device performance was observed to be sensitive to air exposure and devices degraded over the course of minutes.

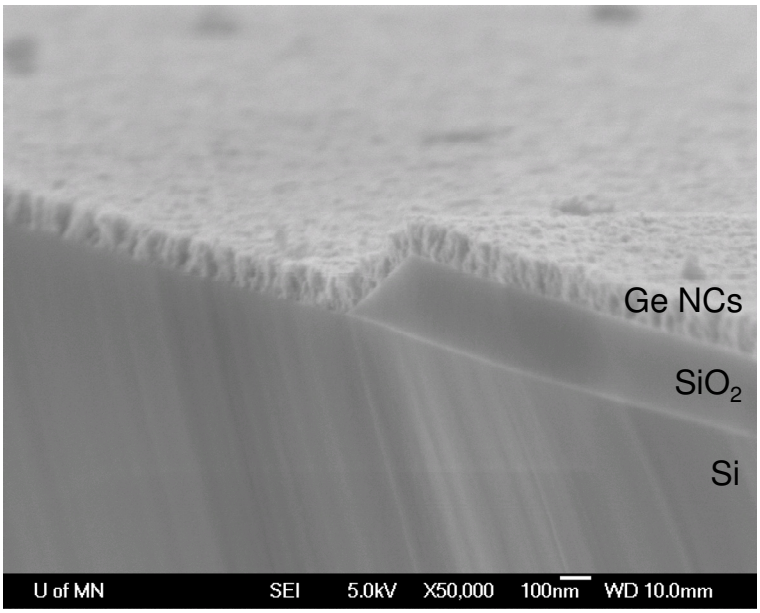

Figure 8-3. Cross-sectional SEM image of the edge of the active area of a Ge NC/Si wafer device prior to metallization. The Ge NC film was impacted and forms a junction with the wafer in the area where the oxide was etched. The sample is angled away from the viewer, giving the unusual perspective.

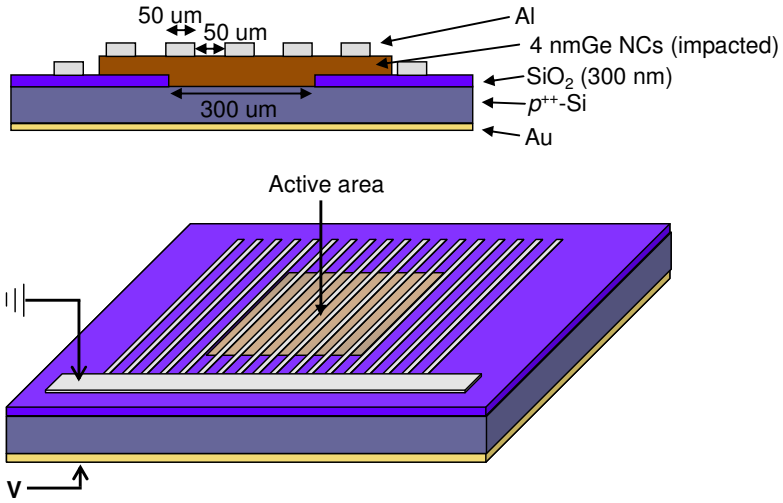

Figure 8-4. Schematic of Ge NC/Si wafer devices with an Al comb top electrode.

The electrical performance of solar cells was measured by recording current-voltage (I-V) characteristics both in the dark and under solar-simulating air mass (AM)

1.5 illumination. Devices were sealed in test boxes in N_2 ambient during measurement to prevent air exposure.

8.4 Results and discussion

Ge NC/metal Schottky barrier devices. We have made several attempts to fabricate Schottky solar cells using Ge NCs spin from DCB or deposited via impaction. Both Al and Au electrodes have been used (in addition to ITO), representing a wide range of metal work functions. Devices have been made using as-deposited NC films and films annealed up to 400 °C. Film thicknesses ranging from 20–2000 nm have been explored. In all cases, the devices either appear to short, or are resistive without any photovoltaic effect. A handful of devices were made using a lithium fluoride (LiF) buffer layer between the Ge NCs and the metal electrode. Other researchers have reported beneficial effects when LiF buffer layers are used in polymer solar cells,[8] and similar buffer layers have been used in PbSe NC solar cells.[9] These Ge NC devices behaved like solar cells, and the best device had an open-circuit voltage (V_{oc}) of 0.05 V and a short-circuit current (I_{sc}) of 0.15 mA cm^{-2}.

Ge NC/P3HT bilayer devices. Liu et al. recently demonstrated solar cells using blends of Si NCs and P3HT with efficiencies exceeding 1.1%.[10] These devices behaved like excitonic solar cells, with Si NCs taking the role of electron acceptor. We have fabricated similar devices using a bilayer structure with impacted Ge NCs. An energy diagram for this device is shown in Fig. 8-5a, and it is clear that there is no incentive for excitons to dissociate at the Ge NC/P3HT interface since it is energetically favorable for

both the electron and hole to transfer to (or remain in) the Ge NCs. The I-V curves (Fig. 8-5b) reflect this and show zero V_{oc}, although the devices are an order of magnitude more conductive under solar simulating light indicating that photogenerated carriers are extracted under applied bias. Identical devices made using impacted Si NCs in the place of Ge NCs perform much better (Fig. 8-6), reflecting the more favorable energy alignment of Si NCs with P3HT. A hybrid solar cell using Ge NCs should be possible using a hole-conducting polymer with a highest-occupied molecular orbital (HOMO) energy of approximately -4.7 eV.

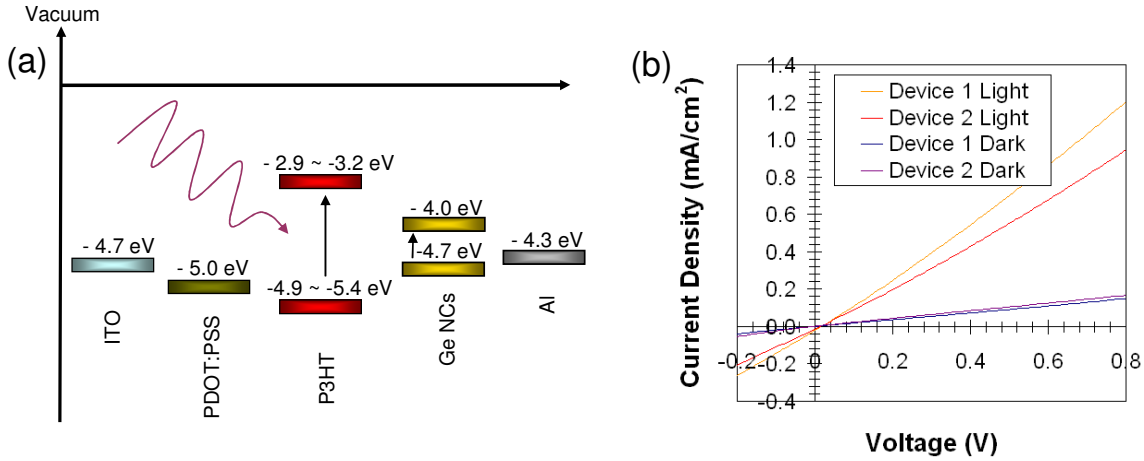

Figure 8-5. (a) Energy diagram of a Ge NC/P3HT bilayer solar cell (bulk values used for Ge) and (b) I-V characteristics for two devices measured in the dark and under AM 1.5 illumination.

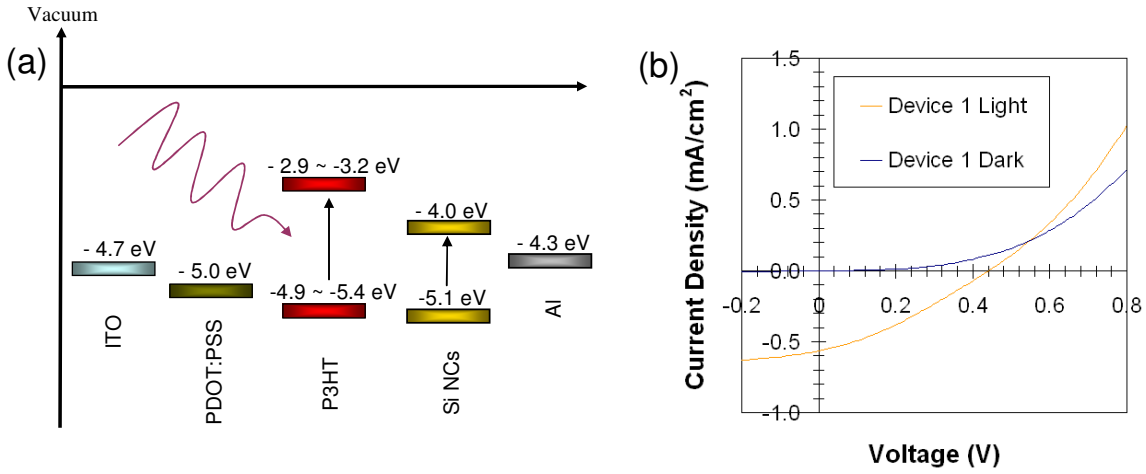

Figure 8-6. (a) Energy diagram of a Si NC/P3HT bilayer solar cell (bulk values used for Si) and (b) I-V characteristics for a device measured in the dark and under AM 1.5 illumination.

Ge NC/Si NC bilayer devices. A few devices were fabricated using bilayers of impacted Ge and Si NCs. Devices were made with the Si NCs on top of the Ge NCs, and with the reverse arrangement. Unfortunately, both of the devices with Ge NC films deposited first (on the ITO) shorted, perhaps due to pinholes in the films. The reverse arrangement, in which the Si NC film is deposited first, is less sensible from an energetic perspective since electrons and holes are usually collected at the Al and ITO electrodes, respectively, and the Si NC film should act as the electron acceptor (Fig. 8-7a). However, these devices exhibited V_{oc} = 0.2 V and I_{sc} = 0.01 mA cm^{-2} and had an incident photon-to-current conversion efficiency (IPCE) spectrum similar to the expected absorption from Si and Ge NC films (Figs. 8-7c and d). The devices functioned better as photodetectors than photovoltaic devices—Fig. 8.7e shows that the current in the device changed very rapidly by over three orders of magnitude when a constant bias was applied and a AM 1.5 light source was switched on or off.

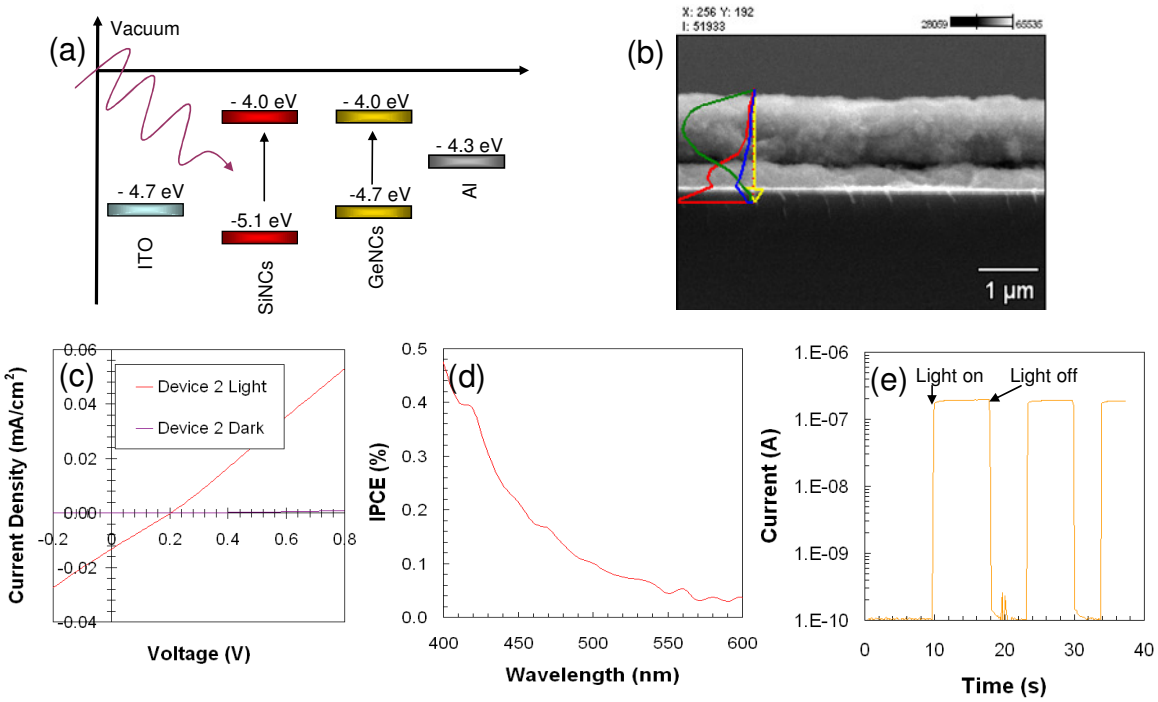

Figure 8-7. (a) Energy diagram of a Si NC/Ge NC bilayer solar cell (bulk values used for Si and Ge). (b) Cross sectional SEM image and energy dispersive spectroscopy line scan (green, red, and blue traces are for Ge, Si, and Sn, respectively), (c) I-V characteristic, (d) IPCE spectrum, and (e) current vs. time under constant bias and changing illumination for a device.

Ge NC/Si wafer junction devices. Germanium NC films were deposited onto *p*-type Si wafers either by impaction or by spin-coating from DCB to form bilayer solar cells. Because the wafers are heavily doped, the junction should be one-sided—the space charge width in the Si will be minimal while the width in the (nominally) intrinsic Ge NC film may well extend throughout the film. These devices are therefore more similar to Schottky junctions than donor-acceptor excitonic solar cells. The initial motivation was to form a *p*-*n* junction after annealing the films since our FET studies indicate that Ge NC films become *n*-type after annealing at 200–400 °C.

Aluminum, Au, and ITO (representing a wide range of work functions) were all tried as top contacts. The best results were obtained with ITO, although there was significant sample-to-sample variation in the performance. It is surprising that devices with Al or Au comb electrodes worked as well as they did, since only 50% of the incident light reached the semiconductor layers and carriers had to diffuse several microns to be collected at the front contact. Figure 8-8 displays I-V characteristics for unannealed devices with Al and ITO top electrodes. For the ITO device, V_{oc} = 0.25 V and I_{sc} = 3.9 mA cm^{-2}, a significant improvement over any previous devices. Control devices without Ge NC films did not exhibit photovoltaic behavior.

Interestingly, devices with Al contacts performed worse after annealing, with V_{oc} decreasing with temperature. Devices with ITO contacts were not annealed. Thin Ge NC films resulted in better devices than thicker films (I_{sc} decreases with thickness because the unannealed Ge NC films are resistive), and our best devices used Ge NC films approximately 100 nm thick. The shapes of the I-V characteristics for all devices are worrisome, with poor fill factors and a distinct reversal in curvature. This can be seen very clearly in the extreme case shown in Fig. 8-9a as the intensity of the incident light is varied. This "roll-over" effect has been observed by others for different material systems (e.g., CdTe) and is attributed to a Schottky junction at one of the contacts that results in back-to-back diodes.[11]

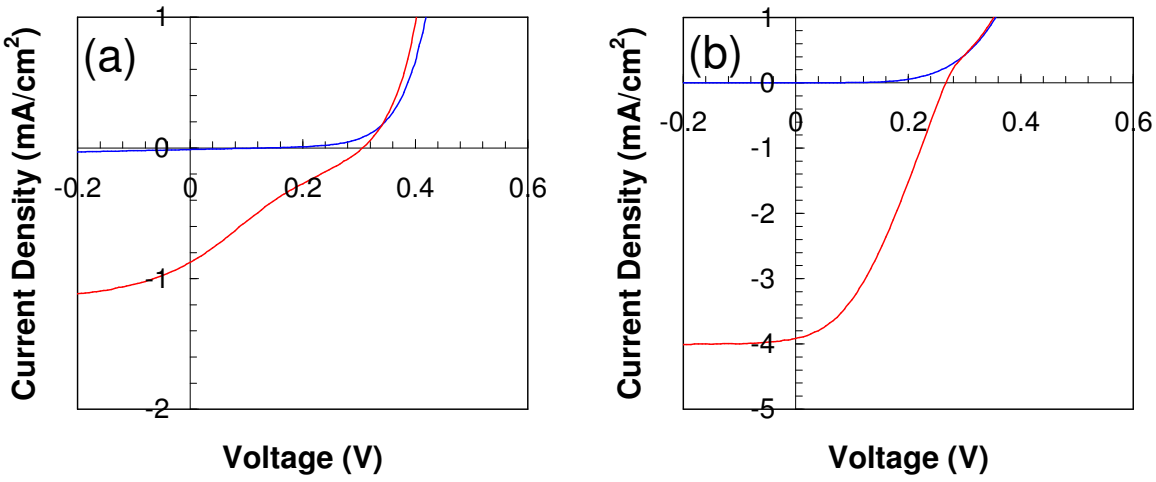

Figure 8-8. I-V characteristics in the dark (blue) and under AM 1.5 illumination (red) for as-deposited Ge NC/Si wafer bilayer solar cells with (a) Al comb and (b) ITO top contacts.

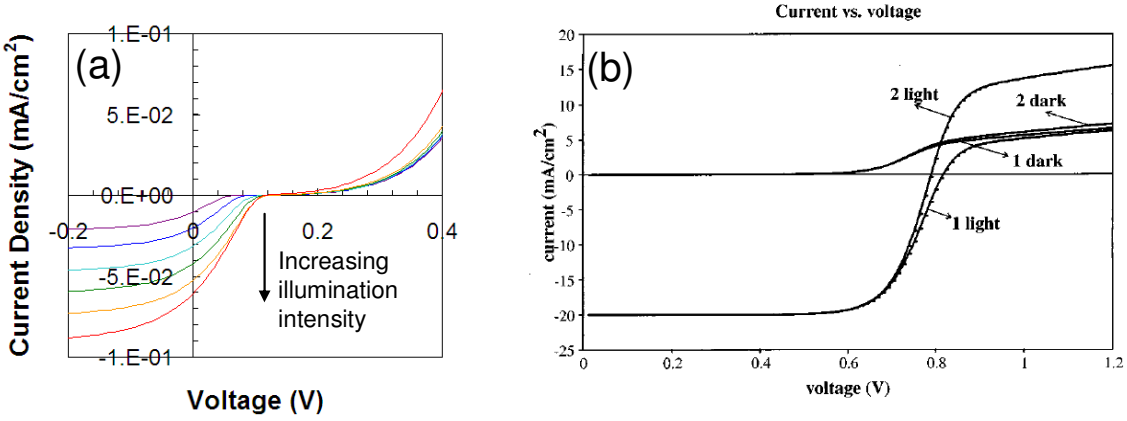

Figure 8-9. I-V characteristics showing roll-over in (a) Ge NC/Si wafer and (b) CdTe solar cells. Adapted from [11].

8.5 Conclusions

Several device structures employing Ge NC thin films were explored, including Schottky junctions and bilayer heterojunctions with P3HT and Si. Many of the devices

performed poorly, in part due to our inadequate understanding of Ge NC/metal junctions. The best devices, which were fabricated by impacting thin Ge NC films onto Si wafers and sputtering ITO on top, had V_{oc} = 0.25 V and I_{sc} = 3.9 mA cm^{-2}. We expect low V_{oc} from Ge NC solar due to the relatively small Ge bandgap, but 0.5 V or larger should be possible. The current is limited by poor carrier conduction in as-deposited films, but we have yet to fabricate better devices using annealed films.

8.6 Future work

Schottky barrier solar cells with 2.1% power conversion efficiency have been reported using PbSe NC thin films,[1] even though these films have lower conductivities and mobilities than annealed Ge NC films. Consequently, there is reason to believe that Ge NC photovoltaics with modest efficiencies can be constructed *if* the interfaces are understood. We suggest that detailed studies be carried out to characterize Ge NC/metal junctions for a variety of metals before additional solar cells are constructed. The junctions of symmetric metal/Ge NC/metal devices can be characterized with I-V and capacitance-voltage (C-V) measurements. I-V measurements yield information about contact resistance (if various Ge NC thicknesses are used), as well as barrier height and diode ideality factor if the data is fit with a standard diode model. Junction capacitance, semiconductor doping concentration, and depletion width can be determined from C-V measurements. After Ge NC/metal junctions have been characterized for a range of metals, bilayer heterojunctions using Ge NCs and traditional semiconductors (like Si) should be considered again. Ultimately, Ge NC *p-n* homojunction are desired, but there

are many questions to answer before these are realizable. These include: Can Ge NC films be controllably doped *p*- and *n*-type with post-deposition surface treatments, or must they be doped during synthesis? And, are there sufficient free carriers in Ge NCs to diffuse across a junction, or will there be an abrupt change in chemical potential at the interface?

8.7 References

[1] J.M. Luther, M. Law, M.C. Beard, Q. Song, M.O. Reese, R.J. Ellingson, and A.J. Nozik, *Nano Lett.* **8**, 3488 (2008).

[2] I. Gur, N.A. Fromer, M.L. Geier, and A.P. Alivisatos, *Science* **310**, 462 (2005).

[3] W.U. Huynh, J.J. Dittmer, and A.P. Alivisatos, *Science* **295**, 2425 (2002).

[4] D.A. Neamen, *Semiconductor Physics and Deices*, 3rd ed (McGraw-Hill, 2003).

[5] A. Dimoulas, P. Tsipas, A. Sotiropoulos, and E.K. Evangelou, *Appl. Phys. Lett.* **89**, 252110 (2006).

[6] R. Gresback, Z. Holman, and U. Kortshagen, *Appl. Phys. Lett.* **91**, 093119 (2007).

[7] L. Mangolini, E. Thimsen, and U. Kortshagen, *Nano Lett.* **5**, 655 (2005).

[8] C.J. Brabec, S.E. Shaheen, C. Winder, N.S. Sariciftci, and P. Denk, *Appl. Phys. Lett.* **80**, 1288 (2002).

[9] K.S. Leschkies, T.J. Beatty, M.S. Kang, D.J. Norris, and E.S. Aydil, *Acs Nano* **3**, 3638 (2009).

[10] C.Y. Liu, Z.C. Holman, and U.R. Kortshagen, *Nano Lett.* **9**, 449 (2009).

[11] A. Niemegeers and M. Burgelman, *J. Appl. Phys.* **81**, 2881 (1997).

Bibliography

Adachi, S., *Optical Constants of Crystalline and Amorphous Semiconductors: Numerical Data and Graphical Information* (Springer, 1999).

Bae, G.; Kumar, S.; Yoon, S.; Kang, K.; Na, H.; Kim, H.J.; Lee, C. *Acta Mater.* **57**, 5654 (2009).

Barry, C.R.; Gu, J.; Jacobs, H.O. *Nano Lett.* **5**, 2078 (2005).

Bostedt, C.; Van Buuren, T.; Plitzko, J.M.; Moller, T.; Terminello, L.J. *J. Phys.: Condens. Matter* **15**, 1017 (2003).

Bostedt, C.; Van Buuren, T.; Willey, T.M.; Franco, N.; Terminello, L.J.; Heske, C.; Moller, T. *Appl. Phys. Lett.* **84**, 4056 (2004).

Bostedt, C.; Van Buuren, T.; Willey, T.M.; Terminello, L.J. *Appl. Phys. Lett.* **85**, 5334 (2004).

Brabec, C.J.; Shaheen, S.E.; Winder, C.; Sariciftci, N.S.; Denk, P. *Appl. Phys. Lett.* **80**, 1288 (2002).

Broqvist, P.; Alkauskas, A.; Pasquarello, A. *Phys. Rev. B* **78**, 075203 (2008).

Buriak, J.M. *Chem. Rev.* **102**, 1271 (2002).

Cardona, M. *Phys. Status Solidi B* **118**, 463 (1983).

Cernetti, P., Ph.D. Thesis, University of Minnesota, 2006.

Chang, P.S.; Brock, J.R.; Trachtenberg, I. *J. Aerosol Sci.* **24**, 31 (1993).

Cheng, K.Y.; Anthony, R.; Kortshagen, U.R.; Holmes, R.J. *Nano Lett.* **10**, 1154 (2010).

Chiu, H.W.; Kauzlarich, S.M. *Chem. Mater.* **18**, 1023 (2006).

Choi, K.; Buriak, J.M. *Langmuir* **16**, 7737 (2000).

Choi, W.K.; Chew, H.G.; Ho, V.; Ng, V.; Chim, W.K.; Ho, Y.W.; Ng, S.P. *J. Cryst. Growth* **288**, 79 (2006).

Christenson, H.K.; Horn, R.G. *Chem. Phys. Lett.* **98**, 45 (1983).

Clarke, E.N. *Phys. Rev.* **95**, 284 (1954).

Clarke, E.N. *Phys. Rev.* **91**, 756 (1953).

Clauws, P. *Mater. Sci. Eng., B* **36**, 213 (1996).

Cohen, M.L.; Chelikowsky, J.R., *Electronic Structure and Optical Properties of Semiconductors*, 2nd ed (Springer, New York, 1989).

Cole, J.J.; Lin, E.C.; Barry, C.R.; Jacobs, H.O. *Appl. Phys. Lett.* **95**, 113101 (2009).

Collier, C.P.; Saykally, R.J.; Shiang, J.J.; Henrichs, S.E.; Heath, J.R. *Science* **277**, 1978 (1997).

Collier, C.P.; Vossmeyer, T.; Heath, J.R. *Annu. Rev. Phys. Chem.* **49**, 371 (1998).

Cullis, A.G.; Canham, L.T. *Nature* **353**, 335 (1991).

Delamora, J.F.; Hering, S.V.; Rao, N.; Mcmurry, P.H. *J. Aerosol Sci.* **21**, 169 (1990).

Delamora, J.F.; Schmidtott, A. *J. Aerosol Sci.* **24**, 409 (1993).

Develyn, M.P.; Yang, Y.M.L.; Cohen, S.M. *J. Chem. Phys.* **101**, 2463 (1994).

Di Fonzo, F.; Gidwani, A.; Fan, M.H.; Neumann, D.; Iordanoglou, D.I.; Heberlein, J.V.R.; Mcmurry, P.H.; Girshick, S.L.; Tymiak, N.; Gerberich, W.W.; Rao, N.P. *Appl. Phys. Lett.* **77**, 910 (2000).

Dimoulas, A.; Tsipas, P.; Sotiropoulos, A.; Evangelou, E.K. *Appl. Phys. Lett.* **89**, 252110 (2006).

Drndic, M.; Jarosz, M.V.; Morgan, N.Y.; Kastner, M.A.; Bawendi, M.G. *J. Appl. Phys.* **92**, 7498 (2002).

Duan, X.F.; Niu, C.M.; Sahi, V.; Chen, J.; Parce, J.W.; Empedocles, S.; Goldman, J.L. *Nature* **425**, 274 (2003).

Dupreyat, G.; Fischer, S.S., *Rarefied Gas Dynamics, Part II* (AIAA, New York, 1981).

Epstein, P.S. *Phys. Rev.* **23**, 710 (1924).

Essick, J.M.; Mather, R.T. *Am. J. Phys.* **61**, 646 (1993).

Fang, C.J.; Gruntz, K.J.; Ley, L.; Cardona, M.; Demond, F.J.; Muller, G.; Kalbitzer, S. *J. Non-Cryst. Solids* **35-6**, 255 (1980).

Feldman, A.; Farabaugh, E.N.; Haller, W.K.; Sanders, D.M.; Stempniak, R.A. *J. Vac. Sci. Technol., A* **4**, 2969 (1986).

Finney, J.L. *Proc. R. Soc. London, Ser. A* **319**, 479 (1970).

Flowers, M.C.; Jonathan, N.B.H.; Liu, Y.; Morris, A. *J. Chem. Phys.* **99**, 7038 (1993).

Fok, E.; Shih, M.L.; Meldrum, A.; Veinot, J.G.C. *Chem. Commun.* **4**, 386 (2004).

Friedlander, S.K., *Smoke, Dust, and Haze*, 2nd ed (Oxford University Press, New York, 2000).

Fujii, M.; Hayashi, S.; Yamamoto, K. *Jpn. J. Appl. Phys., Part 1* **30**, 687 (1991).

Galli, F.; Kortshagen, U.R. *IEEE Trans. Plasma Sci.* **38**, 803 (2010).

Gatti, M.; Kortshagen, U. *Phys. Rev. E* **78**, 046402 (2008).

Gerion, D.; Zaitseva, N.; Saw, C.; Casula, M.F.; Fakra, S.; Van Buuren, T.; Galli, G. *Nano Lett.* **4**, 597 (2004).

Gilmore, D.L.; Dykhuizen, R.C.; Neiser, R.A.; Roemer, T.J.; Smith, M.F. *J. Therm. Spray Technol.* **8**, 576 (1999).

Girshick, S.L. *J. Nanopart. Res.* **10**, 935 (2008).

Goldemberg, J.; Johansson, T.B., *World Energy Assessment Overview: 2004 Update*, www.undp.org, (2004).

Goree, J. *Plasma Sources Sci. Technol.* **3**, 400 (1994).

Green, M.A.; Emery, K.; Hishikawa, Y.; Warta, W. *Prog. Photovoltaics* **16**, 61 (2008).

Gresback, R.; Holman, Z.; Kortshagen, U. *Appl. Phys. Lett.* **91**, 093119 (2007).

Greytak, A.B.; Lauhon, L.J.; Gudiksen, M.S.; Lieber, C.M. *Appl. Phys. Lett.* **84**, 4176 (2004).

Grosjean, C.C.; Devos, A. *J. Phys. D: Appl. Phys.* **14**, 883 (1981).

Gur, I.; Fromer, N.A.; Geier, M.L.; Alivisatos, A.P. *Science* **310**, 462 (2005).

Haller, E.G.; Hansen, W.L.; Goulding, F.S. *Adv. Phys.* **30**, 93 (1981).

Hanrath, T.; Korgel, B.A. *J. Am. Chem. Soc.* **126**, 15466 (2004).

Harting, M.; Zhang, J.; Gamota, D.R.; Britton, D.T. *Appl. Phys. Lett.* **94**, 193509 (2009).

Heath, J.R.; Shiang, J.J. *Chem. Soc. Rev.* **27**, 65 (1998).

Heath, J.R.; Shiang, J.J.; Alivisatos, A.P. *J. Chem. Phys.* **101**, 1607 (1994).

Hines, M.A.; Guyot-Sionnest, P. *J. Phys. Chem. B* **102**, 3655 (1998).

Hoffert, M.I.; Caldeira, K.; Jain, A.K.; Haites, E.F.; Harvey, L.D.D.; Potter, S.D.; Schlesinger, M.E.; Schneider, S.H.; Watts, R.G.; Wigley, T.M.L.; Wuebbles, D.J. *Nature* **395**, 881 (1998).

Holm, J.; Roberts, J.T. *J. Vac. Sci. Technol., A* **28**, 161 (2010).

Holm, J.; Roberts, J.T. *J. Phys. Chem. C* **113**, 15955 (2009).

Holm, J.; Roberts, J.T. *J. Am. Chem. Soc.* **129**, 2496 (2007).

Holm, J.; Roberts, J.T. *Langmuir* **23**, 11217 (2007).

Holman, Z.C.; Kortshagen, U.R. *in preparation.*

Holman, Z.C.; Kortshagen, U.R. *Langmuir* **25**, 11883 (2009).

Holman, Z.C.; Kortshagen, U.R. *Nanotechnology,* **21**, 335302 (2010).

Holman, Z.C.; Liu, C.-Y.; Kortshagen, U.R. *Nano Lett.* **10**, 2661 (2010).

Holmes, J.D.; Ziegler, K.J.; Doty, R.C.; Pell, L.E.; Johnston, K.P.; Korgel, B.A. *J. Am. Chem. Soc.* **123**, 3743 (2001).

Hua, F.J.; Erogbogbo, F.; Swihart, M.T.; Ruckenstein, E. *Langmuir* **22**, 4363 (2006).

Huang, C.; Nichols, W.T.; O'brien, D.T.; Becker, M.F.; Kovar, D.; Keto, J.W. *J. Appl. Phys.* **101**, 064902 (2007).

Huh, S.H.; Riu, D.H.; Naono, Y.; Taguchi, Y.; Kawabata, S.; Nakajima, A. *Appl. Phys. Lett.* **91**, 093118 (2007).

Huynh, W.U.; Dittmer, J.J.; Alivisatos, A.P. *Science* **295**, 2425 (2002).

Jacobs, H.O.; Campbell, S.A.; Steward, M.G. *Adv. Mater.* **14**, 1553 (2002).

Johnson, N.M.; Doland, C.; Ponce, F.; Walker, J.; Anderson, G. *Physica B* **170**, 3 (1991).

Johnson, O.H. *Chem. Rev.* **51**, 431 (1952).

Johnston, K.W.; Pattantyus-Abraham, A.G.; Clifford, J.P.; Myrskog, S.H.; Macneil, D.D.; Levina, L.; Sargent, E.H. *Appl. Phys. Lett.* **92**, 151115 (2008).

Jun, S.; Jang, E.J.; Park, J.; Kim, J. *Langmuir* **22**, 2407 (2006).

Jurbergs, D.; Rogojina, E.; Mangolini, L.; Kortshagen, U. *Appl. Phys. Lett.* **88**, 233116 (2006).

Jurcik, B.J.; Brock, J.R.; Trachtenberg, I. *J. Aerosol Sci.* **20**, 701 (1989).

Kartopu, G.; Bayliss, S.C.; Karavanskii, V.A.; Curry, R.J.; Turan, R.; Sapelkin, A.V. *J. Lumin.* **101**, 275 (2003).

Kim, W.J.; Kim, S.J.; Lee, K.S.; Samoc, M.; Cartwright, A.N.; Prasad, P.N. *Nano Lett.* **8**, 3262 (2008).

Kingston, R.H. *J. Appl. Phys.* **27**, 101 (1956).

Koleilat, G.I.; Levina, L.; Shukla, H.; Myrskog, S.H.; Hinds, S.; Pattantyus-Abraham, A.G.; Sargent, E.H. *ACS Nano* **2**, 833 (2008).

Kortshagen, U. *J. Phys. D: Appl. Phys.* **42**, 113001 (2009).

Kortshagen, U.; Bhandarkar, U. *Phys. Rev. E* **60**, 887 (1999).

Krinke, T.J.; Fissan, H.; Deppert, K.; Magnusson, M.H.; Samuelson, L. *Appl. Phys. Lett.* **78**, 3708 (2001).

Law, M.; Luther, J.M.; Song, O.; Hughes, B.K.; Perkins, C.L.; Nozik, A.J. *J. Am. Chem. Soc.* **130**, 5974 (2008).

Lee, D.C.; Pietryga, J.M.; Robel, I.; Werder, D.J.; Schaller, R.D.; Klimov, V.I. *J. Am. Chem. Soc.* **131**, 3436 (2009).

Leervad Pedersen, T.P.; Jensen, J.S.; Chevallier, J.; Hansen, O.; Jensen, J.M.; Nielsen, B.B.; Larsen, A.N. *Appl. Phys. A* **81**, 1591 (2005).

Leschkies, K.S.; Beatty, T.J.; Kang, M.S.; Norris, D.J.; Aydil, E.S. *Acs Nano* **3**, 3638 (2009).

Lewis, N.S. *MRS Bull.* **32**, 808 (2007).

Li, X.G.; He, Y.Q.; Talukdar, S.S.; Swihart, M.T. *Langmuir* **19**, 8490 (2003).

Liao, Y.C.; Roberts, J.T. *J. Am. Chem. Soc.* **128**, 9061 (2006).

Lie, L.H.; Duerdin, M.; Tuite, E.M.; Houlton, A.; Horrocks, B.R. *J. Electroanal. Chem.* **538**, 183 (2002).

Little, R.G.; Nowlan, M.J. *Prog. Photovoltaics* **5**, 309 (1997).

Liu, C.Y.; Holman, Z.C.; Kortshagen, U.R. *Nano Lett.* **9**, 449 (2009).

Lu, X.M.; Korgel, B.A.; Johnston, K.P. *Chem. Mater.* **17**, 6479 (2005).

Luther, J.M.; Law, M.; Beard, M.C.; Song, Q.; Reese, M.O.; Ellingson, R.J.; Nozik, A.J. *Nano Lett.* **8**, 3488 (2008).

Luther, J.M.; Law, M.; Song, Q.; Perkins, C.L.; Beard, M.C.; Nozik, A.J. *ACS Nano* **2**, 271 (2008).

Maeda, Y. *Phys. Rev. B* **51**, 1658 (1995).

Maeda, Y.; Tsukamoto, N.; Yazawa, Y.; Kanemitsu, Y.; Masumoto, Y. *Appl. Phys. Lett.* **59**, 3168 (1991).

Mangolini, L.; Kortshagen, U. *Adv. Mater.* **19**, 2513 (2007).

Mangolini, L.; Kortshagen, U. *Phys. Rev. E* **79**, 026405 (2009).

Mangolini, L.; Thimsen, E.; Kortshagen, U. *Nano Lett.* **5**, 655 (2005).

Martiradonna, L.; Stomeo, T.; De Giorgi, M.; Cingolani, R.; De Vittorio, M. *Microelectron. Eng.* **83**, 1478 (2006).

Matsoukas, T.; Russell, M. *J. Appl. Phys.* **77**, 4285 (1995).

Micic, O.I.; Ahrenkiel, S.P.; Bertram, D.; Nozik, A.J. *Appl. Phys. Lett.* **75**, 478 (1999).

Micic, O.I.; Sprague, J.R.; Curtis, C.J.; Jones, K.M.; Machol, J.L.; Nozik, A.J.; Giessen, H.; Fluegel, B.; Mohs, G.; Peyghambarian, N. *J. Phys. Chem.* **99**, 7754 (1995).

Milani, P.; Piseri, P.; Barborini, E.; Podesta, A.; Lenardi, C. *J. Vac. Sci. Technol., A* **19**, 2025 (2001).

Miyazaki, S.; Sakamoto, K.; Shiba, K.; Hirose, M. *Thin Solid Films* **255**, 99 (1995).

Mott, N.F., *Metal-Insulator Transitions* (Taylor & Francis, London, 1990).

Murphy, J.E.; Beard, M.C.; Norman, A.G.; Ahrenkiel, S.P.; Johnson, J.C.; Yu, P.R.; Micic, O.I.; Ellingson, R.J.; Nozik, A.J. *J. Am. Chem. Soc.* **128**, 3241 (2006).

Murray, C.B.; Kagan, C.R.; Bawendi, M.G. *Science* **270**, 1335 (1995).

Murray, C.B.; Kagan, C.R.; Bawendi, M.G. *Annu. Rev. Mater. Sci.* **30**, 545 (2000).

Murray, C.B.; Norris, D.J.; Bawendi, M.G. *J. Am. Chem. Soc.* **115**, 8706 (1993).

Murray, C.B.; Sun, S.H.; Gaschler, W.; Doyle, H.; Betley, T.A.; Kagan, C.R. *IBM J. Res. Dev.* **45**, 47 (2001).

Neamen, D.A., *Semiconductor Physics and Deices*, 3rd ed (McGraw-Hill, 2003).

Nesher, G.; Kronik, L.; Chelikowsky, J.R. *Phys. Rev. B* **71**, 035344 (2005).

Niemegeers, A.; Burgelman, M. *J. Appl. Phys.* **81**, 2881 (1997).

Nienow, A.M.; Roberts, J.T. *Chem. Mater.* **18**, 5571 (2006).

Oertel, D.C.; Bawendi, M.G.; Arango, A.C.; Bulovic, V. *Appl. Phys. Lett.* **87**, 213505 (2005).

Otten, F.; Auer, U.; Kruis, F.E.; Prost, W.; Tegude, F.J.; Fissan, H. *Mater. Sci. Technol.* **18**, 717 (2002).

Papyrin, A.; Kosarev, V.; Klinkov, S.; Alkhimov, A.; Fomin, V., *Cold Spray Technology* (Elsevier, Amsterdam, 2007).

Pi, X.D.; Gresback, R.; Liptak, R.W.; Campbell, S.A.; Kortshagen, U. *Appl. Phys. Lett.* **92**, 123102 (2008).

Poponi, D. *Sol. Energy* **74**, 331 (2003).

Poponi, D.; Byrne, J.; Hegedus, S. *Energy Studies Review* **14**, 104 (2006).

Raju, C.; Kurian, J. *Vacuum* **46**, 389 (1995).

Rao, N.P.; Tymiak, N.; Blum, J.; Neuman, A.; Lee, H.J.; Girshick, S.L.; Mcmurry, P.H.; Heberlein, J. *J. Aerosol Sci.* **29**, 707 (1998).

Remacle, F. *J. Phys. Chem. A* **104**, 4739 (2000).

Remacle, F.; Beverly, K.C.; Heath, J.R.; Levine, R.D. *J. Phys. Chem. B* **107**, 13892 (2003).

Ridley, B.A.; Nivi, B.; Jacobson, J.M. *Science* **286**, 746 (1999).

Rivillon, S.; Amy, F.; Chabal, Y.J.; Frank, M.M. *Appl. Phys. Lett.* **85**, 2583 (2004).

Rogol, M., in *Photon International*, January, 84 (2008).

Romero, H.E.; Drndic, M. *Phys. Rev. Lett.* **95**, 156801 (2005).

Sato, S.; Swihart, M.T. *Chem. Mater.* **18**, 4083 (2006).

Shapiro, A.S., *The Dynamics and Thermodynamics of Compressible Fluid Flow* (Ronald Press, New York, 1957).

Shimoda, T.; Matsuki, Y.; Furusawa, M.; Aoki, T.; Yudasaka, I.; Tanaka, H.; Iwasawa, H.; Wang, D.H.; Miyasaka, M.; Takeuchi, Y. *Nature* **440**, 783 (2006).

Shockley, W.; Queisser, H.J. *J. Appl. Phys.* **32**, 510 (1961).

Sinniah, K.; Sherman, M.G.; Lewis, L.B.; Weinberg, W.H.; Yates, J.T.; Janda, K.C. *J. Chem. Phys.* **92**, 5700 (1990).

Stoldt, C.R.; Haag, M.A.; Larsen, B.A. *Appl. Phys. Lett.* **93**, 043125 (2008).

Sulkes, M.; Jouvet, C.; Rice, S.A. *Chem. Phys. Lett.* **87**, 515 (1982).

Surek, T. *J. Cryst. Growth* **275**, 292 (2005).

Takagahara, T.; Takeda, K. *Phys. Rev. B* **46**, 15578 (1992).

Takeoka, S.; Fujii, M.; Hayashi, S.; Yamamoto, K. *Phys. Rev. B* **58**, 7921 (1998).

Talapin, D.V.; Murray, C.B. *Science* **310**, 86 (2005).

Taylor, B.R.; Kauzlarich, S.M.; Delgado, G.R.; Lee, H.W.H. *Chem. Mater.* **11**, 2493 (1999).

Taylor, B.R.; Kauzlarich, S.M.; Lee, H.W.H.; Delgado, G.R. *Chem. Mater.* **10**, 22 (1998).

Troost, D.; Koenders, L.; Fan, L.Y.; Monch, W. *J. Vac. Sci. Technol., B* **5**, 1119 (1987).

Tsipas, P.; Dimoulas, A. *Appl. Phys. Lett.* **94**, 012114 (2009).

Ude, S.; De La Mora, J.F. *J. Aerosol Sci.* **34**, 1245 (2003).

Urban, J.J.; Talapin, D.V.; Shevchenko, E.V.; Murray, C.B. *J. Am. Chem. Soc.* **128**, 3248 (2006).

Valentini, P.; Dumitrica, T. *Phys. Rev. B* **75**, 224106 (2007).

Van Buuren, T.; Dinh, L.N.; Chase, L.L.; Siekhaus, W.J.; Terminello, L.J. *Phys. Rev. Lett.* **80**, 3803 (1998).

Van De Walle, C.G.; Neugebauer, J. *Nature* **423**, 626 (2003).

Wang, D.W.; Wang, Q.; Javey, A.; Tu, R.; Dai, H.J.; Kim, H.; Mcintyre, P.C.; Krishnamohan, T.; Saraswat, K.C. *Appl. Phys. Lett.* **83**, 2432 (2003).

Watanabe, A.; Hojo, F.; Miwa, T. *Appl. Organomet. Chem.* **19**, 530 (2005).

Weber, J.R.; Janotti, A.; Rinke, P.; Van De Walle, C.G. *Appl. Phys. Lett.* **91**, 142101 (2007).

Wilcoxon, J.P.; Provencio, P.P.; Samara, G.A. *Phys. Rev. B* **64**, 035417 (2001).

Wilcoxon, J.P.; Samara, G.A.; Provencio, P.N. *Phys. Rev. B* **60**, 2704 (1999).

Wu, H.P.; Ge, M.Y.; Yao, C.W.; Wang, Y.W.; Zeng, Y.W.; Wang, L.N.; Zhang, G.Q.; Jiang, J.Z. *Nanotechnology* **17**, 5339 (2006).

Yu, D.; Wang, C.J.; Guyot-Sionnest, P. *Science* **300**, 1277 (2003).

Zacharias, M.; Fauchet, P.M. *Appl. Phys. Lett.* **71**, 380 (1997).

Zhu, J.G.; White, C.W.; Budai, J.D.; Withrow, S.P.; Chen, Y. *J. Appl. Phys.* **78**, 4386 (1995)

Appendix

A.1 Copyright permissions

Chapter 2 has been published in an American Institute of Physics (AIP) journal. The AIP copyright policy states that the authors maintain "the nonexclusive right, after publication by AIP, to give permission to third parties to republish print versions of the Article or a translation thereof, or excerpts therefrom, without obtaining permission from AIP, provided the AIP-prepared version is not used for this purpose, the Article is not published in another journal, and the third party does not charge a fee. All copies of the Article made under any of the Author Rights shall include notice of the AIP copyright."

Chapters 3 and 5 have been published in American Chemical Society (ACS) journals. The ACS copyright policy states that "ACS extends blanket permission to students to include in their theses and dissertations their own articles, or portions thereof,

that have been published in ACS journals or submitted to ACS journals for publication, provided that the ACS copyright credit line is noted on the appropriate page(s)."

A.2 Processing recipes

Thin silicon shadow masks. The following recipe describes the fabrication of shadow masks with feature sizes as small as 20 µm made from thin silicon wafers. The recipe requires a 50 mm diameter "mask" wafer that is 150 µm or thinner and a standard 100 mm "carrier" wafer to which the mask wafer will be glued during patterning and etching.

1. Clean and pre-bake mask and carrier wafer.
2. Spin HMDS, then S1805 (3000 rpm, 30 secs) onto carrier wafer and immediately place mask wafer onto tacky carrier wafer, aligning major flats. Press down.
3. Soft bake for 10 mins.
4. Bake in oven for 30 mins at 130 C.
5. Spin HMDS, then SPR-220-7 (3000 rpm, 30 sec) onto mask wafer (on carrier wafer).
6. Bake at 115 C for 95 sec.
7. Expose for 25 secs at gap of 25 um (hard contact).
8. Develop in CD26 long enough that all photoresist is visibly removed from patterned areas (~90 secs).
9. Hard bake 3 mins.
10. Etch for 75 mins (Bosch recipe) in deep trench etcher, or until through mask wafer (use Fowler gauge to check).
11. Soak in acetone overnight to separate wafers. May need to heat or sonicate.

Lift-off for depositing metal electrodes. The following recipe describes the fabrication of patterned metal electrodes on either glass or Si wafers. Features as small as 5 µm are achievable. The wafer is patterned with lift-off resist (LOR) and positive resist,

metal is deposited over the entire wafer, and the resist is removed leaving metal only in the areas where the wafer was exposed.

1. Clean and dry wafer.
2. Pre-bake (2 mins for Si, 5 mins for glass) above 100 C.
3. Spin LOR 3A @ 5000 rpm for 40 secs.
4. Soft-bake (2 mins for Si, 5 mins for glass) @ 190 C.
5. Spin S1813 @ 5000 rpm for 40 secs.
6. Soft-bake (2 mins for Si or glass) @ 115 C.
7. Expose for 4 secs using hard contact.
8. Develop in CD-26 for 45 secs. Rinse and dry. Features should be clear.
9. Bake (2 mins for Si, 5 mins for glass) @ 125 C.
10. Develop in CD-26 for 15 secs to remove LOR. Rinse and dry.
11. Evaporate metal.
12. Soak in 1165 Stripper overnight. Sonicate if necessary.

Preparation of FET substrates. Field-effect transistors (FETs) are made by depositing NC films onto heavily doped Si wafers with an oxide layer on the front and a Au contact on the back, and then depositing source and drain electrodes. Silicon wafers with 300 nm thermal oxide on both sides can be ordered from SVM. The oxide on the back of the wafer must be removed and replaced with a Au contact as described in this recipe to fabricate FET substrates.

1. Clean and dry wafer.
2. Pre-bake 2 mins above 100 C.
3. Spin S1818 @ 3000 rpm for 40 secs on front of wafer.
4. Soft-bake 3 mins @ 120 C.
5. Repeat 3 and 4 to have a thick protective layer over front of wafer.
6. Etch wafer in BOE for 8 mins (51 nm/min etch rate for SiO_2).
7. Rinse and dry.
8. Evaporate 15 nm Al or Cr followed by 75 nm Au *on back* of wafer.
9. Soak in acetone overnight to remove resist.
10. Rinse and dry.
11. Anneal in RTA at 550 C for 5 mins in H_2:N_2 to reduce barrier height to p-type Si. Don't anneal for n-type Si.